Design of Drug Delivery Methods for the

Brain and Central Nervous System

BY

ERIC LUESHEN
B.S., University of Nebraska-Lincoln, 2007

THESIS

Submitted as partial fulfillment of the requirements
for the degree of Doctor of Philosophy in Bioengineering
in the Graduate College of the
University of Illinois at Chicago, 2015

Chicago, IL

Defense Committee:

Prof. Andreas Linninger, Chair and Advisor
Dr. Marvin Rossi, Neurology, Rush University Medical Center
Prof. Urmila Diwekar, Bioengineering
Prof. James Patton, Bioengineering
Prof. Michael Cho, Bioengineering

ACKNOWLEDGEMENTS

First of all, I want to express my gratitude and sincere thanks to my advisor Prof. Andreas Linninger for his guidance and motivation throughout my research. I gained a wealth of knowledge through his tutelage in and out of his classroom and lab. I admire him for his work ethic and passion for the field of bioengineering.

I would also like to thank all of my thesis committee members for serving on my committee and for your valuable input during my preliminary exam. I would like to thank Dr. Marvin Rossi for sharing with me his knowledge of the brain and central nervous system, as well as for access to COMSOL software. I would like to thank Prof. Michael Cho, Prof. Urmila Diwekar, and Prof. James Patton for the immense amount of knowledge I gained through taking their courses.

I also extend my gratitude to all of my current and past lab colleagues: Indu, Sebastian, Kevin, Ian, Chih-Yang, Ying, Cierra, Sukhi, Brian, Nikhil, Seon, Andrej, Madhawa, Jeonghwa, Minh, Jacek, Joe, and Tejen. They provided valuable suggestions and critical reviews of my work especially during group meetings and private discussions.

I would like to acknowledge the invaluable support Indu, Joe, and Tejen provided me with in the intrathecal magnetic drug targeting research. Indu's knowledge of nanoparticle synthesis was necessary to the success of the project. Tejen and Joe helped with reproducing experiments and rebuilding more models. Without all of their help the research would not have progressed as quickly as it did.

I would also like to acknowledge the help I received from Andrej and Cierra throughout the pharmacokinetics research. These two were pivotal in our project's success. Andrej's programming of the parameter estimation, and Cierra's research into

pharmacokinetic scaling laws were major contributions to the success of this project. I would also like to extend my thanks to our collaborators at the Technical University of Denmark, Martina Heitzig, Prof. Rafiqul Gani, and Prof. Gürkan Sin, for their help with the computer-aided framework for facilitating the development of PBPK models.

Special thanks to Dr. Ankit Mehta, Dr. Bakhtiar Yamini, and Dr. Richard Penn for their valuable advice in convection-enhanced delivery. Also, thank you to Dr. Ali Alaraj for his input and guidance in my intrathecal magnetic drug targeting research.

I thank Prof. Gayle Woloschak, Prof. Tatjana Paunesku, and Prof. Wendelin Stark for offering their expertise in nanoparticle synthesis and characterization.

Lastly, I am extremely grateful to all of my family and friends whose invaluable support helped keep me motivated even in the most difficult of times throughout this process. Specifically, I would like to thank my grandma Pat, mom, dad, my two sisters Brandy and Cassie, Dave, and Justin. I would not be where I am today without your love, guidance, and support.

TABLE OF CONTENTS

LIST OF TABLES

LIST OF FIGURES

FIGURE **PAGE**

LIST OF ABBREVIATIONS

AD	Alzheimer's disease
BBB	Blood-brain barrier
CED	Convection-enhanced delivery
CNS	Central nervous system
CSF	Cerebrospinal fluid
DTI	Diffusion tensor imaging
EDS	Energy dispersive x-ray spectroscopy
IA-IT-MDT	Implant-assisted intrathecal magnetic drug targeting
IT	Intrathecal
IT-MDT	Intrathecal magnetic drug targeting
MNP	Magnetic nanoparticle
PBPK	Physiologically-based pharmacokinetics
PD	Parkinson's disease
PK	Pharmacokinetics
SQUID	Superconducting quantum interference device magnetometry
TEM	Transmission electron microscopy

SUMMARY

Due to the impermeability of the blood-brain barrier (BBB) to macromolecules delivered systemically, drug delivery to the brain and central nervous system (CNS) is quite difficult and has become an area of intense research. Techniques such as convection-enhanced intraparenchymal delivery and intrathecal magnetic drug targeting offer a means of circumventing the blood-brain barrier for targeted delivery of therapeutics. This dissertation focuses on three aspects of drug delivery: pharmacokinetics, convection-enhanced delivery, and intrathecal magnetic drug targeting.

Classical pharmacokinetics mainly uses black-box curve fitting techniques without biochemical or biological basis. This dissertation advances the state-of-the-art of pharmacokinetics and pharmacodynamics by incorporating first principles and biochemical/biotransport mechanisms in the prediction of drug fate *in vivo*. A whole body physiologically-based pharmacokinetics (PBPK) modeling framework is engineered which creates multiscale mathematical models for entire organisms composed of organs, tissues, and a detailed vasculature network to predict drug bioaccumulation and to rigorously determine kinetic parameters. These models can be specialized to account for species, weight, gender, age, and pathology. Systematic individual therapy design using the proposed mechanistic PBPK modeling framework is also a possibility.

Biochemical, anatomical, and physiological scaling laws are also developed to accurately project drug kinetics in humans from small animal experiments. Our promising results demonstrate that the whole-body mechanistic PBPK modeling approach not only elucidates drug mechanisms from a biochemical standpoint, but offers better scaling precision. Better models can substantially accelerate the introduction of drug leads to

clinical trials and eventually to the market by offering more understanding of the drug mechanisms, aiding in therapy design, and serving as an accurate dosing tool.

Convection-enhanced drug delivery (CED) is a technique used to bypass the BBB via direct intracranial injection using a catheter driven by a positive pressure gradient from an infusion pump. Although CED boasts the advantage of achieving larger drug distribution volumes compared to diffusion driven methods, difficulty in predicting drug spread and preventing backflow along the catheter shaft commonly occur. In this dissertation, a method for predicting drug distributions in the brain using diffusion tensor imaging (DTI) data is employed to show how small variations in catheter placement can lead to drastically different volumes of drug distribution *in vivo*. The impact that microfluid flow has on deformable brain phantom gel is studied in order to elucidate the causes of backflow, and the results are used to develop backflow-free catheters with safe volumetric flow rates up to 10 μl/min. Through implementation of our backflow-free catheter designs, physicians will be able to target specific regions of the brain with improved accuracy, increased drug concentration, and larger drug distribution geometries.

Intrathecal (IT) drug delivery involves direct drug infusion into the spinal canal and has become standard practice for treating many CNS diseases. Although IT drug delivery boasts the advantage of reduced systemic toxicity compared to oral and intravenous techniques, current IT delivery protocols lack a means of sufficient drug targeting at specific locations of interest within the CNS. In this dissertation, the method of intrathecal magnetic drug targeting (IT-MDT) is developed to overcome the limited targeting capabilities of standard IT drug delivery protocols. The basic idea behind IT-MDT is to guide intrathecally injected, drug-functionalized magnetic nanoparticles (MNPs) using an

external magnetic field to diseased regions within the spinal canal. Cerebrospinal fluid (CSF) transport phenomena are studied, and *in vitro* human spine surrogates are built. Experiments are run on the *in vitro* human spine model to determine the feasibility of IT-MDT and to develop novel treatment therapies. Computer simulations are performed to optimize magnetic field placement and/or implant design for generating high gradient magnetic fields, as well as to study how these fields aid in therapeutic nanoparticle localization.

Large collection efficiencies of MNPs were achieved during *in vitro* IT-MDT and implant-assisted IT-MDT experiments with concentration levels nearly nine times that of the control when no magnetic field was present. Testing different magnetizable implants showed that implant design is a key factor in achieving the largest MNP collection efficiency within the targeting region. Knowledge gained from the *in vitro* IT-MDT experiments and simulations will be used in the future to develop IT-MDT methods in animals and humans.

1. INTRODUCTION

1.1. Summary

Drug delivery to the brain and central nervous system (CNS) is an area of intense research due to the difficulty of delivering large molecular weight therapeutics across the blood-brain barrier (BBB) when administered systemically. Although many drugs for treating neurodegenerative and other diseases have been proven effective *in vitro*, physicians have a hard time proving drug efficacy *in vivo* because reaching therapeutic levels within the brain and CNS is greatly hindered by the BBB. The hypothesis of this dissertation is that drug delivery is an engineering problem, which lacks an engineering approach and theoretical framework. Therefore, improved methods of drug delivery to the brain and CNS are warranted. This dissertation was designed to create a theoretical and experimental framework for three aspects of drug delivery: pharmacokinetics, convection-enhanced delivery, and intrathecal magnetic drug targeting. The outcomes of this research aim to provide more efficient methods for the treatment of neurodegenerative disorders, brain cancer, spasticity, chronic pain, and other diseases.

1.2. Motivation

1.2.1. Drug delivery to the brain and CNS

More than 600 disorders afflict the central nervous system (6). These disorders are often associated with atrophy of nervous system structures, and they affect millions of people worldwide. The two most common types of neurodegenerative disorders are Alzheimer's disease and Parkinson's disease (7). Primary brain and CNS tumors are also becoming more prevalent.

Alzheimer's Disease (AD) and Parkinson's Disease (PD) collectively effect 6 million people within the United States, and around 42 million people worldwide (8–10). These numbers are expected to grow substantially as the average age of the population increases. The current estimated cost of providing care for both AD and PD patients in the U.S. is $215 billion per year (11). It is also estimated that more than 688,000 people are currently living with a diagnosis of a primary brain or CNS tumor in the United States, and 68,470 new cases are expected to be diagnosed in 2015 (12,13).

Drug administration to the central nervous system for treatment of the above mentioned diseases is a challenge due to the highly selective and efficient barrier protecting the brain known as the blood-brain barrier (BBB). Almost 100% of large-molecule drugs and more than 98% of all small-molecule drugs do not penetrate the BBB (14). There are two important characteristics for small-molecule drugs to potentially cross the BBB: high lipophilicity and a molecular mass no greater than 500 Da (15). Many neurodegenerative diseases remain under-treated by effective therapies due to the inability of commonly used drugs to cross the BBB; not because there is a lack of candidate drugs to treat the diseases (16). Therefore, alternative methods to effectively deliver neurotherapeutics and target specific regions of the brain and CNS are necessary.

1.2.1.1. ***Convection-enhanced delivery***

Convection-enhanced delivery (CED) is a localized drug delivery technique used to target specific regions of the brain for the treatment of cancer and neurodegenerative diseases that bypasses the blood-brain barrier. An intracerebral catheter is placed with a continuous infusion of therapeutic molecules that are propelled to the site of drug delivery within the parenchyma through a pump. CED directly distributes therapeutic agents to a

specific target area at dramatically increased doses and has been shown to achieve much larger drug distribution volumes compared to diffusion driven methods (99,126). These major advantages of CED offer great potential for more efficient treatment of neurodegenerative diseases such as Alzheimer's and Parkinson's, as well as for the treatment of brain tumors.

Even with all of the advantages CED has to offer, clinical trials treating gliomas that utilized CED, such as the TransMID and PRECISE trials, have failed to demonstrate statistically significant improvement in survival (17) despite the proven efficacy of therapeutic agents in animal models (18,19). Retrospective analysis of the PRECISE trial found that infusate distribution was highly variable among patients; therefore, any potential efficacy of drugs delivered by CED may be hindered by ineffective delivery (20–22). One of the inherent engineering challenges involved with CED is known as backflow, which has a large impact on infusate distribution volumes and geometries. Backflow is characterized by fluid discharge along the catheter shaft instead of distally into the soft tissue. In order to prevent the possibility of backflow, low volumetric flow rates are applied which limit the achievable drug distribution volumes from CED. This can render CED treatment ineffective since a small convective flow rate produces a narrow drug distribution inside the treatment region. The causes of backflow need to be determined, and more efficient catheter designs and CED protocols are needed to expand the drug distribution inside the treatment region. This is especially important when administering toxic chemotherapeutics which could adversely affect other brain regions when backflow occurs, as well as not reach a therapeutically efficacious concentration within the target region due to backflow.

1.2.1.2. ***Intrathecal magnetic drug targeting***

Intrathecal (IT) drug delivery is a technique which involves the direct infusion of therapeutic molecules into the cerebrospinal fluid (CSF) filled space within the spinal canal. IT delivery is advantageous because the drugs bypass the blood-brain barrier. Furthermore, drugs experience a longer half-life within the CSF since they encounter minimal protein binding and are not exposed to the same enzymatic activities which systemically administered drugs face within the blood (213). Current implications for IT drug delivery include leptomeningeal metastases (149–151), spasticity (152), pain management (153), and spinal anesthesia (154,155). For example, clinical studies on pain management show that IT delivery provides ideal pain control with fewer side effects, while using only a small fraction of the dose required when the drug is administered orally or intravenously (159,214). The IT delivery of neurotrophic factors has also been deemed a promising treatment for neurodegenerative diseases such as amyotrophic lateral sclerosis (ALS), Huntington's disease, and Parkinson's disease (156,157,215). Upon IT drug administration, the drugs are rapidly dispersed within the spinal canal by both molecular diffusion and by the pulsatile motion of CSF (157,178).

Standard intrathecal drug delivery methods rely mainly on empirical observations. The use of current IT guidelines cannot guarantee reproducible outcomes or desired therapeutic concentrations in specific target regions of the spinal canal (157,231). Due to variability in patients' spinal anatomy, as well as the frequency and magnitude of their CSF pulsations, maintaining a therapeutic dose within the targeted region while attempting to avoid systemic toxicity is a major challenge and disadvantage of standard IT delivery methods (178). Current IT protocols require continuous drug infusion in order to maintain

a sufficiently high drug concentration at the target site despite drug distribution throughout the entire central nervous system leading to harmful side effects. For many CNS diseases like leptomeningeal metastases, the effected tissue is located in specific regions of the spinal canal; therefore, a method to target these regions is warranted.

To maximize the therapeutic effect without excessive risk of toxicity in non-targeted zones, the intrathecally injected drugs should be concentrated at specific locations within the spinal canal. At this point there is no delivery technique to confine drugs locally, where it is needed in high concentrations, without having large amounts of drug spread throughout the entire brain and spinal canal, which may cause side effects.

This dissertation proposes the ideas of intrathecal magnetic drug targeting (IT-MDT) and implant-assisted intrathecal magnetic drug targeting (IA-IT-MDT) to achieve localized, high concentrations of magnetic nanocarriers which can be functionalized to different drugs to overcome the limitations of standard IT drug delivery. IT-MDT builds on the method of magnetic drug targeting (MDT), which is a type of active drug targeting method utilizing drug-functionalized magnetic nanoparticles localized to a target region by use of an external magnetic field. The most notable benefits of MDT reside in local drug action and minimization of systemic side effects. Until now, MDT methods have been mainly used to target drugs delivered systemically through blood vessels and have shown great promise (161–169). The novelty of our approach lies in applying the methods of MDT within the CSF-filled spinal canal, not in blood vessels, in order to achieve a localized therapeutic effect using much smaller drug doses and substantially reducing systemic toxicity for novel treatments of CNS diseases.

1.2.2. **Physiologically-based pharmacokinetic models for systemic delivery analysis**

Pharmacokinetic (PK) models aim to establish relationships between drug administration, bioaccumulation, and elimination from dose-response measurements *in vivo*. Typical PK models fit parametric functions with multiple adjustable constants or exponential coefficients (18–20). Non-mechanistic parameters such as volume of distribution, area under the curve (*AUC*), and the intrinsic clearance rates are usually computed. These classical PK models derive little information about drug reaction kinetics and biotransport phenomena; they also do not satisfy conservation laws, so that drug species balances are not necessarily closed. There is a critical need in the pharmaceutical industry for methods which link modeling, simulation, drug approval, and rigorous experimental data analysis (26).

Several authors have since proposed whole body physiologically-based pharmacokinetic (PBPK) prediction and modeling techniques (2,23–25). PBPK models include several biological subsystems such as blood, the lymphatic and the central nervous system, tissues and organs, which can further be subdivided into multiple phases including cells and interstitial fluid. PBPK models are accepted as a recommended approach for inter- and intra-species extrapolations and to simulate pharmacokinetic profiles for various administration modes and dose regimes. These models incorporate data from many sources such as biochemical, physiological, and drug-dependant parameters for various species, individuals, or with pathological changes (31). In the literature, compartmental PBPK models are typically stipulated as a set of interconnected vessels with ideal mixing, where both biochemical and transport mechanisms are given as black-box, empirical relations. The kinetics of novel drugs can be studied more systematically with *mechanistic*

biochemical models in entire organisms. Prediction accuracy in PK models could also be greatly improved by the incorporation of conservation laws, and fundamental transport and biochemical reaction mechanisms, which is beyond the scope of black-box approaches. Several authors have recently used first principles modeling to elucidate the biochemical reaction mechanisms of new drugs *in vivo* (29–36). Their model topology does not account for the physiologically consistent blood or lymph perfusion, in the arteries, capillaries, and veins of individual organs. Consequently, simulation of blood sampling techniques is imprecise, involving significant errors of pharmacokinetic parameter estimates. These errors limit the fidelity of the previous PBPK models for the extrapolation of information from small animals to larger ones, from animals to humans, or for the prediction of drug fate for varying dosing regimes.

1.2.2.1. ***Mechanistic PBPK models with empirical scaling laws***

Traditional *interspecies scaling laws* in pharmacokinetics often deploy simple polynomial relationships between properties of interest such as the intrinsic clearance. The *allometric approach* is empirical, and rests on the assumption that the underlying physiological processes such as cardiac output, heartbeat frequency, and breath duration, are only related to body mass (72). Typical empirical relations for interspecies scaling include: clearance versus body weight, the product of clearance and maximum life-span potential versus body weight, the product of clearance and brain weight versus body weight, and the application of a fixed exponent to clearance (72). Interesting research from Geoffrey West and colleagues about allometric scaling laws in biology shows early attempts to incorporate first principles into determining whole organism metabolic rates in different animals. In particular, West's group developed a model to explain the origin of quarter-

power scaling laws and there use in determining metabolic rates when organism body sizes vary over large orders of magnitude (73,74). Unfortunately, interspecies extrapolation with these simple scaling laws is not satisfactory because it does not account for fundamental biochemical mechanisms, but merely incorporates weight or size factors. It is difficult to predict drug fate for different dosing regimes using non-mechanistic PK models (22). Due to the limitation in predictive capabilities, expensive, and time-consuming dose-response data have to be acquired in extensive animal trials in rats, then dogs and monkeys, until finally arriving at reasonably safe specifications for human trials. Consequently, there is an urgent need in the pharmaceutical industry to develop mechanistic pharmacokinetic (PK) models able to both expedite knowledge gain from experimental trials and, simultaneously, address safety concerns.

1.2.2.2. ***Multiscale mechanistic PBPK model with mechanistic intra- and inter-species scaling***

We propose a multiscale biological system model to describe the drug fate in: cells, tissues, organs, whole body, among individual subjects, and across species. Our model solves the problem of rigorously estimating unknown biochemical reaction and transport parameters from *in vivo* datasets and identifying whole body physiologically-based pharmacokinetic (PBPK) models. These parameters may be scaled according to fundamental chemical and physical principles to create a consistent and rigorous pharmacokinetic model with better predictive capabilities than classical black-box pharmacokinetics.

Our approach uses a first principles PBPK model as a starting point, enforcing the conservation laws and reaction and mass transfer mechanisms based on the scaled

parameters. Therefore, the prediction of the bioaccumulation will not result from simple algebraic scaling but will be the outcome of solving the entire network using the scaled parameters for each category. Such a model is capable of addressing both physiological as well as biochemical and transport variations between each species *with much higher accuracy than can be expected from simple allometric scaling laws*. Better models like the one we propose can substantially accelerate the introduction of drug leads to clinical trials and eventually to the market by offering more understanding of the drug mechanisms, aiding in therapy design, and serving as an accurate dosing tool.

1.3. **Specific Aims**

In debilitating diseases of the central nervous system (CNS), treatment protocols which use systemic drug delivery are limited due to the impermeability of the blood-brain barrier (BBB). Therefore, improved methods of targeted drug delivery are warranted. The outcomes of this dissertation will be as follows: a first principles pharmacokinetic modeling framework with novel interspecies scaling laws, backflow-free catheters for more efficient convection-enhanced intraparenchymal drug delivery, and an intrathecal magnetic drug targeting protocol for improved treatment of CNS diseases. The overall vision of the project aims at improved therapy options for patients suffering from diseases such as brain cancer, spasticity, chronic pain, and other neurodegenerative diseases including Alzheimer's Disease and Parkinson's Disease. The specific aims are as follows:

1.3.1. **Engineer a first principles physiologically-based pharmacokinetic modeling framework for analysis of systemic drug delivery to the CNS**

A novel whole body physiologically-based pharmacokinetics (PK) modeling framework is developed in order to advance the prior black-box PK models by incorporating first principles, conservation of mass, species and momentum, and biochemical/biotransport mechanisms for the prediction of drug fate *in vivo*. A rat blood circulation model was constructed and combined with biotransport, biochemical reactions and metabolism of the immunosuppressant Cyclosporin. The proposed methodology was demonstrated on a case study in male Sprague Dawley rats. A rigorous parameter estimation technique was used to derive the unknown rate parameters from actual drug dose–response experiments in animals. A mathematical programming technique was used for solving the transport and kinetic inversion problem. Key PK parameters were determined to establish drug biodistribution dynamics in all organs and tissues. Prediction of organ drug bioaccumulation as a function of cardiac output, physiology, pathology or administration route is possible with the proposed PBPK framework. Biochemical, anatomical and physiological scaling laws were developed which yield more reliable interspecies and intraspecies extrapolation of drug biodistribution. This work, which resulted in two refereed journal publications (23,24) and three refereed conference proceedings articles (25–27), demonstrated how the whole-body PK modeling approach not only elucidates drug mechanisms from a biochemical standpoint, but offers better confidence in scaling.

1.3.2. **Transport phenomena of convection-enhanced delivery and design of backflow-free catheters**

The second stage of this dissertation was devoted to studying the transport phenomena and drug distribution variability which occurs during convection-enhanced intraparenchymal drug delivery. Physiological and geometric properties of heterogeneous and anisotropic rat brain tissue were obtained from diffusion tensor imaging (DTI) datasets. These DTI datasets helped to construct physiologically consistent transport tensors for nanoparticle and bulk fluid transport within the brain tissue. Computer-assisted image reconstruction was conducted, and simulations were performed using computational fluid dynamics software. *In vitro* CED of trypan blue dye into agarose gel brain phantoms was performed to aid in the understanding of CED transport phenomena. *In vivo* CED of fluorescent nanoparticles into rat striatum was performed, and the distribution geometry was examined histologically with fluorescence microscopy. Knowledge gained from *in silico*, *in vitro*, and *in vivo* CED experiments was then used to design and test novel backflow-free catheters. This work, which resulted in four refereed journal publications (20,28–30), aided in understanding the transport phenomena during CED as well as in the engineering of several novel catheter designs.

1.3.3. **Development of intrathecal magnetic drug targeting methods**

The third stage of this dissertation aims at developing the methods of intrathecal magnetic drug targeting (IT-MDT) and implant-assisted IT-MDT (IA-IT-MDT) in order to increase the targeting capabilities of intrathecally administered drugs for more efficient treatment of CNS diseases. Intrathecal drug transport phenomena were studied, *in vitro*

human spine surrogates were built, magnetic nanoparticles were synthesized, and *in vitro* experiments were performed. Optimization of magnetic field placement and implant design was also studied computationally. This work, which resulted in two refereed journal publications (31,32) and one refereed conference proceedings article (33), offers great promise for improved treatment methods of CNS diseases upon further validation *in vivo*.

2. FIRST PRINCIPLES PHYSIOLOGICALLY-BASED PHARMACOKINETIC MODELING

2.1. Abstract

Unknown dose regimes are typically assessed on animals prior to clinical trials. Recent advances in the evaluation of new leads' efficacy have been achieved by pharmacokinetic modeling. Further improvements, including determination of the drug's mechanism of action and organism biodistribution, require an effective methodology for solving parameter estimation challenges. This research solves the problem of rigorously estimating unknown biochemical reaction and transport parameters from *in vivo* datasets and identifying whole-body physiologically based pharmacokinetic (PBPK) models.

A rat blood circulation model was combined with biotransport, biochemical reactions and metabolism of the immunosuppressant Cyclosporin. We demonstrate the proposed methodology on a case study in Sprague-Dawley rats by bolus *iv* injections of 1.2, 6 and 30 mg/kg. Key pharmacokinetic parameters were determined, including renal and hepatic clearances, elimination half-life, and mass transfer coefficients, to establish drug biodistribution dynamics in all organs and tissues. This multi-scale model satisfies first principles and conservation of mass, species, and momentum.

Prediction of organ drug bioaccumulation as a function of cardiac output, physiology, pathology or administration route may be possible with the proposed PBPK framework. Successful application of our model-based drug development method may lead to more efficient preclinical trials, accelerated knowledge gain from animal experiments, and shortened time-to-market of new drugs.

2.2. **Introduction**

The effect of novel drugs on targeted organs is typically studied in animal drug dosing trials. Pharmacokinetic models establish relationships between drug dosage, bioaccumulation and clearance utilizing dose-response measurements. Classical pharmacokinetic (PK) models relate anatomy and physiology parametrically to dose-response data while fitting exponential functions with multiple adjustable constants or exponential coefficients (34–36). The resulting black-box formula permit the computation of the area under the curve (AUC), the plasma half-life of elimination ($t_{1/2}$) or the intrinsic clearance rates. Limitations are observed when fitted relations are used to extrapolate drug concentration profiles for different doses (37).

Non-mechanistic, classical PK methods derive very little information about reaction kinetics and biotransport phenomena. It is reportedly difficult to scale or extrapolate information among laboratory animals or to predict drug fate for different dosing regimes (38). Hence, large sets of dose-response data have to be acquired in extensive animal trials in rats, then dogs and monkeys, until finally arriving at reasonably safe specifications for human trials. Prediction accuracy in PK models could be greatly improved by the incorporation of conservation laws, and fundamental transport and biochemical reaction mechanisms, which is beyond the scope of black-box approaches.

The efficacy of novel drugs can be studied more systematically with mechanistic biochemical models. Several authors have proposed whole body physiologically-based pharmacokinetic (PBPK) prediction and modeling techniques (2,39–41). A thorough review of whole body physiologically-based pharmacokinetic models (42) recognizes the need for methods linking modeling, simulation, drug approval and rigorous experimental

data analysis. Previous work commonly deployed compartments, typically encompassing several biological subsystems such as blood, plasma, red blood cells, interstitial fluid, the lymphatic system, the central nervous system, tissues and organs (43).

One possible scenario for drug fate modeling in the whole body is to determine the drug transport parameters by *in vitro* measurements, for instance with tissue-to-plasma partitioning coefficients (4,44). However, these compartmental models typically do not account for the physiologically consistent blood perfusion or lymphatic fluid exchange patterns.

Several authors have recently used first principles modeling to elucidate the biochemical reaction mechanisms of new drugs *in vivo* (45–52). Although mechanistic, the underlying algorithms commonly infer systemic circulation with a set of continuity and conservation differential equations. Every part of the whole body flow network has to be entered manually. This soon leads to infeasibility if multiple animal models need to be tested.

In contrast, our improved workflow ensures that for arbitrarily complex PBPK networks with hundreds of biological “compartments”, corresponding differential equations are automatically generated and validated. This allows for testing various circulatory system configurations with greater detail as more data become available on the drug-organ interactions. Given solid data describing individual pharmacokinetic processes, the selection of an accurate but general mechanistic model still remains a scientific challenge.

In this chapter a rigorous engineering approach based on first principles of mass, species and momentum conservation is proposed to build upon the advances in classical

PK modeling. The presented work aims at determining drug reaction kinetics and transport phenomena from actual experimental dose-response measurements. To scientifically examine drug fate in living organisms, we emphasize the need for a closed loop iterative methodological approach: i) obtaining experimental data, ii) constructing first principle models iii) estimating parameters and iv) gaining insights from comparing working hypotheses with experimental sets.

We will demonstrate the advantages of our methodology with a case study on the immunosuppressant Cyclosporin. Our advanced mechanistic model results in a rigorous analysis of biodistribution after a bolus iv injection into a rat. The model will also be used to assess different administration regimes, which in the case of Cyclosporin have been shown to enormously affect interactions with physiology, cardiovascular dynamics and pharmacology (5,39,53,54). We hope to contribute an improved level of understanding in such a complex topic.

This chapter is organized as follows. Section *Mathematical Formulation of Whole Body Pharmacokinetics* lays out the conceptual foundation: (i) steady state systemic blood circulation model, (ii) mechanistic transport, mass transfer and biochemical reaction parameters, and (iii) a parameter estimation technique for determining the unknown model parameters from actual animal experiments. The application of this concept is demonstrated with a case study on Cyclosporin in section 2.4. Results are discussed in section 2.5.

2.3. **Mathematical Formulation of Whole Body Pharmacokinetics**

This section introduces our PBPK model with inherent first principles intraspecies scaling, an overview of which is shown in Figure 1. We present a living system model which predicts the drug biodistribution among individual subjects of the same species, in an organism, organs, tissues, and cells.

1. *Intraspecies scaling* is accomplished by application of physiological and morphological differences onto the underlying first principles PBPK model.
2. *Whole body drug dynamics* results from application of initial and boundary conditions onto the underlying system, for instance dose regime or weight of subject.
3. *Biodistribution in organs* is given by physiology, blood circulation, fat and muscle content. These parameters are obtained experimentally.
4. Drug transiency in tissues is characterized by biotransport through capillary walls into the interstitium. Biotransport is a function of the size of mass transfer area while the specific mass transfer rate of blood-organ interface may be constant. By solving for unknown specific mass transfer rates, tissue:plasma partition coefficients can be calculated.
5. Drug fate on the cellular level is determined by selected biochemical reactions. Metabolism will be scaled according to chemical principles. Metabolic action has to be studied independently and is usually observed in renal cells, hepatocytes or on cytochromes.

We will introduce a *rigorous parameter estimation technique* for deriving the unknown rate parameters from actual drug dose-response experiments in animals. A mathematical programming technique for solving the transport and kinetic inversion problem will be discussed.

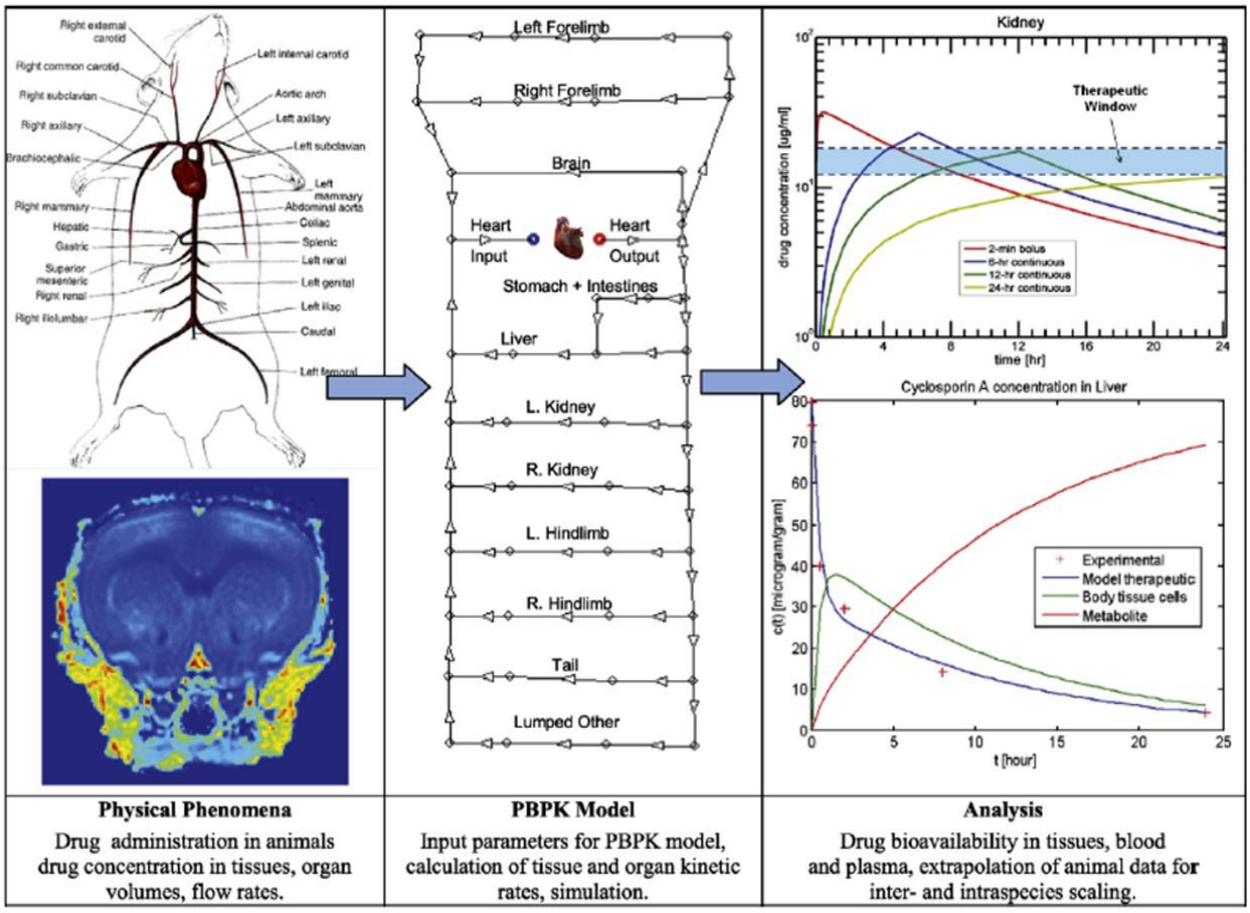

Figure 1. Overview of the "pharmacokinetic modeling framework" and its components. This physiologically based pharmacokinetic model seeks to determine the drug fate in the entire organism through three mechanisms: Systemic blood circulation based on anatomical and physiological facts, biotransport and mass transfer between blood, extracellular space and cytosol, and biochemical reactions accounting for the metabolism of specialized organ cell lines.

Table 1. List of symbols used.

Symbol	*Units*	*Description*	*Type*
Variables and parameters			
c	(µg/ml)	Modeled drug concentration, c_H, c_P, c_A, c_Q, c_M	State variable
$\hat{c}$	(µg/ml)	Experimental drug concentration	State variable
t	(h)	Time	Independent var.
F	(ml/h)	Volumetric flow rate	State variable
V	(ml)	Volume	Parameter
k		Vector of kinetic rates	Design variable
k_{A^+}	(h^{-1})	Kinetic rate of binding from plasma unbound to plasma bound	Design variable
k_{A^-}	(h^{-1})	Kinetic rate of unbinding from plasma bound to plasma unbound	Design variable
k_{H^+}	(h^{-1})	Kinetic rate of binding from plasma unbound to hematocrit	Design variable
k_{H^-}	(h^{-1})	Kinetic rate of unbinding from hematocrit to plasma unbound	Design variable
k_{Q^+}	(m^3h^1)	Kinetic rate of mass transfer from plasma unbound to organ	Design variable
k_{Q^-}	(m^3h^1)	Kinetic rate of mass transfer from organ to plasma unbound	Design variable
k_M	(h^{-1})	Kinetic rate of drug elimination	Design variable
$\hat{\kappa}$		Optimal set of kinetic rate parameters	Design variable
f_P	(vol/vol)	Volume fraction of unbound plasma compartment in plasma	Design variable
f_A	(vol/vol)	Volume fraction of bound plasma compartment in plasma	Design variable
f_H	(vol/vol)	Volume fraction of red blood cells in blood (hematocrit)	Design variable
F_{in}	(ml/h)	Blood flow into a vascular segment	Design variable
F_{out}	(ml/h)	Blood flow out of a vascular segment	Design variable
I	(µg/h)	Drug delivery rate	Design variable
$\dot{R}$	(µg/h)	Reaction term	Design variable
$t_{1/2}$	(h)	Half-life of elimination	State variable
m	(µg)	Mass of drug	State variable
y		Vector of state variables	State variable
A	(m^2)	Surface of mass exchange	State variable
U	(m/s)	Mass transfer coefficient from plasma	State variable
S		Sensitivity matrix	State variable
Φ		Objective function value	State variable
Λ		Variance-covariance matrix	State variable
Ψ		Functional matrix of physiological parameters	Function
τ		Student's t-function	Function
Indices			
B		Blood	Subscript
P		(Volume) fraction of unbound drug in plasma	Subscript
A		(Volume) fraction of bound drug in plasma	Subscript
H		Hematocrit (red blood cells)	Subscript
Q		Organ, tissue	Subscript
M		Metabolites	Subscript
IF		Interstitial fluid in organ or tissue	Subscript
TC		Tissue cells	Subscript
0		Subscript for initial conditions	Index
i		Index over a vasculature segment	Index
j		Index over an organ	Index
k		Index over a clearance term	Index
in		Inflow into a vascular segment	Index
out		Outflow from vascular segment	Index
$+$		Superscript, denoting increase of concentration in compartment	Index
$-$		Superscript, denoting decrease of concentration in compartment	Index

2.3.1. **Steady state model**

Rapid systemic drug distribution is mainly due to the convection of blood, lymph or cerebrospinal fluid. The fluid circulation can be mathematically modeled as directed, cyclic graphs (55). To introduce the principle, the first layer of our multiscale pharmacokinetic model elaborates only a systemic blood circulation network disregarding the lymph or cerebrospinal fluid flow for which the same algorithm would be applied. The network graph holds blood pressures at the vertices and computed blood flow rates at the edges, as described by fluid momentum equations. The solution of the steady state equations gives the volumetric blood perfusion rates and blood pressures.

The blood circulation network has given pressure boundaries for the heart represented by two atria and two ventricles. The large vessels of the vascular system are composed of simple cylindrical segments, with known radii, lengths and flow resistances. The organs' blood supply is maintained by segments with calculated equivalent hydraulic properties from Eq. (1), so that physiologically consistent perfusion rates (1) and pressure drops are ensured. Each organ's blood supply is further divided into arterial, capillary and venous sections. The distribution of blood flow resistances to these three parts is estimated according to known physiological data (1,3).

2.3.1.1. ***Blood flow***

The blood flow in large arteries and veins may be approximated by the Hagen–Poiseuille equation, as a function of radius (r), length (L) and flow resistance (α) as in Eq. (1). We assume this model for all blood vessels in the body.

$$\Delta P = \alpha F = \frac{8\mu L}{\pi r^4} F \qquad (1)$$

Here, ΔP is the pressure drop along a segment, F is the volumetric blood flow rate, and μ is the dynamic viscosity of blood.

2.3.1.2. ***Systemic circulation network***

To complete the systemic circulatory model and close the mass balances, flow rates through the different organs and tissues, pressure drops and physiological blood perfusion rates, as well as the systemic resistances for tissues and organs of juvenile, adult and aged animals were incorporated (1,3). Figure 2 depicts the steady state systemic blood circulation model designed for the Sprague-Dawley rat based on experimentally validated physiological values for twelve main organs to match total cardiac output, arterial, capillary and venous blood pressures and organ perfusion rates.

2.3.2. **Transient drug biotransport**

Drug biodistribution is dynamic with regard to time and space. The differential equations of the species transfer between the blood, plasma and organs are described in the next section and are outlined in Figure 3. What we create does not need to be an exact representation but rather a useful one that leads us with the least effort to correct decisions, thus improving the drug fate prediction capabilities.

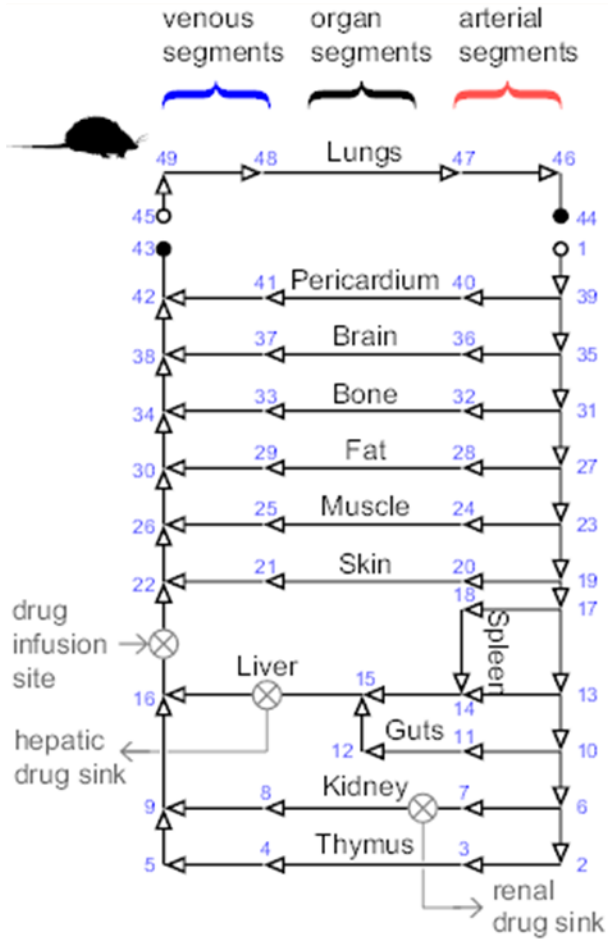

Figure 2. Diagram of a circulatory system model consisting of arterial, venous and capillary segments in a Sprague-Dawley rat. The circles denote constant pressure boundary conditions at heart ventricles, the arrows represent vascular segments, the numbers mark nodes of a segment. Twelve organs/tissues are included in the model with corresponding weights and volumes. The drug delivery sites can be defined arbitrarily as sources in the model equations. Drug elimination and excretion takes place in liver and kidneys. Each organ is further modeled with several blood and tissue compartments as depicted in Figure 3.

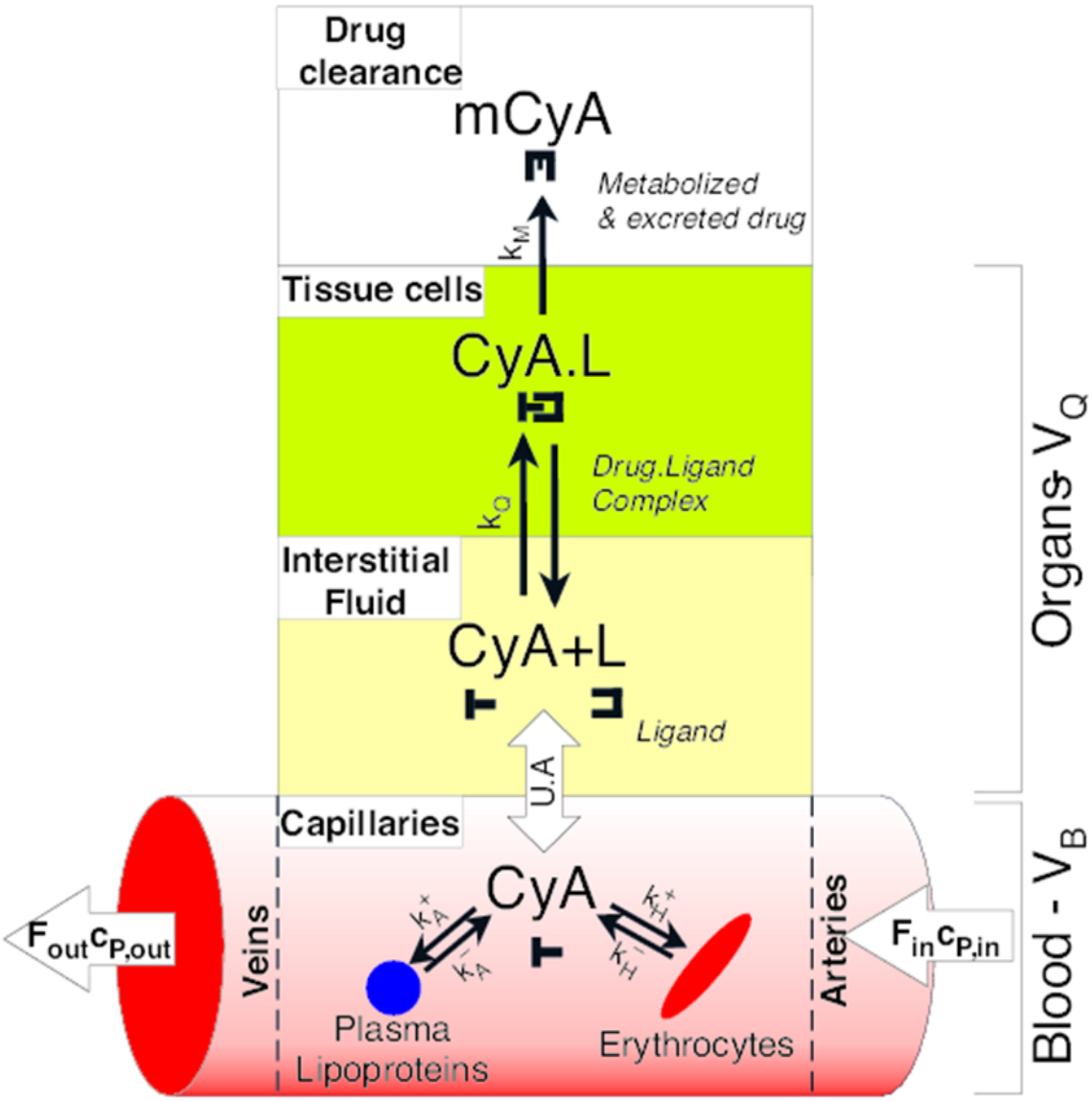

Figure 3. A compartmental model example of the Cyclosporin (*CyA*) physical mass transfer from unbound plasma fraction (c_P) through the capillary membrane into the interstitial fluid and the tissue cells. It is assumed that cyclophilin ligands (*L*) bind with the drug reversibly by an equilibrium reaction to form a ligand-protein complex (*CyA.L*). The drug is only available for mass transfer in blood or interstitial fluid while in the unbound state (*CyA*). In plasma, it binds reversibly to red blood cells, with concentration c_H, and to the plasmic proteins/lipids, termed "drug bound in plasma" with concentration c_A. The convective transfer of drug into the capillaries is mediated by blood flow with the inflow concentrations of unbound drug in plasma $c_{P,in}$, $c_{A,in}$, $c_{H,in}$ and the outflow concentrations $c_{P,out}$, $c_{A,out}$, $c_{H,out}$. The concentration of drug in the organ, c_Q needs to be determined from the unknown overall mass transfer rate (U) and the total mass transfer area (A). V_B is the volume of the blood segment, f_P the fraction of unbound plasma compartment, V_Q the volume of organ or tissue and *mCyA* is the concentration of the metabolite.

2.3.2.1. ***Cyclosporin pharmacokinetics***

Cyclosporin is an immunosuppressive exogenous drug and is described as a cyclic nonribosomal peptide of eleven amino acids, with relatively low molecular mass (1202.61 g/mol) and high lipophilicity (log $P_{octanol:water}$ = 2.92) (56). It may be administered to suppress a patient's immune response in allograft transplantations. The exact action mechanism of Cyclosporin is not known. Experimental evidence suggests that immunosuppression is due to specific and reversible inhibition of immunocompetent lymphocytes in the *G0* or *G1* phase of the cell cycle (57). T-lymphocytes are preferentially inhibited. Cyclosporine also inhibits the production and release of lymphokines including interleukin-2 (IL-2) and T-cell growth factor (TCGF). The presence of membrane-associated proteins which stereospecifically bind Cyclosporin and react with anti-cyclophilin antibodies has been documented in rat and human tissues *in vitro* (57–59).

Because the main route of Cyclosporin elimination in animals and humans is through hepatic metabolism, and since less than 1% of an administered dose is excreted in the urine unchanged, the systemic clearance can be said to equal metabolic clearance *and possibly hepatic clearance* as well (60). Overall Cyclosporin mass excreted through the GI tract of rats over a period of 24 hours is only a minute fraction; therefore, it can be neglected (40,61).

Several authors point out that Cyclosporin also metabolizes in the gastrointestinal tract mainly through Cytochrome P450. We assume that the fraction of these GI tract metabolites is minimal when compared to hepatic and renal excretion and other tissues' metabolites (62,63).

2.3.2.2. ***PBPK model assumptions***

It is assumed that the drug is delivered intravenously, and therefore mathematically modeled as a source term in the free blood plasma portion. Drug elimination can be described as a sink term, and for our purposes *arbitrarily chosen* in the kidneys and liver. No irreversible reactions with surrounding organs, tissues, or blood occur. We assume that the pure Cyclosporin excretion is only a minute fraction.

Next, we describe the assumptions on the cellular level. For a peptide, as is the case with Cyclosporin, peptide-ligand binding will occur in organs and tissues (57–59), which could be described by a set of biochemical reactions:

$$CyA + L \leftrightharpoons CyA.L \tag{2}$$

$$CyA \cdot L \rightarrow mCyA \tag{3}$$

where the drug (CyA) binds with ligand (L) to form a bound complex ($CyA.L$), which is then modeled as an elimination by reaction into a metabolite ($mCyA$). The action mechanism of the immunosuppressant in an organism is depicted schematically in Figure 3.

The kinetic rates in these reactions are tissue and ligand concentration dependent. Additional experiments would be needed for the determination of the ligand-drug complex concentrations. Although the specific binding data may be available in literature (34,40), we assume equilibrium for the reaction characterized by an equilibrium constant, k^{EQ}, as in Eq. (4):

$$[CyA] = \frac{k^{EQ}}{[L]}[CyA \cdot L] \tag{4}$$

We further assume, based on transport mechanisms suggested previously (45), that physical mass exchange is the primary mechanism of drug transport through the capillary

endothelium and that the interstitial fluid concentration is in equilibrium with the ligand-drug complex as given in Eq. , where c_{IF} is the concentration in the interstitial fluid and c_{TC} is the concentration in tissue cells.

$$c_{IF} = \frac{k^{EQ}}{[L]} c_{TC} \tag{5}$$

Because the interstitial fluid concentration, c_{IF}, is hard to observe experimentally (4), it will be eliminated through the following substitution steps. We obtain Eq. (6) which expresses the drug concentration in the interstitial fluid volume V_{IF} as being proportional to the concentration of drug in the entire organ volume V_Q. The unknown parameter k_q is introduced to replace the expression containing the equilibrium constant k_{EQ}:

$$c_{IF} = \frac{V_Q k^{EQ}}{V_{IF} k^{EQ} + V_{TC}[L]} c_Q = k_q c_Q \tag{6}$$

The *mass transfer between unbound plasma and the organs* is assumed to be driven by physical concentration gradient, thus eliminating c_{IF} from the Eq. (7):

$$UA(c_P - c_{IF}) = UA\left(c_P - k_q c_Q\right) = k^+_{Q,j} c_{P,i} - k^-_{Q,j} c_{Q,j} \tag{7}$$

This assumption needs to be carefully revised for other drugs. We finally introduce new unknowns $k_H^+, k_H^-, k_A^+, k_A^-, k_Q^+, k_Q^-$, which can be found in Table 1 and are kinetic rates of mass transfer, to avoid fitting unobservable quantities like *UA* and for simplification of the notation.

The following indexing scheme is defined: vascular segments (*i*), the organs (*j*) and metabolites (*l*). Here, the capillary segment of the vascular network with index *i* is connected to the organ with index *j*.

2.3.2.3. ***Pharmacokinetics in blood compartments***

In the proposed multi-phase model, blood is divided into (1) red blood cells (hematocrit, *H*), (2) plasma lipoproteins, *A*, and (3) the aqueous part of plasma, *P*. The hematocrit level, f_H, is assumed constant over the duration of the experiment, although it may vary in certain diseases (34,40). The relative volume fractions of *A* and *P* are also constant throughout the transient simulation. The plasma lipoprotein fraction compartment will be referred to as plasma bound compartment with volume fraction f_A. The drug dissolved in the aqueous plasma is free to transfer into organs and is named unbound drug in plasma compartment; its volume fraction is f_P. The blood fractions are related to each other as in Eq. (8):

$$f_H + f_A + f_P = 1 \tag{8}$$

The species accumulation in the compartment entitled *plasma fraction of unbound drug in blood*, dc_P/dt, is balanced by drug entering and exiting through convection in the blood, $F_{in}c_{P,in} - F_{out}c_{P,out}$, mass transfer of free drug to the organ, $UA(c_P\text{-}c_{IF})$, and a chemical binding reaction to red blood cells, $\dot{R}_H$, and plasma lipoproteins, $\dot{R}_A$. The reaction terms can be given as:

$$\dot{\mathrm{R}}_{H,i} = k_H^+ c_{P,i} f_P V_{B,i} - k_H^- c_{H,i} f_H V_{B,i} \tag{9}$$

$$\dot{\mathrm{R}}_{A,i} = k_A^+ c_{P,i} f_P V_{B,i} - k_A^- c_{A,i} f_A V_{B,i} \tag{10}$$

Pharmacokinetics in unbound plasma compartment. The change of the concentration in unbound plasma compartment $c_{P,i}$ over time can be expressed as in Eq. :

$$f_P V_{B,i} \frac{dc_{P,i}}{dt} = F_{in}c_{P,in} - F_{out}c_{P,out} - k_{Q,i}^+ c_{P,i} + k_{Q,i}^- c_{Q,i} - \dot{\mathrm{R}}_{A,i} - \dot{\mathrm{R}}_{H,j} + I_i \tag{11}$$

where U is the overall mass transfer coefficient, A is the physical mass transfer exchange area specific to each organ j, c_P is the concentration in the plasma unbound fraction, $F_{in}c_{P,in}$ and $F_{out}c_{P,out}$ are the drug's inflow and outflow for a cylindrical segment. The new unknown parameters k_Q^+, k_Q^- represent the kinetic rates of mass transfer between plasma unbound and an organ. This unknown fraction is determined by the parameter estimation technique described in Section 2.3.3. We also assume that this fraction is constant between different species. In addition, I_j accounts for the drug infusion into the tissue, for example, in intramuscular administration, and I_i from Eq. (11) is the drug infusion rate into the plasma.

Pharmacokinetics in bound plasma compartment and erythrocytes. The change of the *concentration in bound plasma compartment* is given in Eq. (12). The change of the *concentration in erythrocytes* can be described by Eq. (13):

$$f_A V_{B,i} \frac{dc_{A,i}}{dt} = F_{in}c_{A,in} - F_{out}c_{A,out} + \dot{\mathrm{R}}_{A,i} \tag{12}$$

$$f_H V_{B,i} \frac{dc_{H,i}}{dt} = F_{in}c_{H,in} - F_{out}c_{H,out} + \dot{\mathrm{R}}_{H,i} \tag{13}$$

2.3.2.4. ***Pharmacokinetics in organs and tissues***

Let indices Q represent an organ, and P the unbound plasma compartment in the capillary segment i of the vascular network. Each organ has interstitial fluid and tissue cells. The organ volume can be expressed as the sum of the interstitial volume, V_{IF}, and the tissue cell volume, V_{TC}. These volumina are considered to be constant for the duration of the simulations. The drug concentration change in organs and tissues $c_{Q,j}$ over time can be expressed as in Eq. (14):

$$V_{Q,j}\frac{dc_{Q,j}}{dt} = k_{Q,j}^{+}c_{P,i} - k_{Q,j}^{-}c_{Q,i} - \dot{\mathrm{R}}_M V_{Q,j} + I_j \qquad (14)$$

where V_Q is the volume of organ j, k_Q^+ and k_Q^- are the mass transfer rates of drug from plasma into organ interior, c_Q is the average concentration of drug in the given organ, $\dot{R}_M$ is the metabolic and elimination rate of drug from the organ as defined in Eq. (15) and I_j is the drug injection term into the organ.

2.3.2.5. ***Cellular level reaction kinetics***

We define clearance in terms of the biochemical PK reactions in the PBPK model. The drug elimination in selected organs is computed with the help of Eq. (15), where symbol $c_{M,l}$ denotes the *l-th* metabolite concentration in the given organ, j, and $k_{M,l}$ are the metabolic and elimination rate constants assuming linear first order kinetics.

$$\dot{\mathrm{R}}_M = \frac{dc_{M,l}}{dt} = k_{M,l}c_{Q,j} \qquad (15)$$

In summary, Eqs. (8)-(15) constitute the dynamic mathematical model based on first principles of drug dispersion in the entire body. This system of ordinary differential equations can be written in compact form as stated conceptually in Eq. (16). The functional matrix $\Psi(k,t)$ accounts for physiological and anatomical parameters of the reference animal and depends on the unknown kinetics and transport parameters, k. The initial conditions, $c(t_0) = c_0$, specify known initial drug concentrations. The unknown coefficients, k, that parameterize this model can be determined from experiments by an inversion technique described next.

$$c'(k,t) - \Psi(k,t)c(k,t) = 0, \quad c(t_0) = c_0 \qquad (16)$$

2.3.3. **Kinetic inversion problem and solution**

A set of experimentally obtained concentration measurements is needed for each subsystem such as the plasma, blood, and tissues. The optimal parameters for the mechanistic PBPK model are determined from the minimum least squares distance between experimental and predicted drug concentrations. The objective function measures the fit of the first principles model with the measured data set. We propose a slight modification to the least squares fitting objective function. Eq. (17) accounts for the differences in the number of samples for each measured tissue concentration $\hat{c}$ by using a weight $w_i = 1/N_i$, where N_i is the number of discrete time measurements for organ j and N_j is the number of measured tissue concentration profiles:

$$\min_k \varphi[c(t,k), \hat{c}(t), t] = \sum_{j=0}^{N_j} \sum_{i=0}^{N_i} w_i \left\| \frac{c_j(t_i,k)}{\hat{c}(t_i)} - 1 \right\| \quad , \qquad w_i = \frac{1}{N_i} \tag{17}$$

The concentration profiles, c, are obtained by numerically integrating a system of first-order ordinary differential equations (ODEs) in Eqs. (8)-(15). A total of 183 ODEs is automatically generated by our custom-made software.

*2.3.3.1. **Non-linear programming algorithm for parameter estimation***

The general form of the pharmacokinetic model can be written as in Eq. (18):

$$\begin{aligned} &\min_k \varphi[c(t,k), \hat{c}(t), t] \\ &s.t.\ \ c'(k,t) - \Psi(k,t)c(k,t) = 0 \\ &c(t_0) = c_0 \end{aligned} \tag{18}$$

where c is the modeled state and its derivation c', $\hat{c}$ is the experimental measurement of the state dependent on parameters k and the functional matrix of physiological parameters $\Psi(k,t)$. Among several numeric integrators, we recommend the DASSL software package be

used with numerical forward estimation of the ODE system derivatives (64). To solve the minimization problem, a large-scale globally convergent algorithm is needed. Nonlinear programming algorithms have been successfully used previously (65–69). The family of Trust Region (TR) Algorithms (70–73) has been extensively applied for large-scale parameter estimation problems over the last two decades; therefore, they were used in our case study. The optimization was performed at a supervisory level by a Trust Region Algorithm. The trust region algorithm guides the implicit integration performed in the DASSL software package which solves the differential algebraic equation system with a variable time step.

The choice of initial parameters has implications on the speed of convergence and on robustness. Faster convergence is usually of minor importance, but proper scaling and transformations of kinetic rates as described by Tang et al. (74) can help both the convergence as well as transforming the "cliffs" and "valleys" of the objective space. To ensure robustness, the best approach is to use global optimization techniques (75). For an initial estimate of the parameter vector, k, which contains the mass transfer coefficients, the rates of binding and the clearance rates, the initial objective function value from Eq. (**19**) is calculated. The method then evaluates the sensitivity matrix, S, which is a derivative of the objective function with regard to the vector k as shown below:

$$S_{i,j} = \frac{\partial c_i}{\partial k_j} \tag{19}$$

This step is performed by forward numeric differentiation. The solution of the parameter estimation gives the desired kinetic constants and drug clearance for each organ in the organism.

2.3.3.2. ***Approximation of confidence intervals for implicit systems***

This section present a method to assess the confidence in the model choice and its parameter estimates. Quantitative metrics of model fidelity are useful to assess whether the experimental observations are sufficient to justify the model. Selected mechanistic parameter ranges are also necessary to quantify the variability of parameter estimates.

Approximations of the probability distribution functions for the parameter realizations will be addressed by confidence intervals. To set realistic parameter ranges with finite bounds, the method of confidence intervals introduces the concept of a *confidence level*. A confidence level of $\gamma = 0.95$ corresponds to the portion of the uncertain space containing 95% of all possible parameter realizations (76–79). The computation of confidence intervals requires construction of a probability density function of the uncertain parameters from the variance-covariance matrix.

Linear models like in Eq. (20) relate the predicted variables y to the parameter set, k, and the $n \times p$ matrix of inputs, X. The scalar n refers to the dimension of the y vector; p is the number of unknown parameters.

$$\text{Model}: \quad y_m = Xk \tag{20}$$

$$\text{Modeling error}: \quad e = y_m - y_e \tag{21}$$

Minimizing the square modeling error e^Te under the assumption of normal distribution yields the optimal parameter set, $\hat{\kappa}$, as given in Eq. (22).

$$\hat{\kappa} = (X^TX)^{-1}X^Ty \tag{22}$$

The square $p \times p$ variance-covariance matrix Λ_k is defined in Eq. (23). Its diagonal contains the individual parameters' variances (σ_{ii}). The off-diagonal elements represent the cross-covariances of the estimated parameters (σ_{ij}, $i \neq j$).

$$\Lambda_k = \begin{pmatrix} \sigma_{11} & \cdots & \sigma_{1p} \\ \vdots & \ddots & \vdots \\ \sigma_{p1} & \cdots & \sigma_{pp} \end{pmatrix} \tag{23}$$

With Eq. (22), the entries of Λ_k for the optimal parameters, $\hat{\kappa}$, can be computed according to Eq. (24):

$$\Lambda|_{k=\hat{\kappa}} = \Lambda_{\hat{\kappa}} = \frac{e^T e}{n-p}(X^T X)^{-1} = s^2(X^T X)^{-1} \quad \text{where } s^2 = \frac{e^T e}{n-p} \tag{24}$$

The variances, σ_{ii}, and the covariances, σ_{ij}, can be used to construct the parameter probability distribution functions. For distributed systems, we propose the use of *individual confidence regions* (ICR). Individual confidence regions ignore the cross-covariances among parameters (80,81), thus the confidence intervals for each parameter are calculated independently. Eq. (25) yields the width of the ICR parameter range as a function of a Student's *t-test* (τ) for a specified γ-confidence level. ICR defined by Eq. (25) are represented by p-dimensional hyper-cubes in the probabilistic parameter space k.

$$\left|k_j - \hat{\kappa}_j\right| \leq \sigma_{jj} \cdot \tau\left(n-p, \frac{1-\gamma}{2}\right) \tag{25}$$

Unfortunately the predicted concentration profiles resulting from our PBPK model in Eq. (17) are not accessible explicitly; therefore, an implicit approach for parameter confidence estimation is needed. In implicit models like transport and kinetic parameter inversion, the least-squares estimation cannot be solved in closed form. The variable vector, y, can be approximated by a multi-variable Taylor expansion about the optimal parameter set $\hat{\kappa}$, where the first terms $S_{ij} = \partial c_i / \partial k$ signify its parameter *sensitivity information*. The matrix $S(\hat{\kappa})$ is the *Jacobian* of the model. The Taylor expansion permits the approximate solution of the non-linear parameter estimation problems. It also provides

the basis for a first-order approximation of the variance-covariance matrix about the optimal parameter set as given in Eq. (26).

$$\Lambda_{\hat{\kappa}} \approx s^2[S(\hat{\kappa})^T S(\hat{\kappa})]^{-1} \tag{26}$$

Given the recipe for computing $\Lambda_{\hat{\kappa}}$, the individual confidence regions for the parameters (k) could thus be constructed according to Eq. (27) for implicit systems.

$$\text{ICR:} \quad \left|k_j - \hat{\kappa}_j\right| \leq \sqrt{\Lambda_{\hat{\kappa},jj}} \cdot \tau\left(n-p, \frac{1-\gamma}{2}\right) \tag{27}$$

More details on the computation of the individual confidence intervals can be found in (73).

2.4. **Results: Case Study on Cyclosporin**

This section presents the case study on Cyclosporin. It shows the systemic blood circulation model of a rat followed by formulation of the mechanistic PBPK transport and biochemical reaction model. Finally, the nonlinear parameter estimation technique will be used to determine the unknown PBPK model parameters with individual confidence interval estimates to assess model quality. *Specifically, the results demonstrate a parameter estimation technique for therapeutic bolus injection of 6 mg/kg Cyclosporin into a rat*. We will also demonstrate the prediction of the drug fate in the entire organism for various doses, dosing times, and animal pathologies.

An ample set of experimental dose-response data is available with measured Cyclosporin concentration profiles in blood, plasma proteins, unbound plasma, and twelve organs after injection of the drug into Sprague-Dawley rats (40). The first experimental dataset concerns intravenous injection of Cyclosporin solution into the femoral vein. Bolus injections over a period of two minutes were administered in subtherapeutic 1.2 mg/kg,

therapeutic 6.00 mg/kg, and supertherapeutic 30 mg/kg doses into male rats 277 g $\pm$ 15 g in weight. Organ concentrations at specific time instants were recorded and measured by radioimmunoassay after decapitation, bleeding, freezing of samples at -20°C, thawing, and homogenization (2,34,40). The sampling frequency was about 5 rats at each time point, 50 rats in total. The application of the mechanistic modeling framework described in section 2.3 will be presented next.

2.4.1. **Whole body circulation model**

A whole body circulatory model for the 277 g Sprague-Dawley rat based on experimentally obtained physiological values for twelve main organs was constructed as depicted in Figure 2. Key parameters, such as organ and tissue weight, density, physiological blood perfusion rates, the pressure drops, the nominal blood volume, and blood parameters, are summarized in Table 2.

Table 2. Physiological data for Sprague-Dawley rats. Fraction of blood in organ was obtained from (1), the blood flow rate, organ volume and volume fraction of total body from (2,3) and the fractions of cells and interstitium in organs from (4).

Organ	**Fraction of blood in organ** (vol/vol) (1)	**Blood volume** (ml) (2)	**Blood flow rate** (ml/min) (2,3)	**Organ volume** (ml)	**Organ volume fraction** (vol/vol) (1)	**Fraction of total volume** (4)	
						Cells	**Interstitium**
Liver	0.21	2.05	26.10	11.2	0.040	0.82	0.18
Kidneys	0.16	0.40	20.40	2.5	0.009	0.78	0.22
Brain	0.03	0.34	4.42	11.2	0.040	1.00	0.00
Bone	0.04	0.69	5.60	17.1	0.062	0.90	0.10
Fat	0.02	0.22	0.88	10.8	0.039	0.86	0.14
Guts	0.12	1.30	16.60	10.8	0.039	0.90	0.10
Pericardium	0.26	0.23	8.66	0.9	0.003	0.86	0.14
Lungs	0.36	0.39	85.04	1.1	0.004	0.50	0.50
Muscle	0.04	5.24	4.50	132.3	0.478	0.88	0.12
Skin	0.02	0.87	12.90	43.4	0.157	0.69	0.31
Spleen	0.22	0.14	1.40	0.7	0.002	0.79	0.21
Thymus	0.18	0.14	1.55	0.8	0.003	0.79	0.21
Blood	--	--	--	20.7	0.075	--	--

A physiologically accurate vascular network corresponding to the animal subject was generated and solved for the steady state flow rates with a mean average cardiac

output of 85 ml/min (3). The initial conditions for the vascular network were given at both heart ventricles (P_{out}= 115 mmHg) and both atria (P_{in}= 4 mmHg) for non-pulsating, steady flow in rigid tubes.

2.4.2. **Pharmacokinetic model on Cyclosporin bolus injection into a rat**

The transport and biochemical reaction mechanisms of the drug in the entire organism were modeled using Eqs. (8) - (15). A system of ordinary algebraic equations has been automatically generated by our software based on the vascular network graph representation and the proposed PBPK model as in Eqs. (8) - (15). In all 57 segments of the rat network, three equations, Eqs. (11) - (13), are generated for plasma unbound, plasma bound, and erythrocytes. In addition, for each capillary segment belonging to one of the twelve main organs, one additional equation, Eq. (14), is generated. Moreover, two additional clearance equations for the drug elimination are defined for the liver and kidneys. The complete mathematical problem has a total of 186 equations.

2.4.3. **Mechanistic parameter estimation for a therapeutic Cyclosporin intravenous administration**

The nonlinear parameter estimation problem applied to a time series with least square minimization between the experimental and predicted drug concentration profiles leads to a solution of the unknown parameter set *k*, as defined in Eq. (17). The values of the optimal parameters are given in Table 3 with the estimates of individual confidence intervals as outlined in Section 2.3.3.2. Using only the experimental data from the therapeutic dose-response curves, the following mechanistic parameters of the vector *k* were determined: (i) the mass transfer rate for each organ k_Q^+, (ii) the organ specific

constants k_Q^- which includes the equilibrium kinetic constants, the fraction of interstitial fluid in the organ and the equilibrium concentration of the free ligand, (iii) two clearance terms for liver and kidney k_M and (iv) four adsorption and desorption rates for the red blood cells $[k_H^+, k_H^-]$ and the bound plasma lipoprotein fraction $[k_A^+, k_A^-]$.

Table 3. Optimal values of kinetic rates of binding (k_1, ..., k_4), mass transfer coefficients (k_5, ..., k_{28}), kinetic clearance rates (k_{29}, k_{30}), are shown, where (+) denotes mass transfer or binding into, (-) out of the compartment and (*) the clearance terms. Standard deviation was estimated for 95.0% individual confidence interval. The least square fitting objective function value is 3.140.

i	k_i	**Deviation**	**Kinetic term** (units)
1	5.960	±0.498	k_A^+(h^{-1})
2	4.795	±0.447	k_A^-(h^{-1})
3	0.934	±0.197	k_H^+(h^{-1})
4	2.104	±0.296	k_H^-(h^{-1})
5	91.051	±1.946	$k_{Q\ liver}^+$(m^{3}h^{-1})
6	7.809	±0.570	$k_{Q\ kidney}^+$(m^{3}h^{-1})
7	0.818	±0.184	$k_{Q\ brain}^+$(m^{3}h^{-1})
8	14.553	±0.777	$k_{Q\ bone}^+$(m^{3}h^{-1})
9	13.241	±0.742	$k_{Q\ fat}^+$(m^{3}h^{-1})
10	13.525	±0.750	$k_{Q\ gut}^+$(m^{3}h^{-1})
11	1.503	±0.250	$k_{Q\ heart}^+$(m^{3}h^{-1})
12	2.179	±0.301	$k_{Q\ lungs}^+$(m^{3}h^{-1})
13	206.012	±2.927	$k_{Q\ muscle}^+$(m^{3}h^{-1})
14	13.875	±0.760	$k_{Q\ skin}^+$(m^{3}h^{-1})
15	1.844	±0.277	$k_{Q\ spleen}^+$(m^{3}h^{-1})
16	0.413	±0.131	$k_{Q\ thymus}^+$(m^{3}h^{-1})
17	3.350	±0.373	$k_{Q\ liver}^-$(m^{3}h^{-1})
18	0.378	±0.125	$k_{Q\ kidney}^-$(m^{3}h^{-1})
19	3.451	±0.379	$k_{Q\ brain}^-$(m^{3}h^{-1})
20	4.958	±0.454	$k_{Q\ bone}^-$(m^{3}h^{-1})
21	0.802	±0.183	$k_{Q\ fat}^-$(m^{3}h^{-1})
22	3.009	±0.354	$k_{Q\ gut}^-$(m^{3}h^{-1})
23	0.419	±0.132	$k_{Q\ heart}^-$(m^{3}h^{-1})
24	0.457	±0.138	$k_{Q\ lungs}^-$(m^{3}h^{-1})
25	165.578	±2.624	$k_{Q\ muscle}^-$(m^{3}h^{-1})
26	3.989	±0.407	$k_{Q\ skin}^-$(m^{3}h^{-1})
27	0.290	±0.110	$k_{Q\ spleen}^-$(m^{3}h^{-1})
28	0.047	±0.044	$k_{Q\ thymus}^-$(m^{3}h^{-1})
29	0.301	±0.112	$^*k_{M\ liver}$(m^{3}h^{-1})
30	0.173	±0.085	$^*k_{M\ kidney}$(m^{3}h^{-1})

The objective function value indicating the goodness of fit for the optimal solution of the parameter vector k is Φ = 3.14, which was found after 380 iterations. The dynamic simulation with the optimal parameter set gives drug concentration trajectories which closely fit the experimental profiles as seen in Figure 4 for the therapeutic dose. Plasma unbound fraction trajectory does not fit previous literature estimates closely. We discuss in detail the probable causes in section 2.5 under the part entitled "Observability of the plasma binding kinetics".

To validate the model, the overall conservation of mass was verified and is plotted as a function of time in Figure 5. From the trajectory, we determined the biological half-life of Cyclosporin in rats as $t_{1/2}$ = 8.75 h. The graphs also allow the calculation of the area under the curve (AUC).

For individual organs and tissues, the mass fraction of Cyclosporin in each compartment as a function of time is plotted in Figure 6. After the bolus injection of Cyclosporin, the initial concentration peak in the blood is rapidly transferred into the organs, where reversible binding of the peptide to ligands occurs. After the initial peak in blood (free plasma) recedes, the binding is reversed after a drop of concentration is observed in the interstitial fluid.

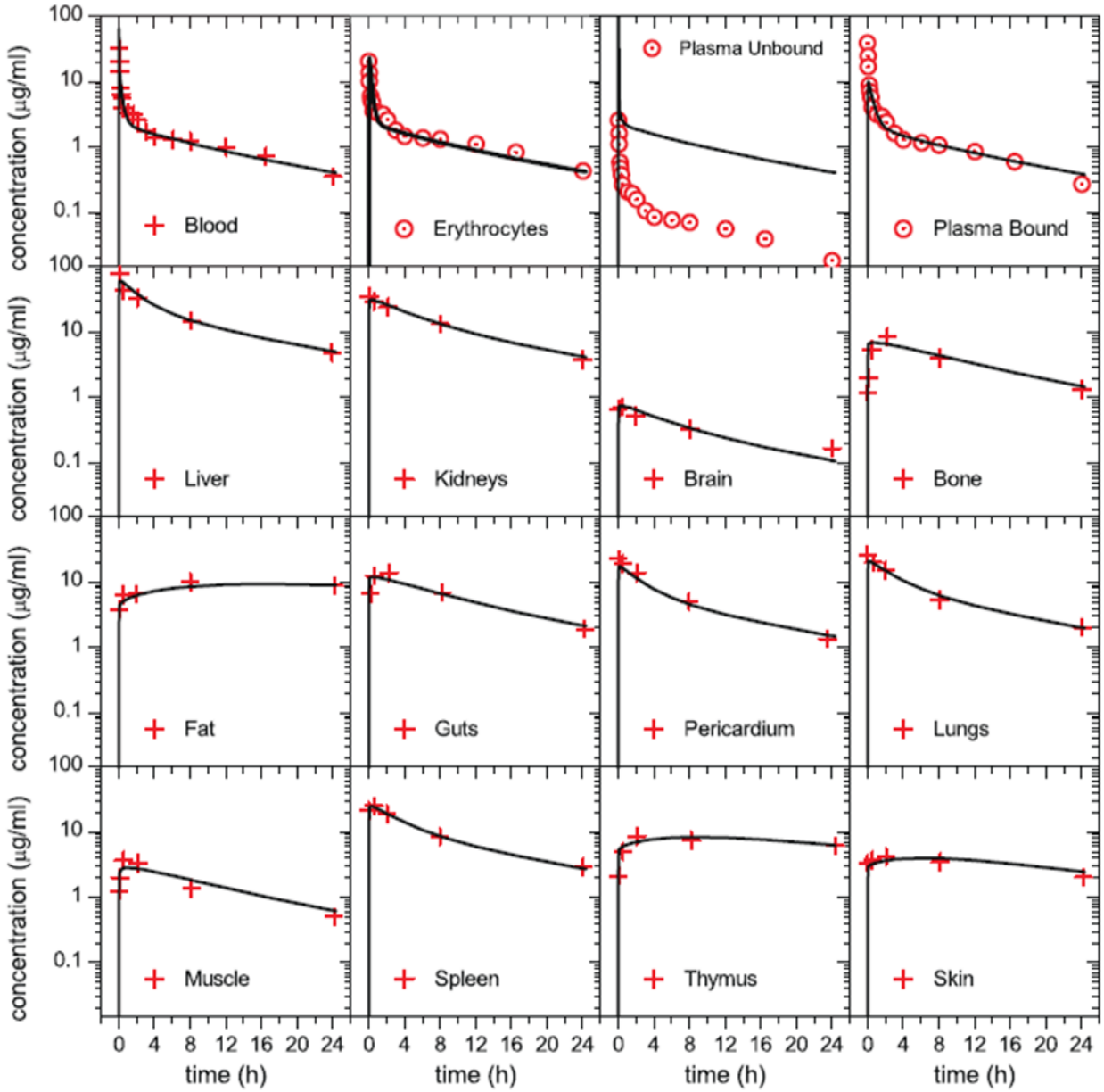

Figure 4. Distribution of Cyclosporin in selected organs, tissues, and blood compartments after an intravenous bolus administration of 6 mg/kg into a Sprague-Dawley rat obtained experimentally (crosses), estimated from literature (circles) and predicted by our PBPK model (lines). Plasma unbound denotes the fraction of the drug that is not bound to erythrocytes or plasma lipoproteins.

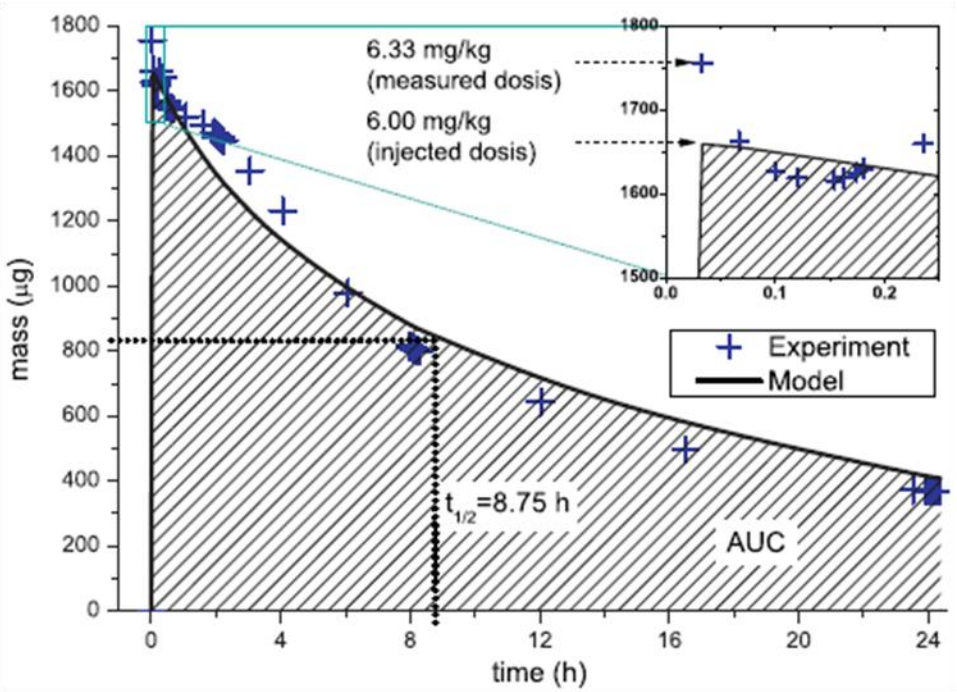

Figure 5. Total mass of Cyclosporin *in vivo* measured (crosses) and predicted by our mechanistic model (lines) as a function of time. The first experimental point at time t = 2 min, 6.33 mg/kg dose, does not correspond to the declared administered dose, 6.00 mg/kg, for a 277 g male Sprague-Dawley rat. The area under the curve (*AUC*) and the half-life ($t_{1/2}$ = 8.75 h) can thus be determined.

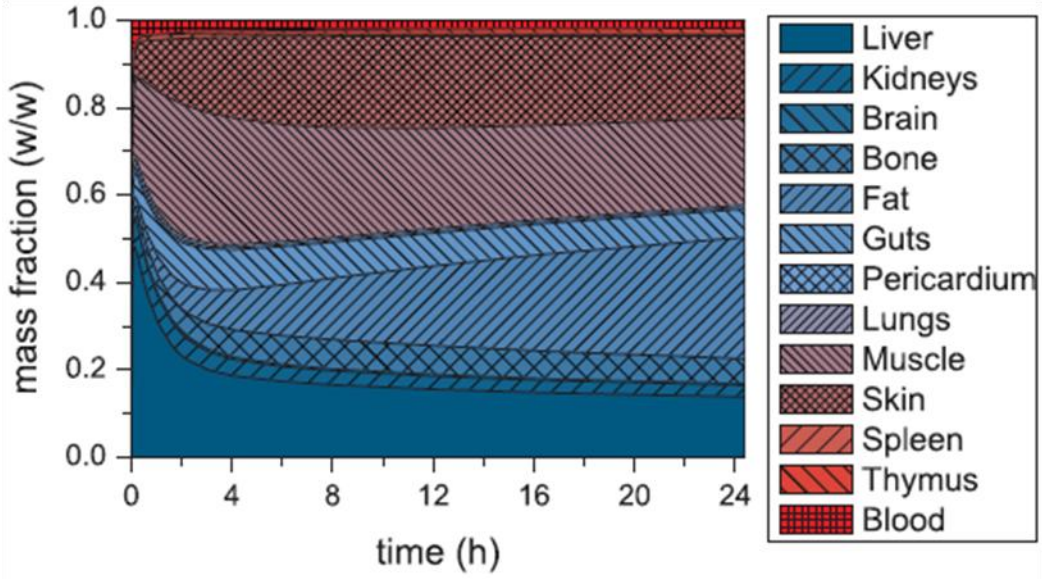

Figure 6. Model results predicting the *in vivo* evolution of the mass fraction of Cyclosporin in tissues and organs of a rat. The concentration in the liver shows a high peak initially, while the adipose tissues successively collect more Cyclosporin. The drug accumulation in fatty tissues is in accord with its high lipophilicity.

Figure 7 demonstrates the accurate conservation of mass and species in the plot of total mass accumulation of administered drug as a function of organ and time, as well as the hepatic and renal clearances in mass units.

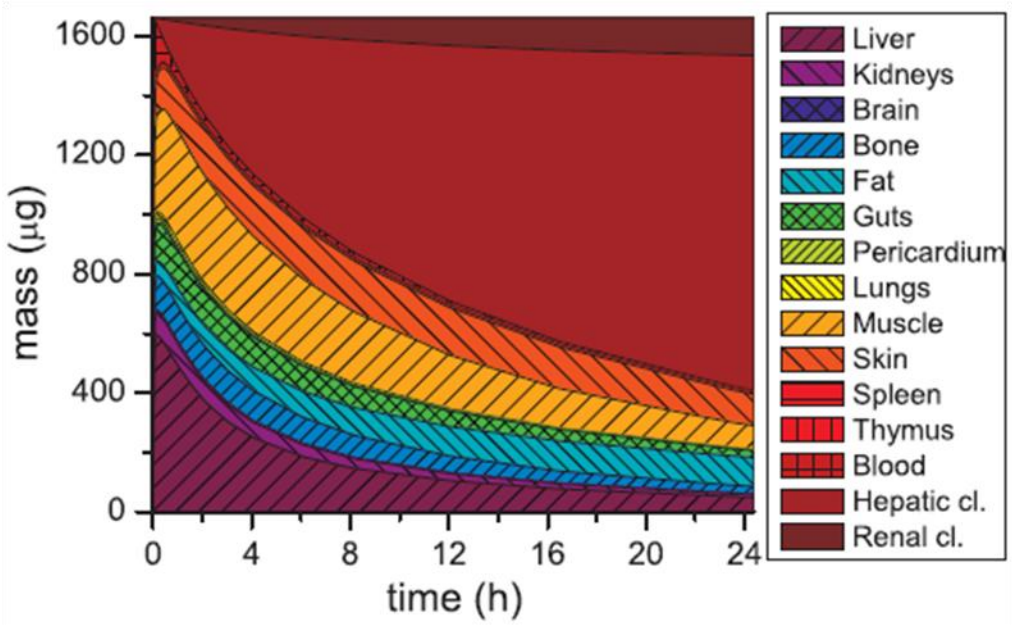

Figure 7. Model results predicting the evolution of total mass of Cyclosporin *in vivo* in tissues and organs of a rat. Total mass in the model is conserved and reaches a final level of 1662 µg after the 2 min bolus injection. The renal and hepatic metabolite levels can be determined in addition to individual bioaccumulation of the drug in organs and tissues.

2.5. **Discussion**

One model fits all dosing regimes. The presented mechanistic physiological workflow determines fundamental transport and reaction mechanisms of Cyclosporin in an entire organism.

A *key outcome* of this study is that the bioaccumulation of Cyclosporin can be predicted for a wide of range of different doses with a mechanistic model, whose *parameters were estimated from a single dose experiment*. In the case study, the unique set of mechanistic parameters, *k*, was determined rigorously from experimental data collected

in response to a therapeutic dose of 6 mg/kg Cyclosporin administered intravenously into the femoral vein. Figure 8 shows that the predicted organ drug concentration profiles match the experimental dose-response measurements well. In addition, we used the same parameters *k* to extrapolate organ concentration profiles for simulated supertherapeutic (30 mg/kg) and subtherapeutic dose levels (1.2 mg/kg). Figure 8 permits the assessment of the extrapolation quality in comparison to *in vivo* experiments not used to fit the model parameters. In addition to the expected good fit at the therapeutic level, the predictions also closely match all organ concentrations for the supertherapeutic dose. For the subtherapeutic level, the simulation is less accurate, but still satisfactory for all organs. One limitation of the presented PBPK model, but not the mathematical principles of scaling, is the lack of a detailed account of the digestive tract with bile excretion and resorption. This might be important for more accurate mass balance in specific organs. However, the accuracy of this model with regard to time concentration trajectories even without taking bile into account is sufficient as compared to state of the art research articles. The high extrapolation fidelity demonstrates that our mechanistic PBPK model properly captured *Cyclosporin pharmacokinetics with a single parameter set acquired from only one dose experiment*. These results strongly suggest that our mechanistic algorithm can predict drug concentrations for a wide range of dosing regimes.

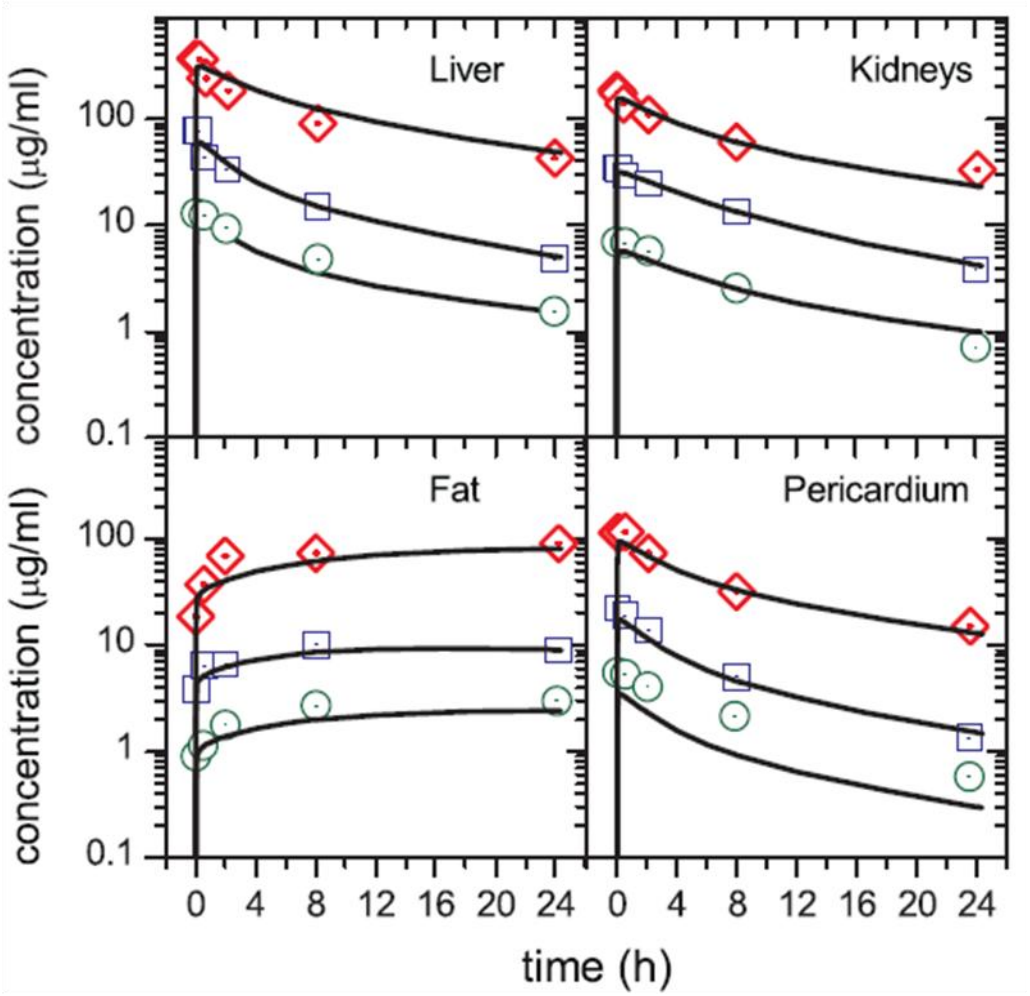

Figure 8. Dose-response curves in selected organs of a rat, based on unique parameter set obtained only from a single therapeutic dose experiment (squares) at 6.0 mg/kg *IV* for two minutes. Our mechanistic PBPK model with the unique parameter set also predicts organ concentrations for different dosages. These extrapolations match the supertherapeutic experiments (30 mg/kg, diamonds) and reasonably well also subtherapeutic data (1.2 mg/kg, circles).

Observability of the plasma binding kinetics. An interesting and rarely discussed problem is the relation of the modeling outcomes to new experiment design. The analysis of the presented case study illuminates several difficulties, which should be addressed in future experiments. Two-minute bolus injection in the subtherapeutic, normal, and supertherapeutic range leads to substantial errors in the measurement of the drug concentration in blood, organs, and tissues. The peak concentration in blood, liver, and

especially in unbound plasma cannot be accurately captured by current analytic methods with short acquisition time. Prolonged blood and plasma sample processing leads to equilibrium binding of the drug onto erythrocytes, and plasma fractions. The experimental results of the free portion of drug in plasma available to mass transfer into the interstitial fluid are therefore underestimated. Our analysis suggests that the unbound plasma concentration of Cyclosporin in rats is from 10 to 40 times larger than the *equilibrium concentration* obtained by various analytic methods previously published in literature (82–84). For the quality of the data, it is crucial to minimize the delays between sample acquisition and analysis, or to extend the bolus injection time, apart from the desirable improvements in the analytic precision.

Although experimentally difficult, measurement of the interstitial fluid concentration simultaneously with blood, plasma, and erythrocytes concentrations would greatly improve our knowledge about drug binding mechanisms.

Simulations with different administration procedures. Figure 9 shows the matrix of calculated scenarios for Cyclosporin injection into a rat. Variations of the drug dose, and administration time (2 min, 2 h, 4 h, 6 h, 8 h) have been calculated. In all cases, the simulation predicts the drug fate in the entire organism, thus demonstrating the excellent extrapolation capability of the method.

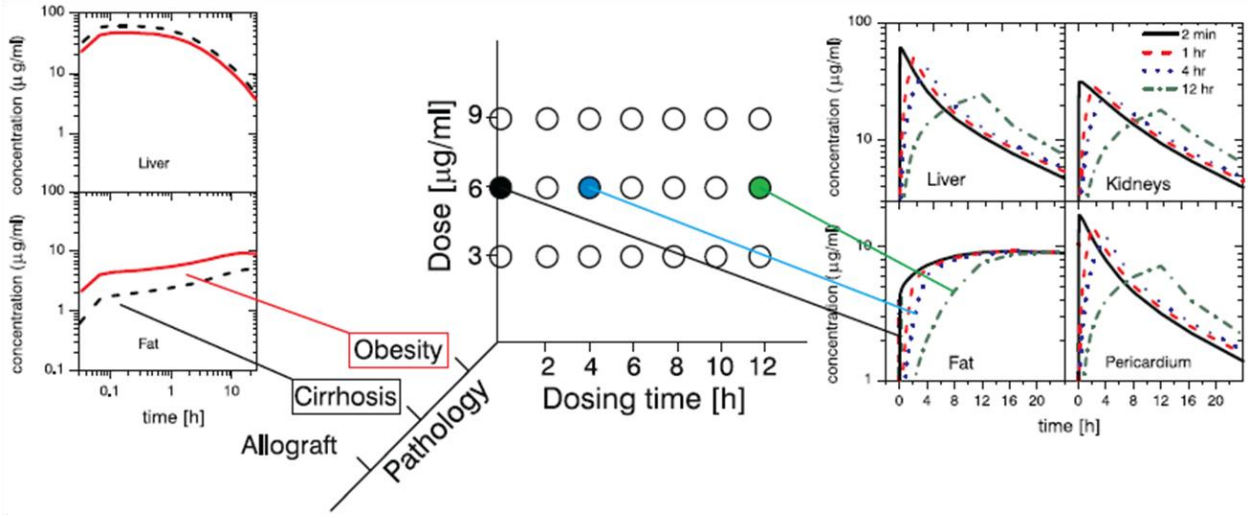

Figure 9. Model matrix showing a set of simulations based on the calculated optimal parameters for Cyclosporin injection into a rat. The *middle* figure shows the possibility of dose variation calculations in selected organs, based on the set of parameters obtained solely from the therapeutic (6.0 mg/kg) set of experiments. The *left* figure shows the results from rats with different pathological conditions, obesity (red line) compared to cirrhosis (black dashed line), in liver and fat tissues. The figure on the *right* depicts the variation of injection time from bolus to 12 h continuous administration.

***Pharmacokinetic model selection*.** We formulated, calculated, and tested several mechanistic models, resulting in three hypotheses of Cyclosporin fate in rat:

Hypothesis #1: The drug is metabolized in liver and in kidneys

Hypothesis #2: The drug is metabolized only in the liver

Hypothesis #3: The drug is metabolized in liver and kidneys with no upper bounds to parameters k.

We calculated the goodness of fit for all three hypotheses in order to perform the model validation and comparison. We used the goodness of fit to the experimental data as the information criterion. Hypothesis #3 has the lowest objective function value, $\Phi = 3.04$, but leads to unrealistically high values in the vector k for mass transfer coefficient of muscle and liver in the order of magnitude 10^6. Accordingly, hypothesis #3 was rejected. Hypothesis #2 with objective function value $\Phi = 3.31$ was inferior to hypothesis #1 with a

value of Φ = 3.14. With the current model formulation, the hypothesis of combined renal and hepatic metabolism, hypothesis #1, has the strongest support based on the experimental evidence. This preliminary comparison based on goodness of fit and dimensions of the individual confidence regions allows for systematic selection among competing mechanistic models.

Computer-aided framework for facilitating the development of PBPK models. First principles based PBPK models have great potential to contribute to drug development efforts; however, the process of developing a PBPK model itself is not a trivial task. Foremost, the development of PBPK models requires a considerable amount of effort in terms of resources, skills, and time due to the large amount of multidisciplinary knowledge needed in areas such as animal physiology, pharmacokinetics, applied mathematics and statistics, experimental data collection, identification and formulation of relevant mechanisms and hypothesis about drug fate, parameter estimation and validation, amongst others. In general, PBPK models tend to have a large number of equations and parameters, a typical characteristic of first principles models. This requires a systematic and formal approach to ensure good modeling practice and quality.

Therefore to facilitate the development, analysis, identification, and validation of PBPK models, a generic computer-aided modeling framework approach is needed. Such a framework, as presented in Figure 10 left, provides a systematic strategy to address the problem of developing and discriminating between different candidate models in order to find the model that is best supported by the available experimental data.

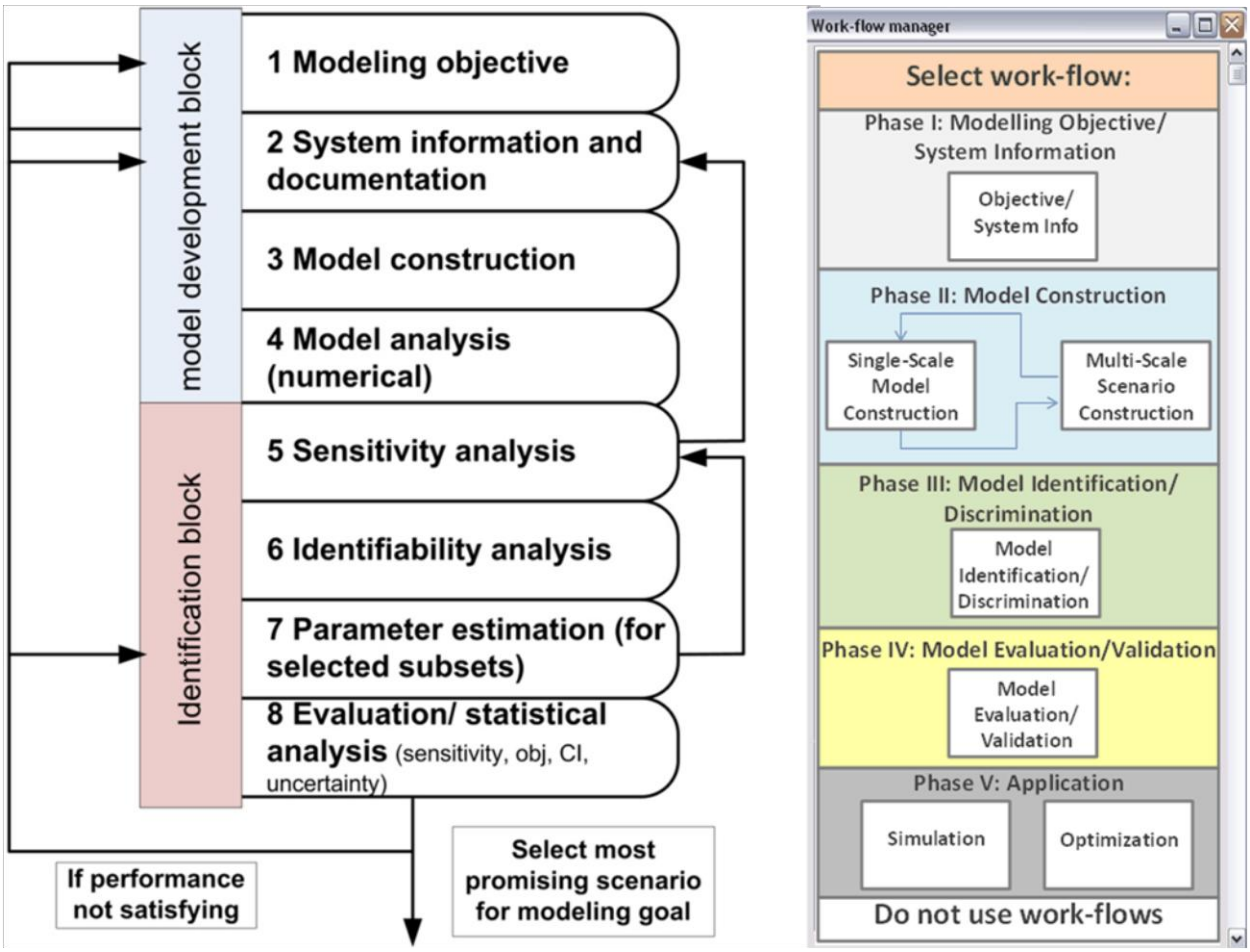

Figure 10. A generic framework for PBPK model development and validation (left), and its computer-aided implementation as a modeling tool (right).

The computer-aided modeling framework is implemented in modeling software called MoT (short for Modeling Testbed) (85,86). The generic computer-aided modeling framework is structured based on work-flows involved in model development such as the modeling objective and documentation, model construction (single or multi-scale with respect to temporal or spatial scales), identification and discrimination, validation, and finally model application such as simulation or optimization. For each step in the work-flows, the framework identifies and provides the required support and tools such as numerical solver/solution strategy, parameter estimation technique, sensitivity and uncertainty analysis techniques, etc. When using the modeling tool (which is built and

configured based on the modeling framework), the user is systematically guided through the required work-flows step by step and provided with all necessary tools. In that way the model development and application process is systematized; thereby, the efficiency of the modeler, the model quality, and the model reliability are improved.

The PBPK model presented in this chapter for Cyclosporin, as well as simplified and more complex versions of this model, was implemented in MoT following the computer-aided framework described above. This involved following the steps all the way from the modeling objective and documentation of multidisciplinary domain knowledge (model structure together with the underlying assumptions and hypothesis), to model construction (equations), model solution, parameter estimation, sensitivity analysis, and finally to model discrimination between the different alternative models. The PBPK model presented in this work resulted to be the best alternative. The models developed and validated following the systematic framework (and its software implementation in MoT) can be stored in a model library for maintenance and reuse in the future for different modeling objectives as well as different drug evaluation efforts. Further presentation and discussion of the details of the computer-aided framework implemented in MoT for PBPK is however beyond the scope of this contribution but subject of a complimentary work.

Administration route and therapy design. Figure 11 shows the modeled concentration curves to treat a rat that has received a heart allograft. The intravenous dose regime for a 12 h injection was determined, such that the concentration in the heart was above the therapeutic level of 1 μg/ml and the peak concentration was minimized. The appropriate injection flow rate over time has been determined in Figure 11B and compared with the same dose, a 12 h continuous injection. These simulations demonstrate the

possibility of systematic individual therapy design using the proposed first principles modeling framework. Optimal desired drug profiles can be achieved based on the knowledge acquired from *in vivo* experiments.

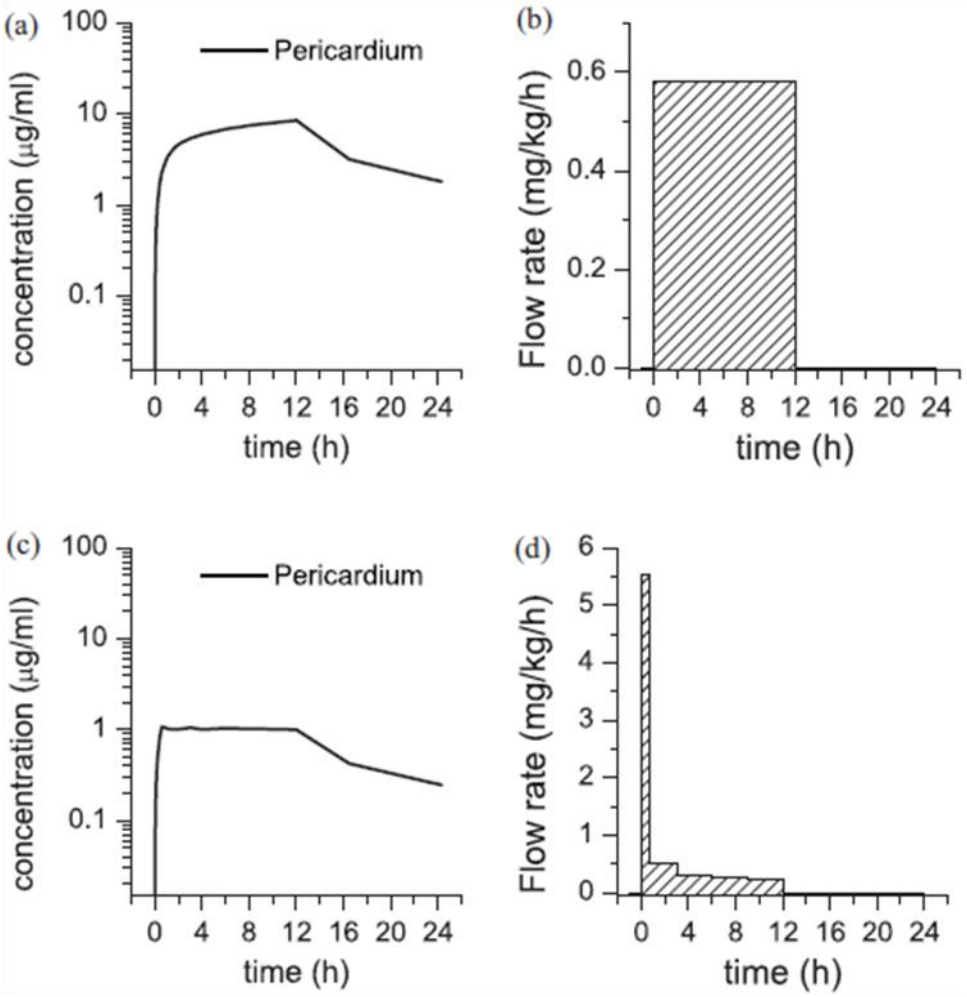

Figure 11. Predicted Cyclosporin concentration profile (a) in a rat's pericardium after (b) *continuous 12 h injection of 7 mg/kg* in contrast to (d) *a controlled flow rate of 7 mg/kg over the same time period*. The aim of the therapy design case study is to maintain a constant concentration of 1 μg/ml in the heart muscle for a period of 11 h as seen in (c).

Intraspecies PBPK scaling and limitations of the proposed algorithm. The ultimate goal of PBPK models is the scaling of animal dose-response curves to humans. In this PBPK modeling approach, coefficients for reaction and transport mechanisms are obtained from dose-response experiments on laboratory animals. The proposed modeling

approach works for arbitrarily defined PBPK models, which can range from systemic to very detailed in anatomy and physiology.

We rigorously determined unknown biochemical kinetic rate constants and transport properties matching experimental dose-response data for novel drugs by parameter estimation with large-scale non-linear programming techniques. PBPK parameters are scaled among rats according to the following categorization.

(1) The physiological group of parameters such as blood perfusion rates and organ sizes can be scaled among individuals based on well-known relationships such as the changes in organ weight as a function of total body weight. (2) The biochemical group of parameters typically include reaction rates in the units of moles per cubic meter. These specific reaction rates summarize the fundamental reaction mechanisms taking place in the tissues of organs. Even though all detailed mechanisms are not accounted for in these models, they nevertheless constitute a specific reaction rate which is only volume dependent. Therefore, such a reaction rate may be used to adjust for intraspecies differences accounting for variations in the metabolism, or chemical reactions kinetics. (3) Finally, transport mechanism parameters usually refer to mass transfer based on physical or active transport. These mechanisms are generally functions of the mass transfer area size. The specific mass transfer coefficient of blood-organ interface may be constant. This third category of parameters could be scaled independently to account for differences in organ surfaces / mass transfer surfaces / specificity of the active transport. PBPK scaling provides advantages over simple allometric scaling laws in the extrapolation, as demonstrated in this case study. More details on intra- and interspecies scaling will be covered in Chapter 3.

2.6. **Conclusions**

This first principles PBPK framework allows modeling of drug dose-response curves for a wide range of variations such as physiology, pathology, and selected administration routes in all organs of a rat. These results are derived from a single laboratory dose experiment dataset combined with constant physiological data. The case study is a proof-of-concept of first principles modeling which is expected to lead to novel insights about the biodistribution, bioaccumulation, and elimination of Cyclosporin.

The presented inversion technique models a drug's fate in organisms based on experimental drug bioavailability. Our model applies conservation balances and thus can be extrapolated beyond the scope of the original dose-response experiment. Such models could be used as a reasonable starting point for intra- and interspecies scaling, and experiment planning in pharmacokinetics and pharmacodynamics. Personalized therapy design could be achieved by adjusting the total weight, hematocrit fraction, injection regime or the dose for determining the therapeutically effective treatment. Mechanistic PBPK models, such as the one presented in this chapter, were shown to accurately predict the drug bioaccumulation over a wide dosing range.

We will further explore allometric scaling laws, aiming at a collection of several animal species such as pigs, nonhuman primates, and ultimately humans to study inter-species differences (23).

We recognize the limitations of the Trust Region Method, which guarantees to converge to a local optimum of the error surface. However, given an initial guess, the algorithm converges reliably to the nearest minimum. Kinetic inversion problems often exhibit solution multiplicity; therefore, the use of global optimization techniques such as

the Global Terrain Method (75) may be necessary to locate all local minima and determine a global optimum. The global optimum, especially when the match is not much different from other local minima, is not necessarily the only choice and is not guaranteed to be physically better than other local minima. All identified local optima are candidate final solutions and are valid in the anatomical, physical, and pharmacokinetic setup. The ultimate choice should incorporate biochemical considerations and kinetic parameters which have physical meaning. If the underlying pharmacokinetics of the drug changes from animal to animal, or from animal to humans, the local optimum solution might be invalid in terms of pharmacokinetic constraints, at which time a different local optimum would be considered.

Another limitation concerns the steady blood circulatory model. In rapid drug uptake like inhalation, a dynamic pulsating blood flow model may be needed. The pulsatile effect of systolic/diastolic cycles can be incorporated with ease using harmonic analysis of the blood convection equations.

The proposed pharmacokinetic framework is essential for quantitative planning of drug administration experiments, intra- and interspecies scaling, and individual therapy design. Mechanistic model approaches are expected to shorten drug development time and may ultimately lead to a rational design of individualized drug therapies.

3. INTERSPECIES SCALING IN PHARMACOKINETICS: DISCOVERING DRUG BIODISTRIBUTION MECHANISMS *IN VIVO*

3.1. Abstract

Drug approval processes require extensive testing and have recently put more emphasis on understanding mechanistic drug action in the body including toxicity and safety (87). Consequently, there is an urgent need in the pharmaceutical industry to develop mechanistic pharmacokinetic (PK) models able to both expedite knowledge gain from experimental trials and, simultaneously, address safety concerns. We previously developed a first principles based whole-body PK model, which incorporated physiological dimensions and drug mass transport and was discussed in Chapter 2 of this dissertation (24).

To follow up from Chapter 2, we demonstrate how the first principles model in combination with novel physiological scaling laws yields more reliable interspecies and intraspecies extrapolation of drug biodistribution. We show how experimental dose–response data in rats for immunosuppressant Cyclosporin are sufficient for predicting the biodistribution of this drug in pigs, monkeys, and humans. The predicted drug concentrations extrapolated by interspecies scaling laws match well with the experimental measurements. These promising results demonstrate that the whole-body PK modeling approach not only elucidates drug mechanisms from a biochemical standpoint, but offers better scaling precision. Better models can substantially accelerate the introduction of drug leads to clinical trials and eventually to the market by offering more understanding of the drug mechanisms, aiding in therapy design, and serving as an accurate dosing tool.

3.2. Introduction

In drug development, the pharmacology of novel drugs is to a great degree unknown, and must be determined by experiments, which in turn require mechanistic interpretation through mathematical models. In clinical first-in-human trials, the determination of pharmacokinetics and pharmacodynamics of novel drugs is critical. The United States Food and Drug Administration (FDA) recommends that human clinical tests be preceded by at least one pre-clinical trial on laboratory animal species, providing substantial evidence for efficacy and tolerable toxicology risk of the lead. Often, however, crude experimental data about possible side effects and the drug action mechanism acquired from these animal trials cannot be fully exploited with classical pharmacokinetic models in order to minimize risks in Phase 0, I and II trials. This chapter discusses better methods for the prediction of drug biodistribution in humans by extrapolating from smaller laboratory animals by using mechanistic pharmacokinetic models.

3.2.1. From classical to mechanistic whole body pharmacokinetic models

Pharmacokinetic (PK) models aim to establish relationships between drug administration, bioaccumulation and elimination from dose-response measurements *in vivo*. Typical PK models fit parametric functions with multiple adjustable constants or exponential coefficients (34–36). Non-mechanistic parameters such as volume of distribution, area under the curve (*AUC*), and the intrinsic clearance rates are usually computed. These classical PK models derive little information about drug reaction kinetics and biotransport phenomena; they also do not satisfy conservation laws, so that drug species balances are not necessarily closed. There is a critical need in the pharmaceutical industry for methods which link modeling, simulation, drug approval, and rigorous

experimental data analysis (42). Several authors have since proposed whole body physiologically-based pharmacokinetic (PBPK) prediction and modeling techniques (2,39–41). PBPK models include several biological subsystems such as blood, the lymphatic and the central nervous system, tissues and organs, which can further be subdivided into multiple phases including cells and interstitial fluid. PBPK models are accepted as a recommended approach for inter- and intra-species extrapolations and to simulate pharmacokinetic profiles for various administration modes and dose regimes. These models incorporate data from many sources such as biochemical, physiological, and drug-dependant parameters for various species, individuals, or with pathological changes (47). In the literature, compartmental PBPK models are typically stipulated as a set of interconnected vessels with ideal mixing, where both biochemical and transport mechanisms are given as black-box, empirical relations. The kinetics of novel drugs can be studied more systematically with *mechanistic biochemical models in entire organisms*. Several authors have recently used first principles modeling to elucidate the biochemical reaction mechanisms of new drugs *in vivo* (45–52). Their model topology does not account for the physiologically consistent blood or lymph perfusion, in the arteries, capillaries, and veins of individual organs. Consequently, simulation of blood sampling techniques is imprecise, involving significant errors of pharmacokinetic parameter estimates. These errors limit the fidelity of the previous PBPK models for the extrapolation of information from small animals to larger ones, from animals to humans, or for the prediction of drug fate for varying dosing regimes.

3.2.2. **Mechanistic PBPK models with empirical scaling laws**

Traditional *interspecies scaling laws* in pharmacokinetics often deploy simple polynomial relationships between properties of interest such as the intrinsic clearance. The *allometric approach* is empirical, and rests on the assumption that the underlying physiological processes such as cardiac output, heartbeat frequency, breath duration, are only related to body mass (88). Typical empirical relations for interspecies scaling include: clearance versus body weight, the product of clearance and maximum life-span potential versus body weight, the product of clearance and brain weight versus body weight, and the application of a fixed exponent to clearance (88). Interesting research from Geoffrey West and colleagues about allometric scaling laws in biology shows early attempts to incorporate first principles into determining whole organism metabolic rates in different animals. In particular, West's group developed a model to explain the origin of quarter-power scaling laws and there use in determining metabolic rates when organism body sizes vary over large orders of magnitude (89,90). Another concept, *interspecies scaling* with invariant pharmacokinetic time, results in the removal of the differences in concentration-time profiles due to chronological time (91). Unfortunately, interspecies extrapolation with these simple scaling laws is not satisfactory because it does not account for fundamental biochemical mechanisms, but merely incorporates weight or size factors. Due to the limitation in predictive capabilities, expensive and time-consuming dose-response data have to be acquired in extensive animal trials in rats, then dogs and monkeys, until finally arriving at reasonably safe specifications for human trials.

3.2.3. **Multiscale mechanistic PBPK model with mechanistic intra- and inter-species scaling**

We propose a multiscale biological system model to describe the drug fate in: cells, tissues, organs, whole body, among individual subjects, and across species. These variables may be scaled according to fundamental chemical and physical principles to create a consistent and rigorous pharmacokinetic model with better predictive capabilities than classical black-box pharmacokinetics. Specifically, we propose the following first principles inter-species scaling laws.

i) Drug fate in cells is determined by selected biochemical reactions. For instance, metabolic activity is observed in hepatocytes or specialized renal cells. These reactions will be scaled according to chemical principles which have to be studied independently, for instance in cell cultures.

ii) Drug action in tissues is characterized by biotransport phenomena, such as the mass transfer between the blood and interstitial fluid. These mechanisms are generally strong functions of the size of mass transfer area while the specific mass transfer rate of blood-organ interface may be constant. This category of parameters may be scaled independently to account for differences in organ surfaces / mass transfer surfaces / specificity of the active transport.

iii) Biodistribution in organs is determined by physiological and anatomical parameters, blood perfusion rate, and age. Physiological and biodistribution parameters must be determined experimentally. Whole body drug biodistribution is

given by initial conditions of the biological system, such as the drug administration regime or systemic pathology.

iv) Individual subject pharmacokinetic variations are determined by distinct phenotypes, most prominently by anatomical and physiological differences, which are a strong function of body mass.

v) Inter-species pharmacokinetic scaling is based on well-known anatomical relationships such as the changes in organ weight as a function of total body weight or blood perfusion rates as a function of different cardiac output.

Our approach uses a first principles PBPK model as a starting point, enforcing the conservation laws and reaction and mass transfer mechanisms based on the scaled parameters. Therefore, the prediction of the bioaccumulation will not result from simple algebraic scaling but will be the outcome of solving the entire network using the scaled parameters for each category. Such a model is capable of addressing both physiological as well as biochemical and transport variations between each species *with much higher accuracy than can be expected from simple allometric scaling laws*.

This chapter is organized as follows. Section 3.3 introduces the steady state systemic blood circulation model, mechanistic transport, mass transfer and biochemical reaction parameters, and a parameter estimation technique for determining the unknown model parameters from actual animal experiments. The interspecies scaling laws are then stipulated. We will demonstrate the scaling of our first principle pharmacokinetics from rats to humans on a case study of the immunosuppressant Cyclosporin in section 3.4. The model will then be used to assess different administration regimes in various species.

Discussion on the accuracy of the interspecies scaling from rat to monkey, pig, and human as well as the prediction capabilities for drug biodistribution in five individual patients follows in section 3.5.

3.3. Interspecies Pharmacokinetic Modeling Framework

3.3.1. Overview of the methods

This section introduces a mechanistic interspecies scaling technique to predict drug biodistribution in entire organisms based on limited experimental data. Therapeutic agents administered into the systemic circulation are distributed mainly by convection through the blood. In the capillaries of organs and tissues, the drug may pass from the blood stream into the extracellular space. Biochemical interactions, binding, and metabolism of the drug take place on the cell surface and in the cytosol. In addition, lipophilic agents within the blood bind to lipoproteins, preventing their transfer into organs.

Our *physiologically-based pharmacokinetic model* seeks to determine the drug fate in entire organisms through three principal mechanisms: (i) systemic *blood circulation* model depicted in Figure 12b, (ii) *biotransport and mass transfer* between blood, extracellular space and cytosol, shown previously in Figure 3 of section 2.3.2, and (iii) *biochemical reactions* accounting for the drug metabolism, as shown in Figure 12c. For new drugs, the biochemical reaction, mass transport mechanisms and their parameters are unknown. Therefore, proper mechanistic biokinetic models with the unknown reaction and transport coefficients need to be determined from *in vivo* experiments. We introduce a *rigorous parameter estimation technique* for discovering the unknown rate parameters from actual drug dose-response experiments in animals. We finally formulate *interspecies scaling laws*

for pharmacokinetic parameters that enable extrapolation of concentration profiles in other vertebrates based on the results in the rat only. This framework is also capable of predicting organ concentration profiles resulting from different dosing regimes. A list of the symbols and indices used in our PBPK modeling framework can be found in Table 1 of section 2.3.

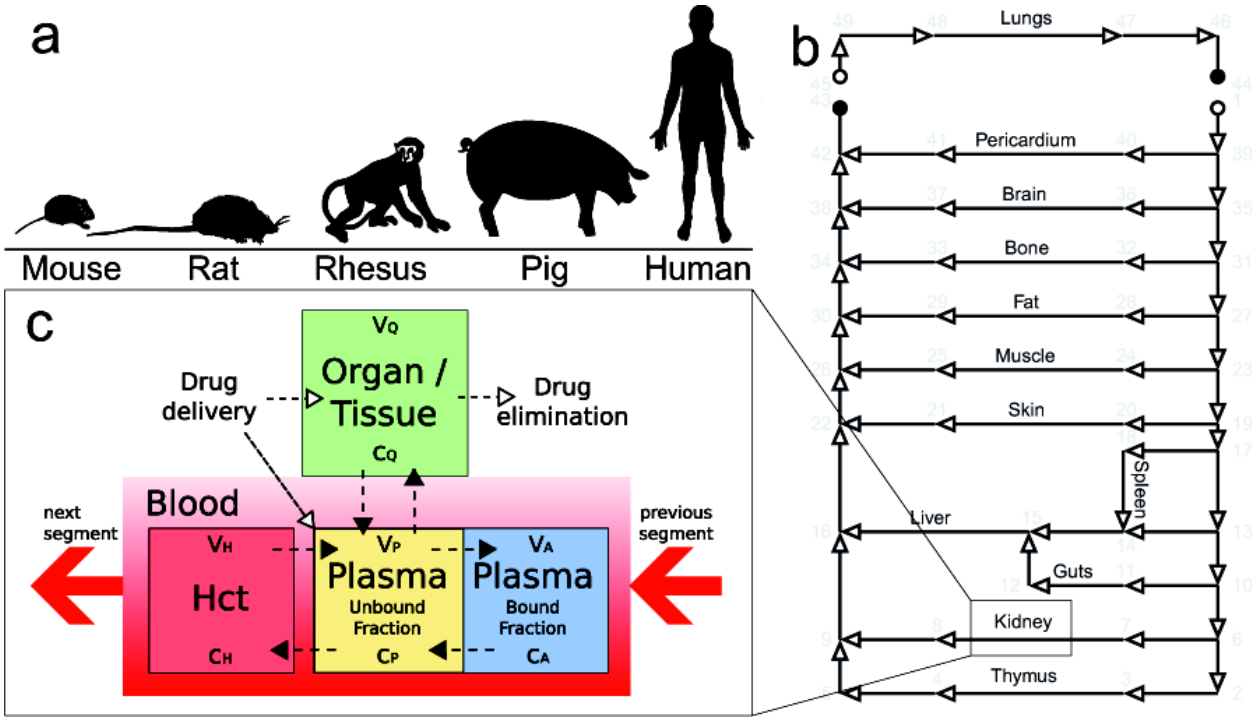

Figure 12. (a) A collection of vertebrates has been compiled for demonstrating interspecies scaling of pharmacokinetics. (b) The topology of the vasculature network is shown on the right with twelve organs including the venous (left), capillary (middle), and arterial (right) parts. The network structure is the same in all species; cardiac output, blood perfusion rates, and organ volumes are different in each species. The circles denote heart ventricles and the arrows represent vascular segments. The multi-compartmental model used for each organ in the network has a tissue and a blood compartment. (c) The blood compartment consisting of red blood cells (Hct), plasma (unbound and bound drug fractions), and organs/tissues is shown on the left.

3.3.2. **Whole body circulation network**

As previously mentioned in section 2.3.1., blood, lymphatics, and cerebrospinal fluid convection are responsible for fast systemic drug biodistribution. These circulatory systems can be mathematically modeled as directed, cyclic graphs (55). Our multiscale

whole body pharmacokinetic model includes the *systemic blood circulation graph* as a central component. The graph is defined by blood pressure values at the vertices and blood flow rates at the edges. Blood pressure boundary conditions are given at the heart as depicted in Figure 12b. The circulation network is modeled as a set of steady state fluid momentum equations, to solve for blood pressures and perfusion rates. The vascular system model consists of rigid tubular segments with known radii, lengths, and volumetric flow resistances. Physiologically consistent blood perfusion rates and pressure drops in all organs/tissues are ensured by selecting suitable hydraulic properties. In each organ, the blood supply is further divided into three sections representing arterial, capillary, and venous blood volumes. The distribution of blood flow resistances in organs is estimated according to known physiological data for mouse, rat, monkey, pig and human (1,3).

3.3.3. **Mathematical formulation of Cyclosporin pharmacokinetics**

This section will briefly outline the mass transfer, metabolism, and biochemical reactions of the immunosuppressant Cyclosporin in an entire organism. *The complete set of equations of the first principles model along with more details can be found in section 2.3.* Our whole body PBPK model includes the reversible mass transfer of Cyclosporin from the blood into tissue, as well as the drug metabolism and excretion.

Drugs administered into the circulatory system can be transferred through endothelial capillary walls into the interstitial fluid of organs and tissues. For a peptide, such as Cyclosporin, peptide-ligand binding occurs in the interstitial fluid, on the cell membranes, and in cells. These processes can be described by a set of biochemical reactions, Eqs. (28)-(29), where the drug, *CyA,* binds with ligand, *L,* to form a bound complex, *CyA.L*, which is then eliminated by reaction into a metabolite, *mCyA* in specialized

cells of liver and kidneys. Ligands in this context may include proteins, phospholipids, and even reactants involved in active transport. Therefore, Eqs. (28)-(29) can account for both passive as well as active transport, including transporter-mediated mass transfer.

$$CyA + L \leftrightharpoons CyA.L \tag{28}$$

$$CyA \cdot L \rightarrow mCyA \tag{29}$$

We assume equilibrium for reaction Eq. (28). Though the metabolic reactions of Cyclosporin attributed to the presence of cytochrome P450 3A in the gastrointestinal (GI) tract have been reported previously (62,63,92,93), we chose not to include this metabolic pathway since the overall effect of cytochrome P450 3A enzymes in the GI tract metabolism has been determined to be less than 1% of the total systemic clearance in rats (62,63,92,93).

Based on the blood distribution model depicted in Figure 12, we formulate a *simplified mechanistic model* for the biodistribution of Cyclosporin in blood and in organs/tissues, as was previously shown in Figure 3. The blood is further subdivided into plasma electrolytes, plasma lipoproteins, and erythrocytes, which are assumed constant in volume.

The dynamic mathematical model based on first principles of drug dispersion in the entire body is formulated as a set of differential equations summarized formally in Eq. (30), where c is the modeled state and c' is its time derivation. The functional matrix of physiological parameters is $\Psi(k)$ and accounts for physiological and anatomical parameters of the reference animal and depends on the unknown set of kinetic and transport parameters, k, $k \supset (k_A, k_H, k_Q, UA)$ which is a superset of biochemical reaction rates k_A, k_H, k_Q and mass transfer rates UA. The initial conditions, $c(t_0)=c_0$, specify known initial drug

concentrations. The full set of equations, Eqs. (8)-(15), was listed in previously in section 2.3.2.3 thru section 2.3.2.5.

$$G[c'(k,t), c(k,t), \Psi(k)] = 0\,, \quad c(t_0) = c_0 \tag{30}$$

3.3.4. **Parameter estimation - kinetic inversion problem and solution**

The unknown coefficients, *k*, that parameterize this model can be determined from experiments by an inversion technique briefly described here and in more detail previously in section 2.3.3. The optimal transport and biochemical reaction parameters of the mechanistic PBPK model are determined from the minimum least squares distance between experimental and predicted drug concentrations, as shown in Eq. (31). The result of the PBPK model is a set of concentration profiles, *c,* in all organs of the body. The objective function, φ, measures the cumulative weighted least squared error between the modeled, *c*, and measured tissue concentration $\hat{c}$, which are the drug concentration profiles in the plasma, blood, tissues and organs, at time, t_i.

$$\begin{aligned} &\min_k \varphi[c(t,k), \hat{c}(t), t] = [c(t,k) - \hat{c}(t)]^T {\Lambda_k}^{-1} [c(t,k) - \hat{c}(t)] \\ &s.t.\ \ G[c'(k,t), c(k,t), \Psi(k)] = 0 \\ &c(t_0) = c_0 \end{aligned} \tag{31}$$

The variance-covariance matrix, Λ_k, accounts for measurement accuracy of experimental data with diagonal elements σ_{ii} representing the variance and the off-diagonal elements σ_{ij} representing the covariance elements as in Eq. (32). More details of the variance-covariance matrix formulation for dynamic systems can be found in the literature (79).

$$\Lambda_k = \begin{pmatrix} \sigma_{11} & \cdots & \sigma_{1p} \\ \vdots & \ddots & \vdots \\ \sigma_{p1} & \cdots & \sigma_{pp} \end{pmatrix} \tag{32}$$

An analytical solution of the system in Eq. (31) is not possible in general. To solve this problem, drug concentration profiles, *c*, are obtained by numerically integrating a system of ordinary differential equations in Eqs. (11)-(15), with numerical forward estimation of the derivatives with the DASSL software package (64). The minimization problem was solved with the Trust Region (TR) Algorithm as described in section 2.3.3. (70–73), which is a large-scale globally convergent method. The solution of this parameter estimation problem gives the desired set of kinetic constants and drug clearances for each organ in the organism.

3.3.5. **Interspecies scaling laws for pharmacokinetics**

Traditional scaling laws propose power-polynomial relationships between properties of interest, such as bioaccumulation in a specific organ like the liver. Based on these simple rules, the concentrations in one organ are extrapolated from values obtained in smaller animals. Unfortunately, the accuracy of these algebraic scaling laws is not satisfactory, because they do not account for biochemical principles, but merely incorporate weight-based scaling factors.

We will first outline the major difference between allometric scaling and our method. The empirical scaling laws utilize direct power-law relations for pharmacokinetic parameters, such as the intrinsic clearance, as in Eq. (33):

$$\begin{gathered}\text{Allometric scaling for species } I, J\text{:} \\ \text{Power Law: } \quad f_J\left(c_J, \pi_J\right) = f_I^{\alpha}(c_I, \pi_I)\end{gathered} \tag{33}$$

where the pharmacologic parameter is a function of drug concentration, *c*, in whole body and physiological parameters π. Subsequently, scaling from species *I* to *J* engages the power-exponent α, which is related to the body weight fraction between *I* and *J*. To improve

the reliability of predictions, we propose a completely different scaling framework which better incorporates fundamental chemical and transport principles. First, our scaling method uses a first principle whole-body pharmacokinetics model as a starting point. In this PBPK model, coefficients for reaction and transport mechanisms are obtained from dose-response experiments on laboratory animals. Next, parameters are grouped into three categories: (i) physiological, (ii) biochemical and (iii) transport. Parameters in each group are scaled according to different scaling laws best suited for each parameter:

1. The *physiological and anatomical group* of parameters such as blood perfusion rates and organ sizes can be scaled from species to species based on well-known relationships such as the changes in organ weight as a function of total body weight or blood perfusion rates as a function of different cardiac output.
2. The *biochemical group* of parameters typically includes specific reaction rates in the units of moles per cubic meter. Specific reaction rates summarize the overall reaction mechanisms taking place in the tissues of organs. Even though all detailed reaction steps can often not be accounted for, they determine yield and selectivity of the components per unit organ volume. Moreover, specific reaction rates may be adjusted for species differences due to variations in the metabolism, susceptibility to different enzymes, or kinetics of the biochemical reactions. The interspecies variations in biochemical kinetics can be quantified with metabolic flux scaling methods (94–97). Further detail regarding metabolic flux scaling can be found in the references to Jia et al. (2011) and other authors (94–97).
3. Finally, *transport mechanism parameters* usually refer to mass transfer based on physical or active transport. These mechanisms are generally strong functions of the

size of mass transfer area while the specific mass transfer coefficient of blood-organ interface may be constant. This third category of parameters can also be scaled separately to account for differences in organ surfaces / mass transfer surfaces / specificity of the active transport.

In addition to categorizing and scaling the model parameters according to suitable laws for each group, we always enforce the conservation laws and reaction and mass transfer mechanisms using the scaled parameters. Therefore, the prediction of the bioaccumulation or concentration profiles do not result from direct scaling, but the outcome of solving the conservation balances in the entire network using the scaled parameter groups. Such a model is capable of addressing both physiological as well as biochemical or transport differences among selected vertebrates. The proposed mechanistic scaling can be summarized by steps outlined in Table 4.

Table 4. Biochemical and Physiological Scaling from Rat (I) to Larger Species (J)

1. Given: Parameter Set for **Species I**: $k_I = \min_k \varphi[c_I(t, k_I), \hat{c}_I(t), t]$, where $k_I \supset \{k_{M,I}, A_I\}$, as in Eq. (31)
2. Scale Parameters from **Species I** to **J** $k_I \rightarrow k_J$:
2.1 Physiological and Anatomical Parameters such as blood perfusion rates and cardiac output
2.2 Drug Biochemical Reaction Rates in **Species J**: $k_{M,J} \rightarrow k_{M,I}$
2.3 Scale Drug Mass Transfer Area for Organs in **Species J**: $A_I \rightarrow A_J$
3. Solve for Extrapolated Concentration in **Species J**: $G\left[c'_J(\boldsymbol{k_J}, t), c_J(\boldsymbol{k_J}, t), \Psi_J(\boldsymbol{k_J})\right] = 0$, as in Eqs. (11)-(15)

The first step, the parameter k_I estimation, is performed on the rat and is a function of the concentration in whole body, c_I. Vector k includes mass transfer area values in whole body, A_I, and biochemical reaction rates, $k_{M,I}$, which are both function of the measured concentration in species I. For the extrapolation, the ***physiological and anatomical group*** of parameters is obtained by experimental measurements. For the ***biochemical group*** of parameters, we assume in step 2.1 of Table 4 the specific biochemical reaction rates to be

the same for all species. Observation differences in drug biodistribution can be accounted for with more data. Mass transfer areas, the ***transport mechanism parameters,*** are scaled in step 2.2 of Table 4 according to physiological and anatomical difference in organ volumes V_Q linearly. The predicted drug biodistribution is finally obtained as in step three, by solving the system of differential equations, Eqs. (11)-(15) from section 2.3.2.3, being a function of the newly scaled vector of parameter k_J and and physiological factors π_J, as previously shown in Eq. (31). The detailed equations and the parameters of the proposed scaling framework will be described next.

3.4. Results: From Pharmacokinetic Rat Trials to Predictions in Monkeys, Pigs, and Humans

We first show how the systemic rat model was created. The unknown parameters for kinetics and biotransport of immunosuppressant Cyclosporin in the rat were determined from experimental dose-response curves. Using the knowledge acquired from the rat combined with the new interspecies scaling framework, we predicted without incorporating any new experimental data the probable biodistribution of Cyclosporin in the monkey, pig, and human. We will demonstrate the scaling principles and show predicted concentration profiles in other vertebrates. Also, the ability of our methodology to predict drug bioaccumulation for different dosing regimes in individual subjects and across species will be discussed.

3.4.1. Systemic blood circulation model for the mouse, rat, monkey, pig, and human

A whole body circulatory model based on experimentally obtained physiological values for twelve main organs was constructed as depicted in Figure 12b for the reference

mouse, Sprague-Dawley rat, rhesus monkey, domestic pig and human. ***Organ and tissue volumes*** were collected from previous studies and are summarized in Table 5 (1,3,98–103). The key organs include the extra-organ blood, which is the average amount of blood found outside of organs in the circulatory system at any given time. Remaining body volume accounts for the sum of other body parts, such as hair, cartilage, adrenals, needed to arrive at a correct body mass. We chose to neglect the variations of tissue density and assume a standard value of 1 g/cm^3, which is an adequate number for tissue homogenates post mortem. ***Blood content in organs*** for the reference mouse, rat, monkey, pig, and human are listed in Table 6 (1,36,104,105). Table 7 shows the ***blood perfusion rate in each organ*** for the mouse, rat, monkey, pig, and humans (1,3,99–101,103,106,107).

Table 5. Organ volumes for the reference mouse, rat, rhesus monkey, pig, and human.

	Mouse[a] 0.030 kg	Rat[b] 0.277 kg	Monkey[c] 4.4 kg	Pig[d] 25.5 kg	Human[e] 73 kg
Organ Volume (mL)					
Liver	1.65	11.17	140.31	588.0	1800
Kidneys	0.51	2.49	21.50	80.0	310
Brain	0.51	11.17	90.30	80.0	1400
Bone	3.21	17.13	400.00*	1400.0	10500
Fat	2.10	10.84	500.00*	6000.0	12500
Guts	1.71	10.84	156.99	1000.0	1200
Pericardium	0.15	0.87	21.51	74.0	330
Lungs	0.21	1.08	45.49	200.0	470
Muscle	11.52	132.28	2000.00[g]	8000.0	30000
Skin	4.95	43.37	444.10[h]	1138.0	3300
Spleen	0.18[f]	0.65	3.89	40.0	180
Thymus	0.33*	0.76	1.00*	40.0*	20*
Extra-Organ Blood	0.21*	8.71	393.80	721.0*	1966
RBW Volume	2.85	25.60	182.00*	6188.0	9024
Total Volume	30.09	276.96	4400.89	25549.0	73000
Total Blood Volume	2.00	20.70	655.80	2045.0	5900

[a] (Brown, Delp et al. 1997)
[b] (Delp, Evans et al. 1998)
[c] (Fremming, Benson et al. 1955)
[d] (Upton 2008)
[e] (Williams and Leggett 1989)
[f] (Thurlby and Trayhurn 1980)
[g] Calculated from (Davies and Morris 1993)
[h] (Forsyth, Nies et al. 1968)
* Estimated

Table 6. Blood volumes for the reference mouse, rat, rhesus monkey, pig, and human.

	Mouse[a] 0.030 kg	Rat[b] 0.277 kg	Monkey[c] 4.4 kg	Pig[d] 25.5 kg	Human[e] 73 kg
Blood Volume (mL)					
Liver	0.51	2.05	39.13	75.3	230
Kidneys	0.12	0.40	11.93	18.0	70
Brain	0.02	0.34	6.97	6.3	111
Bone	0.35	0.69	12.92	74.2	557
Fat	0.002*	0.22	34.55	230.1*	479*
Guts	0.03*	1.30	45.70	161.6*	194*
Pericardium	0.003*	0.23	14.52	27.7*	124*
Lungs	0.11	0.39	20.00	241.0	566
Muscle	0.46	5.24	44.20	200.0	750
Skin	0.15	0.87	31.18	261.7	759
Spleen	0.03	0.14	0.84	20.0	90
Thymus	0.01*	0.14	0.06	8.0	4
Organ Blood	1.79*	11.99	262.00*	1324.0*	3934
Extra-Organ Blood	0.21*	8.71	393.80*	721.0*	1966
Total Blood Volume	2.00	20.70	655.80	2045.0	5900

[a] (Brown, Delp et al. 1997)
[b] (Kawai, Mathew et al. 1998)
[c] (Mohammad Pervaiz 2010)
[d] Human blood fractions used to calculate
[e] (L. Weiss 1980)
* Estimated

Table 7. Blood flow rates for the reference mouse, rat, rhesus monkey, pig and human.

	Mouse[a] 0.030 kg	Rat[b] 0.277 kg	Monkey[c] 4.4 kg	Pig[d] 25.5 kg	Human[e] 73 kg
Blood Flow Rate (mL/min)					
Liver	1.80	11.80	52.13	517.3	364
Kidneys	1.30	9.23	170.50	111.7	1064
Brain	0.26	2.00	58.64	288.0	672
Bone	0.30*	2.53	131.41	520.0*	280
Fat	0.80	0.40	24.98	89.0	280
Guts	1.50	7.52	82.54	103.0	840
Pericardium	0.28	3.92	53.21	360.0	224
Lungs	0.04	38.45	9.77	20.6*	140
Muscle	0.91	2.03	275.84	86.5	952
Skin	0.41	5.83	84.71	61.0	280
Spleen	0.09	0.63	27.15	51.5	168
Thymus	0.30*	0.70	2.17	64.0*	84
Total	8.00	85.05	973.06	2252.0	5348
Percent Cardiac Output	70.18	100.00	89.60	100.9	95.5
Cardiac Output	11.40	85.05	1086.00	2272.6	5600

[a] (Thurlby and Trayhurn 1980; Brown, Delp et al. 1997)
[b] (Delp, Evans et al. 1998)
[c] (Forsyth, Nies et al. 1968; Hoffbrand and Forsyth 1969)
[d] (van Woerkens, Duncker et al. 1990; Upton 2008)
[e] (Williams and Leggett 1989)
* Estimated

A physiological whole-body vascular network corresponding to each animal subject was generated. The initial conditions for the vascular networks at both the heart ventricles and atria were given. The mean average cardiac output was 85 ml/min in rat, 1086 ml/min in rhesus monkey, 2273 ml/min in pig, and 5600 ml/min in man were specified as in Table 7. Finally, the systemic circulation network has been solved as a non-pulsating steady-state flow in rigid tubes.

3.4.2. **Pharmacokinetic model of a Cyclosporin bolus injection into the rat**

The transport and biochemical reaction mechanisms of the drug in the entire organism were modeled using Eqs. (8)-(15). A system of ordinary algebraic equations has been automatically generated by our software based on the vascular network graph representation and the proposed PBPK model. In each vascular segment, three equations, Eqs. (11)-(13), are generated for plasma unbound, plasma bound, and for the erythrocytes. In addition, for each capillary segment associated with one of the twelve main organs, one additional equation, Eq. (14), is generated. Moreover, two additional clearance equations for the drug elimination are defined for the liver and kidneys. All pharmacokinetic parameters for the rat were obtained by the proposed least squares parameter estimation as in Eq. (31). An ample set of experimental dose-response data is available with measured Cyclosporin concentration profiles in blood, plasma proteins, unbound plasma and twelve organs after injection of the drug into Sprague-Dawley rats (40). The first experimental dataset concerns intravenous injection of Cyclosporin solution into the femoral vein. Bolus injections over a period of two minutes were administered in sub-therapeutic 1.2 mg/kg, therapeutic 6.00 mg/kg and super-therapeutic 30 mg/kg dose into male animals with

277 g ± 15 g in weight. Organ concentrations at specific time instants were recorded and measured by radioimmunoassay after homogenization (2,34,40).

3.4.3. **Mechanistic parameter estimation for a therapeutic IV Cyclosporin administration in the rat**

The nonlinear parameter estimation problem applied to a time series with least square minimization between the experimental and predicted drug concentration profiles leads to a solution of the unknown parameter set *k*, as defined in Eq. (31). The values of the optimal parameters are given in Table 8 with the estimates of individual confidence intervals as outlined in (73,79).

Using only the *experimental data from the therapeutic dose-response curves*, the following mechanistic parameters of the vector *k* were determined: (i) the mass transfer rate for each organ UA_Q, (ii) the organ specific constants k_Q representing the fraction of drug available for mass transfer in the interstitial fluid (iii) the clearance terms for liver and kidney k_M (iv) four adsorption and desorption rates have been found for the red blood cells [k_H^+, k_H^-] and the bound plasma lipoprotein fraction [k_A^+, k_A^-]. The graphical comparison of mass transfer areas for mouse, rat, monkey, pig, and human is shown in Figure 13.

The goodness of fit for the optimal solution of the parameter vector *k* is indicated by the objective function value, which was found to be $\Phi = 3.14$. The dynamic simulation with the optimal parameter set gives drug concentration trajectories which closely fit the experimental profiles as shown previously in section 2.4.3 Figure 4 for the therapeutic dose. Some experimental data was estimated previously, such as the concentration of Cyclosporin in the plasma unbound compartment (34,40,82,84).

Table 8. Optimal parameter estimates of kinetic rates of binding (k_1…k_4), mass transfer rates (k_5…k_{28}) and metabolic rates (k_{29}, k_{30}), are shown, where ($^+$) denotes binding into, ($^-$) out of compartment, ($_M$) the metabolic terms and UA the mass transfer rates. The fraction of free drug in each organ, which is available for mass transfer, k_Q, correlates the drug concentration in the interstitial fluid and in entire organ. Deviations were estimated for 95.0 % individual confidence level. The least square fitting objective function value is 3.140. Parameters, which have been scaled from rat to other species based on physiological values are marked with (*).

			Calculated		Scaled from Rat		
			Rat 0.28 kg		Monkey* 3.0 kg	Pig* 30.9 kg	Human* 73.0 kg
i	**Parameter**	**Units**	**k_i**	**Deviation**	**k_i**	**k_i**	**k_i**
1	$k_{\bar{A}}^{+}$	[h^{-1}]	5.960	±0.498	5.960	5.960	5.960
2	$k_{\bar{A}}$	[h^{-1}]	4.795	±0.447	4.795	4.795	4.795
3	$k_{\bar{H}}^{+}$	[h^{-1}]	0.934	±0.197	0.934	0.934	0.934
4	$k_{\bar{H}}$	[h^{-1}]	2.104	±0.296	2.104	2.104	2.104
5	UA liver	[$m^3\,h^{-1}$]	91.050	±1.946	686.400	6721.000	14680.000
6	UA kidneys	[$m^3\,h^{-1}$]	7.809	±0.570	40.400	351.200	970.800
7	UA brain	[$m^3\,h^{-1}$]	0.818	±0.184	3.966	8.210	102.500
8	UA bone	[$m^3\,h^{-1}$]	14.550	±0.777	203.900	1667.000	8920.000
9	UA fat	[$m^3\,h^{-1}$]	13.240	±0.742	366.400	10270.000	15270.000
10	UA gut	[$m^3\,h^{-1}$]	13.530	±0.750	117.500	1749.000	1497.000
11	UA heart	[$m^3\,h^{-1}$]	1.503	±0.250	22.360	179.700	571.600
12	UA lungs	[$m^3\,h^{-1}$]	2.179	±0.301	54.850	563.500	944.500
13	UA muscle	[$m^3\,h^{-1}$]	206.000	±2.927	1869.00	17470.000	46720.000
14	UA skin	[$m^3\,h^{-1}$]	13.880	±0.760	85.250	510.400	1056.000
15	UA spleen	[$m^3\,h^{-1}$]	1.844	±0.277	6.615	158.900	510.100
16	UA thymus	[$m^3\,h^{-1}$]	0.413	±0.131	0.327	30.530	10.890
17	$k_Q$liver	[-]	0.037	±0.004	0.037	0.037	0.037
18	$k_Q$kidneys	[-]	0.048	±0.016	0.048	0.048	0.048
19	$k_Q$brain	[-]	4.221	±0.463	4.221	4.221	4.221
20	$k_Q$bone	[-]	0.341	±0.031	0.341	0.341	0.341
21	$k_Q$fat	[-]	0.061	±0.014	0.061	0.061	0.061
22	$k_Q$gut	[-]	0.223	±0.026	0.223	0.223	0.223
23	$k_Q$heart	[-]	0.279	±0.088	0.279	0.279	0.279
24	$k_Q$lungs	[-]	0.210	±0.063	0.210	0.210	0.210
25	$k_Q$muscle	[-]	0.804	±0.013	0.804	0.804	0.804
26	$k_Q$skin	[-]	0.288	±0.029	0.288	0.288	0.288
27	$k_Q$spleen	[-]	0.157	±0.060	0.157	0.157	0.157
28	$k_Q$thymus	[-]	0.113	±0.107	0.113	0.113	0.113
29	k_M liver	[h^{-1}]	0.301	±0.112	0.301	0.301	0.301
30	k_M kidney	[h^{-1}]	0.173	±0.085	0.173	0.173	0.173

Our model predicted a different drug concentration profile in the plasma unbound compartment compared to the previously estimated profile from the literature (34,40,82,84). This difference is not of great concern since the unbound plasma concentration data was not based on actual measurements, but constituted estimates from literature. Also, studies have shown that the amount of unbound Cyclosporin in plasma has wide variability up to 7.5-fold. This variability depends not only on patients' physiological

differences, but also on the different methods of experimentally measuring or analytically estimating the plasma unbound concentration (82,108).

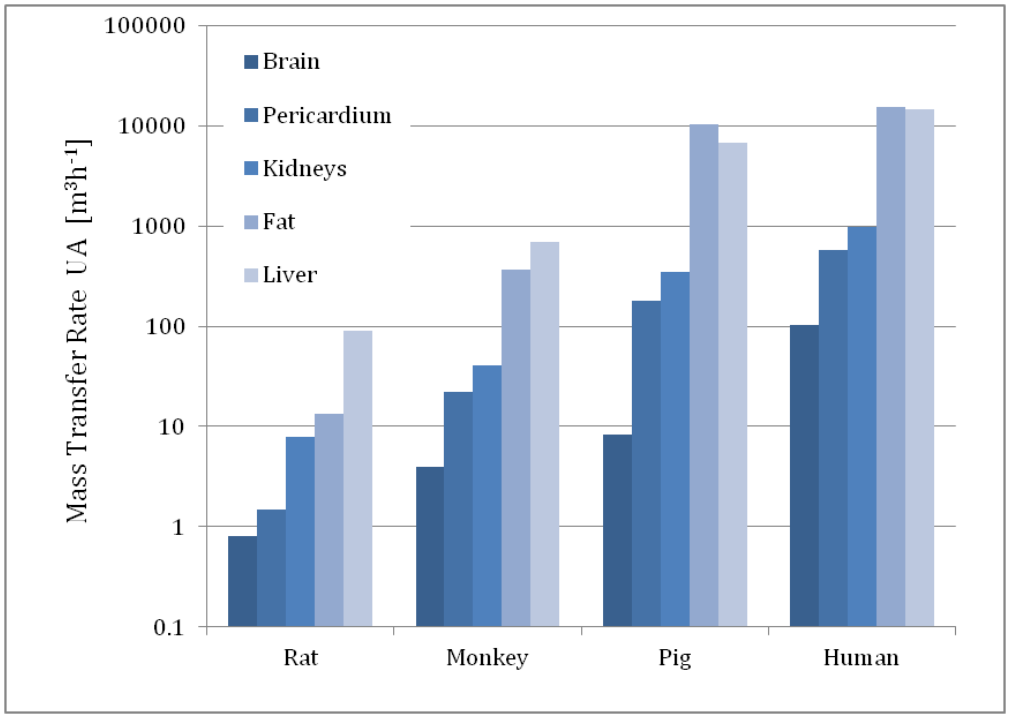

Figure 13. Scaling of mass transfer parameters. Mass transfer rates of Cyclosporin from blood to selected organs in rat, monkey, pig, and human. The parameters were estimated for rat by our transport and kinetic inversion technique. For each animal and human, transport parameters were scaled from rat according to the ratio of organ volumes.

3.4.4. **Interspecies scaling of pharmacokinetics: scaling from rats to monkeys, pigs, and humans**

The mechanistic PBPK model determines the fundamental reaction and transport stages of a drug in an entire organism. We can deploy scaling laws for each category from the biochemical, physiological, and transport parameters. The blood, organs, and tissue concentration profiles can thus be extrapolated from one species to another, based only on physiological differences. The specific scaling for the case study is described next. In a first approximation, the binding and unbinding rates of drug from the plasma unbound fraction

to plasma lipoproteins and erythrocytes per unit volume are also assumed constant among species, as in Eq. (34). However, varying hematocrit and plasma lipoprotein fractions among species influence the drug biodistribution in all organs of the body.

Biochemical group

Scaling for plasma for species I, J: $k_{A,J}^{+,-} = k_{A,I}^{+,-} = constant$ (34)

Scaling for erythrocytes for species I, J: $k_{H,J}^{+,-} = k_{H,I}^{+,-} = constant$

3.4.4.1. ***Scaling of pharmacokinetic parameters in organs***

As a first estimate for first-in-human drug trials, it is often assumed that the drug metabolism does not change when up-scaled from smaller species. This can be described in terms of constant clearance rates in metabolizing and excreting organs as in Eq. (35), where the clearance term k_M (h^{-1}) was previously described in Eq. (15).

Biochemical group

for species I, J: $k_{M,J} = k_{M,I} = constant$ (35)

The drug specific mass transfer coefficient *U,* as well as the fraction of specific area to organ volume is assumed constant among the species. The parameter A (m^2), which represents the specific area available for mass transfer from capillaries into the interstitial fluid can, under simplification, be scaled linearly with the volume of the organ as in Eq (36).

Transport mechanism group

Scaling for organ Q for species I, J: $\frac{A_J}{V_{Q,J}} = \frac{A_I}{V_{Q,I}}$ (36)

We further assume that the specific fractions of drug in an organ available for mass transfer, k_Q, (volume fraction) are also constant across different species as in Eq (37).

Transport mechanism group

Scaling for organ Q for species I, J: $k_{Q,J} = k_{Q,I}$ (37)

Figure 14 presents the physiological differences for the reference mouse, rat, rhesus monkey, pig, and human. Although the body mass scales roughly linearly, the organ proportions exhibit large non-linear variations in mass. In the case study, we omit the mouse model due to the lack of published scientific observations of Cyclosporin administration measured by radioimmunoassay method for all twelve tissues used in our model. The aim will be to predict pharmacokinetics in monkeys, pigs, and humans based on a single preclinical trial of a novel drug in rats. Specifically, the results demonstrate a scaling technique based on a therapeutic bolus injection of 6 mg/kg Cyclosporin into a rat. Using Cyclosporin biodistribution data from these rat experiments along with our proposed pharmacokinetic model, described in Eqs. (11)-(15), the unknown transport and reaction parameters are estimated. The parameters are then scaled according to physiological and anatomical factors as in Eqs. (34)-(35). The scaled parameters for the reference rhesus monkey, pig, and human can be seen in Table 8. The predicted and scaled concentration profiles will be validated against previously published studies on animals and volunteers.

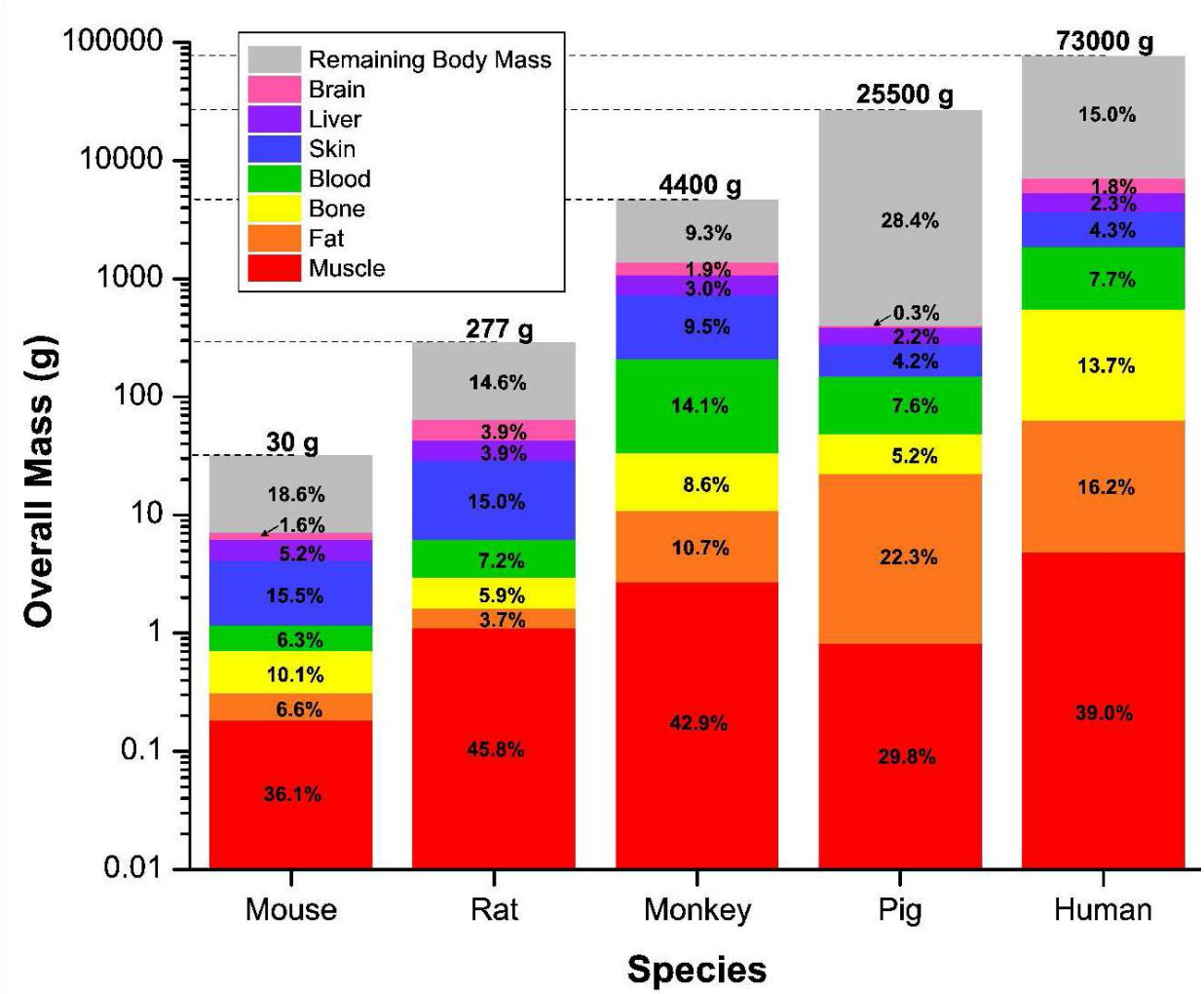

Figure 14. Key physiology library for laboratory animals and human. Compilation of body mass (left axis) and organ weight fractions (column sections) of reference mouse, rat, rhesus monkey, pig, and human. Remaining body mass represents other organs and parts of the body.

3.4.4.2. ***Rhesus monkey***

We simulated the oral administration as an intravenous, continuous injection into the arterial part of the digestive system with a dose of 2.5 mg/kg for a 3.0 kg reference rhesus monkey with the optimal vector of parameters, *k*, scaled from the reference rat to the reference rhesus monkey as can be seen in Table 8. The concentration profiles in typical allograft transplantation organs and in blood can be observed in Figure 15a. Due to lack of data for IV administration of Cyclosporin into rhesus monkeys, we will compare the

model with measurements for oral administration. Cyclosporin given orally is poorly absorbed in primates compared to humans. This has been demonstrated in pharmacokinetic experiments (109) with rhesus monkeys, cynomolgus monkeys, and baboons. Data from rhesus monkey trials on oral Cylosporin administration of 25 mg/kg in microemulsion was obtained from literature (110). The modeled blood concentration profile from muscle closely matches the experimental data, with the absolute bioavailability value of 0.13 matching the observations calculated from Schuurman et al. 2001 (110); the correlation coefficient is R=0.972.

3.4.4.3. ***Pig***

The modeled concentration profiles for blood and selected organs can be seen in Figure 15b for a 30.9 kg reference pig using the optimal vector of parameters, *k*, scaled from the reference rat to the reference pig as in Table 8. Experimental data for intravenous administration of CyA in pigs was obtained from (111). The pigs were randomized into groups: a control group (n = 6) and a group subjected to CyA administration as a single infusion at 3 mg kg^{-1} (n = 6) over one hour under general anesthesia. The femoral artery was cannulated for blood sampling and measurements of blood pressure. Pigs of the Danish Landrace breed aged 80 days and weighing 33±2 kg were housed in individual cages and fed with a standard pig diet. Isotonic saline (sodium chloride 9 g l^{-1}) was given through an ear vein to maintain hydration during anesthesia. Whole blood CyA concentrations were measured from 0 to 7 h, using the EMIT Cyclosporin Specific Assay (Dade Bering, Marburg, Germany) containing monoclonal antibodies with a high specificity for Cyclosporin. The mean averaged whole body Cyclosporin concentration in the blood is substantially higher than the venous muscle concentration. Modeled blood from venous

muscle compartment matches closely the experimental data, the correlation coefficient is R=0.953.

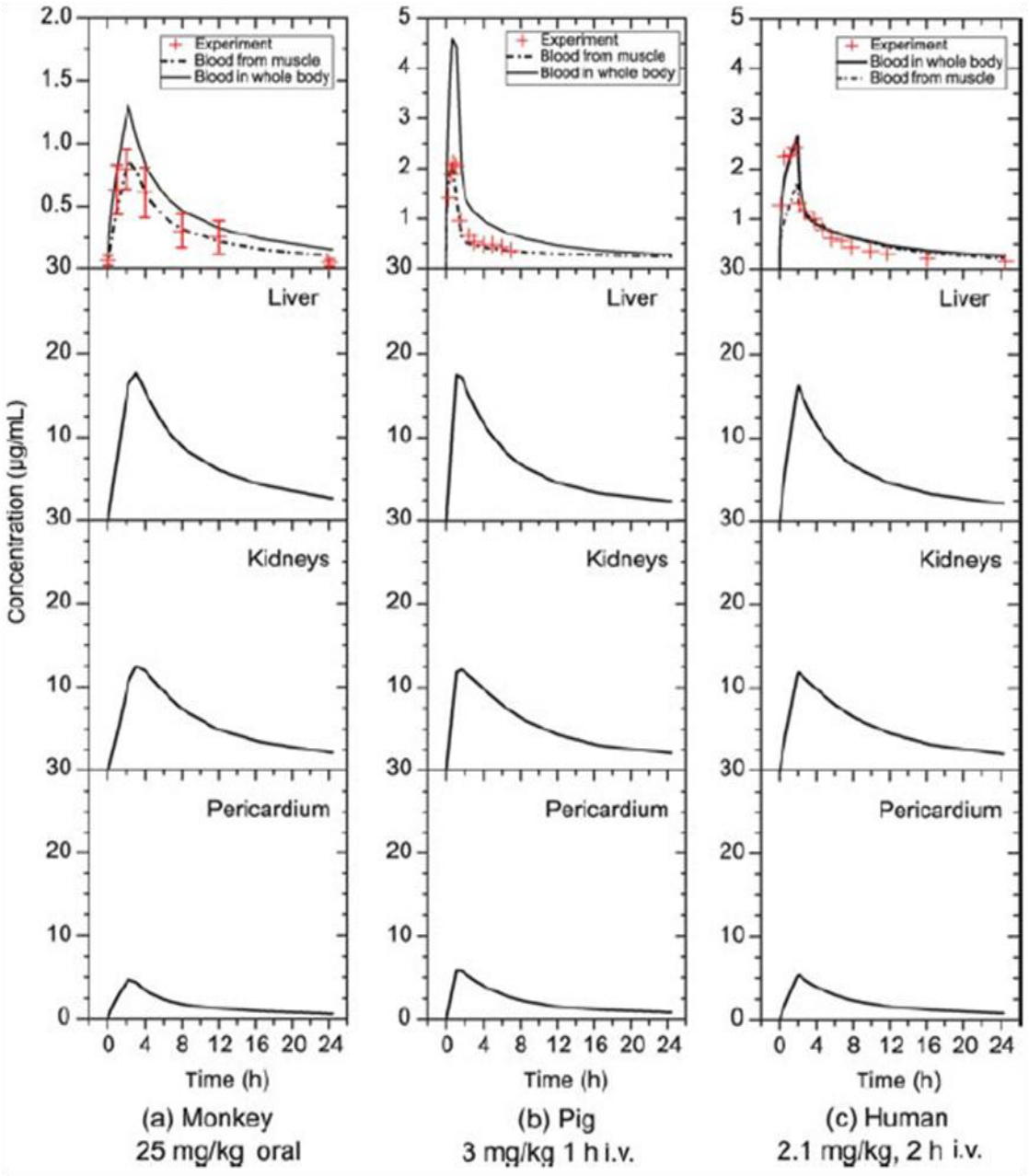

Figure 15. Pharmacokinetic simulations of Cyclosporin administration in monkeys, pigs, and humans based on a single laboratory experiment in rats, and the proposed mechanistic model of biodistribution. The correlation coefficients between the blood drawn from a limb vein, experimental data, and the predicted concentration in arterial blood from the muscle compartment are as follows: R_{monkey} = 0.972, R_{pig} = 0.953, and R_{human} = 0.838.

3.4.4.4. ***Human***

In the simulation, we assume a male 35 year old subject with a weight of 73 kg, and use the optimal vector of parameters, *k*, scaled from the reference rat to the reference rhesus monkey as seen in Table 8. Concentration profiles of Cyclosporin in whole blood were obtained from a previous study (112). The trials were performed on healthy volunteers, where Cyclosporin was administered intravenously into left arm by syringe over 2 hours in a dose 2.1 mg/kg. The experimental data matches the modeled blood concentration profiles from venous muscle compartment with adequate precision for intraspecies scaling, the correlation coefficient is R=0.838.

Another set of experimental data was obtained from literature (5). Cyclosporin was infused intravenously over 24 hours for immunosuppression in allogenic hematopoietic stem cell transplantation patients prior to procedure. Because the weight of the patients is not given, we assume the weight of the 73 kg reference man from the simulation of the whole body concentration profiles. The Cyclosporin concentration in blood, as well as AUC (0-12 h) after IV injection of the specified doses over 24 hours reaches a steady state in concentration. The experimental and simulated concentration, AUC (0-12 h) and the relatively small prediction error ranging from -30% to +117% in steady state concentration and from -30% to 110% in AUC for 12 patients can be seen in Table 9.

Table 9. Comparison of experimental and predicted Cyclosporin binding and pharmacokinetic parameters in individual stem cell transplantation patients after a continuous, 24 h *iv* administration. Experimental data on Cyclosporin dose, concentration and 12 h AUC has been obtained from (5). The data obtained from literature did not specify the weight of each patient or exact dose data; therefore, the predicted values are based on the simulated 24 h injection into a 73 kg reference human with pharmacokinetic parameters obtained by scaling from the male Sprague-Dawley rat trial with 6 mg/kg *iv* bolus administration. Had the exact weight of each patient and dose data been available, prediction errors would have been reduced and a plot with error bars would have been included.

Patient No.	*IV* Dose	*C* Measured	*C* Modelled	Prediction Error	AUC (0-12) Measured	AUC (0-12) Modelled	Prediction Error
	mg/24 h	ng/ml	ng/ml	%	h ng/ml	h ng/ml	%
1	96	590	414	-30	7 110	4 968	-30
2	140	643	603	-6	7 680	7 236	-6
3	130	553	562	2	6 630	6 744	2
4	173	663	748	13	7 950	8 976	13
5	192	677	829	22	7 920	9 948	26
6	125	577	540	-6	6 780	6 480	-4
7	80	527	329	-38	6 330	3 948	-38
8	192	717	829	16	8 730	9 948	14
9	240	477	1 035	117	5 820	12 420	113
10	125	357	539	51	4 350	6 468	49
11	58	257	251	-2	3 090	3 012	-3
12	77	303	332	10	3 690	3 984	8

3.5. Discussion

3.5.1. Scaling of pharmacokinetics between different species

A key outcome of this study is that the bioaccumulation of Cyclosporin can be predicted for a wide of range of different doses with a mechanistic model, whose parameters were estimated from a single dose experiment only. In the case study, the unique set of mechanistic parameters, *k*, was determined rigorously from experimental data collected in response to a therapeutic dose of 6 mg/kg of Cyclosporin administered intravenously into the femoral vein of a rat. Figure 4, shown previously in section 2.4.3, shows that the predicted organ drug concentration profiles match the experimental dose-

response measurements well. We used the same parameters *k* to extrapolate organ concentration profiles for simulated super-therapeutic (30 mg/kg) and sub-therapeutic dose levels (1.2 mg/kg). In addition to the expected good fit at the therapeutic level, the predictions also closely match all organ concentrations for the super-therapeutic dose. For the sub-therapeutic level, the simulation is less accurate, but still reasonable for all organs. The high extrapolation fidelity demonstrates that our mechanistic PBPK model properly captured *the fundamental pharmacokinetics of Cyclosporin with a single parameter set acquired from only one dose experiment in the rat*. These results show that our mechanistic model can predict drug concentrations for a wide range of dosing regimes for a wide range of animals.

3.5.2. **Prediction-quality assessment of interspecies scaling**

The results in Figure 15 demonstrate that the proposed PBPK model is able to predict blood concentration profiles in pigs and rhesus monkeys with remarkable accuracy; in human the match is satisfactory. Experimental venous blood concentration profiles closely match the modeled blood profiles drawn from muscle. The match, we deem reasonable, because no new information has been added to extrapolate from rat experiments to larger animals. Moreover, the administration modes are different for all four experiments: bolus injection of 6 mg/kg in rat study, oral administration of 25 mg/kg in the rhesus monkey, 3 mg/kg IV injection over 1 h in pigs, and 2.1 mg/kg IV injection in humans over 2.5 h.

The prediction errors also have to be considered in relation to measurement accuracy. Radioimmunoassay analytics was used in all experiments. HPLC method is

known to deliver more exact results, as it does not register Cyclosporin metabolites. A more accurate analytic method would improve the prediction capabilities (112).

An additional validation from rat to human was performed by considering a study involving 12 stem cell transplantation patients prior to their procedure. Table 9 lists experimentally acquired pharmacokinetic parameters after a 24 hour intravenous Cyclosporin administration. Our model, based on Cyclosporin rat data scaled with the novel inter-species scaling technique, predicts the concentration levels in whole body for a 73 kg reference man. In the experiment, only blood concentration profiles were measured, without explicitly stating the weight of each patient (5). The prediction error of Cyclosporin concentration ranges from -38% to 51% with an outlier 117%, which can most likely be attributed to the missing weight and exact dose data. Factors influencing the pharmacokinetics of Cyclosporin in man include a highly variable absorption due to the liver function, bile flow, and gastrointestinal status (113). Cytochrome P450 3A was reported to mediate Cyclosporin metabolism in the gastrointestinal tract (62,92). We did not include GI tract metabolism in our model because there are many effects concerning the absorption of Cyclosporin including the presence of Cytochrome enzymes in the GI tract (93) and this was not the objective of our study. In order to improve the prediction accuracy, we propose to utilize HPLC analytical methods for all measurements, to determine the fraction of adipose tissue in a subject, and if possible, other organs in the targeted patient model (112). Further options include *in vitro* determination of drug binding to erythrocytes, lipoproteins, and tissue cells in both species, or complementary measurements of drug concentration in targeted organ, such as in liver biopsy. These complementary measurements may then be used in all future models.

These results show that our first principles model can predict drug concentrations for a wide range of administration regimes in various species. Considering initial assumptions in the scaling of parameters, the intra- and interspecies scaling is applicable for certain drugs, where transport and biochemical reactions do not change substantially among vertebrates. This limitation can be overcome by measuring of *in vivo* parameters, such as metabolic rates as a function of genus. Metabolic flux analysis can provide additional improvements for the biochemical reaction models (94–96). Note that difficulties with oral dosing might arise due to unknown bioavailability as a consequence of polymorphism. In this case, more precise mechanisms of drug action such as in the GI tract or bile transport/recycle might be incorporated for the working hypothesis pharmacokinetics model of certain drugs.

3.5.3. **Pharmacokinetic simulations for human models**

The ultimate goal of mechanistic models based on first principles is the rigorous scaling of animal dose-response curves to humans. We demonstrate in Figure 16 the results of a case study involving five patients who despite an equal drug dose demonstrate concentration variations is tissues and organs such as the kidneys. This reasonable first principles prediction arises only from changed physiological and anatomical parameters among the patient models. The patients are characterized as follows: *#1*, 73 kg, healthy reference man; *#2*, 73 kg man with large adipose fraction, *#3*, 106 kg healthy man; *#4*, 186 kg obese man, *#5*, 73 kg man with renal allograft recipient. The simulation has been performed with scaled transport and kinetic parameters from the rat trial as discussed in section 3.4. Variations in organ volumes among the patients in Figure 16 are chosen arbitrarily due to lack of available data, but could reflect real patient physiology. Such an

approach might be used in determining the first-in-human calculated doses and the suitable dosing regime reflecting patient physiology and anatomy, such as the blood pressure, blood flow rate or hematocrit fraction in blood. Therefore, Figure 16 demonstrates how intraspecies scaling among humans is possible with our model because it is sensitive to a patient's physiology and anatomy.

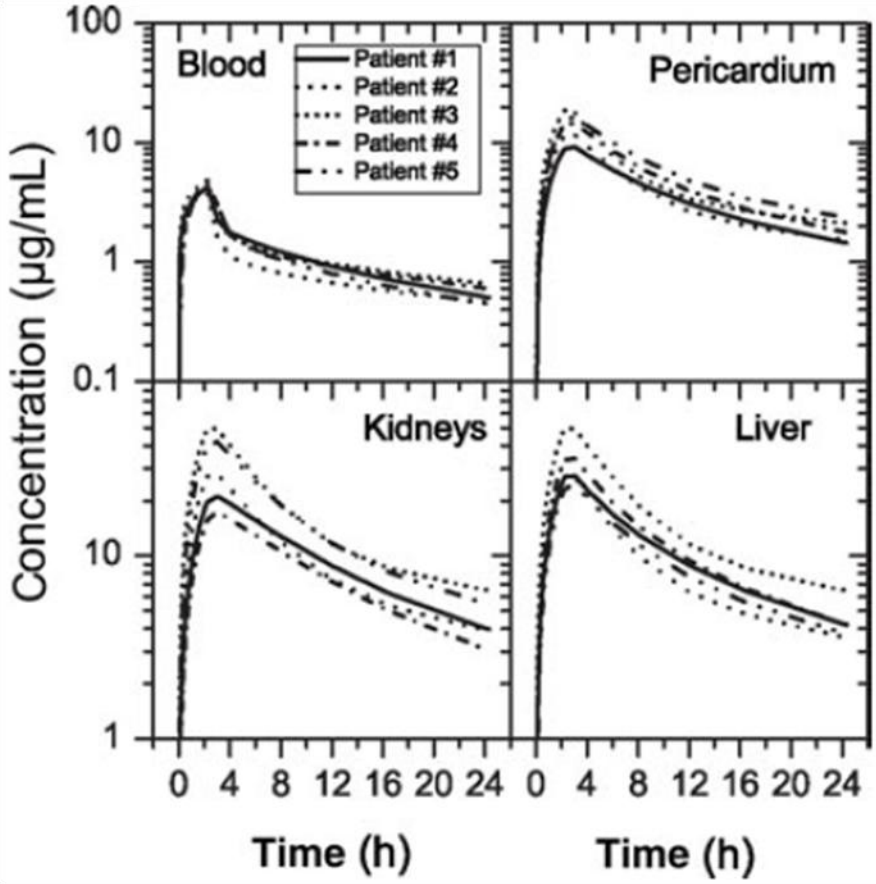

Figure 16. Simulation of population pharmacokinetics on Cyclosporin administered i.v. to five human subjects over 2.5 h at a dose of 4 mg/kg. The concentration profiles in selected organs are based on the pharmacokinetic parameters estimated from animal trials and scaled to each individual based solely on his physiology and anatomy. Patients are characterized as follows: #1, 73 kg healthy reference man; #2, 73 kg man, large adipose fraction; #3, 106 kg healthy man; #4, 186 kg obese man; #5, 73 kg man, renal allograft recipient.

In a worst case scenario, toxic levels may be reached in certain organs for the same dosing regime in affected patients. This sensitivity discovered with our model that the

volume of distribution, plasma half-life, intrinsic clearance, and blood/plasma concentration profiles are insufficient for the determination of safe human dosing regimes. Blood concentration profiles alone cannot directly determine drug biodistribution in organs. Very often, only blood and plasma concentration profiles are available in clinical praxis. This open problem could be addressed by the proposed, first principles PBPK model with mechanistic scaling laws, assuming suitable biochemical binding properties between the drug and the erythrocytes, the plasma lipoproteins, and the tissue cells across different species. This limitation could be addressed by incorporation of appropriate *in vitro* experimental results in all tested species into the mechanistic model. One is also free to perform the parameter estimation problem again, as soon as new experimental data become available. Our results show that our first principles model and scaling laws can rigorously predict drug concentrations in individual patients for a range of administration regimes.

3.6. **Conclusions**

The prediction quality of models in pharmacokinetic scaling strongly depends on the capability to incorporate information about drug exposure, drug action, and drug interaction with physiological and biochemical pathways. To that end, power law relationships have been useful in scaling up properties and parameters in pharmacokinetics in the past. In the future, pharmacokinetic and pharmacodynamic models will very likely dominate drug discovery efforts due to their ability to utilize realistic interactions and parameters to project *in vivo* data from one species to another (114). The knowledge gain in the scaling of biochemistry and biotransport of new drug

leads may be substantially accelerated by the proposed physiologically-based first principles modeling approach. The method enables the prediction of concentration profile variations due to inter- and intra-species differences, ranging from bolus to continuous administration at different dose levels, from healthy to diseased subjects across the compiled species including mouse, rat, rhesus monkey, pig, and human.

The aim of the presented case study was to demonstrate how mechanistic knowledge obtained from one animal drug administration trials can be transferred and scaled to other vertebrates. We first showed that intra-species scaling is feasible with the proposed mechanistic PBPK model with varying doses. Secondly, by using the novel mechanistic scaling laws for biotransport and metabolic rates, we are able to predict dose-response concentration profiles in the whole body of larger species and validate the predicted blood concentration profiles. The correlation coefficients between the experimental concentration and the predicted concentration of venous blood from muscle, R=0.972 for rhesus monkey, R=0.953 for pig, and R=0.838 for human, support our choice of constant biochemical reaction rates across the studied species for this case study. Unfortunately, we were not able to obtain time profiles for other organs or tissues in humans or other animals except for rat, which would require more extensive measurements, such as biopsy. We would like to point out large discrepancies between the averaged whole body blood concentration typically used in black-box compartmental models and the blood concentration at the exact sampling location, which is usually lower than the average. Systemic circulation models with more anatomical detail, such as the one presented here, can accommodate a wide range of blood sampling techniques in simulation.

An implementation of the kinetic inversion and the interspecies scaling techniques in a laboratory can be enumerated in the following way:

1. Administer the drug intravenously to animals at a nominal dose, ideally with additional low and high dose regimes. Sample data for tissue drug accumulation at different times with 3D PET scans, with a radioimmunoassay, or other techniques until the concentration is below a certain threshold.
2. Set up the whole body circulation network model. Then, implement a working hypothesis using the biochemical reaction mechanisms as described in sections 3.2 and 3.3, incorporating mass transfer, chemical kinetics, and also mediated transport equations for each organ for that particular drug.
3. Determine the kinetic rates by using inversion with the equation as described in the inversion problem, section 3.3.4.
4. Validate the experiment from step 1 against the predictions. Revise the model from step 2 if necessary, i.e. if the hypothesis is rejected.
5. Prepare whole body circulation model for next species with correct physiological data, apply scaling laws to biochemical and transport parameters. Perform simulations with the scaled-up model. Repeat the process from step 1 with next species.

These whole body PBPK models with parameters obtained by inversion for multiple species could be used, for example, in scenarios where calculations of clearance, AUC, C_{max}, T_{max} and other pharmacokinetic parameters are needed on a number of individuals with a wide range of physiological parameters. This procedure leads to early detection of possible safe/unsafe dosing regimes.

First principles modeling satisfying conservation balances promises increased accuracy and rigor in drug biodistribution prediction starting from pre-clinical trials, when only limited knowledge about drug fate and action is easily available. Mechanistic scaling of the drug administration from small to larger species, as well as incorporation of individual differences such as obesity, organ failure, or even phenotypes related to drug metabolism, is now possible. The closure leads us to the comparison of traditional interspecies scaling of organ drug levels with the proposed first principles relations that scale only the biochemical and transport phenomena. These first principles modeling techniques may ultimately shorten the modeling-to-measurement cycles from pre-clinical to phase II trials.

4. STUDYING THE VARIABLE DISTRIBUTION GEOMETRY OF CONVECTION-ENHANCED DRUG DELIVERY BOTH *IN SILICO* AND *IN VIVO*

4.1. Abstract

Objective: Convection-enhanced delivery (CED) has emerged as a promising technique for bypassing the blood-brain barrier to deliver therapeutic agents. However, animal studies and clinical trials that utilize the technique suggest that it may require further optimization before it can be safely used in humans. In particular, while volume of distribution in the target tissue can be controlled, the geometrical spread into a desired target region is highly variable from experiment to experiment. In the present chapter we have sought to characterize the non-uniform distribution geometry using fluorescent nanoparticles in both a rat model and computer simulations.

Methods: Using diffusion tensor imaging MRI data of the rat brain, we performed computer simulations of a 0.5 μL/min CED infusion. A step design catheter targeting the striatum was simulated to infuse 20 μL of infusate. Using the same infusion parameters, we then performed *in vivo* CED experiments where we infused fluorescently-labeled polyethylene glycol-polylactide-polycaprolactone nanoparticles (FPNPs) into the rat striatum. Fluorescence microscopy was used to examine the distribution geometry histologically.

Results: The computer simulations demonstrated large variations in distribution patterns when catheter placement was shifted by only 1 mm. Animal infusions also exhibited highly irregular and variable distribution geometries despite the use of relatively small flow rates.

Conclusion: Computer simulations and repeated *in vivo* infusions demonstrate the difficulty of achieving desired drug distribution in target tissue. We have proposed a calculation for sphericity which, along with the ubiquitous volume of distribution measure, may prove helpful in describing distribution geometry. Taken together, our results suggest that CED's limitations must be considered and further optimization may be required before the technique sees widespread use in humans.

4.2. **Introduction**

Convection-enhanced delivery (CED) has been hailed as a promising method to circumvent the blood-brain barrier (BBB) to treat neurological diseases and brain tumors (115–117). While advantageous in many regards, the lack of predictability of the drug spread and reproducibility of results in repeated experiments delay clinical success. To date, clinical trials treating gliomas, in particular the TransMID and PRECISE trials, have failed to demonstrate a sufficient improvement in survival (17) despite the efficacy of the therapeutic agents of interest in animal models (18,19). For example, retrospective analysis of the PRECISE trial found that the distribution of infusate was highly variable among patients, raising concerns about CED's ability to deliver adequate concentrations of drug to a majority of its target cells (22).

In an effort to better predict distribution, we have compared computer simulations with *in vivo* infusions of fluorescent polyethylene glycol-polylactide-polycaprolactone nanoparticles (FPNPs) into rat brain (118). Because emerging studies often use either nanoparticle- or virus-based vectors, we were interested in using a similar agent. Moreover, because viruses and therapeutic nanoparticles are usually relatively large in

size, between 70-200 nm in diameter, they must rely primarily on convection and minimally on diffusion to distribute throughout the target region.

We previously developed a patient-specific, computer-aided modeling technique (119–121), which we have used in this study to simulate CED of nanoparticles in rats. As previously described, this model incorporates diffusion tensor imaging (DTI) MRI to provide anatomical data that captures the anisotropy and inhomogeneity of brain tissue. We modeled a conservative rate of infusion using a well-documented backflow minimizing catheter (122). We compared these simulations with fluorescent microscopy of FPNPs infused into rat brain using the same target, infusion rate, and catheter. Our results demonstrate that the model provides insight into the volume of distribution, and that *in vivo* results reveal a high variability of CED distribution geometry. Our results suggest that because distribution geometry is often irreproducible, CED may require further optimization before it can be predictably and reliably used in human trials.

4.3. **Materials and Methods**

4.3.1. **Computer simulations**

Physiological and geometric properties of heterogeneous and anisotropic rat brain tissue (such as the directionality of axonal fiber tracts, size and shape, rate of diffusion and preferred direction of diffusion for different regions of the brain) were obtained from diffusion tensor imaging (DTI) datasets provided by Johns Hopkins University. The DTI datasets helped to construct physiologically consistent transport tensors for FPNP and bulk fluid transport within the brain tissue. Computer-assisted image reconstruction was then conducted with a proprietary MATLAB program which loads, formats and organizes the

DTI dataset (123). According to what specifications the user defines, the program will format the data for the specified orientation, tensor element, and slice. The resulting slice is then displayed, and the parameters relating to this slice are exported. For our simulations, the coronal slice corresponding to the location of the right caudate putamen at 1.0 mm anterior, 3.0 mm lateral, and 6.0 mm ventral to the bregma was used. Image data such as pixel matrices representing planar brain slices were converted into geometric surfaces and interconnected regions using Mimics software (124). The reconstructed surface domains were imported into Gambit, a meshing software used as a preprocessor for computational fluid dynamics analysis, where domain regularization methods were used to partition the domains into a finite number of quadrilaterals. Each small volume was linked to its neighbors, and therefore created an interconnected computational mesh. The mesh was imported into Fluent, a computational fluid dynamics software, in order to simulate the CED of FPNPs into the right caudate putamen of rat. A step-design catheter with a 100 μm inner diameter fused silica tube attached to a 26 gauge needle was modeled, and a 20 μL infusion of 6.392 mg/mL FPNP solution delivered at 0.5 μL/min was simulated. More detailed information regarding the computer-aided modeling process can be found in our previous publications (119–121).

4.3.2. **Nanoparticle infusions**

Procedures were performed on Lewis rats (Harlan Laboratories, Indianapolis, IN) in accordance with a University of Chicago institutional animal care and use committee-approved protocol. Fluorescein-labeled polyethylene glycol-polylactide-polycaprolactone nanoparticles, less than 200 nm in diameter, were synthesized by LNK Chemsolutions (Lincoln, NE). FPNPs were serially centrifuged and the supernatant was taken to obtain

particles of the appropriate size fraction. Dynamic laser light scattering performed with a Zetasizer Nano ZS (Malvern, Worcestershire, UK) confirmed size distribution and negative surface charge. We used a step-design catheter similar to that previously described (122). Our catheter consisted of a fused silica tube (167 μm outer diameter and 100 μm inner diameter) attached to a 26 gauge needle, which was in turn attached to polyether ether ketone (PEEK) tubing (1.5875 mm outer diameter and 0.508 mm inner diameter). The PEEK tubing was glued to a 25 gauge needle, which was attached to a 250 μL Hamilton syringe driven by a BASi syringe pump and controller. Using a stereotactic frame, the caudate putamen was targeted 1.0 mm anterior, 3.0 mm lateral, and 6.0 mm ventral to the bregma. The catheter was advanced over 60 seconds. After a 5-minute delay, 20 μL FPNPs were infused at a rate of 0.5 μL/min. Following the infusion, after another 5-minute delay, the catheter was retracted over 60 seconds. After animals were sacrificed, brains were removed, fixed with OCT (Sakura Finetek USA Inc., Torrance, California), frozen, and sectioned. Sections were examined at low-power microscopy with UV excitation and a FITC filter, and images were saved for analysis. For each animal, ImageJ (125) was used to select the area of fluorescent hyperintensity in each slice, and summed all slices' areas of distribution (A_d) multiplied by slice distance to arrive at volume of distribution (V_d).

4.3.3. **Sphericity**

We have defined the term *sphericity (S)* to provide a reproducible measure for comparing distribution geometry to an idealized spherical (as in a true 3-dimensional analysis) or rough spherical (as in a sum of 2-dimensional slices) distribution. In a single 2-dimensional slice, the length (l) and width (w) are measured. The width is defined as normal to the length and is drawn from the midpoint of the length as shown in Figure 17A.

The smaller of the length and width is divided by the larger. This measure is then multiplied by that slice's area of distribution (A_d) divided by total volume of distribution (V_d). The resulting value is then summed across all slices, and finally squared, to arrive at the S as shown in Eq. (38). For 3-dimensional analysis (e.g. for computer simulations or high resolution MRI), the depth (d) normal both to the length and width is also measured. As shown in Figure 17B, the depth is measured from the midpoint of both the length and width. The smallest of the length, width, and depth is then divided by the largest, and the resulting value is cubed to arrive at the S as shown in Eq. (39).

2-Dimensional S

$$S = \left(\sum \left[\frac{\min(l, w)}{\max(l, w)} \times \frac{A_d}{V_d} \right] \right)^2 \tag{38}$$

3-Dimensional S

$$S = \left[\frac{\min(l, w, d)}{\max(l, w, d)} \right]^3 \tag{39}$$

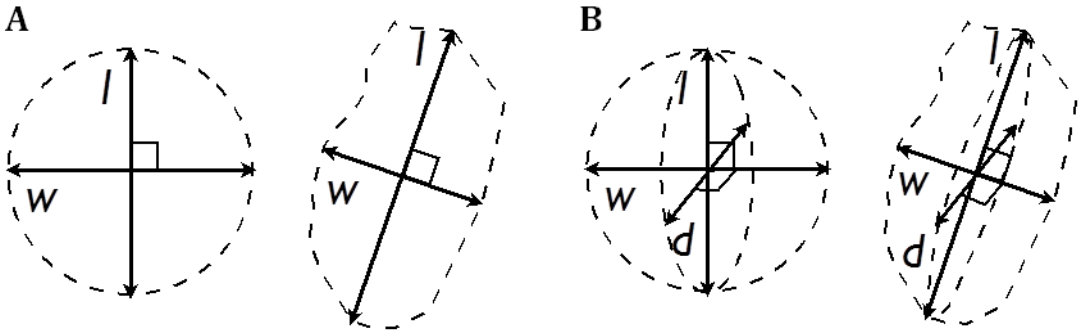

Figure 17. Sphericity (S) provides a simple, objective measure of the conformity of distribution geometry to an idealized rough spherical distribution calculated from 2-dimensional slices (**A**) and an idealized spherical distribution calculated from 3-dimensional data (**B**).

4.4. **Results**

Using rat DTI data to model the anatomy and anisotropy of brain tissue, computer simulations of the CED of 20 µL FPNPs infused at a rate of 0.5 µL/min into the right caudate

putamen were performed. As shown in Figure 18, highly differential distribution geometry was observed between different simulations. In the simulations shown in Figure 18A and Figure 18B, catheter position is the same. Figure 18A shows a relatively circular distribution (S= 0.98) without the occurrence of backflow along the catheter shaft, while Figure 18B shows backflow occurring up along the catheter shaft and then medially following the white matter fiber tracks of the corpus callosum (S = 0.12). When catheter placement was varied medially by only 1 mm, as shown in Figure 18C, larger variation in distribution geometry was observed with a S = 0.07. This small movement in catheter position represents the error in catheter placement which may occur during the surgical procedure. Notice how a 1 mm difference in catheter position resulted in the backflow following the white matter fiber tracks of the corpus callosum both medially and laterally.

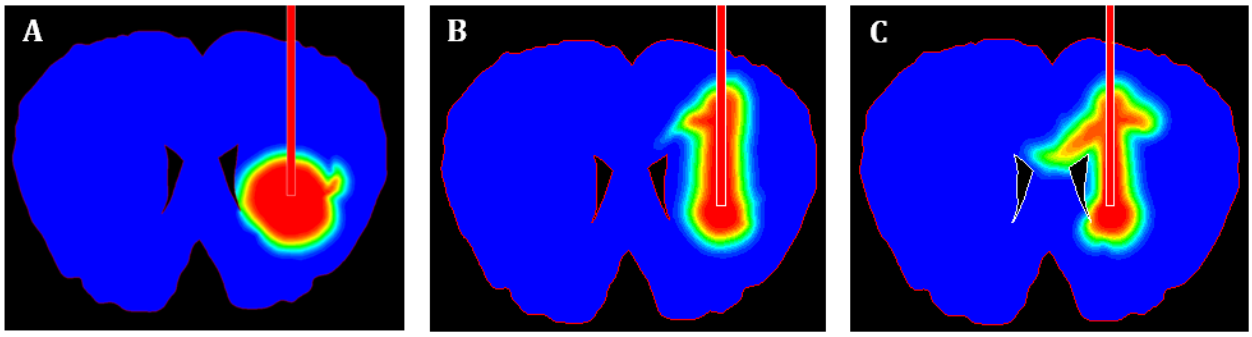

Figure 18. Computer simulations of the CED of 20 µL FPNPs infused at a rate of 0.5 µL/min into the right caudate putamen. Rat DTI data were used to model the anatomy and anisotropy of brain tissue. Despite the close proximity of the catheter in each infusion, highly differential distribution geometry was observed. (**A**) resulted in a relatively circular distribution without backflow along the catheter, while (**B**) and (**C**) resulted in two different patterns of backflow. *Sphericity* values are 0.98 (**A**), 0.12 (**B**), and 0.07 (**C**).

In vivo CED experiments of 20 µL FPNPs were performed on Lewis rats using the exact procedure (same target, infusion rate, and catheter) as used in our computer simulations and described previously in sections 4.3.1-4.3.2. Fluorescence microscopy was

then used to examine the distribution geometry histologically. Figure 19A shows a representative histological sample of a rat right caudate putamen upon completion of a CED experiment. Figure 19B shows the outlined volume of distribution, while Figure 19C shows the length and width of the fluoresced region which are necessary to calculate the sphericity.

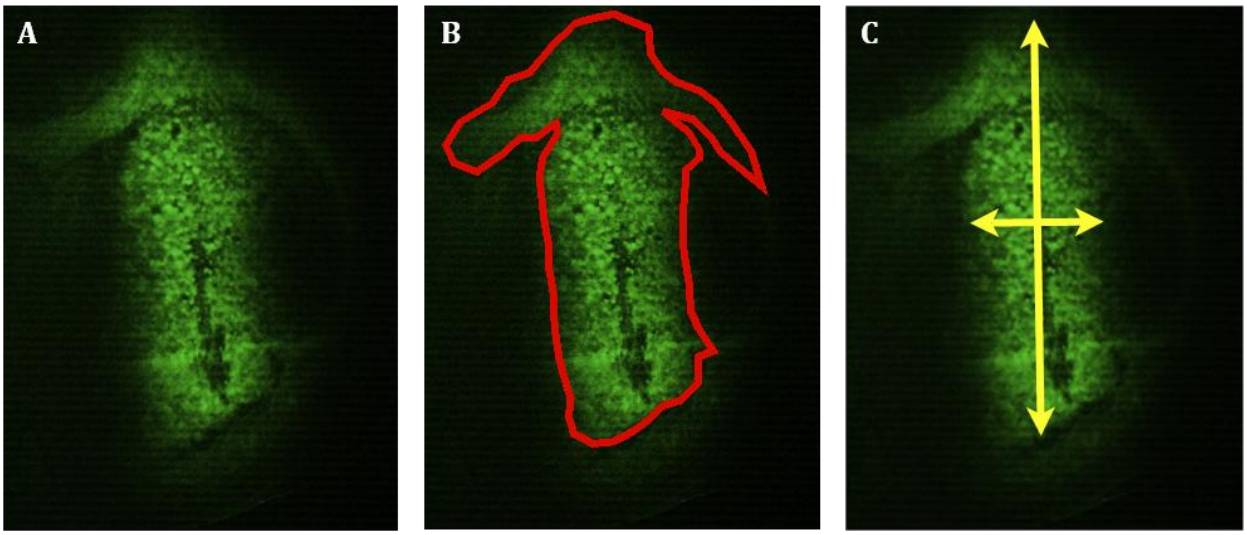

Figure 19. Representative histological sample following 0.5 µL/min CED of 20 µL FPNPs into the right caudate putamen (**A**). In this slice, volume of distribution is outlined (**B**) and length and width are measured to calculate *sphericity* (**C**).

These animal infusions demonstrated highly variable distribution geometries (shown in the Figure 20 boxed inserts) despite relatively similar volumes of distribution (represented as dark bars in Figure 20). As depicted by the white bars and the right y-axis in Figure 20, the sphericity for each of the four animals varied between 0.66 for animal #1 and 0.11 for animal #4. One can see a trend in Figure 20 of increasing relative volume of distribution with a simultaneous decreasing sphericity.

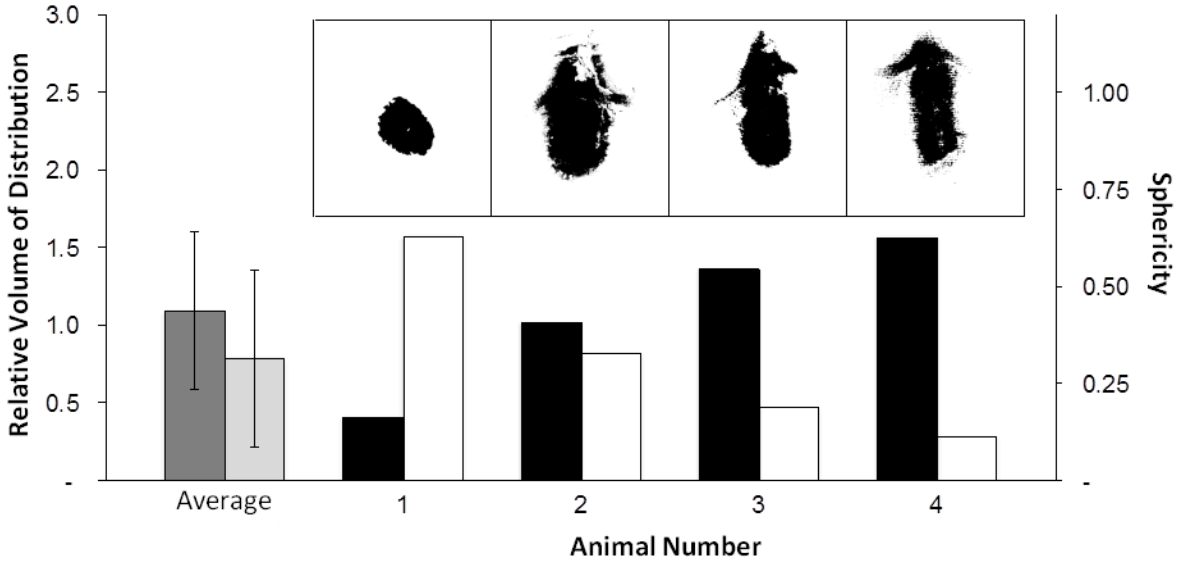

Figure 20. Representative individual distribution geometries (boxed) were compared with corresponding relative volume of distribution (dark bars) and sphericity (light bars). Infusions of 20 µL FPNPs were performed in 4 animals at a rate of 0.5 µL/min.

4.5. **Discussion**

Our computer simulations and *in vivo* nanoparticle results demonstrate the irregular, non-spherical distributions that CED yields. Such distributions are to be expected due to the inhomogeneity and anisotropy of brain tissue, specifically the propensity of white matter tracts to direct flow along their fiber paths. We used nanoparticles because they are transported mainly by convection due to their size, rather than diffusion, allowing us to examine biodistribution via convection while controlling diffusion. Importantly, we chose to use nanoparticles fabricated with specific properties to meet the rigorous demands of any infusate delivered by CED. Due to the properties of the brain extracellular space, infusate properties have an important effect on the volume and boundaries of distribution. The size of the molecule or complex, charge, surface coating, concentration, osmolarity, viscosity, and tissue affinity all affect distribution (126). Investigators have attempted various preinfusion or coinfusion strategies, delivering a therapy with

hyperosmolar agents (116,127,128), heparin (129), preinfusion of an isotonic solution (128), or preinfusion of an enzyme to degrade extracellular proteins (128). As our nanoparticles are below 150 nm in diameter and exhibit a negative surface charge, they do not require any pre- or coinfusion in order to be widely distributed within brain tissue. These nanoparticles distributed in similar geometries as our computer simulations predicted; however, neither the simulations nor the *in vivo* infusions yielded uniform spheres of infusate.

It should be noted that our computer model takes into account the sink effect of CSF-filled spaces, such as the ventricles and subarachnoid space. Animals 2, 3, and 4 in Figure 20 were found to have nanoparticles in the lateral and third ventricles. Such an effect would be magnified if the cortex or any periventricular structure were targeted, rather than the comparatively well-insulated putamen. Bankiewicz's group noted that perivascular spaces can act as a conduit for the removal of infusate (130); yet these spaces (about 20 μm in width (131)) are too small to be resolved by MRI, further confounding the ability to predict CED distribution.

By carefully analyzing the distribution geometry of each experiment, rather than only the distribution volume, we saw a high variability in distribution geometry. Each of our experiments yielded different distributions of nanoparticles despite conducting infusions with the same volume, flow rate, catheter type, and target position in the brain. Our measure of sphericity provides a useful, objective measure for quantifying the irregularity of distribution geometries. As shown in Figure 20, three of our four *in vivo* experiments produced a relative volume of distribution value greater than 1, whereas those same infusions yielded sphericity values of less than 0.5.

Infusion rate is a crucial parameter of CED, and has essentially been optimized (117,122,132). Experiments have attempted to balance time constraints (i.e. higher flow rates) with regularity in distributions, elimination of backflow, and minimum tissue damage. For instance, Krauze and colleagues' isotropic gel experiments demonstrated spherical distributions of trypan blue dye infusate at flow rates of 0.5 and 5 μL/min while using their step-design catheter; however, they found that higher flow rates yielded irregular distributions. Additionally, hematoxylin and eosin staining following *in vivo* rat infusions showed minimal tissue damage around the catheter tip at 0.5 and 5 μL/min, but considerably more damage at higher infusion rates (122). For our *in vivo* experiments, we used 0.5 μL/min with the intention of minimizing backflow and tissue damage, and because this flow rate generated the most regular distributions in isotropic agarose gel experiments. Therefore, when moving to anisotropic brain tissue, we sought to eliminate any contribution the infusion rate could have on an irregular distribution geometry. As a component of the irregularity of our distributions, a jet effect of fluid leaving the catheter tip was seen in three of our animal experiments. Using computer simulations, we have studied this hydrodynamic jet effect and found that it depends on microscopic tissue and catheter dimensions, as well as differential flow rates and variations in tissue compliance at the catheter outlet.

The appropriate catheter type for a given infusion rate is also critical to the efficacy of CED. Catheter design has implications for V_d and boundaries of distribution, which themselves depend on the prevention of infusate backflow, or reflux, over the catheter track. Backflow along the catheter tract not only allows infusate to flow to other regions of the brain along white matter tracts, but also allows loss of infusate into the subarachnoid

space. In 2005, Krauze and colleagues attempted to solve the problem of reflux by testing various single port catheter designs in 0.5% agarose gel. They showed that while small diameter fused silica tubing itself produced backflow, a step-design catheter, wherein the fused silica tube was glued to a 27 G needle, minimized backflow (122). Though the precise mechanics are not fully understood, the larger diameter steps may create a barrier to block flow of fluid, and the brain tissue may seal (132) about the fused silica tube, thereby reducing reflux. We built similar catheters for our studies and tested them in agarose gels, and we were able to duplicate their results (118). However, some of our nanoparticle infusions using the step-design catheter did yield backflow at flow rates said to be safe for this type of catheter (below 5 μL/min). Several novel catheter designs have attempted to solve the problem of backflow. Side-port (133), multi-port (120), and porous membrane (134) catheters have been fabricated for this or other applications. Kanner and colleagues have pioneered a novel approach using ultrasound to vibrate the catheter tip, driving infusate using a mechanism different from conventional CED (135). The variety of catheter strategies employed in the above experiments evidence the importance of the catheter design, but they also highlight the fact that even this most basic and critical aspect of CED has not yet been optimized, which is a topic of discussion in the next chapter.

While we delivered infusate to healthy brain tissue, CED's problems are compounded considerably when infusing the bulk of a glioma. Because glioblastoma reduces the integrity of the adjacent BBB, these areas of breakdown can act as a sink for infusate. Tumor geometries are also markedly irregular, with glioblastoma multiforme infiltrating beyond the visible tumor boundary. Moreover, tumor tissue is highly anisotropic and inhomogeneous, with neovasculature, uneven growth throughout the

tumor bulk, and regions of necrosis. As an additional complication, fluid pressure within the tumor is often higher than in surrounding tissue, and extracellular edema in and around the tumor may further alter the distribution of infusate. Clinical trials for the delivery of tumor therapies, therefore, represent perhaps the most challenging applications of CED.

A less complex application of CED may be drug delivery to small, homogeneous, isotropic gray matter targets. For instance, infusion of growth factors to the putamen is likely to be technically less complex and more likely to generate successful treatment outcomes. However, CED's technical obstacles may be to blame for the failure of a recent clinical trial of intraputamenal glial cell line-derived neurotrophic factor (GDNF) for the treatment of Parkinson's disease (136). Interestingly, intraputamenal CED of GDNF was performed in non-human primates using the same infusion parameters as the human trial (137). In addition to generating highly variable volumes of distribution spanning a 4-fold range, the variation among individual infusion geometries was also considerable.

4.6. **Conclusions**

Despite CED's utility and promise, further refinement is required before it can be reliably and reproducibly used to deliver therapies to gliomas and to other targets in the brain. Our proposed model of the sphericity provides a distinct measure from volume of distribution that can aid in the verification and comparison of distribution geometries across multiple infusions. In CED's current state, it may be possible to accurately target small, well-delimited targets of homogeneous and isotropic tissue. However, CED may require further optimization if it is to be used in clinical trials with large, heterogeneous,

anisotropic targets. Ultimately, when considering CED's use in human clinical trials, it is critical that infusion parameters are first predetermined through careful primate experiments to ensure that the appropriate concentrations of therapy reach the intended treatment target.

In order to help make CED a more viable treatment option for patients suffering from neurodegenerative disorders and brain cancer, the engineering challenges of CED need to be addressed. Backflow is a considerable challenge; therefore, we set out to determine the causes of backflow in order to engineer backflow-free catheters capable of much greater performance than those previously developed. These topics are covered in the next chapter. Once the challenge of backflow has been overcome, physicians can then focus on drug efficacy and engineers can focus on improving methods for predicting drug distribution during CED, both of which are critical for patient care.

5. TRANSPORT PHENOMENA OF CONVECTION-ENHANCED DELIVERY AND DESIGN OF BACKFLOW-FREE CATHETERS

5.1. Abstract

Convection-enhanced delivery (CED) is a localized drug delivery technique used to target specific regions of the brain for the treatment of cancer and neurodegenerative diseases that bypasses the blood-brain barrier. An intracerebral catheter is placed with a continuous infusion of therapeutic molecules that are propelled to the site of drug delivery within the parenchyma through a pump. There are inherent engineering challenges involved with CED. The primary challenge is backflow, which is characterized by fluid discharge along the catheter shaft instead of distally into the soft tissue. In order to prevent the possibility of backflow, low volumetric flow rates are applied which limit the achievable drug distribution volumes from CED. This can render CED treatment ineffective since a small convective flow rate produces a narrow drug distribution inside the treatment region. More efficient catheter designs and CED protocols are needed to expand the drug distribution inside the treatment region. This is especially important when administering toxic chemotherapeutics which could adversely affect other brain regions when backflow occurs, as well as not reach a therapeutically efficacious concentration within the target region due to backflow. In order to help elucidate the causes of backflow and to improve catheter design to avoid backflow, we have studied the impact that microfluid flow has on deformable brain phantom gels experimentally as well as computationally. We found that fluid injections into porous media have considerable effects on local transport properties such as porosity and hydraulic conductivity. These phenomena not only alter the bulk flow

velocity distribution of the microfluid flow due to the changing porosity, but significantly modify flow direction and even volumetric flow distribution due to induced local hydraulic conductivity anisotropy. These studies led us to the development of novel backflow-free catheters with safe volumetric flow rates up to 10 µl/min. The catheter designs, numerical simulations, and experimental results are presented in this chapter.

5.2. **Introduction**

Neurodegenerative diseases of the central nervous system (CNS) are often treated by systemic delivery of large molecular weight drugs either orally or intravenously. However, the blood brain barrier (BBB) prevents most of these molecules from entering the interstitium, rendering systemic delivery methods highly ineffective (115). One solution to bypass the BBB is through a direct intracranial injection, a technique known as convection-enhanced delivery (CED). This invasive technique utilizes a positive pressure gradient created by an infusion pump to infuse drugs through a catheter and into the brain tissue. CED directly distributes therapeutic agents to a specific target area at dramatically increased doses and has been shown to achieve much larger drug distribution volumes compared to diffusion driven methods (115,138). These major advantages of CED offer great potential for more efficient treatment of neurodegenerative diseases such as Alzheimer's and Parkinson's, as well as for the treatment of brain tumors.

Alzheimer's Disease (AD) and Parkinson's Disease (PD) collectively effect 6 million people within the United States, and around 42 million people worldwide (8–10). These numbers are expected to grow substantially as the average age of the population increases. For AD alone, it is estimated that by 2050 between 11-16 million Americans will have AD

and 115.4 million people worldwide (8). The estimated cost of providing care for AD patients in the U.S. is $200 billion per year, while for PD patients it's $14.4 billion(11). The cost of providing care for AD patients alone is projected to grow to over $1.1 trillion per year by 2050 – an overwhelming economic burden (8). It is also estimated that more than 688,000 people are currently living with a diagnosis of a primary brain or CNS tumor in the United States, and 68,470 new cases are expected to be diagnosed in 2015 (12,13). Due to the BBB limiting the delivery of systemically administered drugs to the brain and CNS, an appealing mode of delivery of therapeutics to these populations is through CED.

Clinical trials treating gliomas that utilized CED, such as the TransMID and PRECISE trials, have failed to demonstrate statistically significant improvement in survival (17) despite the proven efficacy of therapeutic agents in animal models (18,19). Retrospective analysis of the PRECISE trial found that infusate distribution was highly variable among patients; therefore, any potential efficacy of drugs delivered by CED may be hindered by ineffective delivery (20–22). Alternative catheter designs may improve delivery, thereby increasing the efficacy of drugs delivered by CED (22). This is an engineering problem where the therapeutic does not get to the site of disease.

One undesirable effect often associated with CED is known as backflow or reflux, which is characterized by fluid discharge along the catheter shaft instead of distally into the soft tissue. Backflow is especially dangerous when toxic drugs used for treating CNS diseases and cancer escape from the target region and negatively affect other regions of the brain and spinal cord through flow through the CSF space. Backflow can also render treatments unsuccessful due to therapeutics not reaching an efficacious concentration within the target region, which may be one explanation as to why the PRECISE trial failed.

Unpredictable distribution of a therapeutic agent due to backflow and anisotropic tissue properties is a serious obstacle to the safe clinical application of CED. Figure 21, adapted from our previous work (20), shows CED's non-uniform distribution geometry in both computer simulations (A and C) and a rat model (B and D) while using a very low volumetric flow rate of 0.5 μL/min and infusing with a common 32G single-port catheter. Low volumetric flow rates limit the achievable drug distribution volumes from CED. Although Figure 21 A and B show relatively spherical distributions, Figure 21 C and D clearly show backflow even while operating at a low volumetric flow rate and delivery through a very small 32G single-port catheter. In order to have CED become a clinically viable treatment option, CED protocols and catheter design need to be optimized in order for backflow occurrence to be minimized and drug distribution geometries more predictable.

A main goal in the optimization of CED methods is to determine the causes of backflow phenomena. Once the causes of backflow are known, optimal catheter designs for CED can be developed. Therefore, the transport processes which occur during drug delivery into porous media such as a human brain should be elucidated using experiments as done in our previous work (139). Several theories describing the effects of fluid flow in porous media have been developed (140–144). However, most of these theories are based on the idealized soil model of porous media and are not able to entirely describe the living, soft porous brain tissue.

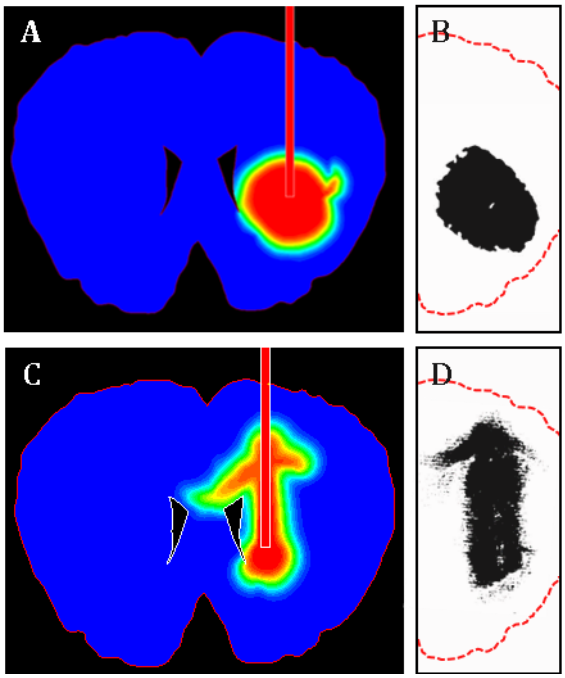

Figure 21. Unpredictable and non-uniform distribution geometries from *in silico* (A and C) and *in vivo* (B and D) CED experiments even though very low volumetric flow rate of 0.5 µL/min were used. (Adapted from our previous work.(20))

5.2.1. **Background**

Live brain tissue is known to be comprised more than 80% water; therefore, it can be considered as a porous deformable matrix consisting of incompressible elements (cells). Interstitial fluid fills the space (porosity) between these cells. Due to the cell incompressibility, deformation of the solid matrix is linked to the porosity or fluid fraction change. The deformation is associated with a volumetric strain, $e(\vec{x},t)$, that is directly related to the porosity, $\zeta(\vec{x},t)$, as shown in Eq. (40), where ζ_0 is an initial porosity.

$$\zeta(\vec{x},t) = \frac{e(\vec{x},t) + \zeta_0}{1 + e(\vec{x},t)} \qquad e = \sum_{i=1}^{3} \varepsilon_i = \sum_{i=1}^{3} \frac{du_i}{dx_i} \tag{40}$$

Since the deformation influences the local tissue porosity, $\zeta(\vec{x},t)$, it also impacts the fluid continuity equation shown below in Eq. (41).

$$-\nabla \cdot \left[\zeta(\vec{x},t)\vec{v}_f\right] + q = \frac{d\zeta(\vec{x},t)}{dt} \tag{41}$$

Here q accounts for the fluid injection and $\vec{v}_f$ is the superficial flow velocity vector which induces a stress in the porous matrix. Deformation also induces a change in hydraulic conductivity, K, as shown in Eq. (42) where M is a coefficient of approximately one.

$$K(\vec{x},t) = K_0 exp[Me(\vec{x},t)] \tag{42}$$

Darcy's law, shown below in Eq. (43), is used to describe a relationship between the velocity, $\vec{v}_f$, and pressure gradient, ∇p, inside the porous media.

$$\vec{v}_f = K(\vec{x},t)\nabla p \tag{43}$$

Fluid flow affects the porous media's characteristics by inducing a deformation. The reasons for this deformation are fluid pressure gradient, shear stress induced by fluid friction (related to fluid velocity), and fluid pressure. For example, Terzaghi's consolidation theory states that the local stress is related to a fluid pressure, and this pressure can be utilized to calculate the porous media strain (117,143,144). However, the brain's solid matrix consists of incompressible elements (cells). Therefore, we have to look for the porous matrix deformation rather than compression of matrix elements. In this case, the dominating effects are the fluid pressure gradient and the shear stress induced by fluid friction. According to Darcy's law, fluid flow induces friction forces and pressure gradients in the flow direction. This results in volumetric forces inside the deformable porous media/matrix. For this model, the strain as well as an effective stress does not depend on the absolute fluid pressure, but instead depends on the fluid flow velocity which is proportional to the pressure gradient. This statement is consistent with our experimental observations which revealed that the local fluid-induced stresses in the porous matrix are

related to fluid pressure gradients (139). This experimental data was used to validate a computational model. The deformation of the porous matrix was found to be linked to the porosity and consequently hydraulic conductivity change induced by the microfluid injection (139). Another important aspect that affects tissue deformation and catheter performance is catheter geometry.

It has been shown that a reduction in the diameter of a single-port catheter from 27 to 32 gauge decreases the chance of backflow occurrence (145–147). This has led some researchers to incorporate smaller diameter catheters through the development of microfluidic-devices in hopes of improving the performance of a single-port catheter (133). Researchers have also tried to prevent backflow by incorporating an additional axial structure which extended distally out of the catheter shaft (122). However, this "step-design" catheter still uses the idea of a smaller diameter distal end for the infusion catheter in order to decrease the chance of backflow. Nonetheless, even 32-gauge catheters must be used at low flow rates of 0.5 μl/min in order to reduce backflow occurrence.

These lower flow rates result in smaller volumetric distribution due to a small convective flux. Therefore, in order to reduce the porous media deformation so that backflow does not occur, the fluid velocity has to be decreased. Low flow velocities induce very weak convection, which results in a smaller volumetric drug distribution. This is a challenge, because we want to increase the volumetric flow rate (i.e. increase the fluid velocity) in order to create a larger volumetric distribution of therapeutic agent. A device or method which could operate at an increased volumetric flow rate, while simultaneously decreasing the stresses in the porous matrix, would be beneficial for the prevention of

backflow. The following section presents the methods of both the *in vitro* experiments and the simulations.

5.3. Materials and Methods

5.3.1. *In vitro* experiments

Due to similarities in mechanical and transport properties, agarose gel has frequently been used as a brain phantom model to determine the behavior of soft porous tissue under a high flow micro-infusion and was therefore used in our experiments as well (148,149). Agarose gel solution was prepared by adding 0.6 wt% agarose (Sigma Aldrich A6013) and 0.9 wt% NaCl (Sigma Aldrich S7653) into boiling deionized water. The solution was constantly agitated by a magnetic stirrer until it became clear (150). The gel solution was then cooled to 50˚C in a constant temperature water bath before pouring it into a glass infusion chamber with the catheter already in place where the gel then set. A stereotactic frame was used to stabilize the catheter, and polyethylene tubing was used to connect the catheter to the syringe pump which provided the assigned volumetric flow rate. Trypan blue dye was mixed with water in order to visualize the volumetric distributions of infusion experiments. Since the gel is transparent, volumetric dye distributions could be observed optically as a blue stain. Photographs of the distributions were taken at specific time intervals by a camera connected to a computer. Figure 22 below shows a schematic of the experimental setup described.

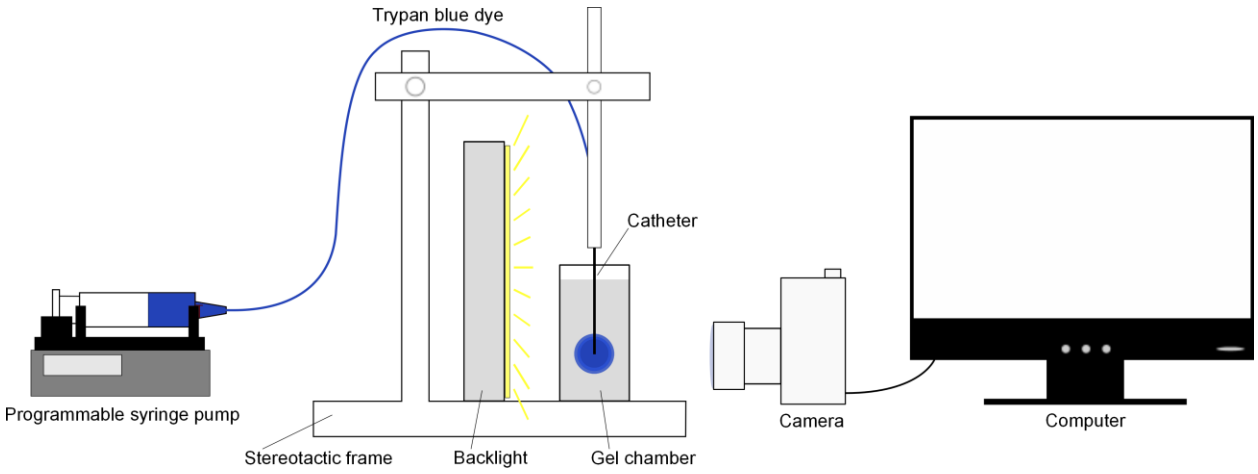

Figure 22. Schematic of experimental setup for catheter testing by CED infusion experiments.

5.3.2. **Computer simulations**

Simulations were executed with the use of the commercial software ANSYS (151). A steady, axisymmetric, viscous model was used with a half cross-section computational domain. The dimensions of the domain were 1.0 cm by 0.6 cm in order to get a close up view of the transport phenomena around catheter tips. A symmetric boundary condition was applied along the x-axis, while a no slip boundary condition was applied to the walls of the catheter and the walls of the domain (minus the axis of symmetry). Porosity was set according to that of grey matter brain tissue at 0.26. Catheter dimensions were exactly the same as those used in our *in vitro* experiments. Bulk fluid flow of 5 µl/min was set as our inlet condition into the catheter lumen.

5.4. **Results**

5.4.1. **Channel-inducing catheter**

One way to prevent backflow is to consider alternative catheter designs. These catheters will need to decrease the stresses felt by the porous media. Researchers at Twin Star Medical Inc. in Minneapolis, MN have developed an infusion catheter based on the idea

of having a very large outlet area/volumetric flow rate ratio. Twin Star's catheter design makes use of a hollow fiber with numerous fenestrations each with a diameter around 0.45 μm in order to increase the surface area of tissue into which the drug is infused (145,147). These hollow fiber catheters show an increase in the infusate mass transfer, as well as production of a uniform spread with wider drug distribution, while simultaneously reducing backflow (152).

We also developed a backflow-free catheter that exploits the idea of a large outlet area/volumetric flow rate ratio. The term outlet area refers to the area of the interface between porous media and the catheter's outlet through which fluid exits into the porous media. As this ratio increases, the stress felt by the porous media into which drug is infused decreases. With the goal of a large outlet area/volumetric flow rate ratio, our catheter utilizes an internal wire to create a cylindrical, void channel inside the porous media. This channel has large porous tissue surface area into which the infusate can be injected. This should result in a significant pressure gradient reduction around the catheter tip, thereby decreasing the chance of backflow immensely. Broad and uniform drug distributions are expected as a result of minimal interstitial flow velocity variance for equivalent volumetric flow rates. Figure 23 shows a schematic of the novel channel-inducing, backflow-free catheter.

The shaft of the catheter is 65 mm in length and is made from 23-gauge type 304 stainless steel Hypo Tube (Component Supply Co., HTX-23R). Polyethylene tubing (Scientific Commodities Inc., BB31695-PE/3) was used to connect the catheter to the infusion pump for CED experiments. A 0.23 mm diameter hypodermic stainless-steel wire was inserted into the lumen of the catheter approximately 2.0 mm above the

catheter/PE-tubing connection. In order to prevent leakage of infusate, the tiny wire and PE-tubing connection were sealed with 100% silicone rubber sealant (Dow Corning, 734 Flowable Sealant). At roughly 50 mm above the wire/PE-tubing connection, the wire was bent to 90° in order to serve as an actuator in which to insert/retract the wire into the porous media. Although this specific design is constructed with metal components, it is important to note that this catheter can also be made from only plastic parts if MRI compatibility is desired. In order to test this novel catheter design, numerical simulations and infusion experiments were performed.

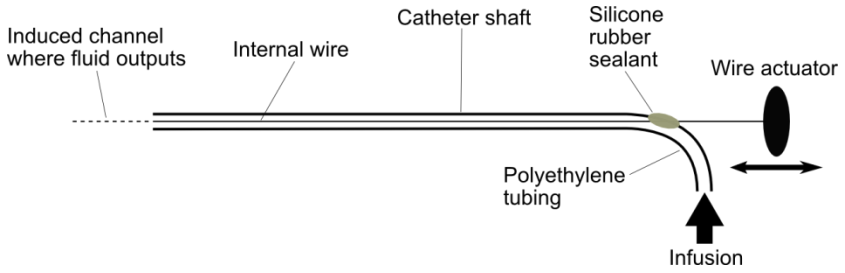

Figure 23. Schematic of novel, backflow-free channel-inducing catheter.

5.4.2. **Simulations of channel-inducing catheter experiments**

In ANSYS (151) a steady, axisymmetric, viscous model was used with a half cross-section computational domain. Figure 24a and Figure 24b show the geometry of the computational domain, where the bottom line represents the axis of symmetry; therefore, only half of each catheter is shown. Figure 24 also shows contour plots of the pressure and velocities for bulk fluid flow of 5 µl/min in order to compare a common single-port catheter to our novel channel-inducing catheter. The three figures on the left (Figure 24a, c, e) are for the channel-inducing catheter, while the three figures on the right (Figure 24b, d, f) show the simulation results for a common single-port catheter. As mentioned above the pressure gradient is proportional to velocity according to Darcy's law. A comparison

of Figure 24a and Figure 24b shows that the maximum fluid pressure in the porous media for our novel catheter is only 65 Pa, while for the ordinary single-port catheter the maximum fluid pressure is 1040 Pa. This is a maximum fluid pressure for the single-port catheter which is sixteen times larger than that of the channel-inducing catheter. The axial, x, velocity contour of the channel-inducing catheter shown in Figure 24c is almost similar to the axial, x, velocity contour of the single-port catheter shown in Figure 24d, except that in the vicinity of the channel-inducing catheter the axial velocity is 17 times less than that of the single-port catheter (0.03 cm/s). When comparing the radial, y, velocity contours shown in Figure 24e and Figure 24f, it can be seen that maximum radial velocity in the channel-inducing catheter is ten times smaller than that of the single-port catheter. Therefore, during infusions at the same volumetric flow rate, the novel catheter will create approximately ten times lower stress on the tissue than an ordinary single-port catheter. Broad and uniform drug distributions are expected when using the channel-inducing catheter as a result of minimal interstitial flow velocity variance for equivalent volumetric flow rates. Both of our hypotheses regarding pressure gradient reduction around the catheter tip and minimal interstitial flow velocity variance for equivalent volumetric flow rates agreed well with our numerical simulations. These promising results encouraged us to develop and test a prototype of our channel-inducing catheter.

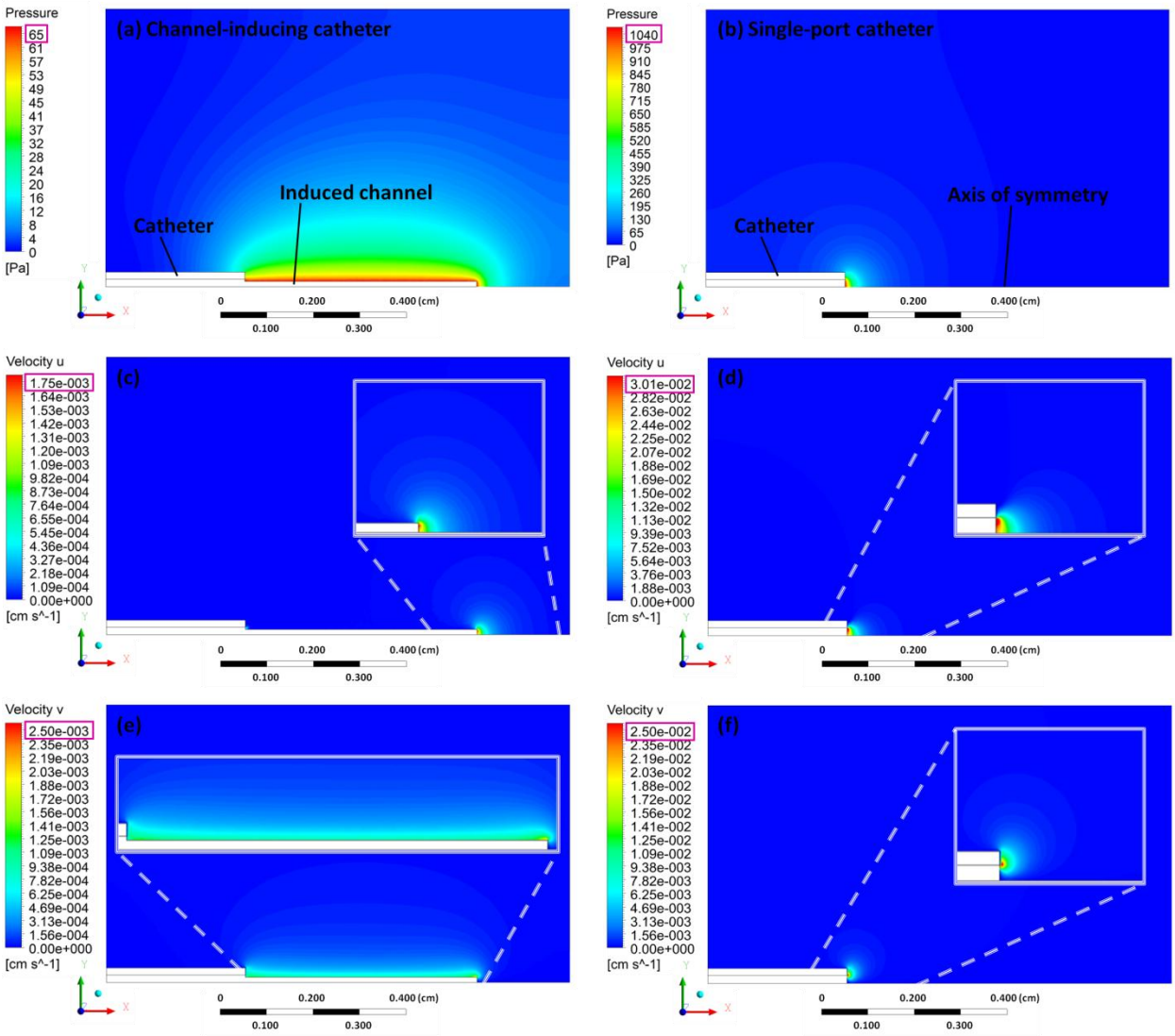

Figure 24. Simulations comparing the channel-inducing and common single-port catheters.

5.4.3. **Testing and analysis of channel-inducing catheter**

Our experimental research and simulations enabled us to design and test our novel channel-inducing, backflow-free catheter. Figure 25 shows a comparison between the channel-inducing catheter and the single-port catheter during infusion experiments. It should be noted that the diameter of the single-port catheter in Figure 25 is 27-gauge which is smaller than the 23-gauge diameter of the novel catheter. This discrepancy was purposely implemented since other experiments performed with a 23-gauge single-port

catheter produced backflow frequently even at volumetric flow rates of 0.5 µl/min. As one can see from Figure 25, the smaller 27-gauge single-port catheter produced backflow in both cases of 1.0 µl/min and 3.0 µl/min (Figure 25e and Figure 25k respectively). All other experimental results at flow rates greater than 3.0 µl/min are not shown for the single-port catheter since it produced substantial backflow. Figure 25a and Figure 25g show the novel catheter when the wire has been lowered into the porous gel matrix. Several minutes after the start of infusion, the wire was retracted, which produced the necessary channel inside the porous media for efficient distribution without the occurrence of backflow. We found that the induced porous channel wall creates a significantly lower pressure gradient and smaller stress in the porous media when compared to a single-port catheter. Experiments with flow rates of up to 10 µl/min were conducted with similar results; the novel catheter sustained delivery without backflow, while producing a uniform and considerably larger distribution volume than the single-port catheter.

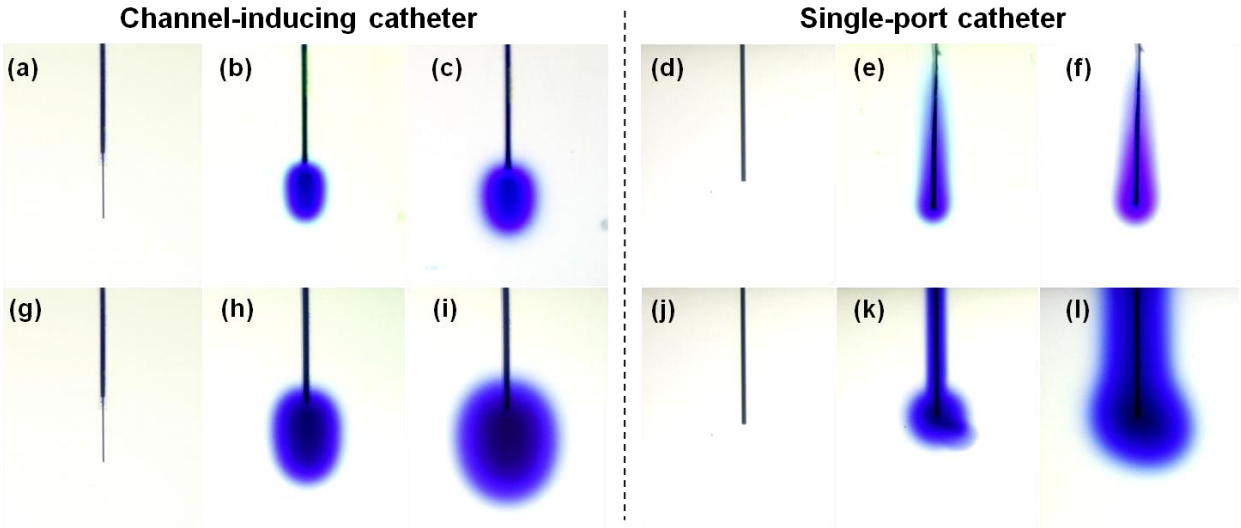

Figure 25. Photographs of channel-inducing (a, b, c, g, h, and i) vs. single-port (d, e, f, j, k, and l); catheter experiments at flow rate 1.0 µl/min (a-f) and 3.0 µl/min (g-l).

Figure 26 (a-d) shows the novel channel-inducing catheter operating at a flow rate of 5.0 µl/min without backflow for 150 min, and still no backflow after the flow rate was increased up to 10.0 µl/min for 50 min Figure 26e.

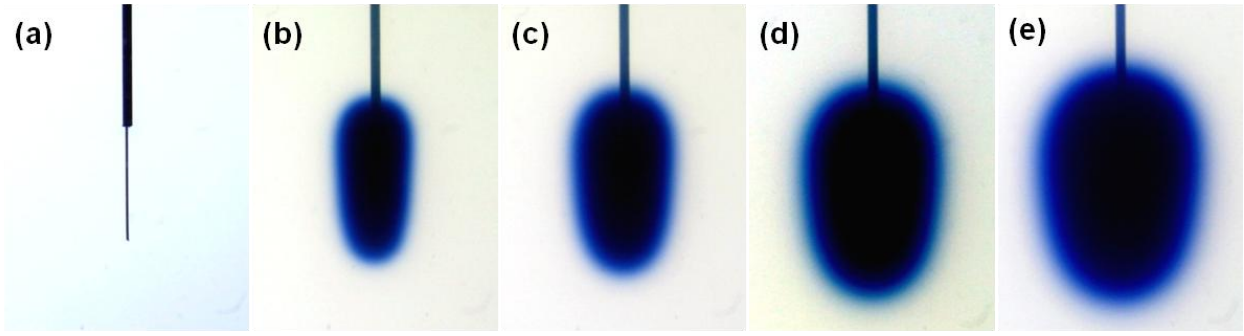

Figure 26. Photographs of channel-inducing catheter at 5.0 µL/min at **(a)** 0 min, **(b)** 50 min, **(c)** 100 min, **(d)** 150 min, and then flow rate increased to 10 µL/min for an additional 50 minutes **(e)** 200 min.

Experiments performed with the hollow, fibrous catheter from Twin Star, Inc. at flow rates up to several µl/min have shown comparable results (147) to those of our novel channel-inducing catheter; however, the channel-inducing catheter offers the following advantages:

- Cheaper, both in material costs and construction.
- Able to provide higher volumetric flow without backflow.
- Ability to drive fluid infusion by smaller pressure compared to porous membrane catheter, because no need to overcome the fibrous membrane resistance.
- Produces a more homogeneous distribution.
- Capable of inducing different channel lengths.
- Option for making MRI compatible channel-inducing catheters by incorporating only plastic or non-metal materials.

5.4.4. **Dual-action backflow-free catheter systems**

Our second design proposes a different solution for a backflow-free catheter system to use during intracranial infusions. This design resulted from our study of fundamental transport mechanisms governing invasive CED of macromolecules in a systematic series of experiments and computer simulations (139). When fluid is injected into a porous media during CED, gel/tissue porosity in the vicinity of the catheter increases. This may create a pathway for fluid flow and initiate backflow. This mechanism is especially relevant near the catheter tip (i.e. in the infusion domain). However, we discovered that applying suction along the catheter shaft reduces the permeability and matrix porosity by decreasing the fluid content. Thus, local low flow rate suction in the vicinity of the catheter shaft may be used to *prevent or arrest backflow along the catheter shaft*. The reduced porosity and permeability along the shaft in the vicinity of the suction port prevents backflow by locally closing new flow paths along the catheter shaft without interfering with the infusion. Even if backflow does propagate along the shaft in spite of a reduced permeability, the suction will intercept and redirect the backflow into the suction tube. Taking into account these transport properties, we designed, fabricated and tested novel backflow-free catheters that were based on dual action of *infusion* and *suction*.

5.4.5. **Dual-action catheter prototype designs**

Schematic drawings of the two dual-action catheter designs (coaxial and series) are presented in Figure 27. Both designs have infusion and suction sections. The distinction between these two dual-action catheter designs is geometrical, which can be either coaxial or in series. The shaft of each catheter measures 65 mm in length and is made from 30-gauge stainless steel Hypo-Tube (Component Supply Co., HTX-30R). Polyethylene

tubing (Scientific Commodities Inc., BB31695-PE/2) was used to connect each catheter to the infusion pump for CED experiments. The suction line for both dual-action catheter designs was made of a larger diameter polyethylene tubing (Scientific Commodities Inc., BB31695-PE/6), and started 5 mm above the infusion port. It was very important that the suction zone be located at this particular distance from the catheter tip in order to prevent interference with the infusion. It was also crucial that low suction (10-30% of main infusion flow rate) be employed to effectively arrest backflow by decreasing the porosity and permeability along the catheter shaft.

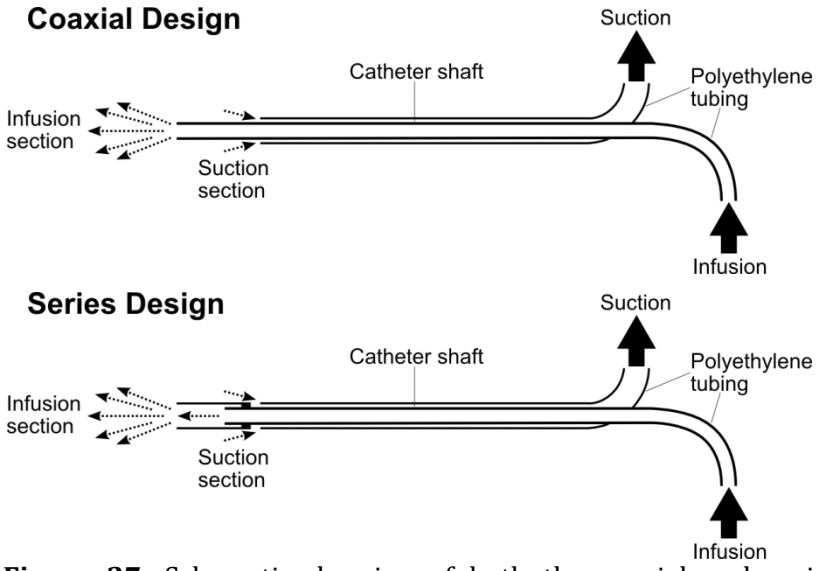

Figure 27. Schematic drawing of both the coaxial and series dual-action novel backflow-free catheters.

5.4.6. **Testing and analysis of dual-action catheters**

These catheter designs were tested in agarose gel models using volumetric flow rates from 0.5 up to 5 µl/min. The experimental setup for these experiments was the same as the one described in section 5.3.1. The coaxial dual-action catheter was tested together with a standard single-port catheter to compare their performances at different volumetric flow rates. Figure 28 shows results from an infusion experiment in which the coaxial

dual-action catheter was used at a 3 µl/min flow rate over 90 min. The start of infusion at 10 min from the internal 30-gauge metallic catheter is shown in Figure 28a. As the infusion progressed, a spherical/tear-drop volumetric distribution started to develop (Figure 28b-Figure 28c). At around 70 min, since the volumetric flow is greater than 0.5 µl/min, backflow started along the metallic shaft as shown in Figure 28c. However, due to the suction zone decreasing the porosity and permeability of the gel proximal to the infusion, backflow was successfully arrested as shown in Figure 28d and e.

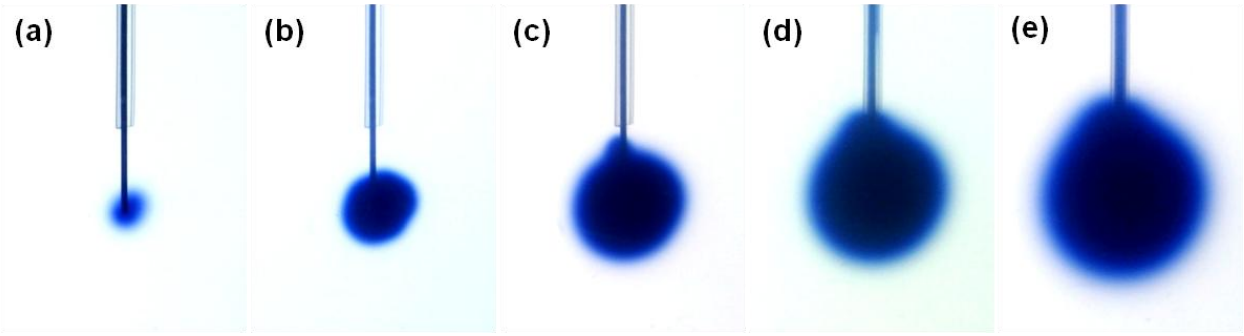

Figure 28. Photographs of coaxial dual-action catheter at 3.0 µL/min at **(a)** 10 min, **(b)** 30 min, **(c)** 50 min, **(d)** 70 min, and **(e)** 90 min.

The same results were obtained with flow rates up to 5 µl/min for coaxial as well as for serial dual-action catheters. The novel series dual-action catheter can be seen while in operation at a 3 µl/min flow rate over 150 min below in Figure 29. Once again backflow was successfully halted by the reduced permeability and porosity generated by the suction section, as shown in Figure 29d and Figure 29e.

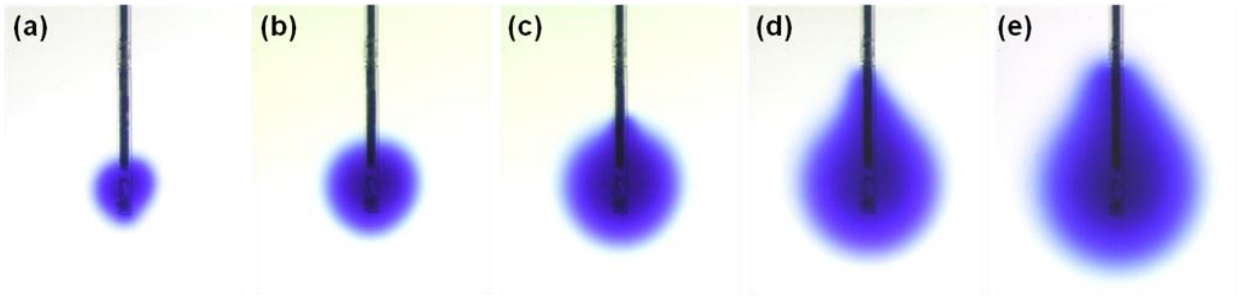

Figure 29. Photographs of series dual-action catheter at 3.0 µL/min at **(a)** 30 min, **(b)** 60 min, **(c)** 90 min, **(d)** 120 min, and **(e)** 150 min.

5.5. Discussion

Our engineering approach to designing and testing backflow-free catheters resulted in three prototype designs: a channel-inducing catheter and two types of dual-action catheters (coaxial and series). All three novel catheter designs are capable of supporting high volumetric flow rate infusions without permitting backflow. This is a vast improvement upon the single-port catheter which requires low volumetric flow rate infusions (<0.5 µl/min) and a reduction in catheter diameter (32 gauge) in order to just minimize the chance of backflow occurrence. Table 10 summarizes a comparison of our three novel backflow-free catheters along with the standard single-port catheter.

Table 10. Comparison of backflow-free and single-port catheters.

Catheter Type		Backflow Occurrence at 1.0 µl/min	Volumetric Flow Rate Limit	Recommended Use
Single-port (27G)		75%	<0.5 µl/min	low flow rates; long infusion time; drug pump
Channel-inducing		0%	<10.0 µl/min	high flow rates; short infusion time; bolus
Dual-action	coaxial	0%	<5.0 µl/min	high flow rates; short infusion time; bolus
	series	0%	<5.0 µl/min	high flow rates; short infusion time; bolus

As displayed in Table 10, the occurrence of backflow while operating at a 1.0 µl/min volumetric flow rate is 75% when using the common 27G single-port catheter. When

properly implemented, our three backflow-free catheter designs completely suppress backflow occurrence at this volumetric flow rate. Actually, both dual-action catheters (coaxial and series) were capable of eliminating backflow at flow rates up to 5 μl/min, and the channel-inducing catheter was backflow-free up to 10 μl/min.

We recommend the use of our backflow-free catheter designs when shorter CED application times (<6 hrs) are necessary and when high infusion flow rates (>0.5 μl/min) are required. However, our backflow-free catheters are not limited to only short infusion times and high flow rates. The channel-inducing and dual-action catheters may be used alongside a drug pump while operating at very slow infusion flow rates (<0.1 μl/min) for an extended period of time as well. A common 32G single-port catheter may also suffice in situations when a drug pump at very slow infusion flow rates is warranted. However, when it is necessary to target a larger region of the brain, for example when treating gliomas, it is recommended to use our backflow-free catheters in order to get large drug distribution geometries as a result of increased convective flux.

By developing backflow-free catheters, we have eliminated one more obstacle on the path towards making CED a reliable treatment option for patients suffering from neurodegenerative diseases such as Alzheimer's, Parkinson's, and brain tumors. The engineering problem of eliminating backflow has been addressed with improved catheter designs. Without backflow, neurosurgeons and neuroncologists will be able to focus on the drug mechanisms rather than the efficacy of delivery. As a result of introducing our backflow-free catheters, there will be increased drug concentration at the target area due to greatly reduced extraparenchymal leakage into cerebrospinal fluid-filled spaces. Also, drug distribution geometries inside porous brain tissue following CED will be more

predictable, and methods such as those described in our previous papers (119–121,149) will serve to aid in these predictions. Through implementation of our three backflow-free catheter designs, physicians will be able to target specific regions of the brain with improved accuracy, increased drug concentration, and larger drug distribution geometries.

Our backflow-free catheters were tested in homogenous brain phantom gels; therefore, it is necessary to validate these in animal models and eventually humans. Since living brain tissue provides unique challenges due to the anatomy of brain parenchyma and the ventricular system, we recommend co-infusion of tracers, such as gadolinium-DTPA, and therapeutics be employed in order to better predict infusate transport (153). Such methods have been shown to be a safe way to estimate drug distribution *in vivo* during CED (153). Through better planning and more predictable patterns of delivery, the engineering obstacles will be decreased and there can be more emphasis on the therapeutic formulation.

5.6. **Conclusions**

Clinical efficacy in patients with neurological conditions is challenging due to the blood-brain barrier. Circumventing this barrier through CED holds a great deal of promise but considerable engineering challenges. As more therapeutics are being developed for patients, these engineering challenges need to be identified and addressed because they hold a large role in clinical efficacy for patients. Backflow is a considerable challenge, and the engineering of a backflow-free catheter will provide a means of allowing the therapeutics to reach an increased concentration at the site of delivery and a more predictable distribution that is critical for patient care.

This chapter provided a new approach to designing backflow-free catheters that provide large volumetric distributions at a targeted domain. This approach was based on our consideration of the physical mechanisms involved in the interaction between fluid flow and porous media. Novel channel-inducing and dual-action catheters were successfully tested without the occurrence of backflow and are recommended for future animal experiments in order to validate their effectiveness for the treatment of neurodegenerative diseases and brain cancer.

6. INTRATHECAL MAGNETIC DRUG TARGETING

6.1. Abstract

Intrathecal drug delivery is a standard technique involving direct injection of drugs into the cerebrospinal fluid. Current indications include chronic pain, cancers, anesthesia, and spasticity. We have developed a physiologically and anatomically consistent *in vitro* human spine model to test the feasibility of intrathecal magnetic drug targeting (IT-MDT). Gold-coated magnetite nanoparticles are infused into the model and targeted to specific regions using external magnetic fields. Experiments and simulations aiming to determine the effect of key parameters such as magnet strength, duration of magnetic field exposure, magnet location, and ferrous implants on the collection efficiency of superparamagnetic nanoparticles in targeted regions were performed. The experimental results aid in understanding nanoparticle distribution and retention in different intrathecal regions guided by magnetic fields. Our experiments indicate that IT-MDT is a promising technique for concentrating and localizing drugs at targeted sites within the spinal canal for treating diseases affecting the central nervous system.

6.2. Introduction

Intrathecal (IT) drug delivery has been a standard treatment for different central nervous system (CNS) disorders such as leptomeningeal metastases (154–156) and spasticity (157), and has been widely used for pain management (158) and in spinal anesthesia (159,160). Recent attempts even aim at using intrathecally delivered siRNA to treat diseases of the CNS (161,162). Once injected, the drugs are rapidly dispersed within

the spinal canal by both molecular diffusion and by the pulsatile motion of cerebrospinal fluid (CSF) (162).

To maximize the therapeutic effect without excessive risk of toxicity in non-targeted zones, the intrathecally injected drugs should be concentrated at specific locations within the spinal canal. For example, in pain management therapies morphine needs to reach specific receptor sites located on the dorsal horns of the spinal cord to elicit an analgesic effect (163–165). In the case of IT morphine administration, the drug molecules need to transport across the pia mater and then diffuse through spinal cord tissue in order to reach the dorsal horns. Intrathecally administered therapeutics for chemotherapy also have small local targets in which similar transport processes are necessary to cross the ependymal surfaces in the spinal canal and then diffuse to the desired site of action. Such issues are currently overcome by using high drug doses so that the required concentration reaches the target region to aid diffusion into the spinal cord and produce a therapeutic effect. Due to CSF pulsations, as well as the presence of nerve roots and trabeculae which enhance mixing, these high drug concentrations are rapidly spread throughout the entire CNS. At this point there is no delivery technique to confine drugs locally, where it is needed in high concentrations, without having large amounts of drug spread throughout the entire brain and spinal canal, which may cause side effects.

We have recently shown that pulsatile CSF motion causes intense mixing of intrathecally delivered drugs (162). Even though CSF flow within the spinal canal has a small Reynolds number, there is still vivid fluid exchange because the fluid laminae are intertwined due to CSF pulsations. In this chapter, we present a novel approach of using magnetically-guided nanoparticles, which are capable of being functionalized with different

types of drugs, for localizing and concentrating the particles at specific locations in an *in vitro* model of the human spine. Our results indicate that superparamagnetic gold-coated magnetite nanoparticles can be preferentially confined within an area of interest by guiding the particles with an external magnetic field. We have also provided computational results which aided in determining the optimal magnetic field for efficient intrathecal magnetic drug targeting (IT-MDT). If this novel technique can be successfully utilized with the required drug conjugated to the nanoparticles, the drugs can be locally delivered within the spinal canal at high concentrations, minimizing unwanted side effects of the drug away from the target region.

Our approach builds on the methods of magnetic drug targeting (MDT). Magnetic drug targeting is a type of active drug targeting method in which drug-functionalized magnetic nanoparticles (MNPs) are injected into the body and then localized to the target region by use of an external magnetic field. The drug will then desorb from the MNPs and begin its therapeutic mechanism of action. The most notable benefits of MDT reside in local drug action and minimization of systemic side effects. Until now, MDT methods have been mainly used to target drugs delivered systemically through blood vessels and have shown great promise (166–174). The novelty of our approach lies in applying the methods of MDT within the CSF-filled spinal canal, not in blood vessels, in order to achieve a localized therapeutic effect using much smaller drug doses and substantially reducing systemic toxicity for novel treatments of CNS diseases.

This chapter is organized as follows. Nanoparticle synthesis is presented first, followed by a description of our *in vitro* human spine model and experimental setup. The results section presents the MNP characterization and the outcomes from experiments to

determine MNP collection efficiency as a function of magnetic field strength, duration of magnetic field exposure, and distance between the target location and injection site. Preliminary results from implant-assisted IT-MDT experiments are also presented. The chapter closes with a discussion of our experimental results and conclusions.

6.3. Materials and Methods

In all of our experiments, we used externally placed permanent magnets to target superparamagnetic gold-coated magnetite nanoparticles at specific locations within an *in vitro* model of the human spine. The main aim of these experiments was to systematically study the spatial distribution of the magnetic nanoparticles in the presence of static magnetic fields within the intrathecal space, and to investigate the possibility of localizing and concentrating the nanoparticles at different regions within the human spine model. In this section, we explain (i) the materials and methods used for nanoparticle synthesis, (ii) our *in vitro* human spine model, (iii) the simulations used to determine optimal magnetic fields, and (iv) our experimental procedure to determine MNP collection efficiency.

6.3.1. Synthesis of gold-coated magnetite nanoparticles (Fe_3O_4@Au MNPs)

The nanoparticles utilized for all of our experiments had a magnetite core with diameter varying between 8-12 nm as shown in Figure 30A. Magnetite cores within this diameter range are beneficial because they display the property of superparamagnetism, which means they exhibit net magnetization only in the presence of an external magnetic field. Superparamagnetism allows the nanoparticles to transport freely throughout the spine model until they are in the presence of the externally applied magnetic field, which

then acts to trap the nanoparticles at that defined location. Once the applied magnetic field is removed, these superparamagnetic nanoparticles lose their previously induced magnetization and re-disperse in the fluid. The nanoparticle cores were synthesized by a coprecipitation technique, described in Mandal et al. (2005) and various other articles, using ferrous and ferric salts to form magnetite (Fe_3O_4) (175). These superparamagnetic magnetite cores were then coated by a gold layer of thickness varying between 8-15 nm by a surface adsorption technique. The overall hydrodynamic diameter of the particles was found to be between 20-25 nm as shown in Figure 30B. The gold coating on the magnetite served two purposes. (i) It prevented oxidation of the magnetite core into maghemite by forming an inert biocompatible protective coating. (ii) It also forms an excellent platform for conjugating drugs to the nanoparticle surface since gold has a natural affinity for thiol bonds (176). These particles were suspended in a TX-100 surfactant solution to introduce micelles and help prevent agglomeration. The nanoparticles were characterized by using transmission electron microscopy (TEM), energy dispersive x-ray spectroscopy (EDS) and superconducting quantum interference device (SQUID) magnetometry.

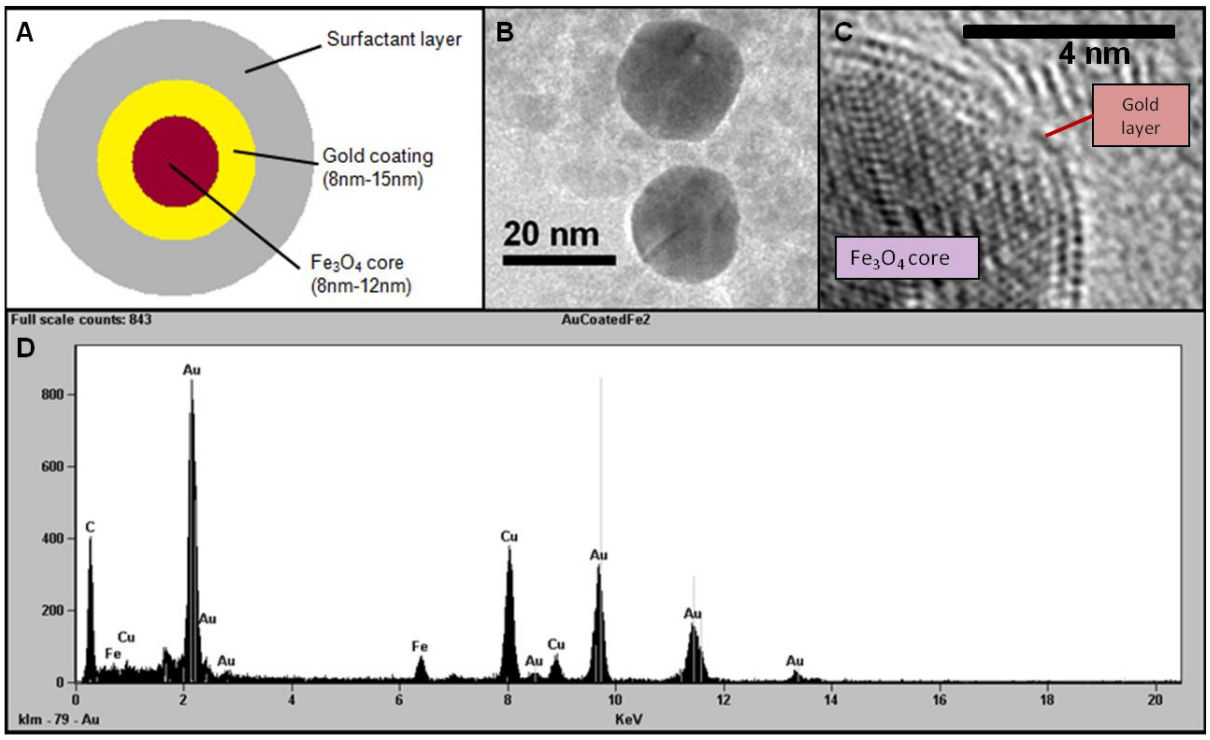

Figure 30. (**A**) Schematic of Fe_3O_4@Au nanoparticle; (**B**) TEM image of nanoparticles showing hydrodynamic diameter to be between 20-25 nm; (**C**) TEM image showing a partially gold-coated Fe_3O_4 core which confirms the core diameter to be around 8-12 nm; (**D**) The energy density spectrum of the gold-coated magnetite nanoparticles determined using EDS which indicates the presence of elements Au, Fe and O.

6.3.2. ***In vitro* human spine model**

An *in vitro* model of the human spine was built to conduct MDT experiments in order to help determine the feasibility of IT-MDT. It was important that the model possessed physiologically and anatomically consistent dimensions in order to conserve the main hydrodynamic properties of CSF which are crucial to intrathecal drug delivery *in vivo*. These essential components include the spinal canal, spinal cord, nerve roots, filum terminale, as well as the ability of the CSF to pulsate.

6.3.2.1. ***Geometry and anatomy***

The model, as shown in Figure 31, consisted of a cylindrical polystyrene tube (49.0 cm length; 1.52 cm inner diameter) which represented the spinal canal (177–179) and a

cylindrical section of pressure-treated hard wood (45.0 cm length, 0.79 cm diameter) at the center of the tube which served as a surrogate for the spinal cord (178–181). Black rubber pieces (each 2 mm in diameter) were used to represent spinal nerve roots (182) located above the cauda equina which are important in enhancing the mixing of intrathecally-injected nanoparticles (183–185). A latex deformable membrane was tightly fixed to the mouth of the distal neck and served as the filum terminale which expands and contracts during the pulsatile motion of fluid inside the model. The void volume, which served as the subarachnoid space, was filled with artificial CSF.

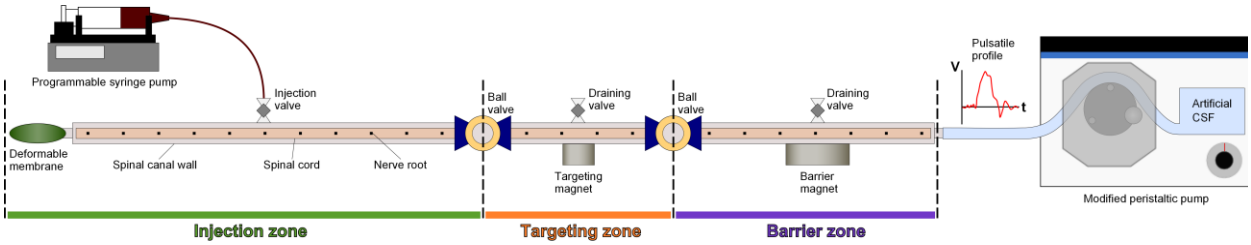

Figure 31. Schematic of entire experimental setup with the *in vitro* human spine model which clearly shows the three different zones (injection, targeting, and barrier zones).

6.3.2.2. ***CSF pulsations***

Intrathecal drug distribution varies depending on different patient-specific parameters such as the frequency and magnitude of CSF pulsations, the velocity and stroke volume of CSF, and heart rate (183). Previous research has shown CSF flow velocities varying from 0.3-5.1 cm/s and CSF stroke volumes varying from 0.1-3.0 mL/s depending on a patient's health, spinal anatomy, heart rate, and blood pressure (186–190). In our experiments, a CSF velocity of 1.5 cm/s and a stroke volume of 2 mL were imposed, which are within the ranges cited previously. To produce pulsatile fluid motion equal in amplitude and frequency to that of a typical resting human's CSF pulsations, the proximal end of the model was connected to a masterflex peristaltic pump (Cole-Parmer, IL, USA)

and two of the three metal cylinders that drive the pump were removed. This created a ramping pulse function. Since CSF pulsates at a frequency of the heart beat (191), the pump was set at 72 beats per minute which, according to the American Heart Association, is within the 60-80 bpm range of normal resting heart rate in humans. The inclusion of pulsatile fluid motion and spinal nerve roots in our model was important because of the large effects these two parameters have on CSF fluid mechanics as seen *in vivo* (55,183–185,192–194).

6.3.2.3. ***Nanoparticle injection***

For controlled nanoparticle injection into the model, a programmable syringe pump (model #NE-1800; New Era Pump Systems**,** NY, USA) was used. The BD 15 ml syringe was connected to the model via a plastic catheter which allowed for controlled infusion of nanoparticles into the spinal canal. Nanoparticles were always injected into the lumbar region of our model.

6.3.2.4. ***Magnetic targeting***

Nanoparticles were targeted to a specific site in the spine model by using an external magnetic field (targeting magnet) placed exactly below the region of interest. This field was produced in our system by using NdFeB rare earth magnets (K&J Magnetics, Inc., PA, USA) of various dimensions, lbs pull force values, and surface field strengths – 0.396 T (3960 gauss), 0.507 T (5070 gauss), 0.528 T (5280 gauss) and 1.05 T (10,500 gauss). As depicted in Figure 31, magnetic fields were applied along the spinal canal at two specific locations: target site (middle of apparatus) and barrier site (right end of apparatus). The target site was located at the treatment area where nanoparticles should by concentrated. The barrier site magnet was placed to prevent any nanoparticles from exiting the spinal

model. Ball valves were used to separate the spine model and its contained fluid into three different zones: injection, targeting, and barrier zones (Figure 31). To determine the mass fraction of nanoparticles retained by the magnet within the target region and the remaining nanoparticles in the other two zones, the ball valves were closed and the fluid contained within each zone was eluted through individual draining valves, dried, and weighed.

6.3.3. **Multiphysics simulation-based determination of optimum magnetic field**

COMSOL 4.2a, a finite element software for the modeling and simulation of any physics-based system, was used to study the magnetic fields produced by different permanent magnets and to design appropriate fields with these magnets for use in our experiments. A detailed description of the theoretical background for these simulations can be found in Appendix B.

Figure 32 and Figure 33 display the magnetic fields produced by the simulations, which match the fields produced by the magnets used for the *in vitro* IT-MDT experiments. Specifically, Figure 32A shows the magnetic field lines of our *in vitro* spine model with the exact magnets used experimentally, while Figure 32B displays the magnetic field lines when both the targeting and barrier magnets have the same dimensions and strength. Figure 33 shows the magnetic fields present around both the targeting magnet and barrier magnet in our model. From the inserts displayed in Figure 33, one can see that the strength of the magnetic field $\vec{B}$ in the CSF-filled subarachnoid space opposite the targeting magnet is in the range of 0.051-0.098 T, while the strength of $\vec{B}$ in the subarachnoid space opposite the barrier magnet is in the range of 0.092-0.167 T. Both of these magnetic field strength ranges were shown to be strong enough to capture MNPs while overcoming the pulsatile motion and mixing of the CSF.

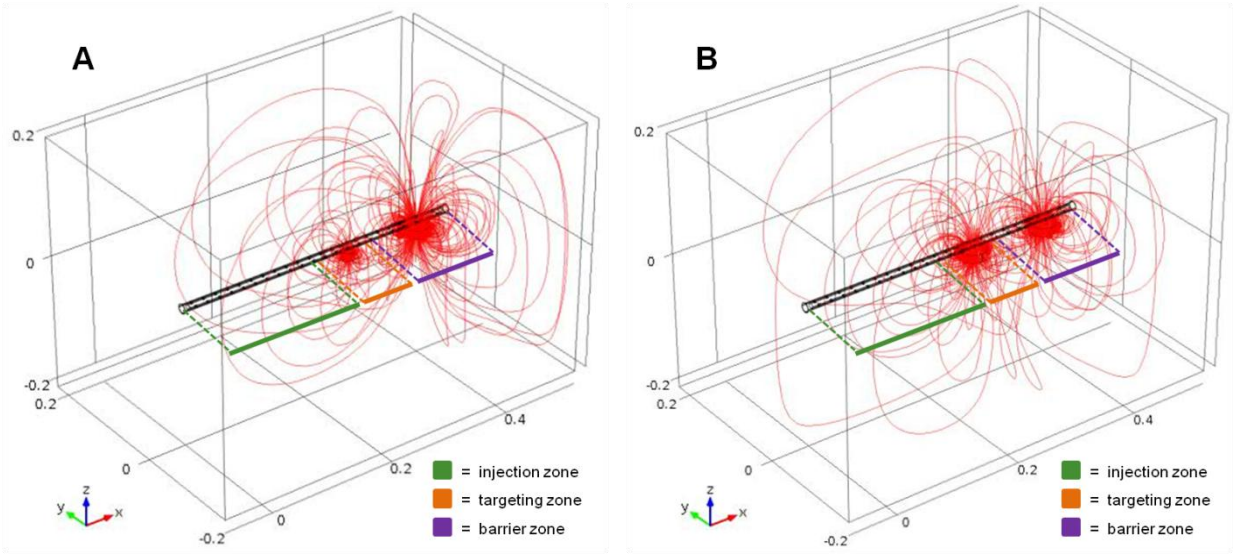

Figure 32. Magnetic field lines produced by (**A**) *in vitro* human spine model used in our experiments with the 0.528 T surface field strength targeting magnet and the 1.05 T surface field strength barrier magnet and by (**B**) spine model in which both magnets are of equal 1.05 T surface field strength.

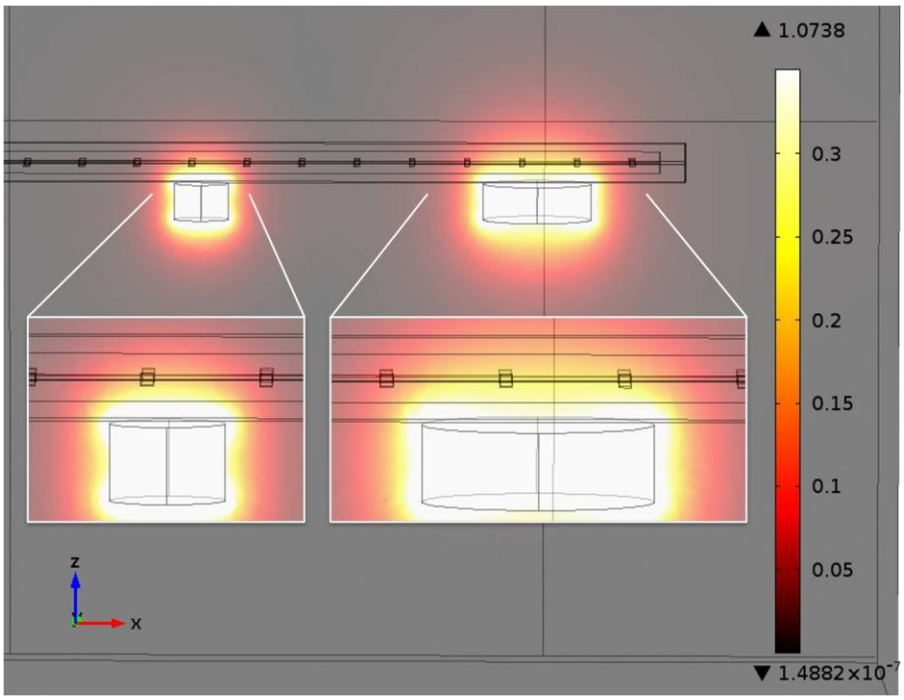

Figure 33. Magnetic field produced by targeting magnet and barrier magnet (shown in xz-plane). CSF-filled subarachnoid space opposite the targeting magnet experiences a magnetic field $\vec{B}$ in the range of 0.051-0.098 T (510-980 gauss), while the subarachnoid space opposite the barrier magnet experiences a $\vec{B}$ field in the range of 0.092-0.167 T (920-1670 gauss). Figure inserts are close-up views of both magnets to show more detail.

6.3.4. **Experimental procedure to determine MNP collection efficiency**

All experiments were conducted by injecting 1 ml of 0.017 g/ml Fe_3O_4@Au nanoparticle solution into the *in vitro* human spine model in the lumbar region using a programmable syringe pump over 1 minute. The surface field strength of the barrier magnet used was 1.05 T. The strength of the target magnet varied depending on the experiment under consideration. Once the experiments were completed, each compartment — corresponding to a particular zone — was rinsed separately and magnetically decanted. The solutions collected from each compartment were placed in a convection oven in small borosilicate glass containers and heated for 1 hour (175 °C) until completely dry in order to determine the dry weight of these fractions. The fraction of nanoparticles collected within each zone was used to determine the overall collection efficiency of each experiment trial.

Three different sets of experiments were performed to determine the nanoparticle collection efficiency in each zone depending on either the strength of the applied external magnet, the time duration of magnetic field exposure, or the distance between the target location and the site of nanoparticle solution injection. Additional preliminary experiments to determine the effect of a 4 cm physiological distance between the spinal canal and the magnet located on the skin surface, as well as the effect of ferrous implants, on the nanoparticle collection efficiency were also performed. Statistical analysis of the resultant nanoparticle collection efficiencies was performed and the means were compared using a Student's *t*-test. A two-tailed *p*-value <0.05 was considered statistically significant.

6.4. **Results**

6.4.1. **Nanoparticle characterization**

The nanoparticles were characterized by transmission electron microscopy (TEM) and energy-dispersive x-ray spectroscopy (EDS) at the UIC Research Resources Center, as well as by superconducting quantum interference device (SQUID) magnetometry at Northwestern University. The TEM images confirmed the size of both our magnetite core to be about 8-12 nm (Figure 30C) and the entire gold-coated magnetite nanoparticle to be between 20-25 nm (Figure 30B). These TEM results, along with the SQUID magnetometer results shown in Figure 34, confirmed that our nanoparticles were superparamagnetic which helped prevent agglomeration in the absence of an external magnetic field. From the plot of magnetization vs. applied magnetic field (*M*-*H* loop) at 265 K (Figure 34) the saturation magnetization (M_s), remnant magnetization (M_r), and coercivity (H_c) were determined for our Fe_3O_4@Au nanoparticles to be as follows: M_s = 29.5 emu/g; M_r = 0.52 emu/g; H_c = 21.1 Oe at 265 K. The EDS results (Figure 30D) indicated the presence of gold (Au), iron (Fe) and oxygen (O) in our nanoparticle sample. Disregarding the other elements present from the EDS sample grid, carbon (C) and copper (Cu), Figure 30D validated the presence of both Au and Fe_3O_4 in our nanoparticle samples.

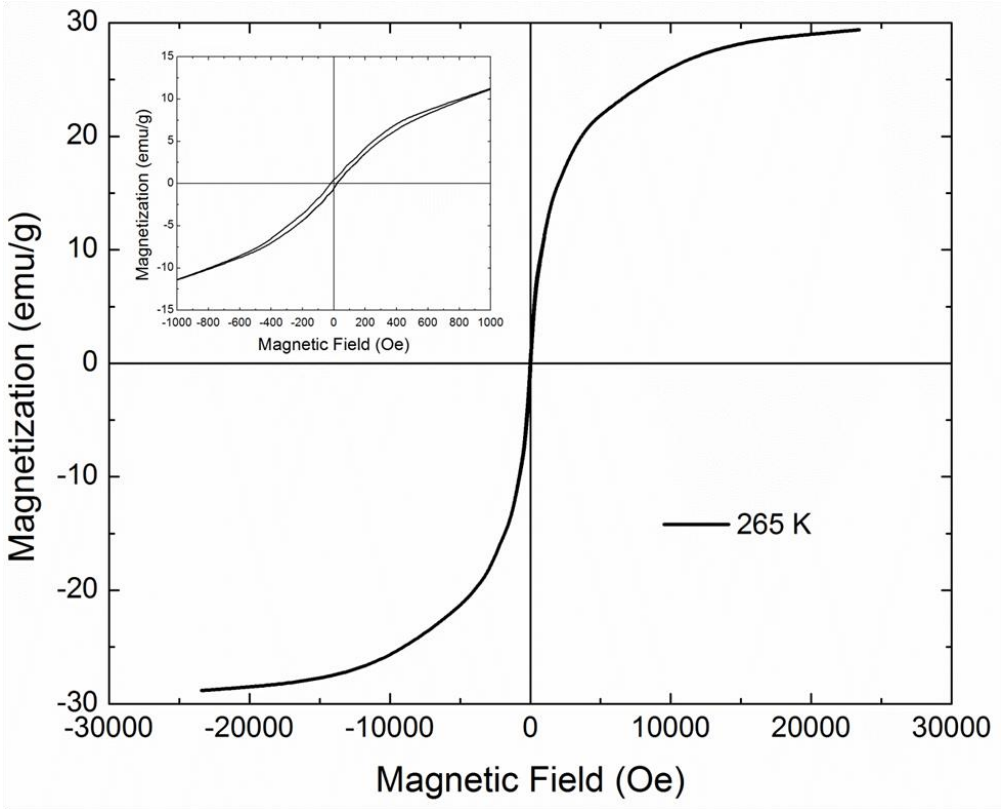

Figure 34. Plot of magnetization vs. magnetic field, obtained by SQUID magnetometry, for the Fe_3O_4@Au magnetic nanoparticles used in our *in vitro* intrathecal magnetic drug targeting experiments.

6.4.2. **Collection efficiency as a function of magnet strength**

To prove the hypothesis that stronger magnets achieve more efficient MNP retention, we performed experiments in which the magnet strength within the targeting zone was varied. Based on the results from our simulations of magnetic field gradients and field strengths produced by magnets of differing size and composition, NdFeB magnets with surface field strengths of 0.396 T, 0.507 T, and 0.528 T were selected for use in the targeting zone. These magnets were shown to have magnetic field gradients and strengths within the subarachnoid space of our human spine model capable of confining the bulk of the nanoparticle transport within the target region. Experimental run times (duration for which the pulsations were produced after injection) remained fixed at 15 minutes for all

the trials. Two different 0.528 T surface field strength magnets, but with differing pull force strengths (35 lb pull force and 1045 lb pull force), were tested as well.

MNP collection efficiency within the targeting zone increased as the surface field strength and lb pull force strength of the magnet increased, while the nanoparticle retention simultaneously decreased in both the injection and barrier zones, as can be seen in Figure 35. Percentage retentions of 48%, 62%, 73%, and 98% were observed for the surface magnetic field strengths of 0.396 T, 0.507 T, 0.528 T (35 lb pull force), and 0.528 T (1045 lb pull force) respectively. Note that the stronger lbs pull force magnet out of the two 0.528 T surface field strength magnets was able to capture nearly all of the MNPs and showed a 98% collection efficiency. Statistical analysis revealed significant differences between the nanoparticle collection efficiencies obtained when any of the different magnet strengths were applied; all *p*-values were much smaller than the 0.05 significance level, with the largest *p*-value of 0.00006 being between the 0.507 T and 0.528 T (35 lb pull force) magnets. These MNP collection efficiencies within the targeting zone when a magnetic field was applied were substantially greater than the average collection efficiency in the targeting zone of control experiments in which no magnetic field was applied. For example, the 35 lb pull force, 0.528 T surface field strength magnet exhibited a 664% increase in nanoparticle collection efficiency within the targeting zone as compared to the control, and the 1045 lb pull force, 0.528 T surface field strength magnet exhibited an astonishing 891% increase in collection efficiency.

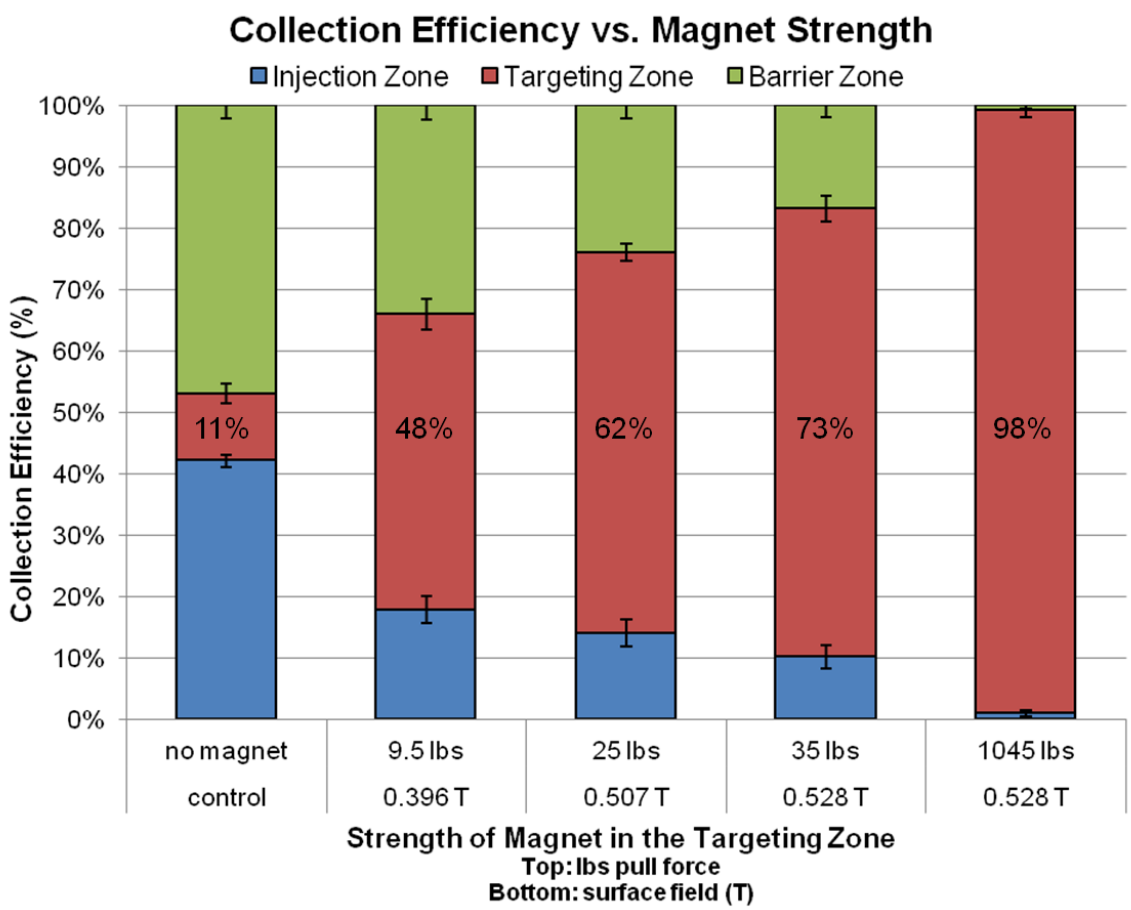

Figure 35. Graph showing the nanoparticle collection efficiency (*CE*) as a function of magnet strength at the targeting zone. Error bars represent the standard deviation in nanoparticle *CE* within each zone for the different experiments. With magnetic targeting, the nanoparticle *CE* increased almost 9-fold when compared to the control experiments.

The collection efficiency vs. magnet strength experiments showed that the nanoparticle collection efficiency (*CE*) depended on the magnitude of the applied external magnetic field, as well as the pull force strength of the magnet, within the targeting zone of the spine model. Although the strongest magnet with 1045 lb pull force strength gave the highest nanoparticle *CE* of 98% within the targeting zone (Figure 35), its bulky size (4" diameter x 2" thick) may be a disadvantage in future clinical trials. Therefore, the much smaller 35 lb pull force magnet (3/4" diameter x 1/2" thick) was selected as our target magnet of choice for the remainder of our experiments in which magnet placement was

within the epidural space of our model. In future clinical trials of IT-MDT, magnets with different strength, size, and shape may be optimized to fit the needs of patients or the disease being treated.

6.4.3. **Collection efficiency as a function of time**

The variation in MNP collection efficiency with time at a specific target site within the *in vitro* human spine model was investigated. In these experiments a target magnet of 0.528 T surface field strength and 35 lb pull force strength was used within the targeting zone and experimental times were varied before the nanoparticles were collected from each zone. Different sets of trials were run for each of the following experimental times: 0.5 min, 1 min, 2 min, 5 min, 10 min, 15 min, and 60 min.

The time dependent variations in nanoparticle collection efficiency are shown in Figure 36. During the first five minutes of each experiment, a significant portion of the nanoparticles still resided within the injection zone. As each experiment progressed, the nanoparticle recovery from the targeting zone increased due to the transport of nanoparticles into this zone by the pulsatile fluid flow and subsequent capture of these nanoparticles by the externally-applied magnetic field.

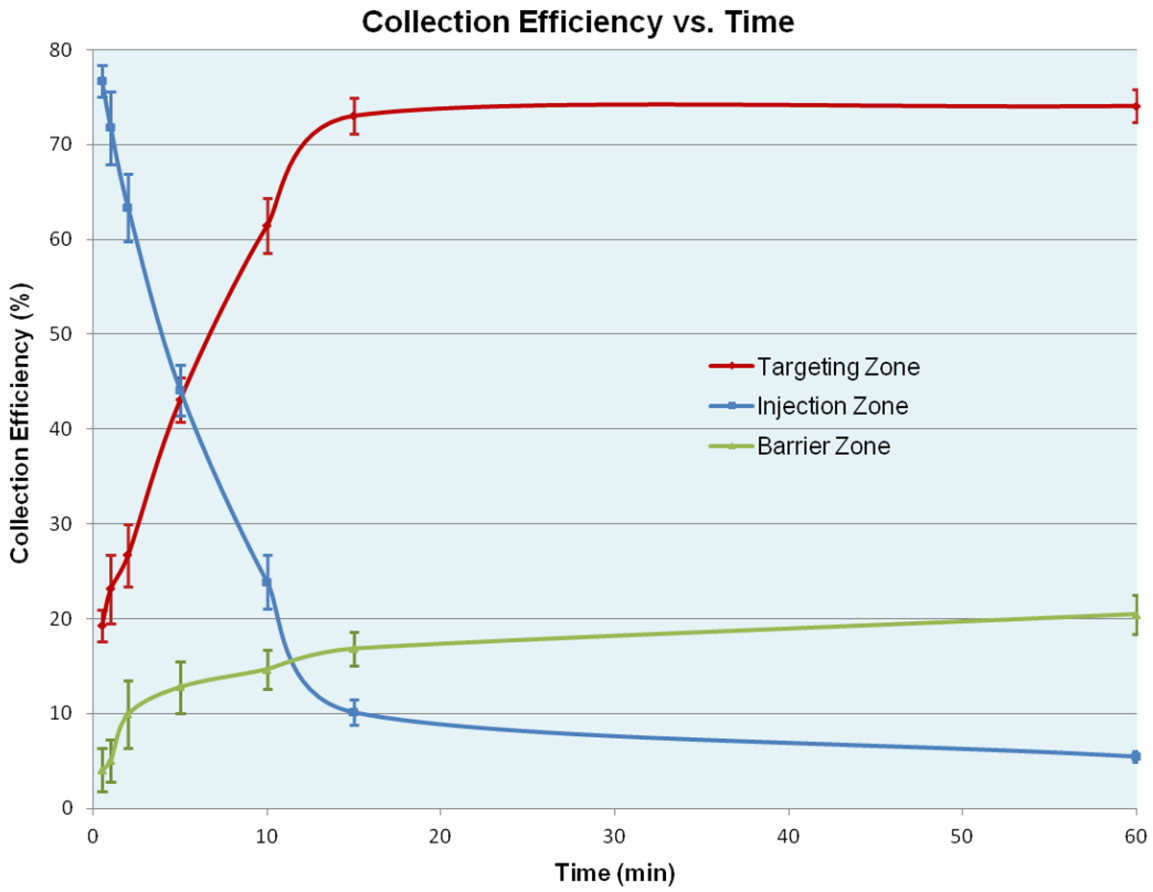

Figure 36. Graph showing the nanoparticle collection efficiency (*CE*) as a function of time. Error bars represent the standard deviation in nanoparticle *CE* within each zone at the different measurement times. As *CE* within the targeting zone increases, *CE* within both the injection and barrier zones simultaneously decrease.

It was observed that the collection efficiency in the targeting zone increased significantly during the first 15 minutes of these experiments, reaching a 73.0% *CE*. After 15 minutes, nanoparticle capture in the targeting zone was practically completed with a mean *CE* of 74.1% at 60 minutes (p-value = 0.4085). No significant change in the magnetic retention value was observed beyond 60 minutes. The collection efficiency vs. time experiments showed that the nanoparticle collection efficiency at the target site in the spine model increased with time and reached a final steady value around 74%.

6.4.4. **Collection efficiency as a function of magnet location along spine model**

To test whether any desired region could be effectively targeted with high nanoparticle collection efficiency, we performed experiments in which we varied the location of the applied external magnetic field along the spine model. Hence, we varied the physical location of the target zone. While it was expected that only the hydrodynamic drag force and the magnetic force affect nanoparticle collection, it was essential to prove that targeting was possible in any zone with the same level of efficiency for the same magnet. These experiments were also important to demonstrate that surface effects or surface friction from the model acting on the nanoparticles did not significantly impact nanoparticle collection and that gravity effects could be assumed negligible. A target magnet with 0.528 T surface field strength and 35 lb pull force was placed in the injection zone (at 3.0 cm from the injection site), targeting zone (at 16.0 cm from the injection site) and barrier zone (at 26.0 cm from the injection site) during three separate sets of experiments and experimental run time was maintained at 15 minutes.

In these experiments, maximum retention values between 73% and 75% were observed at each targeting location within the three different zones. High collection efficiencies were achieved for nanoparticle localization in the lumbar region ("injection zone" from Figure 31) with 75% *CE*, thoracic region ("targeting zone" from Figure 31) with 73% *CE*, as well as the cervical region ("barrier zone" from Figure 31) with 74% *CE*. It is important to note that the maximum retention at every zone had little variance (73% - 75%) as shown in Figure 37. Statistical analysis revealed no significant differences between the nanoparticle collection efficiencies obtained at any of the target magnet

locations along the spine model: 3.0 cm vs. 16.0 cm (p-value = 0.3429), 16.0 cm vs. 26.0 cm (p-value = 0.4128), and 3.0 cm vs. 26.0 cm (p-value = 0.6985).

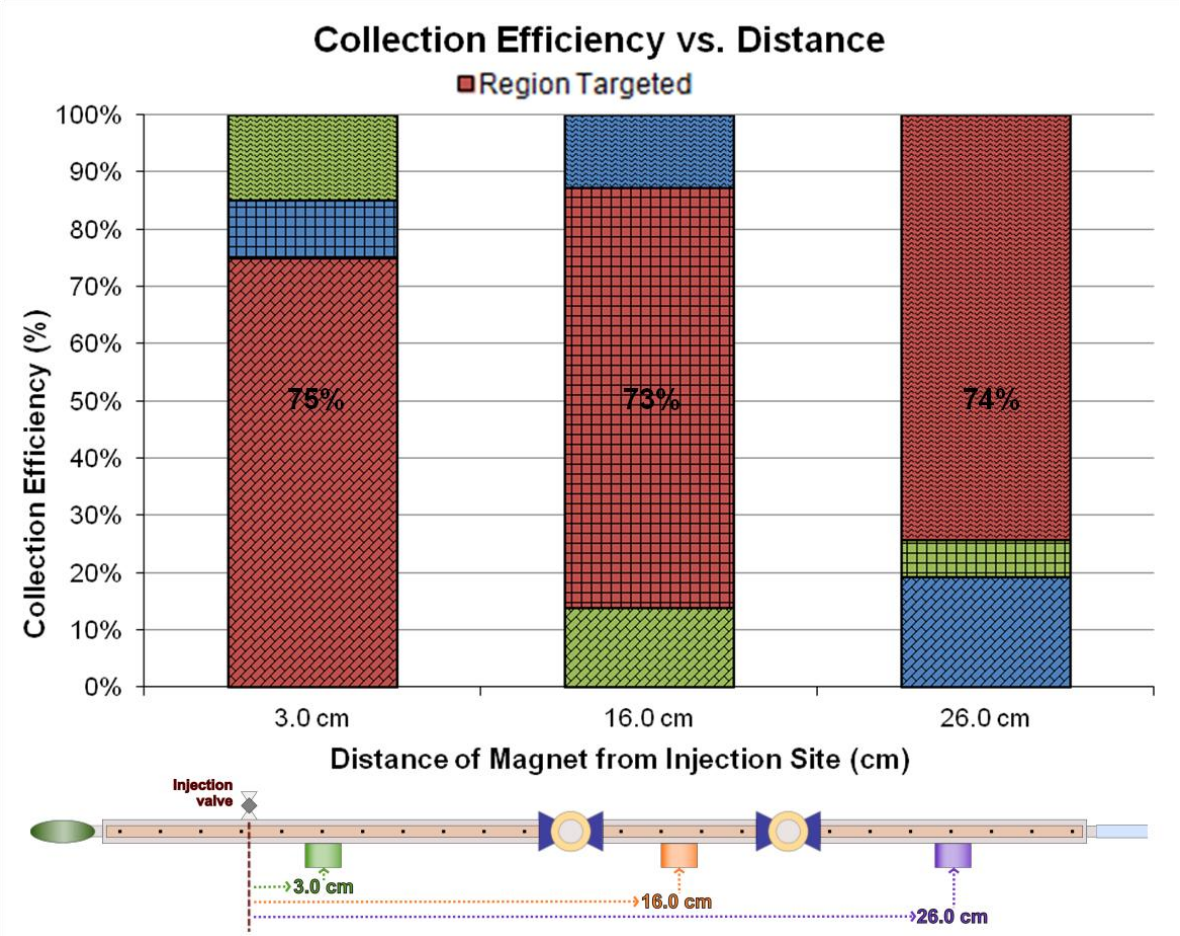

Figure 37. Graph showing the variation of nanoparticle collection efficiency (*CE*) at different target zones in the *in vitro* human spine model as a function of the distance of the targeting magnetic field from the injection site. No matter which zone was chosen as the treatment site where the magnet was to be placed (region targeted; displayed in red), *CE* reached between 73% - 75%. Green and blue colored bars correspond to the non-targeted regions. Note, the different patterns correspond to the three zones as previously defined in Figure 31: diagonal brick pattern = "injection zone"; square pattern = "targeting zone"; horizontal wave pattern = "barrier zone".

The collection efficiency vs. distance of targeting magnetic field from injection site experiments showed that the position of the applied magnetic field always yielded high nanoparticle retention irrespective of its distance from the injection site. In order to determine if the amount of nanoparticles leaving the spine model from the barrier zone

due to the pulsations was significant, prussian blue staining test (used for indicating the presence of magnetite) was performed on the solution leaving the model. The test showed that the amount of nanoparticles that escaped the magnetic barrier was negligible (no staining of the filter paper).

6.4.5. **Magnetic guidance at physiological distance & implant-assisted guidance**

The previous experiments used permanent magnets placed in the epidural space of our *in vitro* human spine model. To test whether effective IT-MDT could be achieved at physiological distances, meaning the distance between spinal canal and the epidermis (as shown in Figure 38A), we conducted additional experiments with a 4 cm void space between the targeting magnet and the *in vitro* human spine model. This distance is equivalent to placing magnets non-invasively on the surface of a patient's back when performing IT-MDT clinically. Two different sets of experiments were conducted; one set with only the 4 cm physiological separation; the other set with the 4 cm separation and the inclusion of two ferrous implants within the epidural space of the model. Both sets of experiments used the 0.528 T surface field strength, 1045 lb pull force strength magnet in order to achieve a strong magnetic field at a physiological distance from the magnet surface.

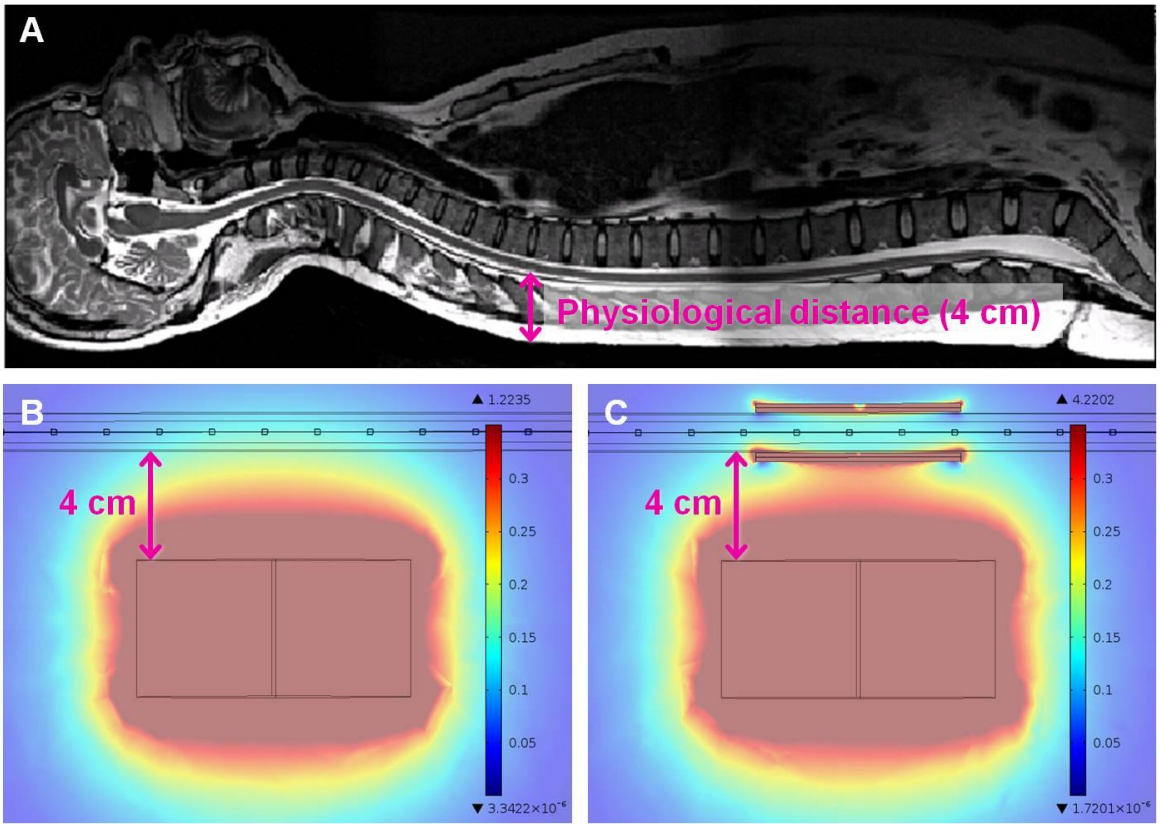

Figure 38. (**A**) Patient MRI showing the 4 cm physiological distance between intrathecal space and epidermis; (**B**) Simulated magnetic field $\vec{B}$ produced by the 0.528 T surface field, 1045 lb pull force strength magnet placed at a 4 cm distance away from the spinal canal; magnetic field within the spinal canal is within a 0.116-0.160 T range; (**C**) Simulated $\vec{B}$ field when two ferrous implants were placed within epidural space; high gradient magnetic field created within the spinal canal is within a 0.067-0.626 T range.

In the first set of experiments with only the 4 cm physiological separation, an average nanoparticle collection efficiency of 52% was obtained within the targeting zone during both 15- and 60-minute trials. These results are a 473% increase (nearly 5-fold increase) in MNP collection efficiency when compared to the control where no magnetic field was applied. The magnetic field simulations indicated that the field within the spinal canal dropped to a range of 0.116-0.160 T (Figure 38B) from the previous range of 0.068-0.332 T (Figure 33) obtained obtained during experiments in which the smaller 0.528 T surface field strength, 35 lb pull force strength magnet was placed within the epidural

space of the spine model. Along with this drop in field strength, the simulations also showed that the magnetic field within the spinal canal had smaller gradients when the magnet was placed at a 4 cm physiological distance away from the model compared to when the targeting magnet was placed within the epidural space. This computed drop in magnetic field strength and magnetic field gradient is consistent with the experimental results of a 52% MNP collection efficiency compared to the 73% *CE* obtained in previous experiments with magnet placement within the epidural space of our spine model.

In the second set of experiments, two cylindrical ferrous implants (1/8" diameter x 3" length) were placed within the epidural space of the model, one dorsal implant and one ventral implant, while maintaining the magnet placement at a physiological 4 cm distance. This preliminary test mimics the effect of implant-assisted MDT, which aims to create a high gradient magnetic field in order to obtain larger nanoparticle retention values. The results from these implant-assisted IT-MDT experiments showed an average nanoparticle collection efficiency around 76% within the targeting zone during both 15- and 60-minute experiments. The implant-assisted IT-MDT results produced a 146% increase in nanoparticle *CE* over the IT-MDT experiments which only had the physiological separation and no implant; a highly efficient 691% increase over the control experiments. As shown in Figure 38C, the ferrous implants concentrated the magnetic flux density ($\vec{B}$ field) around the spinal canal, which created a high gradient field (0.067-0.626 T) within the subarachnoid space. Due to the high gradient field, large nanoparticle collection efficiencies were obtained, similar to those obtained when the 35 lb pull force targeting magnet was placed within the epidural space and no implants were present.

6.5. **Discussion**

Our experiments confirm that IT-MDT can be controlled using three critical parameters: targeting magnet strength, magnet placement along the spinal canal, and magnetic field gradient. The experiments with varying targeting magnet strength showed that an increase in the surface field and lbs pull force strengths enhanced nanoparticle retention within the targeting zone with collection efficiencies up to nine-times greater than the control. During these experiments we observed that the MNPs preferentially collected towards the edges of the magnet surface (regions with largest field gradients). This preference emphasizes the importance of generating high gradient magnetic fields in MDT applications (195,196). Our implant-assisted IT-MDT experiments confirm that a high gradient magnetic field is desirable within the targeting region in order to achieve the highest concentration of drug-functionalized nanoparticles.

When the targeting magnet location was varied along the *in vitro* human spine model, the position of the applied magnetic field always yielded high nanoparticle retention regardless of its distance from the injection site. Therefore, very high nanoparticle concentrations can be attained at any desired targeting location within the spinal canal. This is a significant point to consider when developing patient specific therapies. Our collection efficiency vs. time experiments established that MNP targeting and settlement reached final values within 15 minutes when experiments were conducted using the spinal canal dimensions and CSF pulsation parameters given in section 6.3.2. For different dimensions and pulsation parameters, the duration of magnetic targeting and nanoparticle settlement is expected to vary. Recent studies quantify how the frequency and magnitude of a patient's CSF pulsations influence intrathecal drug distribution (183). Accordingly,

minor deviations from the suggested 15 minute MNP targeting and settlement time can be expected during clinical trials. However, the relatively short duration of magnetic targeting may be advantageous for future clinical applications of IT-MDT. Also, another result crucial for developing personalized therapies is that high collection efficiencies can be achieved when placing a strong magnet at a distance equal to the physiological separation between a patient's spinal canal and epidermis, either with or without a ferrous spinal implant.

Our envisioned therapy for CNS disorders consists of delivering and localizing MNPs, which would be conjugated to the required drugs, to specific regions within the spinal canal using an external magnetic field, followed by controlled release of the drug for desired treatment. For example, while treating leptomeningeal metastases or other CNS tumors where the chemotherapeutic drug needs to be concentrated near the site of cancerous cell proliferation, we could conjugate the nanoparticles to a drug such as methotrexate and then guide them to the required treatment location using an external magnetic field (169). Our method of IT-MDT may also be a candidate treatment option for IT gene therapies where only a localized effect is desired. For gene therapies to be successful, very high concentrations of infused siRNA around the targeting region are required. IT-MDT offers one way to achieve localized, high concentrations of nanocarriers which may be beneficial for overcoming the barriers of current gene therapies.

With regards to patient specific therapies, IT-MDT shows great promise since large nanoparticle collection efficiencies are possible within a short duration (only 15 minutes) regardless of the targeting location along the spinal canal. The specific site within the spinal canal, as well as the amount of drug to be delivered to the site, would determine the placement of the external magnetic field and its strength for personalized treatment.

IT-MDT has clear advantages for targeted drug delivery in very high concentrations with the potential to greatly diminish systemic toxicity while using much smaller drug doses as compared to standard IT drug infusion protocols in which continuous infusion is required for maintaining a sufficiently high drug concentration at the target site despite dispersion throughout the entire CNS.

For example, during standard IT baclofen infusions, the drug is continuously administered at rates of 100-900 μg/day (197,198). We hypothesize that a much smaller dose of baclofen would be required using our magnetically targeted intrathecal treatment since most of the infused drug-functionalized nanoparticles would be confined to the desired treatment area. Although continuous intrathecal baclofen infusion has demonstrated benefits such as >80% and >65% of patients showing improvement in tone and spasticity, respectively, severe side effects due to high baclofen dosages commonly occur. Overdose due to pump and spinal catheter system malfunction, which has occurred in 40% of patients receiving IT baclofen therapy (199), produces symptoms such as respiratory arrest, hypotension, hyporeflexia, quadriplegia, apnea, seizures, autonomic instability, hallucinations, hypothermia, cardiac abnormalities and absence of all reflexes (200–202). Severe withdrawal symptoms such as hallucinations, tachycardia, hyper or hypotension, seizures, rebound spasticity, rhabdomyolysis (198,199,203) and life threatening complications like coma, may arise due to baclofen overdose (200,204). Such problems may potentially be resolved using our proposed magnetically targeted IT treatment where the quantity of drug injected would be minimal as compared to the current continuous IT infusion method.

In our *in vitro* model, the barrier magnet prevented the escape of nanoparticles from the spinal canal to the brain region. Such a barrier function that seals the brain from IT delivered drugs could have an important clinical significance in reducing side effects and patients' risks. For example, in cases with toxic drugs like baclofen, this barrier magnetic field could serve as a valuable safety net to block drug from reaching the brain. The small amount of nanoparticles at the barrier magnet could then be guided back down to the target thoracic region by physical translocation. Once within the target region, the magnet would remain in place until the drug has desorbed from the nanoparticles and produced a therapeutic effect. The magnets would then be removed, and the bare gold-coated nanoparticles would become dispersed in the pulsatile CSF due to their superparamagnetic nature and continue transportation into the brain where they would be cleared by the body's natural processes and excreted by the kidneys (205,206).

While performing IT-MDT *in vivo*, biological surfactants such as lecithin (207,208) or surfactin (209,210) may enhance biocompatibility and prevent side effects. Even though iron oxide nanoparticles appear to be biologically safe (211–213), any possible adverse reaction to the magnetite core of the nanoparticles would be prevented by the gold coating since gold is inert and well-tolerated by the human body. Similarly, before implanting a NdFeB magnet *in vivo*, the magnet would be coated with a thin layer of biocompatible silicone in order to reduce the possibility of magnet corrosion and degradation from exposure to physiological conditions. Toxicological studies during subcutaneous and vascular delivery of gold nanoparticles *in vivo* have also shown no cytotoxic effects (205,206,214,215). Once the nanoparticles are cleared from the CNS, and if the gold coating happens to desorb from the nanoparticles, magnetite can be metabolized into elemental

iron by hydrolytic enzymes and the generated reactive oxygen species regulated by ferritin and transferrin receptors (216). The iron will then be integrated into the normal body stores and later incorporated into hemoglobin (217).

Like all models, there are limitations to our procedure. For example, the localization and collection efficiency of the nanoparticles needs to be further tested *in vivo* using animal models. Also, despite the fact that gold acts as an inert biocompatible layer around the magnetite core, the long term safety and exact metabolic fate of the nanoparticles needs to be studied in animal trials. Conjugation of our nanoparticles to drug molecules and cell-specific delivery is also an area of future research. The pharmacokinetics and pharmacodynamics of certain drugs conjugated to our MNPs, as well as the release kinetics and cellular uptake, will need to be studied. Also, in much of our research discussed here the magnet was placed directly against the spinal canal wall of our model; thus, the specific site of magnet placement within the epidural space needs to be investigated.

6.6. **Conclusions**

Our experiments provided a thorough study on the feasibility and benefits of intrathecal magnetic drug targeting. The careful design and placement of magnetic fields for targeted delivery at a specific site, as well as the development of advanced nanoparticle drug-functionalization techniques, will enable physicians to exercise precise control over the distribution, concentration, and release of drugs at any desired location within the spinal canal. We have provided *in vitro* experimental results which show great potential for intrathecal magnetic drug targeting to be used as a novel treatment method for diseases of the central nervous system upon completion of *in vivo* animal studies. Our experimental

results showed that external magnetic fields can be used to guide and localize intrathecally-injected magnetic nanoparticles at desired locations within the spinal canal with large collection efficiencies and at concentration levels nearly nine-times that of control experiments when no magnetic field was present. The results also indicated that external magnetic fields can capture intrathecally-delivered nanoparticles within a targeted region of the spinal canal despite the convective transport and mixing effects caused by the pulsatile motion of CSF and the presence of spinal nerve roots and trabeculae. The current indications in which our novel IT-MDT technique may prove beneficial in the future include chronic pain, cancers, anesthetic agents, spasticity, and other debilitating disorders of the central nervous system.

7. IMPLANT-ASSISTED INTRATHECAL MAGNETIC DRUG TARGETING

7.1. Abstract

There is an ongoing struggle to develop efficient drug delivery and targeting methods within the central nervous system. One technique known as intrathecal drug delivery, involves direct drug infusion into the spinal canal and has become standard practice for treating many central nervous system diseases due to reduced systemic toxicity from the drug bypassing the blood-brain barrier. Although intrathecal drug delivery boasts the advantage of reduced systemic toxicity compared to oral and intravenous drug delivery techniques, current intrathecal delivery protocols lack a means of sufficient drug targeting at specific locations of interest within the central nervous system. In chapter 6, we proposed the method of intrathecal magnetic drug targeting in order to overcome the limited targeting capabilities of standard intrathecal drug delivery protocols, while simultaneously reducing the systemic toxicity as well as the amount of drug required to produce a therapeutic effect. Building off of our previous work, this chapter presents the concept of implant-assisted intrathecal magnetic drug targeting. Ferritic stainless steel implants were incorporated within the subarachnoid space of our *in vitro* human spine model, and the targeting magnet was placed at a physiological distance away from the model and implant to mimic the distance between the epidermis and spinal canal. Computer simulations were performed to optimize implant design for generating high gradient magnetic fields and to study how these fields may aid in therapeutic nanoparticle localization. Experiments aiming to determine the effects of different magnetically-susceptible implants placed within an external magnetic field on the

targeting efficiency of gold-coated magnetite nanoparticles were then performed on our *in vitro* human spine model. Our results indicate that implant-assisted intrathecal magnetic drug targeting is an excellent supplementary technique to further enhance the targeting capabilities of our previously established method of intrathecal magnetic drug targeting.

7.2. **Introduction**

Intrathecal (IT) drug delivery is a technique which involves the direct infusion of therapeutic molecules into the cerebrospinal fluid (CSF) filled space within the spinal canal. IT delivery is advantageous because the drugs bypass the blood brain barrier, which serves to limit the access of different types of molecules and systemically administered drugs to the central nervous system (CNS). Furthermore, drugs experience a longer half-life within the CSF since they encounter minimal protein binding and are not exposed to the same enzymatic activities which systemically administered drugs face within the blood (218). Current implications for IT drug delivery include leptomeningeal metastases (154–156), spasticity (157), pain management (158), and spinal anesthesia (159,160). For example, clinical studies on pain management show that IT delivery provides ideal pain control with fewer side effects, while using only a small fraction of the dose required when the drug is administered orally or intravenously (164,219). The IT delivery of neurotrophic factors has also been deemed a promising treatment for neurodegenerative diseases such as amyotrophic lateral sclerosis (ALS), Huntington's disease, and Parkinson's disease (161,162,220). Upon IT drug administration, the drugs are transported within the spinal canal mainly by the pulsatile motion of the CSF, but also by molecular diffusion (162,183).

For many CNS diseases like leptomeningeal metastases, the effected tissue is located in specific regions of the spinal canal; therefore, a method to target these regions is warranted. In chapter 6, we proposed the method of intrathecal magnetic drug targeting (IT-MDT) in order to concentrate high doses of drug functionalized magnetic nanoparticles (MNPs) at desired locations within the spinal canal (31). The basic idea behind IT-MDT is to guide intrathecally injected, drug-functionalized MNPs using an external magnetic field to diseased regions within the spinal canal. IT-MDT offers advantages over standard IT drug delivery protocols by providing a way to achieve a localized therapeutic effect using much smaller drug doses and substantially reducing systemic toxicity. Our previous results, found in section 6.4, indicated that external magnetic fields can capture the intrathecally delivered nanoparticles within a targeted region of the spinal canal despite the convective transport and enhanced mixing effects caused by the pulsatile motion of the CSF and the presence of the spinal nerve roots and trabeculae. Large collection efficiencies of MNPs were achieved using our method of IT-MDT with concentration levels nearly nine times that of control experiments when no magnetic field was present (31).

In chapter 6, we used rare earth permanent magnets placed within the epidural space of our *in vitro* human spine model during IT-MDT experiments. However, for situations in which the *in vivo* implantation of a permanent magnet within the epidural space is not practical, a different method of IT-MDT is nessecary. One way to magnetically target intrathecally-injected MNPs would be by placing a magnet non-invasively on the surface of a patient's back. This would require the use of a rather large and powerful magnet in order for the magnetic field to penetrate deep enough through the tissue and into the spinal canal, since the magnetic field strength drops off as the cube of the distance

from its source. Due to the magnetic field strength decreasing strongly with distance, the resulting magnetic field within the spinal canal at a physiological distance of 4 cm away from surface of the patient's skin would be a more homogeneous and low gradient field. We know from the equation for magnetic force on a single ferromagnetic particle that a spatially varying magnetic field $\left(\partial\vec{H}/\partial\vec{x} \neq 0\right)$ is required to create magnetic forces, as shown in the first relation of Eq. (44). The second relation of Eq. (44) results from performing the chain rule on the first relation, and states that the magnetic force on a particle is along the gradient of the magnetic field intensity squared $\left(\nabla\left\|\vec{H}\right\|^2\right)$.

$$\begin{aligned}\vec{F}_M &= \frac{4\pi a^3}{3}\cdot\frac{\mu_0\chi}{1+\chi/3}\left(\frac{\partial\vec{H}}{\partial\vec{x}}\right)^T\vec{H} \\ &= \frac{2\pi a^3}{3}\cdot\frac{\mu_0\chi}{1+\chi/3}\nabla\left\|\vec{H}\right\|^2\end{aligned} \tag{44}$$

Here $\vec{H}$ is the magnetic field intensity [A/m], χ is the magnetic susceptibility [unitless], $\mu_0 = 4\pi\times10^{-7}$ [N/A^2] is the permeability of vacuum, and a is the radius of the particle [m]. From Eq. (44) it is evident that a high gradient magnetic field is desirable for IT-MDT and that by simply placing a larger magnet on the surface of a patient's back may not be the best method for achieving the highest possible magnetic nanoparticle collection efficiency within the targeted treatment region.

In order to create a high gradient magnetic field within the target region of the spinal canal, we used a magnetically susceptible implant. Numerous studies of implant-assisted magnetic drug targeting have been performed and show great promise for use within tissue vasculature (173,195,221–225). The ferromagnetic implant is magnetized upon exposure to the long range, low gradient magnetic field, which results in the creation

of a localized high gradient magnetic field around the implant. In this chapter we build upon our previous IT-MDT research, which was presented in chapter 6, by using different implants placed within the subarachnoid space of our *in vitro* human spine model to create a high gradient magnetic field to enhance nanoparticle collection efficiency when a magnet is placed at a physiological distance away from the spinal canal on top of the epidermis. To our knowledge, this is the first study of its kind for subarachnoid implant-assisted intrathecal magnetic drug targeting (IA-IT-MDT).

This chapter is organized as follows. We begin by briefly presenting the synthesis of our gold-coated magnetite nanoparticles, as well as the description of our *in vitro* human spine model and experimental setup. We close the materials and methods section with a description of our experimental procedure used to determine the MNP collection efficiency. We then present the results from our IA-IT-MDT experiments which were performed to determine the MNP collection efficiency within each spinal zone. The chapter closes with a discussion of our experimental results and the conclusions section.

7.3. **Material and Methods**

In all of our experiments, we used different designs of ferromagnetic implants and an externally placed magnet to create a high gradient magnetic field to successfully target superparamagnetic gold-coated magnetite nanoparticles at a specific location within an *in vitro* model of the human spine. The main aim of these experiments was to study the effect of a magnetically susceptible implant within the subarachnoid space of our spine model on the collection efficiency of intrathecally-injected MNPs, and to determine if this method of IA-IT-MDT would be useful for potential future clinical trials. In this section, we

explain (i) the materials and methods used for nanoparticle synthesis, (ii) our *in vitro* human spine model and ferromagnetic implants, and (iii) our experimental procedure to determine MNP collection efficiency.

7.3.1. **Synthesis of gold-coated magnetite nanoparticles (Fe_3O_4@Au MNPs)**

The nanoparticle synthesis technique used was identical to the one used in chapter 6, section 6.3.1 (31); however, a more detailed explanation will be given here as well. Magnetite (Fe_3O_4) nanoparticle cores were synthesized by a coprecipitation technique using ferrous and ferric salts (175). This resulted in superparamagnetic magnetite cores of 8-12 nm in diameter. The magnetite cores were then coated with a gold layer of thickness varying between 8-15 nm by a surface adsorption technique using hydrogen tetrachloroaurate(III) hydrate and D(+)-glucose. The overall hydrodynamic diameter of the gold-coated magnetite nanoparticles was found to be between 20-25 nm, as determined by transmission electron microscopy (TEM) and shown in Figure 39A. These particles were suspended in a TX-100 surfactant solution to introduce micelles in order to increase their stability in solution and help prevent agglomeration.

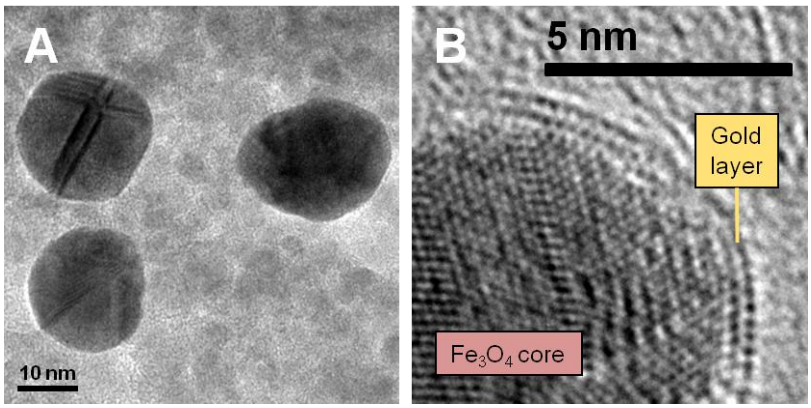

Figure 39. (A) TEM image of nanoparticles showing hydrodynamic diameter to be between 20-25 nm; (B) TEM image showing a partially gold-coated Fe_3O_4 core which confirms the core diameter to be around 8-12 nm.

It was important for the magnetite cores to be within the 8-12 nm diameter range (Figure 39B) in order to possess *superparamagnetic* properties, which means they only exhibit a net magnetization when in the presence of an external magnetic field. Superconducting quantum interference device (SQUID) magnetometry helped confirm the superparamagnetic properties of our nanoparticles which exhibited saturation magnetization (M_s) = 29.5 emu/g, remnant magnetization (M_r) = 0.52 emu/g, and coercivity (H_c) = 21.1 Oe at 265 K. Due to the nanoparticles exhibiting superparamagnetism, which helped prevent self agglomeration, they are able to transport freely throughout the spine model until they are in the presence of the high gradient magnetic field created by the ferromagnetic implant within the externally applied magnetic field. This high gradient magnetic field then acts to trap the nanoparticles at that defined location. Once the applied magnetic field is removed, these superparamagnetic nanoparticles lose their previously induced magnetization and are re-dispersed in the fluid. The enhanced mixing effects caused by the pulsatile motion of CSF within the spinal canal, as well as the presence of nerve roots and trabeculae, help re-disperse the nanoparticles and break up particle agglomerates which may be caused by different forces such as electrostatic interactions and Van der Waals forces (226–230). The gold coating prevents oxidation of the magnetite core into maghemite by forming an inert biocompatible protective layer, and serves as an excellent platform for drug conjugation to the nanoparticle surface due to gold's natural affinity for thiol bonds (176). TEM, energy-dispersive x-ray spectroscopy (EDS), and SQUID magnetometry confirmed the size, composition, and superparamagnetic properties of our gold-coated magnetite nanoparticles (31). A description of our modified synthesis technique follows next.

7.3.1.1. ***Preparation of the iron stock solution***

6.173 g of ferric ammonium sulfate (Acros Organics, NJ, USA) and 2.51 g of ferrous ammonium sulfate (Acros Organics, NJ, USA) were dissolved in 100 ml of 0.40 M aqueous sulfuric acid solution (Fisher Scientific, NJ, USA) to make the iron stock solution in which the molar concentrations of the two iron salts were 0.128 M and 0.064 M respectively (31).

7.3.1.2. ***Synthesis of the Fe_3O_4 nanoparticles***

1.5 ml of 1 M TX-100 solution (Fisher Scientific, NJ, USA) was added to 250 ml of 1 M NaOH solution (Sigma Aldrich, MO, USA), which was then heated to 75 ˚C in a water bath. 25 ml of the iron stock solution was slowly added dropwise to this solution along with vigorous non-magnetic stirring. After the stock solution had been completely added, the stirring continued for another 20 minutes. The temperature was maintained at 75 ˚C during this entire procedure. The resulting black Fe_3O_4 nanoparticle cores were allowed to settle before centrifugation at 5000 rpm to remove the supernatant. After centrifugation the particles were washed multiple times with nanopure water (Barnstead NANOpure Water Purification System; Thermo Scientific, IL, USA) to remove any excess surfactant. These nanoparticles were then suspended in nanopure water (31).

7.3.1.3. ***Coating the Fe_3O_4 nanoparticles with gold (Au)***

A solution containing the above prepared Fe_3O_4 nanoparticles and hydrogen tetrachloroaurate(III) hydrate (Alfa Aesar, MA, USA) was taken in a 1:1 molar ratio. 0.5 g of D(+)-glucose (Acros Organics, NJ, USA) was then added to the solution before sonication for 15 minutes. This solution was then heated in the water bath for 1 hour while stirring slowly. During this process the nanoparticle solution turned wine-red color due to the nanoparticles gradually being coated with gold. The solution was then centrifuged and

washed several times with nanopure water before ultimately being suspended in nanopure water to obtain a required concentration of the gold-coated magnetite nanoparticle solution (31).

7.3.2. *In vitro* human spine model & experimental setup

It was important that the *in vitro* human spine model possess physiologically and anatomically consistent dimensions in order to conserve the main hydrodynamic properties of CSF and drug transport as observed clinically during intrathecal drug delivery. The essential components of our model include the spinal canal (polystyrene tube 49.0 cm length and 1.52 cm inner diameter) (177–179), spinal cord (wood cylinder 45.0 cm length and 0.79 cm diameter) (178–181), nerve roots (rubber pieces 2 mm in diameter) (182), filum terminale (latex deformable membrane), and the ability of the CSF to pulsate. The proximal end of the model was connected to a modified masterflex peristaltic pump (Cole-Parmer, IL, USA) set at 72 beats per minute, which is within the 60-80 bpm range of humans' normal resting heart rate, to create a ramping pulse function. This pulsatile flow rapidly transports the injected nanoparticles from the lumbar region towards the cervical region of our model. Nerve roots were included in the model to enhance the mixing effects of the infusate and artificial CSF. The inclusion of pulsatile fluid motion and spinal nerve roots in our model was important because of the large effects these two parameters have on CSF fluid mechanics as seen *in vivo* (55,183–185,192–194).

The targeting magnet was placed at a physiological distance of 4 cm away from the spinal canal in order to mimic the distance between the intrathecal space and the surface of a patient's back. The targeting zone was designed to accommodate the large targeting magnet's magnetic field so that the majority of nanoparticle localization remained within

this zone. Different ferromagnetic implant designs were placed within the subarachnoid space of the spine model to create a locally high gradient magnetic field within the targeting zone. Figure 40, shows a schematic of the *in vitro* human spine model used for the IA-IT-MDT experiments when a spiral implant was used.

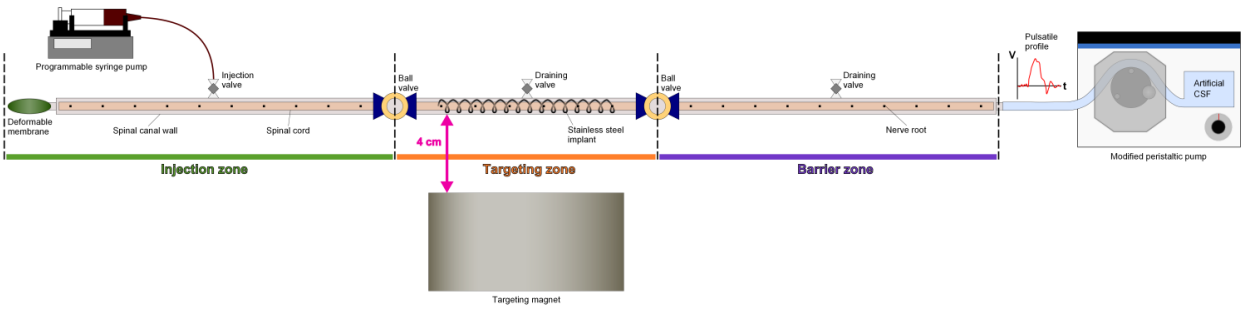

Figure 40. Schematic of entire experimental setup with the *in vitro* human spine model which clearly shows the three different zones (injection, targeting, and barrier zones), as well as the magnetically susceptible implant (spiral) and the targeting magnet placed at a 4 cm physiological distance away from the spinal canal.

The targeting magnet was a 1045 lb pull force, 0.528 T surface field strength neodymium-iron-boron grade N52 magnet (product No. DZX0Y0-N52, K&J Magnetics, Jamison, PA). Two different implant designs, both of which had the same composition and weight, were tested. The first implant (spiral) was made of 812.8 µm diameter Type 430 stainless steel wire (product No. 89065K61, McMaster-Carr, Elmhurst, IL) coiled 15 times around the spinal canal and suspended within the subarachnoid space of the targeting zone in our *in vitro* human spine model. The second implant (mesh) was made of 457.2 µm diameter Type 430 stainless steel wire configured into a mesh with square openings and 51% open area (product No. 9481T15, McMaster-Carr, Elmhurst, IL). The mesh implant was formed into a 120° arc and inserted into the subarachnoid space of spine model. Figure 41 shows 3D wireframe images of both the spiral (Figure 41A) and mesh (Figure 41B) implants.

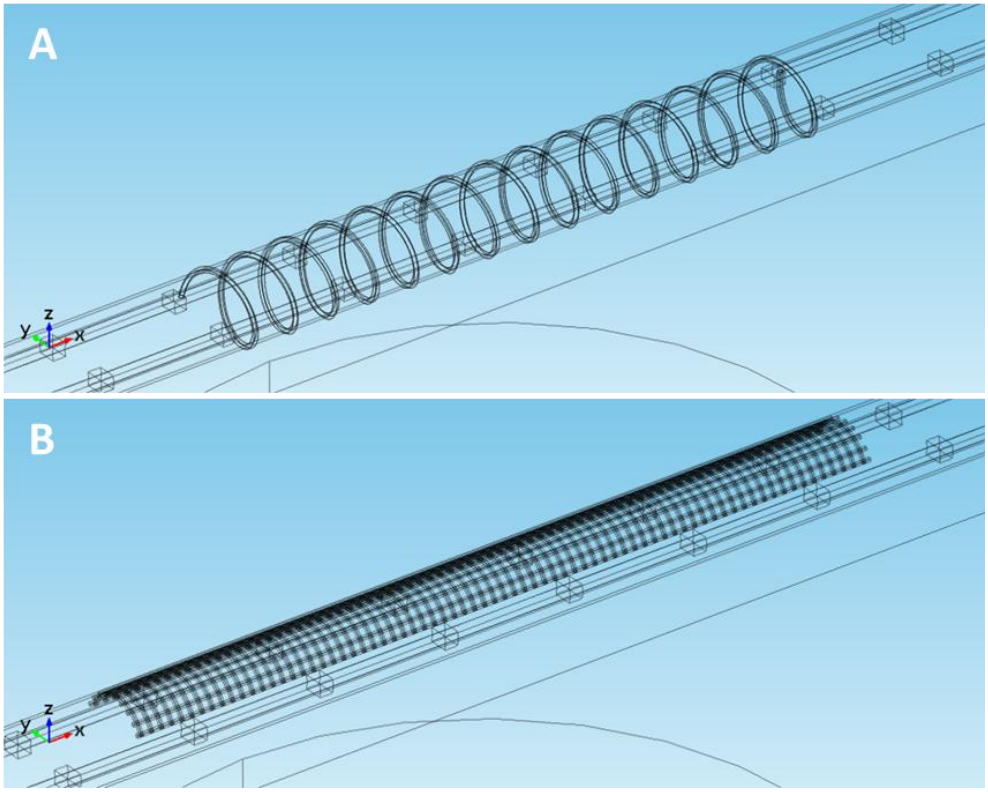

Figure 41. 3D wireframe images built in COMSOL 4.3a of both the (**A**) spiral and (**B**) mesh implants inside the subarachnoid space of the *in vitro* human spine model which were used in our experiments.

7.3.3. **Experimental procedure to determine MNP collection efficiency**

A programmable syringe pump (model #NE-1800; New Era Pump Systems, NY, USA) was used to inject 1 ml of the 0.017 g/ml Fe_3O_4@Au nanoparticle solution into the *in vitro* human spine model in the lumbar region over a 1 minute period. Nanoparticles were targeted to a specific site in the spine model over a 15 minute period by using a high gradient magnetic field produced by a ferromagnetic implant within the subarachnoid space of the targeting zone and an external magnetic field (targeting magnet) placed at a 4 cm physiological distance below the spinal canal model and implant. The 15 minute MNP targeting and settlement time was chosen based off of our previous experiments in which no significant difference was found between MNP collection efficiencies at 15 and

60 minutes (31). Ball valves were used to separate the spine model, and its contained fluid, into three different zones: injection, targeting, and barrier zones. To determine the mass fraction of nanoparticles retained by the high gradient magnetic field within the target region and the remaining nanoparticles in the other two zones, the ball valves were closed and the fluid contained within each zone was eluted through individual draining valves. Each compartment was then rinsed separately and magnetically decanted in order to remove any residual nanoparticles. The solutions collected from each compartment were placed in a convection oven in small borosilicate glass containers and heated for 1 hour (175 °C) until they were completely dry in order to determine the dry weight of these fractions. The fraction of nanoparticles collected within each zone was used to determine the overall collection efficiency of each experiment trial (31). Statistical analysis of the resultant nanoparticle collection efficiencies was performed and the means were compared using a Student's *t*-test. A two-tailed *p*-value <0.05 was considered statistically significant.

7.4. **Results**

7.4.1. **Computer-aided design of a high gradient magnetic field**

In order to optimize implant design and study the magnetic fields used in our *in vitro* experiments, simulations were performed in COMSOL Multiphysics v4.3a (31). These simulations used the same model parameters as present in our *in vitro* human spine model and experimental setup. Different 3D implants were designed and tested in COMSOL. An important parameter in these simulations was the relative magnetic permeability of Type 430 stainless steel. We used a relative permeability value of 1000, which was based off of previous literature values (231–234). The implants' large relative magnetic

permeability allowed for a high degree of magnetization when in the presence of an external magnetic field. Figure 42 shows a comparision of the magnetic fields used in our experiments when the 1045 lb pull force strength magnet was placed at a physiological distance of 4 cm away from the spinal canal (Figure 42B) and when one of two different ferromagnetic implants was present within the subarachnoid space (spiral implant, Figure 42C; mesh implant, Figure 42D). Figure 42A shows a physical representation of the 4 cm physiological distance between the spinal canal and the epidermis using a human MRI.

In the absence of a ferromagnetic implant, the magnetic field within the targeting region is a rather homogeneous and low gradient field. As shown in Figure 42B, the magnetic field within the spinal canal is within a 0.116-0.248 T range when no implant is present, and exhibits a magnetic field gradient ranging from 0.356-0.480 T/cm. Upon addition of a ferromagnetic implant, which concentrates the magnetic flux density ($\vec{B}$ field) within the spinal canal, the magnetic field within the subarachnoid space becomes a high gradient magnetic field with values ranging from 0.062-12.027 T for the spiral implant (Figure 42C) and 0.101-28.316 T for the mesh implant (Figure 42D). The magnetic field gradients varied from 6.129-26.346 T/cm for the spiral implant and from 25.676-150.222 T/cm for the mesh implant. A graph showing values of the generated high gradient magnetic fields as they vary along the length of the two different implants in the x direction is shown in Figure 43, as well as a close-up view of the fields generated around each implant.

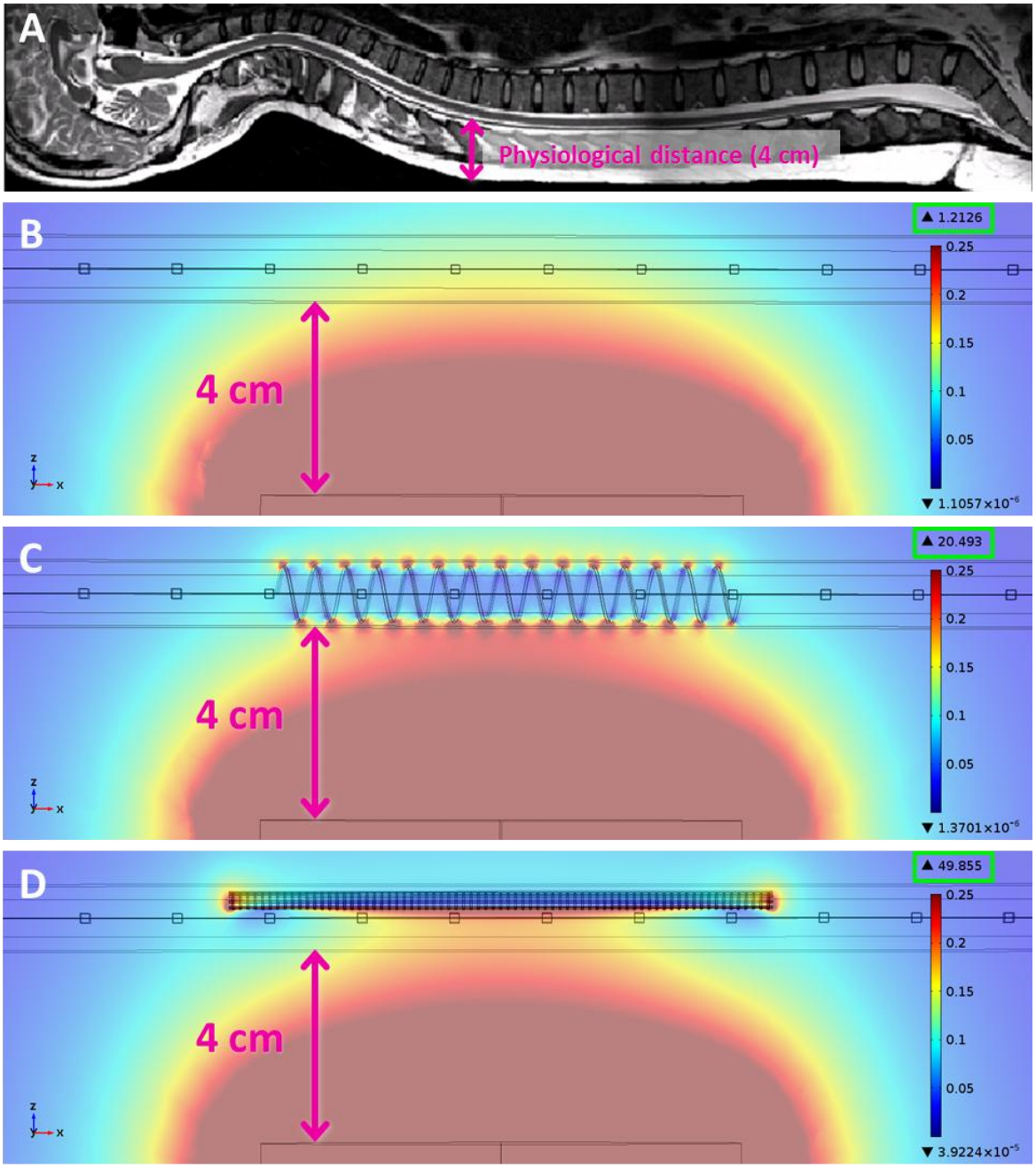

Figure 42. (**A**) Patient MRI showing the 4 cm physiological distance between intrathecal space and epidermis; (**B**) Simulated magnetic field produced by the 0.528 T surface field, 1045 lb pull force strength magnet placed at a 4 cm distance away from the spinal canal; magnetic field within the spinal canal is within a 0.116-0.248 T range (magnetic field gradient ranging from 0.356-0.480 T/cm); (**C**) Simulated field when a spiral implant was placed within subarachnoid space; high gradient magnetic field created inside the spinal canal with field values between 0.062-12.027 T (magnetic field gradient ranging from 6.129-26.346 T/cm); (**D**) Simulated field when a mesh implant was placed within subarachnoid space creating a high gradient magnetic field inside the spinal canal with field values between 0.101-28.316 T (magnetic field gradient ranging from 25.676-150.222 T/cm).

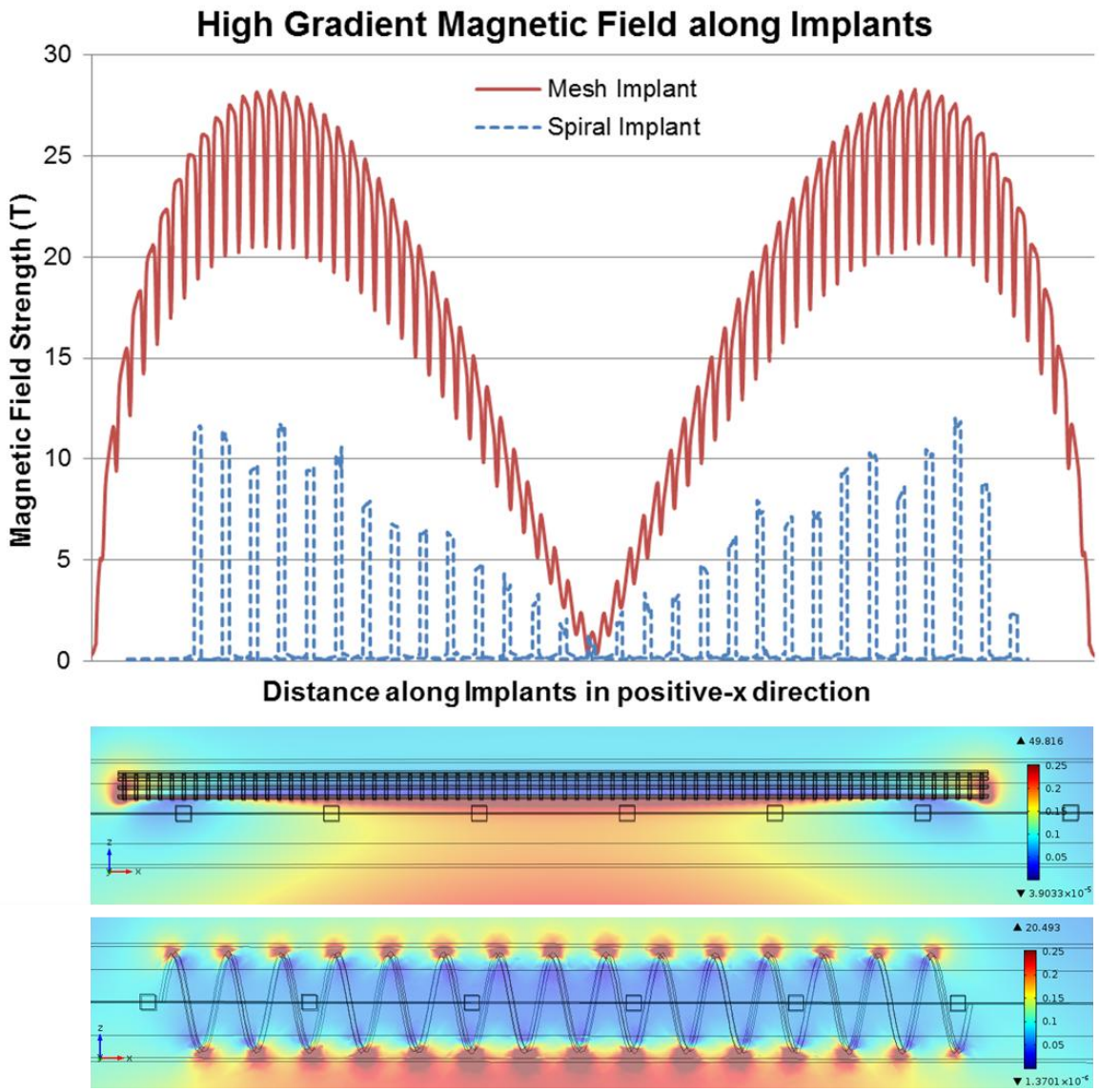

Figure 43. Graph showing the high gradient magnetic fields around both implants, which have field strengths varying from 0.101-28.316 T for the mesh implant and from 0.062-12.027 T for the spiral implant. Magnetic field gradients varied from 25.676-150.222 T/cm for the mesh implant and from 6.129-26.346 T/cm for the spiral implant. Figure inserts are zoomed-in views of the high gradient magnetic fields along the mesh (middle insert) and spiral (bottom insert) implants, as determined using COMSOL Multiphysics v4.3a, which were used in our IA-IT-MDT experiments.

7.4.2. *In vitro* IT-MDT experiments at a physiological distance: implant vs. no implant

To prove the hypothesis that including a ferromagnetic implant within the subarachnoid space would generate a high gradient magnetic field resulting in higher

nanoparticle collection efficiencies in the targeting zone, three different types of experiments were performed. The first set served as the control in which neither the targeting magnet nor the implant was present. The second set was the IT-MDT experiments where the 1045 lb pull force targeting magnet was placed at a 4 cm physiological separation, but without a ferromagnetic implant present. The third set was the implant-assisted IT-MDT experiments in which a ferromagnetic implant, either the spiral or mesh implant design, was introduced inside the subarachnoid space of our model and centered above the external magnet.

In the IT-MDT experiments with the targeting magnet, but no implant, an average nanoparticle collection efficiency of 47% was obtained within the targeting zone of the spine model, as shown in Figure 44. Compared to the 26% collection efficiency resulting from control experiments where no magnetic field was applied, these results are a 181% increase in MNP collection efficiency.

Upon addition of the spiral ferromagnetic implant within the subarachnoid space of the model, the MNP collection efficiency increased to 65%, as shown in Figure 44. Thus, the spiral implant-assisted IT-MDT experiments produced a 138% increase in MNP collection efficiency over the IT-MDT experiments in which no implant was present. These spiral IA-IT-MDT experiments were also a 250% increase over the control. Changing the implant design from a spiral to a mesh configuration, while maintaining the composition and weight, increased the collection efficiency even further. The mesh implant assisted IT-MDT experiments produced a 187% increase in MNP collection efficiency over the regular IT-MDT experiments, and a 135% increase in collection efficiency over the spiral

IA-IT-MDT experiments. These mesh IA-IT-MDT experiments amounted to a 338% increase over the control.

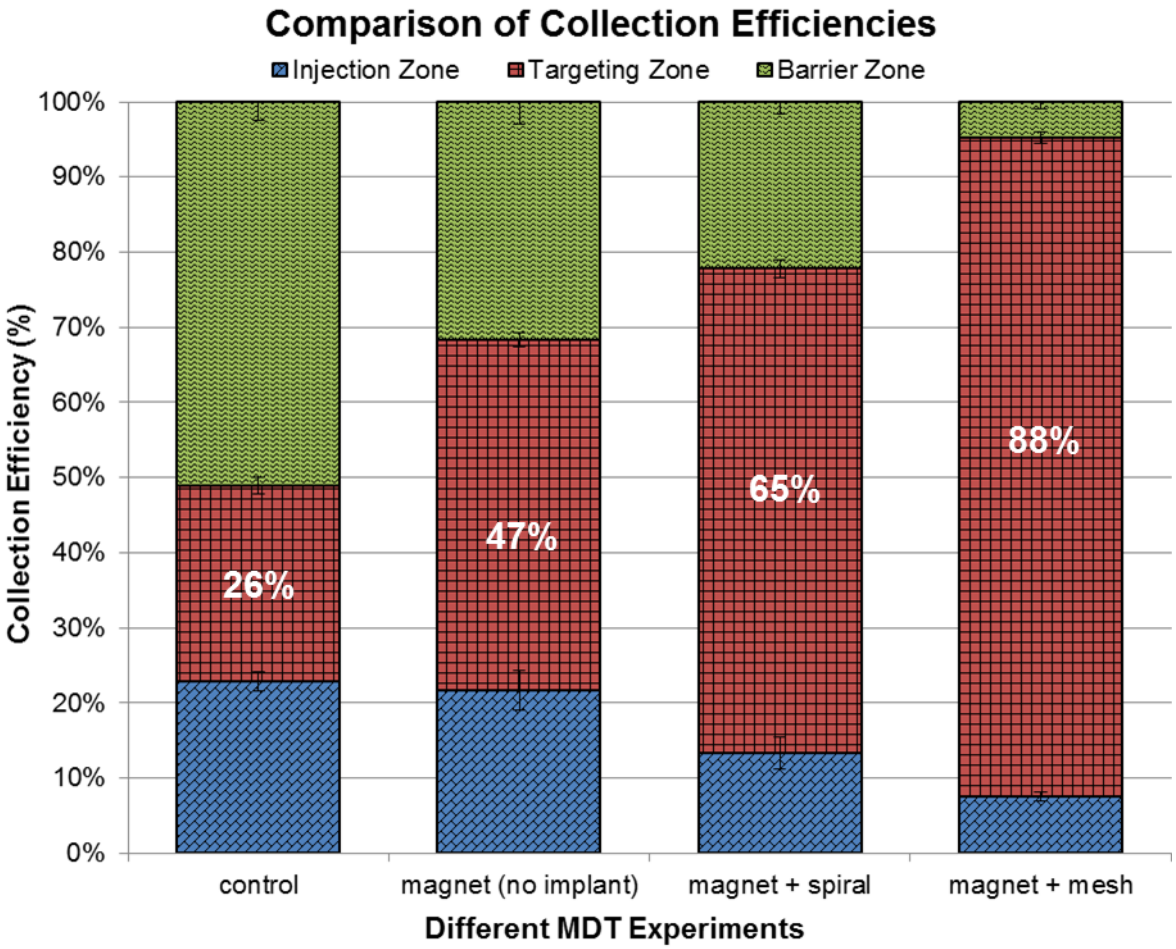

Figure 44. Graph showing a comparison of the nanoparticle collection efficiencies from three different types of experiments: (i) control, (ii) magnet at a physiological distance, and (iii) magnet at a physiological distance while ferromagnetic implant, either spiral or mesh, is within subarachnoid space. With mesh implant-assisted IT-MDT, the nanoparticle collection efficiency increased 3.4-fold when compared to the control experiments.

Statistical analysis revealed significant differences between the nanoparticle collection efficiencies obtained from each of the different sets of experiments; all *p*-values were much smaller than the 0.05 significance level, with the largest *p*-value of $4*10^{-6}$ being between the spiral IA-IT-MDT and mesh IA-IT-MDT experiments.

7.5. Discussion

We successfully targeted 47% and 88% of all injected nanoparticles using IT-MDT and implant-assisted IT-MDT, respectively, showing that these are both promising methods for highly concentrating magnetic nanoparticles within desired regions of the spinal canal. The IT-MDT experiments showed that successful targeting of MNPs can be achieved while maintaining a physiological separation between the spinal canal and the top of the epidermis. The IA-IT-MDT experiments showed that the MNP retention values achieved with IT-MDT could be increased even greater due to the presence of the ferromagnetic implant creating a high gradient magnetic field within the subarachnoid space of the spine model. Both the IT-MDT and IA-IT-MDT experiments resulted in significantly larger nanoparticle collection efficiencies within the targeting zone as compared to the control. IT-MDT resulted in a 1.8-fold increase in MNP collection efficiency over the control, while spiral IA-IT-MDT increased the collection efficiency 2.5-fold and mesh IA-IT-MDT increased it 3.4-fold.

The large difference in nanoparticle collection efficiency between the IA-IT-MDT and IT-MDT experiments, when comparing both to the control, shows the importance of a high gradient magnetic field in magnetic drug targeting applications. When treating patients with spinal diseases, it may be beneficial to have a ferromagnetic implant within the desired treatment area in order to greatly enhance the localization of drug-functionalized nanoparticles. Since these nanoparticles are capable of being conjugated to numerous drugs, they may be efficacious in developing new treatment methods with high drug targeting capabilities for many diseases effecting the central nervous system such as leptomeningeal metastases and spasticity. If the use of a

ferromagnetic implant is warranted, the implant would be coated with a thin layer of biocompatible silicone prior to implantation in order to reduce the possibility of implant corrosion and degradation from exposure to physiological conditions. Once the implant has been coated and made biocompatible, it can be placed either permanently or temporarily at the site of diseased tissue depending on the treatment application. For example, when treating chronic pain it may be beneficial to have the implant placed permanently inside the spinal canal in order to provide the capability of administering therapeutic magnetic nanoparticles whenever necessary.

In our implant-assisted IT-MDT experiments we tested two different implant designs, a spiral and a mesh. With the spiral implant, it was thought that by encircling the spinal cord large concentrations of nanoparticles would be retained and more evenly distributed within the targeting region. Even though these spiral IA-IT-MDT experiments resulted in MNP collection efficiencies 2.5-fold larger than that of the control, due to the rigidity of ferritic stainless steel this design may be difficult to implant *in vivo*. Therefore, with the help of computer simulations, we designed the more feasible mesh implant while maintaining the same composition and weight as the first spiral implant. *In vivo* implantation of the mesh implant would involve the surgeon opening the dura mater and inserting the mesh inside the subarachnoid space so as not to obstruct the spinal nerve roots lateral to the midline of the spinal cord. Simulations of both implant designs showed high gradient magnetic fields within the subarachnoid space around each implant, as shown previously in Figure 43. The high gradient magnetic field varied from 25.676-150.222 T/cm for the mesh implant and from 6.129-26.346 T/cm for the spiral implant; therefore, it was expected that the mesh implant-assisted IT-MDT experiments

would result in higher MNP collection efficiencies. The mesh IA-IT-MDT experiments confirmed an even larger nanoparticle collection efficiency at an increase of 3.4-fold over the control.

Both implants were constructed out of Type 430 stainless steel wires with the same relative magnetic permeability values, which for our simulations a value of 1000 was used (231–234). However, the two different implants had differing diameter wires (812.8 μm for the spiral implant and 457.2 μm for the mesh implant). It has been shown that smaller wires generate larger magnetic field gradients in their vicinity when exposed to an external magnetic field (235). This results because the magnetic flux is now confined within a smaller area, which equates to a reduction in the dimensions of the area of magnetic field non-uniformity.

Standard intrathecal drug delivery methods rely mainly on empirical observations. The use of current IT guidelines cannot guarantee reproducible outcomes or desired therapeutic concentrations in specific target regions of the spinal canal (162,236). Due to variability in patients' spinal anatomy, as well as the frequency and magnitude of their CSF pulsations, maintaining a therapeutic dose within the targeted region while attempting to avoid systemic toxicity is a major challenge and disadvantage of standard IT delivery methods (183). Current IT protocols require continuous drug infusion in order to maintain a sufficiently high drug concentration at the target site despite drug distribution throughout the entire central nervous system leading to harmful side effects. IT-MDT and IA-IT-MDT are methods to achieve localized, high concentrations of magnetic nanocarriers. Both IT-MDT and IA-IT-MDT offer the potential to greatly diminish systemic toxicity while using much smaller drug doses as compared to standard IT drug delivery methods.

There are limitations to our procedure, as well as areas of future research. First and foremost, both IT-MDT and IA-IT-MDT need to be further established *in vivo* using animal models. Histological and pharmacokinetic studies will need to be performed in order to determine cellular uptake of drug-functionalized nanocarriers. Different implant designs need to be researched and developed, and the long-term stability of *in vivo* spinal implants should be considered.

7.6. **Conclusions**

Our experiments provided a thorough study on the benefits of intrathecal magnetic drug targeting and implant-assisted intrathecal magnetic drug targeting. The importance of a high gradient magnetic field for magnetic drug targeting applications was also addressed, and *in vitro* experiments were performed which proved how high gradient magnetic fields result in larger nanoparticle collection efficiencies within the target region. The careful design and placement of ferromagnetic implants for magnetic drug targeting will enable physicians to exercise precise control over the distribution and concentration of drugs at any desired location within the spinal canal. Our promising *in vitro* experimental results are a step towards IT-MDT and IA-IT-MDT becoming novel treatment methods for diseases of the central nervous system. The results showed that both IT-MDT and IA-IT-MDT are capable of highly concentrating magnetic nanoparticles within the spinal canal, while IA-IT-MDT yielded the highest retention values. The current indications in which our novel IT-MDT and IA-IT-MDT techniques may prove beneficial in the future include chronic pain, cancers, anesthetic agents, spasticity, and other debilitating disorders of the central nervous system.

8. CONCLUSIONS AND FUTURE WORK

8.1. Summary

This dissertation focused on three aspects of drug delivery: pharmacokinetics, convection-enhanced delivery (CED), and intrathecal magnetic drug targeting (IT-MDT). As shown in Figure 45, these three areas fall under one of two categories, systemic delivery or localized delivery. A major achievement of this dissertation in the area of systemic delivery was the development of a first principles physiologically-based pharmacokinetic (PBPK) modeling framework. This PBPK modeling framework is capable of predicting drug biodistribution dynamics in all organs and tissues of an animal or human from dose-response curves in rats and offers better prediction and scaling capabilities than classical pharmacokinetic models. Major advancements were also made in localized delivery to the brain and central nervous system in convection-enhanced delivery and intrathecal magnetic drug targeting. The phenomena of backflow were studied experimentally and computationally in order to help elucidate the causes of backflow, and novel backflow-free catheters were designed and tested for use during CED. The methods of intrathecal magnetic drug targeting (IT-MDT) and implant-assisted intrathecal magnetic drug targeting (IA-IT-MDT) were developed and show promising results for potential use in treatment of diseases affecting the central nervous system.

The overall goal of this research was to improve upon existing treatment methods, as well as engineer new treatment methods for patients suffering from neurodegenerative diseases, brain cancer, spasticity, chronic pain, and many others. Much progress was made

in the area of drug delivery as a result of this dissertation. In this final chapter, the significance and contributions are outlined followed by a description of future work.

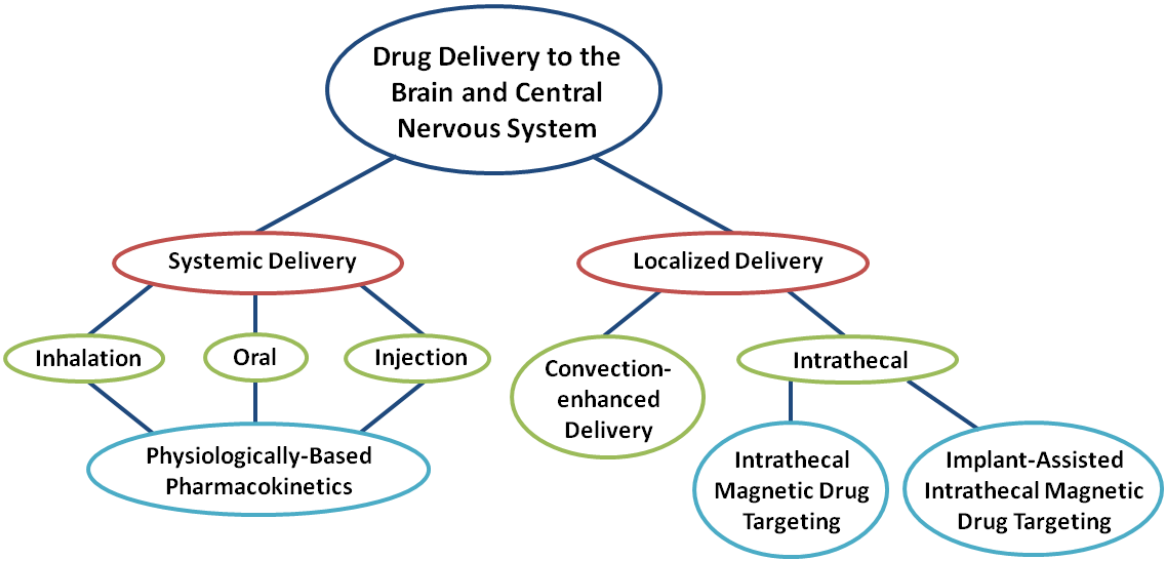

Figure 45. Diagram showing the areas of drug delivery to the brain and central nervous system in which this dissertation helped advance.

8.2. Contributions of This Dissertation

8.2.1. First principles physiologically-based pharmacokinetics modeling framework for use in systemic delivery

Mechanistic physiologically-based pharmacokinetics modeling framework. A whole body physiologically-based pharmacokinetics (PBPK) modeling framework was engineered which creates multiscale mathematical models for entire organisms composed of organs, tissues, and a detailed vasculature network to predict drug bioaccumulation and to rigorously determine kinetic parameters. Our PBPK modeling framework was developed in order to advance the prior black-box pharmacokinetic (PK) models by incorporating first principles, conservation of mass, species and momentum, and biochemical/biotransport mechanisms for the prediction of drug fate *in vivo*. Typical PK models merely fit parametric

functions with multiple adjustable constants or exponential coefficients to determine non-mechanistic parameters such as volume of distribution and area under the curve (*AUC*). These classical PK models derive little information about drug reaction kinetics and biotransport phenomena, and do not satisfy conservation laws. Consequently, these non-mechanistic PK models have limited fidelity for intra- and inter-species scaling.

For our mechanistic PBPK modeling framework, a rat blood circulation model was constructed and combined with biotransport, biochemical reactions, and metabolism of the immunosuppressant Cyclosporin. The proposed methodology was demonstrated on a case study in Sprague Dawley rats. A rigorous parameter estimation technique was used to derive the unknown rate parameters from actual drug dose–response experiments in animals. A mathematical programming technique was used for solving the transport and kinetic inversion problem. Key PK parameters were determined to establish drug biodistribution dynamics in all organs and tissues. Prediction of organ drug bioaccumulation as a function of cardiac output, physiology, pathology, or administration route is possible with the proposed PBPK framework. Another key outcome is that the bioaccumulation of Cyclosporin can be predicted for a wide of range of different doses with our mechanistic model, whose *parameters were estimated from a single dose experiment*. The high extrapolation fidelity demonstrates that our mechanistic PBPK model properly captured Cyclosporin pharmacokinetics with a single parameter set acquired from only one dose experiment. These results strongly suggest that our mechanistic algorithm can predict drug concentrations for a wide range of dosing regimes. Systematic individual therapy design using the proposed first principles modeling framework is also a possibility.

Our proposed mechanistic PBPK modeling framework is essential for quantitative planning of drug administration experiments, intra- and interspecies scaling, and individual therapy design. Mechanistic model approaches are expected to shorten drug development time and may ultimately lead to a rational design of individualized drug therapies.

Mechanistic intra- and inter-species scaling. Biochemical, anatomical, and physiological scaling laws were developed which yield more reliable intra- and inter-species extrapolation of drug biodistribution. Traditional interspecies scaling laws in pharmacokinetics often utilize simple polynomial relationships between properties of interest such as the intrinsic clearance. The allometric approach is empirical, and rests on the assumption that the underlying physiological processes such as cardiac output, heartbeat frequency, breath duration, are only related to body mass. Interspecies extrapolation with simple allometric scaling laws is not satisfactory because it does not account for fundamental biochemical mechanisms, but merely incorporates weight or size factors.

We demonstrated how our first principles mechanistic PBPK modeling framework in combination with novel physiological scaling laws yields more reliable intra- and inter-species extrapolation of drug biodistribution. We showed how experimental dose–response data in rats for immunosuppressant Cyclosporin are sufficient for predicting the biodistribution of this drug in pigs, monkeys, and humans. The predicted drug concentrations extrapolated by interspecies scaling laws match well with the experimental measurements. These promising results demonstrate that the whole-body PK modeling approach not only elucidates drug mechanisms from a biochemical standpoint, but offers

better scaling precision. Better models can substantially accelerate the introduction of drug leads to clinical trials and eventually to the market by offering more understanding of the drug mechanisms, aiding in therapy design, and serving as an accurate dosing tool.

8.2.2. **Localized delivery via convection-enhanced delivery**

Causes of backflow phenomena. We studied the transport processes which occur during drug delivery into porous media such as brain phantom gels experimentally and computationally in order to help elucidate the causes of backflow. We found that fluid injections into porous media have considerable effects on local transport properties such as porosity and hydraulic conductivity. These phenomena not only alter the bulk flow velocity distribution of the microfluid flow due to the changing porosity, but significantly modify flow direction and even volumetric flow distribution due to induced local hydraulic conductivity anisotropy.

Novel backflow-free catheters. Based on our consideration of the physical mechanisms involved in the interaction between fluid flow and porous media, we developed novel backflow-free catheters for use during convection-enhanced intraparenchymal drug delivery. Specifically, we developed two types of backflow-free catheters: channel-inducing and dual-action. The channel-inducing catheter exploits the idea of a large outlet area/volumetric flow rate ratio in order to decrease the stress felt by the porous media into which drug is infused by using an internal wire to create a cylindrical, void channel within the porous media. This resulted in a significant pressure gradient reduction around the catheter tip, and eliminated backflow occurrence. Our simulations showed that during

infusions at the same volumetric flow rate, the novel catheter will create approximately ten times lower stress on the tissue than an ordinary single-port catheter.

The dual-action catheter designs (coaxial and series) apply suction along the catheter shaft in order to reduce the permeability and matrix porosity by decreasing its fluid content. The reduced porosity and permeability along the shaft in the vicinity of the suction port prevents backflow by locally closing new flow paths along the catheter shaft without interfering with the infusion.

The channel-inducing and dual-action catheters were successfully tested without the occurrence of backflow at high volumetric flow rates up to 10 µl/min. They also produced large volumetric distributions at the target region. This is a vast improvement upon the single-port catheter which requires low volumetric flow rate infusions (<0.5 µl/min) and a reduction in catheter diameter (32 gauge) in order to just minimize the chance of backflow occurrence. Backflow is a considerable challenge to overcome in order for convection-enhanced delivery to become a more viable treatment option clinically. The engineering of a backflow-free catheter will provide a means of allowing the therapeutics to reach an increased concentration at the site of delivery and a more predictable distribution that is critical for patient care. Through implementation of our three backflow-free catheter designs, physicians will be able to target specific regions of the brain with improved accuracy, increased drug concentration, and larger drug distribution geometries.

Sphericity. Our proposed model of the sphericity provides a distinct measure from volume of distribution that can aid in the verification and comparison of distribution geometries across multiple infusions.

8.2.3. **Localized delivery via intrathecal magnetic drug targeting**

Intrathecal magnetic drug targeting. Building off of the concepts from magnetic drug targeting, we developed the method of intrathecal magnetic drug targeting (IT-MDT) in order to maximize the therapeutic effect of intrathecally injected drugs without excessive risk of toxicity in non-targeted regions of the spinal canal. Superparamagnetic *gold-coated magnetite nanoparticles* were synthesized and used in *in vitro* experiments. A physiologically and anatomically consistent *in vitro human spine model* was engineered. Simulations were performed to study the magnetic fields produced by different permanent magnets and to design appropriate fields with these magnets for use in our experiments. Experiments to determine magnetic nanoparticle collection efficiency as a function of magnetic field strength, duration of magnetic field exposure, and distance between the target location and injection site were conducted on the *in vitro* human spine model.

Our experiments provided a thorough study on the feasibility and benefits of intrathecal magnetic drug targeting. The careful design and placement of magnetic fields for targeted delivery at a specific site, as well as the development of advanced nanoparticle drug-functionalization techniques, will enable physicians to exercise precise control over the distribution, concentration, and release of drugs at any desired location within the spinal canal. We provided *in vitro* experimental results which show great potential for IT-MDT to be used as a novel treatment method for diseases of the central nervous system upon completion of *in vivo* animal studies. Our experimental results showed that external magnetic fields can be used to guide and localize intrathecally-injected magnetic nanoparticles at desired locations within the spinal canal with large collection efficiencies and at concentration levels nearly nine-times that of control experiments when no

magnetic field was present. The results also indicated that external magnetic fields can capture intrathecally-delivered nanoparticles within any targeted region of the spinal canal despite the convective transport and mixing effects caused by the pulsatile motion of CSF and the presence of spinal nerve roots and trabeculae. The current indications in which our novel IT-MDT technique may prove beneficial in the future include chronic pain, cancers, anesthetic agents, spasticity, and other debilitating disorders of the central nervous system.

Implant-assisted intrathecal magnetic drug targeting. Using our knowledge of how a spatially varying magnetic field is required to create magnetic forces on magnetic nanoparticles (MNPs), we developed the method of implant-assisted intrathecal magnetic drug targeting (IA-IT-MDT) to generate high gradient magnetic fields within the target region and achieve the highest possible MNP collection efficiency. Ferritic stainless steel implants were incorporated within the subarachnoid space of our *in vitro* human spine model, and the targeting magnet was placed at a physiological distance away from the model and implant to mimic the distance between the epidermis and spinal canal. Computer simulations were performed to optimize implant design for generating high gradient magnetic fields and to study how these fields may aid in therapeutic nanoparticle localization. Experiments aiming to determine the effects of different magnetically-susceptible implants placed within an external magnetic field on the targeting efficiency of gold-coated magnetite nanoparticles were then performed on our *in vitro* human spine model. The computer simulations and *in vitro* experiments showed that our mesh implant design was superior to our spiral implant design; however, both designs achieved a much larger MNP collection efficiency compared to regular IT-MDT and control experiments. The mesh design IA-IT-MDT experiments resulted in a 3.4-fold increase in nanoparticle

collection efficiency when compared to the control when no magnet or implant was present. Our results indicate that IA-IT-MDT is an excellent supplementary technique to further enhance the targeting capabilities of our previously established method of IT-MDT by generating high gradient magnetic fields within the target region.

The careful design and placement of ferromagnetic implants for magnetic drug targeting will enable physicians to exercise precise control over the distribution and concentration of drugs at any desired location within the spinal canal. Our promising *in vitro* experimental results are a step towards IT-MDT and IA-IT-MDT becoming novel treatment methods for diseases of the central nervous system. The results showed that both IT-MDT and IA-IT-MDT are capable of highly concentrating magnetic nanoparticles within the spinal canal, while IA-IT-MDT yielded the highest retention values.

8.3. **Future Work**

8.3.1. **First principles physiologically-based pharmacokinetics modeling framework**

Inclusion of gastrointestinal tract metabolism in our mechanistic PBPK model. One limitation of our mechanistic PBPK model, but not the mathematical principles of scaling, is the lack of a detailed account of the gastrointestinal (GI) tract with bile excretion and resorption. This might be important for more accurate mass balance in specific organs. However, the accuracy of our mechanistic PBPK model with regard to time concentration trajectories even without taking bile into account is sufficient as compared to state-of-the-art research articles. The high extrapolation fidelity demonstrates that our mechanistic PBPK model properly captured Cyclosporin pharmacokinetics with a single parameter set acquired from only one dose experiment, and that our mechanistic algorithm can predict

drug concentrations for a wide range of dosing regimes. Although the metabolic reactions of Cyclosporin attributed to the presence of cytochrome P450 3A in the GI tract have been reported previously (62,63,92,93), we chose not to include this metabolic pathway since the overall effect of cytochrome P450 3A enzymes in the GI tract metabolism has been determined to be less than 1% of the total systemic clearance in rats (62,63,92,93). Incorporation of GI tract metabolism into our mechanistic PBPK modeling framework is reserved for future work.

Global optimization techniques. We recognize the limitations of the Trust Region Method used in our mechanistic PBPK modeling framework, which guarantees to converge to a local optimum of the error surface. However, given an initial guess, the algorithm converges reliably to the nearest minimum. Kinetic inversion problems often exhibit solution multiplicity; therefore, the use of global optimization techniques such as the Global Terrain Method (104) may be necessary to locate all local minima and determine a global optimum. The global optimum, especially when the match is not much different from other local minima, is not necessarily the only choice and is not guaranteed to be physically better than other local minima. All identified local optima are candidate final solutions and are valid in the anatomical, physical, and pharmacokinetic setup. The ultimate choice should incorporate biochemical considerations and kinetic parameters which have physical meaning. If the underlying pharmacokinetics of the drug changes from animal to animal, or from animal to humans, the local optimum solution might be invalid in terms of pharmacokinetic constraints, at which time a different local optimum would be considered. The use of global optimization techniques in our PBPK modeling framework needs to be researched further.

Methods to improve prediction accuracy of our PBPK modeling framework. In order to improve the prediction accuracy of our mechanistic PBPK modeling framework, we propose to utilize HPLC analytical methods for all drug measurements, to determine the fraction of adipose tissue in a subject, and if possible, other organs in the targeted patient model. Further options include *in vitro* determination of drug binding to erythrocytes, lipoproteins, and tissue cells in both species, or complementary measurements of drug concentration in targeted organ, such as in liver biopsy. These complementary measurements may then be used in all future models since our modeling framework allows for their inclusion. Measurement of *in vivo* parameters, such as metabolic rates as a function of genus, can also improve the prediction accuracy of our PBPK model. Metabolic flux analysis can provide additional improvements for the biochemical reaction models, and should be considered in future work.

8.3.2. **Backflow-free catheters for localized convection-enhanced delivery**

Validation of backflow-free catheters in animal models. Our backflow-free catheters were tested in homogenous brain phantom gels; therefore, it is necessary to validate these in animal models and eventually humans. Since living brain tissue provides unique challenges due to the anatomy of brain parenchyma and the ventricular system, we recommend co-infusion of tracers, such as gadolinium-DTPA, and therapeutics be employed in order to better predict infusate transport. Such methods have been shown to be a safe way to estimate drug distribution *in vivo* during CED (148). Through better planning and more predictable patterns of delivery, the engineering obstacles will be decreased and there can be more emphasis on the therapeutic formulation.

8.3.3. **Intrathecal magnetic drug targeting**

In vivo intrathecal magnetic drug targeting. Both IT-MDT and implant-assisted IT-MDT need to be further established *in vivo* using animal models. Our lab has recently been successful at conjugating our gold-coated magnetite nanoparticles with the anti-cancer chemotherapy drug doxorubicin. Also, the influence of magnetic fields on increased uptake of doxorubicin conjugated MNPs on tumor cell cultures has been shown using MTT assays and flow cytometry. Creating a spinal cord tumor model, and performing treatment using doxorubicin-conjugated magnetic nanoparticle during IT-MDT in this tumor model is the subject of future work.

8.3.4. **Treatment protocol for brain cancer using pharmacokinetics, convection-enhanced delivery, and intrathecal magnetic drug targeting**

Aspects from all three of the major areas of this dissertation may be incorporated into a single treatment protocol in order to treat brain cancer or other neurodegenerative disorders. The following paragraph proposes a potential treatment strategy for a primary brain tumor within the putamen using CED, IT-MDT, and pharmacokinetics.

After detection of the brain tumor within the putamen by imaging techniques such as MRI, resection of the tumor would occur. Injection of gold-coated magnetite nanoparticles functionalized with the chemotherapy drug doxorubicin (DOX) via CED into and around the cavity where the tumor was previously located would then occur. At the same time as the administration of CED, intrathecal delivery of the DOX-functionalized magnetic nanoparticles (MNPs) may be performed. Simultaneously, an external magnetic field would be used to concentrate the DOX-MNPs at the targeted sight in and around the putamen. The location, strength, shape, and gradient of this magnetic field would be

optimized beforehand via computer simulations. These DOX-MNPs could also be functionalized to target tumor-specific antigens overly expressed on brain tumor cells. Our PBPK modeling framework could then be used to determine where the DOX distributes throughout the body over time. However, in order to perform accurate PBPK modeling, one would first need *in vivo* drug dose-response data of similar experiments performed in rats or other animals, as well as drug binding rates and other parameters. A similar protocol, without any tumor resection, could be used within the putamen to treat Parkinson's disease with dopamine agonists.

CITED LITERATURE

1. Brown RP, Delp MD, Lindstedt SL, Rhomberg LR, Beliles RP. Physiological parameter values for physiologically based pharmacokinetic models. Toxicol Ind Health. 1997 Aug;13(4):407–84.

2. Kawai R, Mathew D, Tanaka C, Rowland M. Physiologically based pharmacokinetics of cyclosporine A: extension to tissue distribution kinetics in rats and scale-up to human. J Pharmacol Exp Ther. 1998 Nov;287(2):457–68.

3. Delp MD, Evans MV, Duan C. Effects of aging on cardiac output, regional blood flow, and body composition in Fischer-344 rats. J Appl Physiol. 1998 Nov;85(5):1813–22.

4. Schmitt W. General approach for the calculation of tissue to plasma partition coefficients. Toxicol Vitro Int J Publ Assoc BIBRA. 2008 Mar;22(2):457–67.

5. Kimura S, Oshima K, Okuda S, Sato K, Sato M, Terasako K, et al. Pharmacokinetics of CsA during the switch from continuous intravenous infusion to oral administration after allogeneic hematopoietic stem cell transplantation. Bone Marrow Transpl. 2010 Jun;45(6):1088–94.

6. European Commission. Neurodegenerative Disorders [Internet]. 2014. Available from: http://ec.europa.eu/health/major_chronic_diseases/diseases/brain_neurological/index_en.htm

7. NIH. Neurodegenerative Diseases [Internet]. 2014. Available from: http://www.niehs.nih.gov/research/supported/diseases/neurodegenerative/

8. Prince M, Prina M, Guerchet M. World Alzheimer Report 2013: Journey of Caring: An analysis of long-term care for dementia [Internet]. London; 2013 p. 1–92. Available from: http://www.alz.co.uk/research/WorldAlzheimerReport2013.pdf

9. Parkinson's Disease Backgrounder: National Institute of Neurological Disorders and Stroke (NINDS) [Internet]. Parkinson's Disease Backgrounder. [cited 2014 Dec 29]. Available from: http://www.ninds.nih.gov/disorders/parkinsons_disease/parkinsons_disease_backgrounder.htm

10. European Parkinson's Disease Association [Internet]. [cited 2014 Dec 29]. Available from: http://www.epda.eu.com/en/

11. National Parkinson Foundation - NPF Statement on the Economic Burden of Parkinson's Disease [Internet]. [cited 2014 Dec 29]. Available from: http://www.parkinson.org/About-Us/Press-Room/Press-Releases/2013/February/NPF-Statement-on-the-Economic-Burden-of-Parkinson-

12. Porter KR, McCarthy BJ, Freels S, Kim Y, Davis FG. Prevalence estimates for primary brain tumors in the United States by age, gender, behavior, and histology. Neuro-Oncol. 2010 Feb 8;nop066.

13. 2014 Central Brain Tumor Registry of the United States Fact Sheet [Internet]. [cited 2014 Dec 28]. Available from: http://www.cbtrus.org/factsheet/factsheet.html

14. Pardridge WM. The Blood-Brain Barrier: Bottleneck in Brain Drug Development. NeuroRx. 2005 Jan;2(1):3–14.

15. Pardridge WM. Blood-brain barrier drug targeting: the future of brain drug development. Mol Interv. 2003 Mar;3(2):90–105, 51.

16. Chen Y, Liu L. Modern methods for delivery of drugs across the blood–brain barrier. Adv Drug Deliv Rev. 2012 May 15;64(7):640–65.

17. Kunwar S, Chang S, Westphal M, Vogelbaum M, Sampson J, Barnett G, et al. Phase III randomized trial of CED of IL13-PE38QQR vs Gliadel wafers for recurrent glioblastoma. Neuro-Oncol. 2010 Aug;12(8):871–81.

18. Husain SR, Joshi BH, Puri RK. Interleukin-13 receptor as a unique target for anti-glioblastoma therapy. Int J Cancer J Int Cancer. 2001 Apr 15;92(2):168–75.

19. Laske DW, Ilercil O, Akbasak A, Youle RJ, Oldfield EH. Efficacy of direct intratumoral therapy with targeted protein toxins for solid human gliomas in nude mice. J Neurosurg. 1994 Mar;80(3):520–6.

20. Lueshen E, LaRiviere M, Yamini B, Linninger A. Computer simulations and in vivo convection-enhanced delivery of fluorescent nanoparticles demonstrate variable distribution geometry. Comput Chem Eng. 2014 Dec 4;71:672–6.

21. Mueller S, Polley M-Y, Lee B, Kunwar S, Pedain C, Wembacher-Schröder E, et al. Effect of imaging and catheter characteristics on clinical outcome for patients in the PRECISE study. J Neurooncol. 2011 Jan;101(2):267–77.

22. Sampson JH, Archer G, Pedain C, Wembacher-Schröder E, Westphal M, Kunwar S, et al. Poor drug distribution as a possible explanation for the results of the PRECISE trial. J Neurosurg. 2010 Aug;113(2):301–9.

23. Hall C, Lueshen E, Mošat' A, Linninger AA. Interspecies scaling in pharmacokinetics: A novel whole-body physiologically based modeling framework to discover drug biodistribution mechanisms in vivo. J Pharm Sci. 2012 Mar;101(3):1221–41.

24. Mošat' A, Lueshen E, Heitzig M, Hall C, Linninger AA, Sin G, et al. First principles pharmacokinetic modeling: A quantitative study on Cyclosporin. Comput Chem Eng. 2013 Jul 11;54:97–110.

25. Lueshen E, Hall C, Mošat' A, Linninger A. Pharmacokinetic Parameter Estimation of Drug Distribution in an Entire Organism. Salt Lake City, UT; 2010. Available from: http://www3.aiche.org/proceedings/Abstract.aspx?PaperID=200531

26. Lueshen E, Hall C, Mošat' A, Linninger A. Quality by Design Approach to Pharmacokinetic Modeling. A Case Study on Cyclosporin A. Salt Lake City, UT; 2010. Available from: http://www.aiche.org/academy/videos/conference-presentations/quality-design-approach-pharmacokinetic-modeling-case-study-on-cyclosporin

27. Lueshen E, Hall C, Mošat' A, Linninger A. Physiologically-Based Pharmacokinetic Modeling: Parameter Estimation for Cyclosporin A. In: E.N. Pistikopoulos MCG and ACK, editor. Computer Aided Chemical Engineering [Internet]. Elsevier; 2011. p. 1543–7. Available from: http://www.sciencedirect.com/science/article/pii/B9780444542984500878

28. Sindhwani N, Ivanchenko O, Lueshen E, Prem K, Linninger AA. Methods for determining agent concentration profiles in agarose gel during convection-enhanced delivery. IEEE Trans Biomed Eng. 2011 Mar;58(3):626–32.

29. Li D, Ivanchenko O, Sindhwani N, Lueshen E, Linninger AA. Optimal Catheter Placement for Chemotherapy. In: Ferraris SP and GB, editor. Computer Aided Chemical Engineering [Internet]. Elsevier; 2010. p. 223–8. Available from: http://www.sciencedirect.com/science/article/pii/S1570794610280380

30. Lueshen E, Mehta AI, Linninger AA. Backflow-Free Catheters for Efficient and Safe Convection-Enhanced Delivery of Therapeutics. Med Eng Phys. 2015;Under review.

31. Lueshen E, Venugopal I, Kanikunnel J, Soni T, Alaraj A, Linninger A. Intrathecal magnetic drug targeting using gold-coated magnetite nanoparticles in a human spine model. Nanomed. 2014;9(8):1155–69.

32. Lueshen E, Venugopal I, Soni T, Alaraj A, Linninger A. Implant-Assisted Intrathecal Magnetic Drug Targeting to Aid in Therapeutic Nanoparticle Localization for Potential Treatment of Central Nervous System Disorders. J Biomed Nanotechnol. 2015 Feb 1;11(2):253–61.

33. Lueshen E, Venugopal I, Linninger A. Intrathecal Magnetic Drug Targeting: A New Approach to Treating Diseases of the Central Nervous System. Boston, MA: ASME; 2013.

34. Legg B, Rowland M. Cyclosporin: measurement of fraction unbound in plasma. J Pharm Pharmacol. 1987 Aug;39(8):599–603.

35. Ursino M, Avanzolini G, Barbini P. Qualitative simulation of dynamic physiological models using the KEE environment. Artif Intell Med. 1992 Feb;4(1):53–73.

36. Buss WC, Stepanek J. Characterization of the inhibition of renal translation in the Sprague-Dawley rat following in vivo cyclosporin A. Int J Immunopharmacol. 1993 Jan;15(1):63–76.

37. Ring BJ, Chien JY, Adkison KK, Jones HM, Rowland M, Jones RD, et al. PhRMA CPCDC initiative on predictive models of human pharmacokinetics, part 3: Comparative assessement of prediction methods of human clearance. J Pharm Sci [Internet]. 2011 May; Available from: http://www.ncbi.nlm.nih.gov/pubmed/21541938

38. Nestorov IS, Hadjitodorov ST, Petrov I, Rowland M. Empirical versus mechanistic modelling: comparison of an artificial neural network to a mechanistically based model for quantitative structure pharmacokinetic relationships of a homologous series of barbiturates. AAPS PharmSci. 1999;1(4):E17.

39. Kawai R, Lemaire M, Steimer JL, Bruelisauer A, Niederberger W, Rowland M. Physiologically based pharmacokinetic study on a cyclosporin derivative, SDZ IMM 125. J Pharmacokinet Biopharm. 1994 Oct;22(5):327–65.

40. Tanaka C, Kawai R, Rowland M. Dose-dependent pharmacokinetics of cyclosporin A in rats: events in tissues. Drug Metab Dispos Biol Fate Chem. 2000 May;28(5):582–9.

41. Gueorguieva I, Nestorov IA, Rowland M. Reducing whole body physiologically based pharmacokinetic models using global sensitivity analysis: diazepam case study. J Pharmacokinet Pharmacodyn. 2006 Feb;33(1):1–27.

42. Edginton AN, Theil F-P, Schmitt W, Willmann S. Whole body physiologically-based pharmacokinetic models: their use in clinical drug development. Expert Opin Drug Metab Toxicol. 2008 Sep;4(9):1143–52.

43. De Buck SS, Sinha VK, Fenu LA, Nijsen MJ, Mackie CE, Gilissen RAHJ. Prediction of human pharmacokinetics using physiologically based modeling: a retrospective analysis of 26 clinically tested drugs. Drug Metab Dispos Biol Fate Chem. 2007 Oct;35(10):1766–80.

44. Haritova AM, Fink-Gremmels J. A simulation model for the prediction of tissue:plasma partition coefficients for drug residues in natural casings. Vet J Lond Engl 1997. 2010 Sep;185(3):278–84.

45. Von Kleist M, Huisinga W. Physiologically based pharmacokinetic modelling: a sub-compartmentalized model of tissue distribution. J Pharmacokinet Pharmacodyn. 2007 Dec;34(6):789–806.

46. Von Kleist M, Huisinga W. Pharmacokinetic-pharmacodynamic relationship of NRTIs and its connection to viral escape: an example based on zidovudine. Eur J Pharm Sci Off J Eur Fed Pharm Sci. 2009 Mar;36(4-5):532–43.

47. Espié P, Tytgat D, Sargentini-Maier M-L, Poggesi I, Watelet J-B. Physiologically based pharmacokinetics (PBPK). Drug Metab Rev. 2009;41(3):391–407.

48. Garg A, Balthasar JP. Physiologically-based pharmacokinetic (PBPK) model to predict IgG tissue kinetics in wild-type and FcRn-knockout mice. J Pharmacokinet Pharmacodyn. 2007 Oct;34(5):687–709.

49. Laplanche R, Meno-Tetang GML, Kawai R. Physiologically based pharmacokinetic (PBPK) modeling of everolimus (RAD001) in rats involving non-linear tissue uptake. J Pharmacokinet Pharmacodyn. 2007 Jun;34(3):373–400.

50. Lüpfert C, Reichel A. Development and application of physiologically based pharmacokinetic-modeling tools to support drug discovery. Chem Biodivers. 2005 Nov;2(11):1462–86.

51. Peters SA, Hultin L. Early identification of drug-induced impairment of gastric emptying through physiologically based pharmacokinetic (PBPK) simulation of plasma concentration-time profiles in rat. J Pharmacokinet Pharmacodyn. 2008 Feb;35(1):1–30.

52. Yates JWT. Structural identifiability of physiologically based pharmacokinetic models. J Pharmacokinet Pharmacodyn. 2006 Aug;33(4):421–39.

53. Omar AG, El-Mas MM. Time-domain evaluation of cyclosporine interaction with hemodynamic variability in rats. Cardiovasc Drugs Ther Spons Int Soc Cardiovasc Pharmacother. 2004 Nov;18(6):461–8.

54. Kovarik JM, Villamil F, Otero A, Levy G, Lynch S, Cillo U, et al. Cyclosporine pharmacokinetics and blood pressure responses after conversion to once-daily dosing in maintenance liver transplant patients. Clin Transplant. 2008 Feb;22(1):68–75.

55. Linninger AA, Xenos M, Sweetman B, Ponkshe S, Guo X, Penn R. A mathematical model of blood, cerebrospinal fluid and brain dynamics. J Math Biol. 2009 Dec;59(6):729–59.

56. El Tayar N, Mark AE, Vallat P, Brunne RM, Testa B, van Gunsteren WF. Solvent-dependent conformation and hydrogen-bonding capacity of cyclosporin A: evidence from partition coefficients and molecular dynamics simulations. J Med Chem. 1993 Nov;36(24):3757–64.

57. Fanghänel J, Fischer G. Thermodynamic characterization of the interaction of human cyclophilin 18 with cyclosporin A. Biophys Chem. 2003 Jan;100(1-3):351–66.

58. Kieffer LJ, Thalhammer T, Handschumacher RE. Isolation and characterization of a 40-kDa cyclophilin-related protein. J Biol Chem. 1992 Mar;267(8):5503–7.

59. Thalhammer T, Kieffer LJ, Jiang T, Handschumacher RE. Isolation and partial characterization of membrane-associated cyclophilin and a related 22-kDa glycoprotein. Eur J Biochem FEBS. 1992 May;206(1):31–7.

60. Sangalli L, Bortolotti A, Jiritano L, Bonati M. Cyclosporine pharmacokinetics in rats and interspecies comparison in dogs, rabbits, rats, and humans. Drug Metab Dispos. 1988;16(5):749–53.

61. Bleck JS, Schlitt HJ, Christians U, Thiesemann C, Strohmeyer S, Schottmann R, et al. Urinary excretion of ciclosporin and 17 of its metabolites in renal allograft recipients. Pharmacology. 1989;39(3):160–4.

62. Sadrieh N, Thomas PE. Characterization of rat cytochrome P450 isozymes involved in the covalent binding of cyclosporin A to microsomal proteins. Toxicol Appl Pharmacol. 1994 Aug;127(2):222–32.

63. Kelly PA, Wang H, Napoli KL, Kahan BD, Strobel HW. Metabolism of cyclosporine by cytochromes P450 3A9 and 3A4. Eur J Drug Metab Pharmacokinet. 1999 Dec;24(4):321–8.

64. Petzold LR. Recent developments in the numerical solution of differential/algebraic systems. Comput Methods Appl Mech Eng. 1989 Oct;75(1-3):77–89.

65. Zavala VM, Biegler LT. Large-Scale Parameter Estimation in Low-Density Polyethylene Tubular Reactors. Ind Eng Chem Res. 2006 Nov;45(23):7867–81.

66. Zavala VM, Laird CD, Biegler LT. Interior-point decomposition approaches for parallel solution of large-scale nonlinear parameter estimation problems. Chem Eng Sci. 2008 Oct;63(19):4834–45.

67. Bonami P, Biegler LT, Conn AR, Cornuéjols G, Grossmann IE, Laird CD, et al. An algorithmic framework for convex mixed integer nonlinear programs. Discrete Optim. 2008 May;5(2):186–204.

68. Fuente RL-N de la, Flores-Tlacuahuac A. Integrated Design and Control Using a Simultaneous Mixed-Integer Dynamic Optimization Approach. Ind Eng Chem Res. 2009 Feb;48(4):1933–43.

69. Harjunkoski I, Jain V, Grossman IE. Hybrid mixed-integer/constraint logic programming strategies for solving scheduling and combinatorial optimization problems. Comput Chem Eng. 2000 Jul;24(2-7):337–43.

70. Conn AR, Gould NIM, Toint PL. Global Convergence of a Class of Trust Region Algorithms for Optimization with Simple Bounds. SIAM J Numer Anal. 1988 Apr;25(2):433–60.

71. Toint PL, Tomanos D, Weber-Mendonca M. A multilevel algorithm for solving the trust-region subproblem. Optim Methods Softw. 2009 Apr;24:299–311.

72. Zhang L, Xue C, Malcolm A, Kulkarni K, Linninger AA. Distributed System Design Under Uncertainty. Ind Eng Chem Res. 2006 Dec;45(25):8352–60.

73. Kulkarni K. Mathematical modeling, problem inversion and design of distributed chemical and biological systems. [Doctoral Thesis]. [Chicago, IL, U.S.A.]: University of Illinois at Chicago; 2007.

74. Tang W, Zhang L, Linninger AA, Tranter RS, Brezinsky K. Solving Kinetic Inversion Problems via a Physically Bounded Gauss−Newton (PGN) Method. Ind Eng Chem Res. 2005 May 1;44(10):3626–37.

75. Lucia A, Gattupalli RR, Kulkarni K, Linninger A. A Barrier-Terrain Methodology for Global Optimization. Ind Eng Chem Res. 2008 Apr;47(8):2666–80.

76. Kulkarni K, Zhang L, Linninger AA. Model and Parameter Uncertainty in Distributed Systems. Ind Eng Chem Res. 2006 Nov;45(23):7832–40.

77. Kulkarni K, Larsen P, Linninger AA. Assessing chronic liver toxicity based on relative gene expression data. J Theor Biol. 2008 Sep;254(2):308–18.

78. Bard Y. Nonlinear Parameter Estimation. New York: Academic Press; 1974.

79. Donaldson JR, Schnabel RB. Computational Experience with Confidence Regions and Confidence Intervals for Nonlinear Least Squares. Technometrics. 1987 Feb;29(1):67–82.

80. Rooney WC, Biegler LT. Incorporating joint confidence regions into design under uncertainty. Comput Chem Eng. 1999 Dec;23(10):1563–75.

81. Rooney WC, Biegler LT. Design for model parameter uncertainty using nonlinear confidence regions. AIChE J. 2001 Aug;47(8):1794–804.

82. Akhlaghi F, Ashley J, Keogh A, Brown K. Cyclosporine plasma unbound fraction in heart and lung transplantation recipients. Ther Drug Monit. 1999 Feb;21(1):8–16.

83. Mendonza AE, Gohh RY, Akhlaghi F. Blood and plasma pharmacokinetics of ciclosporin in diabetic kidney transplant recipients. Clin Pharmacokinet. 2008;47(11):733–42.

84. Yang H, Elmquist WF. The binding of cyclosporin A to human plasma: an in vitro microdialysis study. Pharm Res. 1996 Apr;13(4):622–7.

85. Heitzig M, Sin G, Sales-Cruz M, Glarborg P, Gani R. Computer-Aided Modeling Framework for Efficient Model Development, Analysis, and Identification: Combustion and Reactor Modeling. Ind Eng Chem Res. 2010;50(9):5253–65.

86. Heitzig M, Rong Y, Gregson C, Sin G, Gani R. Systematic Multi-Scale Model Development Strategy for the Fragrance Spraying Process and Transport. Chem Eng Technol. 2012;35(8):1381–91.

87. Mathieu M. New Drug Development: A Regulatory Overview. 8 Revised edition. Waltham, MA: Parexel Intl Corp; 2008. 362 p.

88. Mahmood I. Pharmacokinetic allometric scaling of antibodies: application to the first-in-human dose estimation. J Pharm Sci. 2009 Oct;98(10):3850–61.

89. West GB, Brown JH, Enquist BJ. A General Model for the Origin of Allometric Scaling Laws in Biology. Science. 1997 Apr 4;276(5309):122–6.

90. West GB, Brown JH, Enquist BJ. The Fourth Dimension of Life: Fractal Geometry and Allometric Scaling of Organisms. Science. 1999 Jun 4;284(5420):1677–9.

91. Ritschel WA, Vachharajani NN, Johnson RD, Hussain AS. The allometric approach for interspecies scaling of pharmacokinetic parameters. Comp Biochem Physiol C. 1992 Oct;103(2):249–53.

92. Podder H, Stepkowski SM, Napoli KL, Clark J, Verani RR, Chou TC, et al. Pharmacokinetic interactions augment toxicities of sirolimus/cyclosporine combinations. J Am Soc Nephrol JASN. 2001 May;12(5):1059–71.

93. Lindholm A, Henricsson S, Lind M, Dahlqvist R. Intraindividual variability in the relative systemic availability of cyclosporin after oral dosing. Eur J Clin Pharmacol. 1988;34(5):461–4.

94. Stephanopoulos GN, Aristidou AA, Nielsen J. Metabolic Engineering: Principles and Methodologies. 1 edition. San Diego: Academic Press; 1998. 725 p.

95. Villadsen J, Nielsen J, Lidén G. Bioreaction Engineering Principles. 3rd ed. 2011 edition. New York: Springer; 2011. 561 p.

96. Palsson BØ. Systems Biology: Properties of Reconstructed Networks. 1 edition. Cambridge University Press; 2006. 336 p.

97. Jia G, Stephanopoulos GN, Gunawan R. Parameter estimation of kinetic models from metabolic profiles: Two-phase dynamic decoupling method. Bioinformatics. 2011 May 9;btr293.

98. Fremming BD, Benson RE, Young RJ. Weights of Organs in Sixty-Six Male Macaca Mulatta Monkeys. J Appl Physiol. 1955 Sep 1;8(2):155–8.

99. Upton RN. Organ weights and blood flows of sheep and pig for physiological pharmacokinetic modelling. J Pharmacol Toxicol Methods. 2008 Dec;58(3):198–205.

100. Williams LR, Leggett RW. Reference values for resting blood flow to organs of man. Clin Phys Physiol Meas. 1989 Aug 1;10(3):187.

101. Thurlby PL, Trayhurn P. Regional blood flow in genetically obese (ob/ob) mice. Pflüg Arch. 1980 Jun 1;385(3):193–201.

102. Davies B, Morris T. Physiological Parameters in Laboratory Animals and Humans. Pharm Res. 1993 Jul 1;10(7):1093–5.

103. Forsyth RP, Nies AS, Wyler F, Neutze J, Melmon KL. Normal distribution of cardiac output in the unanesthetized, restrined rhesus monkey. J Appl Physiol. 1968 Dec 1;25(6):736–41.

104. Pervaiz M, Khan N, John G, Mell S. Design of a drug delivery model for the rhesus monkey. University of Illinois at Chicago; 2010.

105. Weiss L, Haydock K, Pickren JW, Lane WW. Organ vascularity and metastatic frequency. Am J Pathol. 1980 Oct;101(1):101–14.

106. Hoffbrand BI, Forsyth RP. Validity Studies of the Radioactive Microsphere Method for the Study of the Distribution of Cardiac Output, Organ Blood Flow, and Resistance in the Conscious Rhesus Monkey. Cardiovasc Res. 1969 Oct 1;3(4):426–32.

107. Van Woerkens LJ, Duncker DJ, Huigen RJ, van der Giessen WJ, Verdouw PD. Redistribution of cardiac output caused by opening of arteriovenous anastomoses by a combination of azaperone and metomidate. Br J Anaesth. 1990 Sep;65(3):393–9.

108. Akhlaghi F, Trull AK. Distribution of cyclosporin in organ transplant recipients. Clin Pharmacokinet. 2002;41(9):615–37.

109. Schuurman HJ, Hengy JC, Ringers J, Vonderscher J, Schuler W, Jonker M. Neoral pharmacokinetics in cynomolgus monkeys: relation to efficacy in renal allografting. Transplant Proc. 1996 Dec;28(6):3142–4.

110. Schuurman HJ, Slingerland W, Mennninger K, Ossevoort M, Hengy JC, Dorobek B, et al. Pharmacokinetics of cyclosporine in monkeys after oral and intramuscular administration: relation to efficacy in kidney allografting. Transpl Int Off J Eur Soc Organ Transplant. 2001 Sep;14(5):320–8.

111. Cibulskyte D, Pedersen M, Jakobsen P, Hansen HE, Mortensen J. Pharmacokinetic characterization of a pig model of ciclosporin A nephrotoxicity following intravenous administration. Pharmacol Res Off J Ital Pharmacol Soc. 2007 Oct;56(4):311–7.

112. Ptachcinski RJ, Venkataramanan R, Burckart GJ, Gray JA, Van Thiel DH, Sanghvi A, et al. Cyclosporine kinetics in healthy volunteers. J Clin Pharmacol. 1987 Mar;27(3):243–8.

113. Lindholm A. Factors influencing the pharmacokinetics of cyclosporine in man. Ther Drug Monit. 1991 Nov;13(6):465–77.

114. Mager DE, Woo S, Jusko WJ. Scaling pharmacodynamics from in vitro and preclinical animal studies to humans. Drug Metab Pharmacokinet. 2009;24(1):16–24.

115. Bobo RH, Laske DW, Akbasak A, Morrison PF, Dedrick RL, Oldfield EH. Convection-enhanced delivery of macromolecules in the brain. Proc Natl Acad Sci. 1994 Mar 15;91(6):2076–80.

116. Mamot C, Nguyen JB, Pourdehnad M, Hadaczek P, Saito R, Bringas JR, et al. Extensive distribution of liposomes in rodent brains and brain tumors following convection-enhanced delivery. J Neurooncol. 2004 May;68(1):1–9.

117. Morrison PF, Chen MY, Chadwick RS, Lonser RR, Oldfield EH. Focal delivery during direct infusion to brain: role of flow rate, catheter diameter, and tissue mechanics. Am J Physiol - Regul Integr Comp Physiol. 1999 Oct 1;277(4):R1218–29.

118. LaRiviere M, Mansour N, Galanopoulos N, Rawlani V, Prem K, Ferguson S, et al. Convection Enhanced Delivery of Biodegradable Nanoparticles for the Treatment of Malignant Glioma. San Francisco, CA; 2010.

119. Linninger AA, Somayaji MR, Erickson T, Guo X, Penn RD. Computational methods for predicting drug transport in anisotropic and heterogeneous brain tissue. J Biomech. 2008 Jul 19;41(10):2176–87.

120. Linninger AA, Somayaji MR, Mekarski M, Zhang L. Prediction of convection-enhanced drug delivery to the human brain. J Theor Biol. 2008 Jan 7;250(1):125–38.

121. Somayaji MR, Xenos M, Zhang L, Mekarski M, Linninger AA. Systematic design of drug delivery therapies. Comput Chem Eng. 2008 Jan;32(1–2):89–98.

122. Michal T. Krauze, Ryuta Saito, Charles Noble, Matyas Tamas, John Bringas, John W. Park, et al. Reflux-free cannula for convection-enhanced high-speed delivery of therapeutic agents [Internet]. http://dx.doi.org/10.3171/jns.2005.103.5.0923. 2009 [cited 2013 Sep 23]. Available from: http://thejns.org/doi/abs/10.3171/jns.2005.103.5.0923

123. The MathWorks, Inc. MATLAB - The Language of Technical Computing [Internet]. 2014. Available from: http://www.mathworks.com/products/matlab/

124. Materialise, Inc. Mimics® [Internet]. 2014. Available from: http://biomedical.materialise.com/mimics

125. NIH. ImageJ [Internet]. 2014. Available from: http://imagej.nih.gov/ij/

126. Allard E, Passirani C, Benoit J-P. Convection-enhanced delivery of nanocarriers for the treatment of brain tumors. Biomaterials. 2009 Apr;30(12):2302–18.

127. Mastakov MY, Baer K, Xu R, Fitzsimons H, During MJ. Combined injection of rAAV with mannitol enhances gene expression in the rat brain. Mol Ther J Am Soc Gene Ther. 2001 Feb;3(2):225–32.

128. Neeves KB, Sawyer AJ, Foley CP, Saltzman WM, Olbricht WL. Dilation and degradation of the brain extracellular matrix enhances penetration of infused polymer nanoparticles. Brain Res. 2007 Nov 14;1180:121–32.

129. Hamilton JF, Morrison PF, Chen MY, Harvey-White J, Pernaute RS, Phillips H, et al. Heparin coinfusion during convection-enhanced delivery (CED) increases the distribution of the glial-derived neurotrophic factor (GDNF) ligand family in rat striatum and enhances the pharmacological activity of neurturin. Exp Neurol. 2001 Mar;168(1):155–61.

130. Hadaczek P, Yamashita Y, Mirek H, Tamas L, Bohn MC, Noble C, et al. The "perivascular pump" driven by arterial pulsation is a powerful mechanism for the distribution of therapeutic molecules within the brain. Mol Ther J Am Soc Gene Ther. 2006 Jul;14(1):69–78.

131. Iliff JJ, Wang M, Liao Y, Plogg BA, Peng W, Gundersen GA, et al. A paravascular pathway facilitates CSF flow through the brain parenchyma and the clearance of interstitial solutes, including amyloid β. Sci Transl Med. 2012 Aug 15;4(147):147ra111.

132. Chen MY, Lonser RR, Morrison PF, Governale LS, Oldfield EH. Variables affecting convection-enhanced delivery to the striatum: a systematic examination of rate of infusion, cannula size, infusate concentration, and tissue-cannula sealing time. J Neurosurg. 1999 Feb;90(2):315–20.

133. Neeves KB, Lo CT, Foley CP, Saltzman WM, Olbricht WL. Fabrication and characterization of microfluidic probes for convection enhanced drug delivery. J Controlled Release. 2006 Apr 10;111(3):252–62.

134. Herdeg C, Oberhoff M, Baumbach A, Haase KK, Horch B, Kranzhoefer A, et al. Local drug delivery with porous balloons in the rabbit: assessment of vascular injury for an improvement of application parameters. Cathet Cardiovasc Diagn. 1997 Jul;41(3):308–14.

135. Vogelbaum MA. Convection enhanced delivery for treating brain tumors and selected neurological disorders: symposium review. J Neurooncol. 2007 May;83(1):97–109.

136. Lang AE, Gill S, Patel NK, Lozano A, Nutt JG, Penn R, et al. Randomized controlled trial of intraputamenal glial cell line-derived neurotrophic factor infusion in Parkinson disease. Ann Neurol. 2006 Mar;59(3):459–66.

137. Salvatore MF, Ai Y, Fischer B, Zhang AM, Grondin RC, Zhang Z, et al. Point source concentration of GDNF may explain failure of phase II clinical trial. Exp Neurol. 2006 Dec;202(2):497–505.

138. Rosenberg GA, Kyner WT, Estrada E. Bulk flow of brain interstitial fluid under normal and hyperosmolar conditions. Am J Physiol - Ren Physiol. 1980 Jan 1;238(1):F42–9.

139. Ivanchenko O, Sindhwani N, Linninger A. Experimental Techniques for Studying Poroelasticity in Brain Phantom Gels Under High Flow Microinfusion. J Biomech Eng. 2010 Mar 29;132(5):051008–051008.

140. De Boer R. Theory of Porous Media — Past and Present. ZAMM - J Appl Math Mech Z Für Angew Math Mech. 1998;78(7):441–66.

141. Bowen RM. Incompressible porous media models by use of the theory of mixtures. Int J Eng Sci. 1980;18(9):1129–48.

142. Li C, Borja RI, Regueiro RA. Dynamics of porous media at finite strain. Comput Methods Appl Mech Eng. 2004 Sep 10;193(36–38):3837–70.

143. Prévost JH. Mechanics of continuous porous media. Int J Eng Sci. 1980;18(6):787–800.

144. Wang H. Theory of Linear Poroelasticity with Applications to Geomechanics and Hydrogeology. Princeton University Press; 2000. 300 p.

145. Bidros DS, Liu JK, Vogelbaum MA. Future of convection-enhanced delivery in the treatment of brain tumors. Future Oncol. 2010 Jan 1;6(1):117–25.

146. Chen Z-J, Broaddus WC, Viswanathan RR, Raghavan R, Gillies GT. Intraparenchymal drug delivery via positive-pressure infusion: experimental and modeling studies of poroelasticity in brain phantom gels. IEEE Trans Biomed Eng. 2002 Feb;49(2):85–96.

147. Twin Star Medical [Internet]. [cited 2014 Dec 28]. Available from: http://www.twinstarmedical.com/drug_delivery.html

148. Chen Z-J, Gillies GT, Broaddus WC, Prabhu SS, Fillmore H, Mitchell RM, et al. A realistic brain tissue phantom for intraparenchymal infusion studies. J Neurosurg. 2004 Aug 1;101(2):314–22.

149. Linninger AA, Somayaji MR, Zhang L, Hariharan MS, Penn RD. Rigorous Mathematical Modeling Techniques for Optimal Delivery of Macromolecules to the Brain. IEEE Trans Biomed Eng. 2008 Sep;55(9):2303–13.

150. Hall CW. Laws and Models: Science, Engineering, and Technology. 1 edition. CRC Press; 1999.

151. ANSYS - Simulation Driven Product Development [Internet]. [cited 2014 Dec 28]. Available from: http://www.ansys.com/

152. Seunguk O, Odland R, Wilson SR, Kroeger KM, Liu C, Lowenstein PR, et al. Improved distribution of small molecules and viral vectors in the murine brain using a hollow fiber catheter. J Neurosurg. 2007 Sep;107(3):568–77.

153. Sampson JH, Brady M, Raghavan R, Mehta AI, Friedman AH, Reardon DA, et al. Colocalization of gadolinium-diethylene triamine pentaacetic acid with high-molecular-weight molecules after intracerebral convection-enhanced delivery in humans. Neurosurgery. 2011 Sep;69(3):668–76.

154. Glantz MJ, Van Horn A, Fisher R, Chamberlain MC. Route of intracerebrospinal fluid chemotherapy administration and efficacy of therapy in neoplastic meningitis. Cancer. 2010 Apr 15;116(8):1947–52.

155. Stemmler H-J, Mengele K, Schmitt M, Harbeck N, Laessig D, Herrmann KA, et al. Intrathecal trastuzumab (Herceptin) and methotrexate for meningeal carcinomatosis in HER2-overexpressing metastatic breast cancer: a case report. Anticancer Drugs. 2008 Sep;19(8):832–6.

156. Band PR, Holland JF, Bernard J, Weil M, Walker M, Rall D. Treatment of central nervous system leukemia with intrathecal cytosine arabinoside. Cancer. 1973 Oct;32(4):744–8.

157. Penn RD. Intrathecal baclofen for spasticity of spinal origin: seven years of experience. J Neurosurg. 1992 Aug;77(2):236–40.

158. Paice JA, Winkelmüller W, Burchiel K, Racz GB, Prager JP. Clinical realities and economic considerations: efficacy of intrathecal pain therapy. J Pain Symptom Manage. 1997 Sep;14(3 Suppl):S14–26.

159. Shahriari A, Khooshideh M. Intrathecal fentanyl added to lidocaine for Cesarean delivery under spinal anesthesia--a randomised clinical trial. Middle East J Anaesthesiol. 2007 Jun;19(2):397–406.

160. Jabbari A, Hassan-nasab B, Maleh P, Bani-hashem N, Pour E, Nabavi A. Addition of intrathecal Dexamethasone to Bupivacaine for spinal anesthesia in orthopedic surgery. Saudi J Anaesth. 2011;5(4):382.

161. Luo M-C, Zhang D-Q, Ma S-W, Huang Y-Y, Shuster SJ, Porreca F, et al. An efficient intrathecal delivery of small interfering RNA to the spinal cord and peripheral neurons. Mol Pain. 2005 Sep 28;1(1):29.

162. Hettiarachchi HDM, Hsu Y, Harris TJ, Penn R, Linninger AA. The effect of pulsatile flow on intrathecal drug delivery in the spinal canal. Ann Biomed Eng. 2011 Oct;39(10):2592–602.

163. Ghafoor VL, Epshteyn M, Carlson GH, Terhaar DM, Charry O, Phelps PK. Intrathecal drug therapy for long-term pain management. Am J Health-Syst Pharm AJHP Off J Am Soc Health-Syst Pharm. 2007 Dec 1;64(23):2447–61.

164. Onofrio BM, Yaksh TL. Long-term pain relief produced by intrathecal morphine infusion in 53 patients. J Neurosurg. 1990 Feb;72(2):200–9.

165. Penn RD. Intrathecal medication delivery. Neurosurg Clin N Am. 2003 Jul;14(3):381–7.

166. Chertok B, Moffat BA, David AE, Yu F, Bergemann C, Ross BD, et al. Iron oxide nanoparticles as a drug delivery vehicle for MRI monitored magnetic targeting of brain tumors. Biomaterials. 2008 Feb;29(4):487–96.

167. Chertok B, David AE, Yang VC. Polyethyleneimine-modified iron oxide nanoparticles for brain tumor drug delivery using magnetic targeting and intra-carotid administration. Biomaterials. 2010 Aug;31(24):6317–24.

168. Chertok B, David AE, Yang VC. Brain tumor targeting of magnetic nanoparticles for potential drug delivery: effect of administration route and magnetic field topography. J Control Release Off J Control Release Soc. 2011 Nov 7;155(3):393–9.

169. Alexiou C, Jurgons R, Seliger C, Brunke O, Iro H, Odenbach S. Delivery of superparamagnetic nanoparticles for local chemotherapy after intraarterial infusion and magnetic drug targeting. Anticancer Res. 2007 Aug;27(4A):2019–22.

170. Alexiou C, Tietze R, Schreiber E, Jurgons R, Richter H, Trahms L, et al. Cancer therapy with drug loaded magnetic nanoparticles—magnetic drug targeting. J Magn Magn Mater. 2011 May;323(10):1404–7.

171. Krukemeyer MG, Wagner W, Jakobs M, Krenn V. Tumor regression by means of magnetic drug targeting. Nanomed. 2009 Dec;4(8):875–82.

172. Krukemeyer MG, Krenn V, Jakobs M, Wagner W. Magnetic drug targeting in a rhabdomyosarcoma rat model using magnetite-dextran composite nanoparticle-bound mitoxantrone and 0.6 tesla extracorporeal magnets - sarcoma treatment in progress. J Drug Target. 2012 Feb;20(2):185–93.

173. Banerjee MK, Datta A, Ganguly R. Magnetic Drug Targeting in Partly Occluded Blood Vessels Using Magnetic Microspheres. J Nanotechnol Eng Med. 2010 Oct 21;1(4):041005–041005.

174. Nacev A, Komaee A, Sarwar A, Probst R, Kim SH, Emmert-Buck M, et al. Towards Control of Magnetic Fluids in Patients: Directing Therapeutic Nanoparticles to Disease Locations. IEEE Control Syst. 2012 Jun;32(3):32–74.

175. Mandal M, Kundu S, Ghosh SK, Panigrahi S, Sau TK, Yusuf SM, et al. Magnetite nanoparticles with tunable gold or silver shell. J Colloid Interface Sci. 2005 Jun 1;286(1):187–94.

176. Sperling RA, Parak WJ. Surface modification, functionalization and bioconjugation of colloidal inorganic nanoparticles. Philos Trans R Soc Lond Math Phys Eng Sci. 2010 Mar 28;368(1915):1333–83.

177. Ouellet JA, Arlet V. Surgical anatomy of the pelvis, sacrum, and lumbar spine relevant to spinal surgery. Semin Spine Surg. 2004 Jun;16(2):91–100.

178. Loth F, Yardimci MA, Alperin N. Hydrodynamic modeling of cerebrospinal fluid motion within the spinal cavity. J Biomech Eng. 2001 Feb;123(1):71–9.

179. Ros L, Mota J, Guedea A, Bidgood D. Quantitative measurements of the spinal cord and canal by MR imaging and myelography. Eur Radiol. 1998;8(6):966–70.

180. Ishikawa M, Matsumoto M, Fujimura Y, Chiba K, Toyama Y. Changes of cervical spinal cord and cervical spinal canal with age in asymptomatic subjects. Spinal Cord. 2003 Mar;41(3):159–63.

181. Ko H-Y, Park JH, Shin YB, Baek SY. Gross quantitative measurements of spinal cord segments in human. Spinal Cord. 2004 Jan;42(1):35–40.

182. Groot JD. Correlative Neuroanatomy and Functional Neurology. 19th edition. Chusid JG, editor. Los Altos, Calif.: Appleton & Lange; 1986. 476 p.

183. Hsu Y, Hettiarachchi HDM, Zhu DC, Linninger AA. The frequency and magnitude of cerebrospinal fluid pulsations influence intrathecal drug distribution: key factors for interpatient variability. Anesth Analg. 2012 Aug;115(2):386–94.

184. Stockman HW. Effect of anatomical fine structure on the flow of cerebrospinal fluid in the spinal subarachnoid space. J Biomech Eng. 2006 Feb;128(1):106–14.

185. Stockman HW. Effect of anatomical fine structure on the dispersion of solutes in the spinal subarachnoid space. J Biomech Eng. 2007 Oct;129(5):666–75.

186. Bhadelia RA, Bogdan AR, Kaplan RF, Wolpert SM. Cerebrospinal fluid pulsation amplitude and its quantitative relationship to cerebral blood flow pulsations: a phase-contrast MR flow imaging study. Neuroradiology. 1997 Apr;39(4):258–64.

187. Freund M, Adwan M, Kooijman H, Heiland S, Thomsen M, Hähnel S, et al. Measurement of CSF flow in the spinal canal using MRI with an optimized MRI protocol: experimental and clinical studies. RöFo Fortschritte Auf Dem Geb Röntgenstrahlen Nukl. 2001 Apr;173(4):306–14.

188. Henry-Feugeas MC, Idy-Peretti I, Blanchet B, Hassine D, Zannoli G, Schouman-Claeys E. Temporal and spatial assessment of normal cerebrospinal fluid dynamics with MR imaging. Magn Reson Imaging. 1993;11(8):1107–18.

189. Hamer J, Alberti E, Hoyer S, Wiedemann K. Influence of systemic and cerebral vascular factors on the cerebrospinal fluid pulse waves. J Neurosurg. 1977 Jan;46(1):36–45.

190. Zhu DC, Xenos M, Linninger AA, Penn RD. Dynamics of lateral ventricle and cerebrospinal fluid in normal and hydrocephalic brains. J Magn Reson Imaging JMRI. 2006 Oct;24(4):756–70.

191. Laitinen L. Origin of Arterial Pulsation of Cerebrospinal Fluid. Acta Neurol Scand. 1968;44(2):168–76.

192. Linninger AA, Tsakiris C, Zhu DC, Xenos M, Roycewicz P, Danziger Z, et al. Pulsatile cerebrospinal fluid dynamics in the human brain. IEEE Trans Biomed Eng. 2005 Apr;52(4):557–65.

193. Linninger AA, Xenos M, Zhu DC, Somayaji MR, Kondapalli S, Penn RD. Cerebrospinal fluid flow in the normal and hydrocephalic human brain. IEEE Trans Biomed Eng. 2007 Feb;54(2):291–302.

194. Sweetman B, Linninger AA. Cerebrospinal fluid flow dynamics in the central nervous system. Ann Biomed Eng. 2011 Jan;39(1):484–96.

195. Polyak B, Fishbein I, Chorny M, Alferiev I, Williams D, Yellen B, et al. High field gradient targeting of magnetic nanoparticle-loaded endothelial cells to the surfaces of steel stents. Proc Natl Acad Sci U S A. 2008 Jan 15;105(2):698–703.

196. Alexiou C, Diehl D, Henninger P, Iro H, Rockelein R, Schmidt W, et al. A High Field Gradient Magnet for Magnetic Drug Targeting. IEEE Trans Appl Supercond. 2006 Jun;16(2):1527–30.

197. Mohammed I, Hussain A. Intrathecal baclofen withdrawal syndrome- a life-threatening complication of baclofen pump: A case report. BMC Pharmacol Toxicol. 2004 Aug 9;4(1):6.

198. Kao LW, Amin Y, Kirk MA, Turner MS. Intrathecal baclofen withdrawal mimicking sepsis. J Emerg Med. 2003 May;24(4):423–7.

199. Bardutzky J, Tronnier V, Schwab S, Meinck H-M. Intrathecal baclofen for stiff-person syndrome: life-threatening intermittent catheter leakage. Neurology. 2003 Jun 24;60(12):1976–8.

200. Shirley KW, Kothare S, Piatt JH, Adirim TA. Intrathecal baclofen overdose and withdrawal. Pediatr Emerg Care. 2006 Apr;22(4):258–61.

201. Perry HE, Wright RO, Shannon MW, Woolf AD. Baclofen overdose: drug experimentation in a group of adolescents. Pediatrics. 1998 Jun;101(6):1045–8.

202. Vanneste J, Augustijn P. Intrathecal baclofen for treatment of spasticity. J Neurol Neurosurg Psychiatry. 1990 Aug;53(8):721.

203. Dawes WJ, Drake JM, Fehlings D. Microfracture of a baclofen pump catheter with intermittent under- and overdose. Pediatr Neurosurg. 2003 Sep;39(3):144–8.

204. Tunali Y, Hanimoglu H, Tanriverdi T, Hanci L, Hanci M. Intrathecal baclofen toxicity and deep coma in minutes. J Spinal Cord Med. 2006;29(3):237–9.

205. Hainfeld JF, Slatkin DN, Smilowitz HM. The use of gold nanoparticles to enhance radiotherapy in mice. Phys Med Biol. 2004 Sep 21;49(18):N309–15.

206. Connor EE, Mwamuka J, Gole A, Murphy CJ, Wyatt MD. Gold nanoparticles are taken up by human cells but do not cause acute cytotoxicity. Small Weinh Bergstr Ger. 2005 Mar;1(3):325–7.

207. Sharma D. A biologically friendly single step method for gold nanoparticle formation. Colloids Surf B Biointerfaces. 2011 Jul 1;85(2):330–7.

208. Spitzer HL, Norman JR. The biosynthesis and turnover of surfactant lecithin and protein. Arch Intern Med. 1971 Mar;127(3):429–35.

209. Banat IM, Makkar RS, Cameotra SS. Potential commercial applications of microbial surfactants. Appl Microbiol Biotechnol. 2000 May 1;53(5):495–508.

210. Arima K, Kakinuma A, Tamura G. Surfactin, a crystalline peptide lipid surfactant produced by Bacillus subtilis: isolation, characterization and its inhibition of fibrin clot formation. Biochem Biophys Res Commun. 1968 May 10;31(3):488–94.

211. Lee J-H, Huh Y-M, Jun Y, Seo J, Jang J, Song H-T, et al. Artificially engineered magnetic nanoparticles for ultra-sensitive molecular imaging. Nat Med. 2007 Jan;13(1):95–9.

212. Wang YX, Hussain SM, Krestin GP. Superparamagnetic iron oxide contrast agents: physicochemical characteristics and applications in MR imaging. Eur Radiol. 2001;11(11):2319–31.

213. Weissleder R, Stark DD, Engelstad BL, Bacon BR, Compton CC, White DL, et al. Superparamagnetic iron oxide: pharmacokinetics and toxicity. AJR Am J Roentgenol. 1989 Jan;152(1):167–73.

214. Lasagna-Reeves C, Gonzalez-Romero D, Barria MA, Olmedo I, Clos A, Sadagopa Ramanujam VM, et al. Bioaccumulation and toxicity of gold nanoparticles after repeated administration in mice. Biochem Biophys Res Commun. 2010 Mar 19;393(4):649–55.

215. Shukla R, Bansal V, Chaudhary M, Basu A, Bhonde RR, Sastry M. Biocompatibility of Gold Nanoparticles and Their Endocytotic Fate Inside the Cellular Compartment: A Microscopic Overview. Langmuir. 2005 Nov 1;21(23):10644–54.

216. Tomkins A. Assessing micronutrient status in the presence of inflammation. J Nutr. 2003 May;133(5 Suppl 2):1649S – 1655S.

217. Jun Y, Lee J-H, Cheon J. Chemical design of nanoparticle probes for high-performance magnetic resonance imaging. Angew Chem Int Ed Engl. 2008;47(28):5122–35.

218. Misra A, Ganesh S, Shahiwala A, Shah SP. Drug delivery to the central nervous system: a review. J Pharm Pharm Sci Publ Can Soc Pharm Sci Société Can Sci Pharm. 2003 Aug;6(2):252–73.

219. Lamer TJ. Treatment of cancer-related pain: when orally administered medications fail. Mayo Clin Proc. 1994 May;69(5):473–80.

220. Charbel Issa P, Lever IJ, Michael GJ, Bradbury EJ, Malcangio M. Intrathecally delivered glial cell line-derived neurotrophic factor produces electrically evoked release of somatostatin in the dorsal horn of the spinal cord. J Neurochem. 2001 Jul;78(2):221–9.

221. Avilés MO, Mangual JO, Ebner AD, Ritter JA. Isolated swine heart ventricle perfusion model for implant assisted-magnetic drug targeting. Int J Pharm. 2008 Sep 1;361(1–2):202–8.

222. Kempe H, Kempe M. The use of magnetite nanoparticles for implant-assisted magnetic drug targeting in thrombolytic therapy. Biomaterials. 2010 Dec;31(36):9499–510.

223. Yellen BB, Forbes ZG, Halverson DS, Fridman G, Barbee KA, Chorny M, et al. Targeted drug delivery to magnetic implants for therapeutic applications. J Magn Magn Mater. 2005 May;293(1):647–54.

224. Tefft BJ, Gooden JY, Uthamaraj S, Harburn JJ, Klabusay M, Holmes DR, et al. Magnetizable Duplex Steel Stents Enable Endothelial Cell Capture. IEEE Trans Magn. 2013;49(1):463–6.

225. Chorny M, Fishbein I, Yellen BB, Alferiev IS, Bakay M, Ganta S, et al. Targeting stents with local delivery of paclitaxel-loaded magnetic nanoparticles using uniform fields. Proc Natl Acad Sci. 2010 May 4;107(18):8346–51.

226. Skebo JE, Grabinski CM, Schrand AM, Schlager JJ, Hussain SM. Assessment of metal nanoparticle agglomeration, uptake, and interaction using high-illuminating system. Int J Toxicol. 2007 Apr;26(2):135–41.

227. Jiang J, Oberdörster G, Biswas P. Characterization of size, surface charge, and agglomeration state of nanoparticle dispersions for toxicological studies. J Nanoparticle Res. 2009 Jan 1;11(1):77–89.

228. Liao W-H, Krueger DA. Theory of large agglomerates in magnetic colloids. J Colloid Interface Sci. 1979 Jul;70(3):564–76.

229. Sano K, Doi M. Theory of Agglomeration of Ferromagnetic Particles in Magnetic Fluids. J Phys Soc Jpn. 1983 Aug 15;52(8):2810–5.

230. Peterson EA, Krueger DA. Reversible, field induced agglomeration in magnetic colloids. J Colloid Interface Sci. 1977 Oct 15;62(1):24–34.

231. Avilés MO, Ebner AD, Ritter JA. Implant assisted-magnetic drug targeting: Comparison of in vitro experiments with theory. J Magn Magn Mater. 2008 Nov;320(21):2704–13.

232. Harvey PD, Metals AS for. Engineering properties of steel. American Society for Metals; 1982. 544 p.

233. Cregg PJ, Murphy K, Mardinoglu A, Prina-Mello A. Many particle magnetic dipole–dipole and hydrodynamic interactions in magnetizable stent assisted magnetic drug targeting. J Magn Magn Mater. 2010 Aug;322(15):2087–94.

234. Moosbrugger C. ASM Ready Reference: Electrical and Magnetic Properties of Metals. ASM International; 2000. 298 p.

235. Ritter JA, Ebner AD, Daniel KD, Stewart KL. Application of high gradient magnetic separation principles to magnetic drug targeting. J Magn Magn Mater. 2004 Sep;280(2–3):184–201.

236. Hassenbusch SJ, Portenoy RK. Current practices in intraspinal therapy--a survey of clinical trends and decision making. J Pain Symptom Manage. 2000 Aug;20(2):S4–11.

APPENDIX A - LICENSES & PERMISSION GRANTED TO USE MY PREVIOUSLY PUBLISHED ARTICLES IN MY DISSERTATION

This is a statement from ELSEVIER granting permission for use of my articles (20,24,30).
http://www.elsevier.com/about/open-access/open-access-policies/article-posting-policy

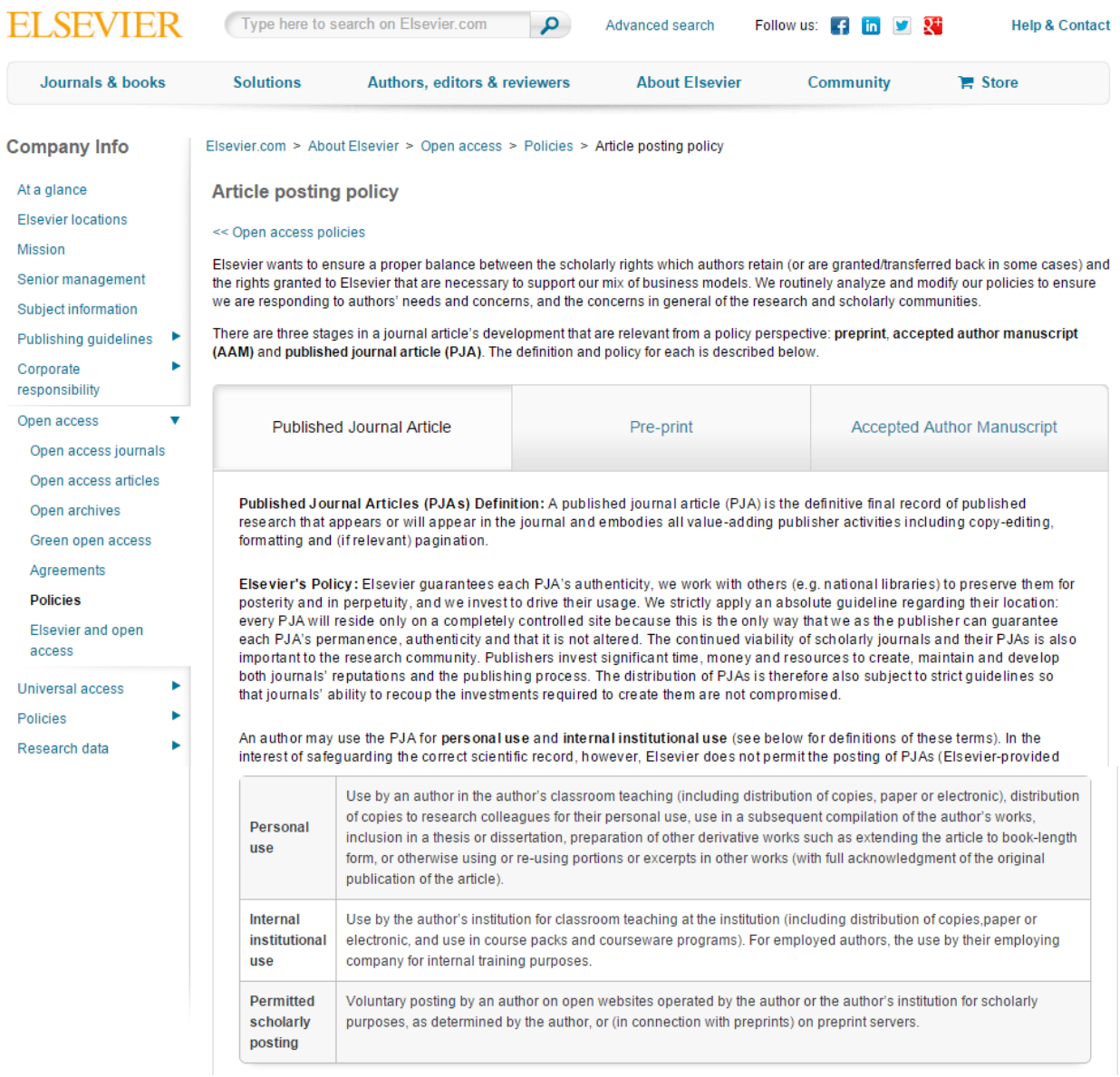

ELSEVIER

Type here to search on Elsevier.com

Advanced search Follow us: Help & Contact

Journals & books | Solutions | Authors, editors & reviewers | About Elsevier | Community | Store

Company Info

- At a glance
- Elsevier locations
- Mission
- Senior management
- Subject information
- Publishing guidelines
- Corporate responsibility
- Open access
  - Open access journals
  - Open access articles
  - Open archives
  - Green open access
  - Agreements
  - **Policies**
  - Elsevier and open access
- Universal access
- Policies
- Research data

Elsevier.com > About Elsevier > Open access > Policies > Article posting policy

Article posting policy

<< Open access policies

Elsevier wants to ensure a proper balance between the scholarly rights which authors retain (or are granted/transferred back in some cases) and the rights granted to Elsevier that are necessary to support our mix of business models. We routinely analyze and modify our policies to ensure we are responding to authors' needs and concerns, and the concerns in general of the research and scholarly communities.

There are three stages in a journal article's development that are relevant from a policy perspective: **preprint**, **accepted author manuscript (AAM)** and **published journal article (PJA)**. The definition and policy for each is described below.

Published Journal Article | Pre-print | Accepted Author Manuscript

Published Journal Articles (PJAs) Definition: A published journal article (PJA) is the definitive final record of published research that appears or will appear in the journal and embodies all value-adding publisher activities including copy-editing, formatting and (if relevant) pagination.

Elsevier's Policy: Elsevier guarantees each PJA's authenticity, we work with others (e.g. national libraries) to preserve them for posterity and in perpetuity, and we invest to drive their usage. We strictly apply an absolute guideline regarding their location: every PJA will reside only on a completely controlled site because this is the only way that we as the publisher can guarantee each PJA's permanence, authenticity and that it is not altered. The continued viability of scholarly journals and their PJAs is also important to the research community. Publishers invest significant time, money and resources to create, maintain and develop both journals' reputations and the publishing process. The distribution of PJAs is therefore also subject to strict guidelines so that journals' ability to recoup the investments required to create them are not compromised.

An author may use the PJA for **personal use** and **internal institutional use** (see below for definitions of these terms). In the interest of safeguarding the correct scientific record, however, Elsevier does not permit the posting of PJAs (Elsevier-provided

Personal use	Use by an author in the author's classroom teaching (including distribution of copies, paper or electronic), distribution of copies to research colleagues for their personal use, use in a subsequent compilation of the author's works, inclusion in a thesis or dissertation, preparation of other derivative works such as extending the article to book-length form, or otherwise using or re-using portions or excerpts in other works (with full acknowledgment of the original publication of the article).
Internal institutional use	Use by the author's institution for classroom teaching at the institution (including distribution of copies,paper or electronic, and use in course packs and courseware programs). For employed authors, the use by their employing company for internal training purposes.
Permitted scholarly posting	Voluntary posting by an author on open websites operated by the author or the author's institution for scholarly purposes, as determined by the author, or (in connection with preprints) on preprint servers.

This is a statement from John Wiley and Sons granting permission for use of my article (23).
http://onlinelibrary.wiley.com/journal/10.1002/(ISSN)1520-6017/homepage/Permissions.html

AUTHORS - If you wish to reuse your own article (or an amended version of it) in a new publication of which you are the author, editor or co-editor, prior permission is not required (with the usual acknowledgements). However, a formal grant of license can be downloaded free of charge from RightsLink if required.

JOHN WILEY AND SONS LICENSE TERMS AND CONDITIONS

Jan 05, 2015

This Agreement between Eric K Lueshen ("You") and John Wiley and Sons ("John Wiley and Sons") consists of your license details and the terms and conditions provided by John Wiley and Sons and Copyright Clearance Center.

License Number	3542740837647
License date	Jan 05, 2015
Licensed Content Publisher	John Wiley and Sons
Licensed Content Publication	Journal of Pharmaceutical Sciences
Licensed Content Title	Interspecies scaling in pharmacokinetics: A novel whole-body physiologically based modeling framework to discover drug biodistribution mechanisms in vivo
Licensed Content Author	Cierra Hall,Eric Lueshen,Andrej Mošat\',Andreas A. Linninger
Licensed Content Date	Nov 21, 2011
Pages	21
Type of use	Dissertation/Thesis
Requestor type	Author of this Wiley article
Format	Print and electronic
Portion	Full article
Will you be translating?	No
Title of your thesis / dissertation	Design of Drug Delivery Methods for the Brain and Central Nervous System
Expected completion date	Jan 2015
Expected size (number of pages)	200

The following four pages are a permission form as well as a statement through email correspondence from Future Medicine granting permission for use of my article (31).

Permission to use Future Medicine Ltd copyright material

Request from:

- Contact name: Eric Lueshen
- Publisher/company name:
- Address:
- Telephone/e-mail: elueshen@hotmail.com

Request details:

- Request to use the following content: Full text and figures, Nanomedicine, Vol. 9, No. 8, Pages 1155-1169.
- In the following publication: As part of thesis
- In what media (print/electronic/print & electronic): Print and Electronic
- In the following languages: All

We, Future Medicine Ltd, grant permission to reuse the material specified above within the publication specified above.

Notes and conditions:

1. This permission is granted free of charge, for one-time use only.
2. Future Medicine Ltd grant the publisher non-exclusive world rights to publish the content in the publication/website specified above.
3. Future Medicine Ltd retains copyright ownership of the content.
4. Permission is granted on a one-time basis only. Separate permission is required for any further use or edition.
5. The publisher will make due acknowledgement of the original publication wherever they republish the content: citing the author, content title, publication name and Future Medicine Ltd as the original publisher.
6. The publisher will not amend, abridge, or otherwise change the content without authorization from Future Medicine Ltd.
7. Permission does not include any copyrighted material from other sources that may be incorporated within the content.
8. Failure to comply with the conditions above will result in immediate revocation of the permission here granted.

Date: 15/01/2015.....

Future Medicine Ltd, Unitec House, 2 Albert Place, London, N3 1QB, UK
T: +44 (0)20 8371 6080 **F:** +44 (0) 20 8371 6099 **E:** info@futuremedicine.com
www.futuremedicine.com

RE: permission for use of my published article (#8207) in dissertation

---

From: **Sam Cavana** (s.cavana@future-science-group.com)
Sent: Thu 1/08/15 3:49 AM
To: Eric Lueshen (elueshen@hotmail.com)

Dear Eric,

We do not have a license available.

Please could you use this email as the license and if there are any questions please do not hesitate to forward them to my email address.

Kind regards,

Sam

Sam Cavana
Reprint Sales Manager

future science group
tel: +44 (0)20 8371 6099 | fax: +44 (0)20 8343 2313 | www.future-science-group.com

email: s.cavana@future-science-group.com

Future Medicine Ltd, Unitec House, 2 Albert Place, London, N3 1QB, UK (registered in England & Wales, No: 4059017); VAT No: GB 833 0029 67

Subject: RE: permission for use of my published article (#8207) in dissertation
Date: Wed, 7 Jan 2015 10:49:48 +0000
From: s.cavana@future-science-group.com
To: elueshen@hotmail.com

Dear Eric,

We would be happy for you to use the article in your dissertation in this instance.

Kind regards,

Sam

Sam Cavana
Reprint Sales Manager

future science group
tel: +44 (0)20 8371 6099 | fax: +44 (0)20 8343 2313 | www.future-science-group.com

email: s.cavana@future-science-group.com

Future Medicine Ltd, Unitec House, 2 Albert Place, London, N3 1QB, UK (registered in England & Wales, No: 4059017); VAT No: GB 833 0029 67

From: Eric Lueshen [mailto:elueshen@hotmail.com]
Sent: 06 January 2015 00:29
To: Sam Cavana
Subject: permission for use of my published article (#8207) in dissertation

Dear Mr. Cavana,

I previously have corresponded with Ms. Hannah Stanwix and Mr. Duc Hong Le who both appear to no longer be at Future Medicine Group according to the response I received after trying to contact them through their email addresses.

I am writing to ask permission to use a previously published article in Nanomedicine of mine in my dissertation (#8207 -- "Intrathecal magnetic drug targeting using gold-coated magnetite nanoparticles in a human spine model"). The website for Future Medicine said the following: "Requests for posting of the final published version on personal, institutional or commercial websites should be directed to the publisher."

Any help regarding this matter would be greatly appreciated as I am wanting to defend my dissertation in the very near future. Thank you.

Best regards,

Eric Lueshen
PhD Candidate & Research Assistant
Laboratory for Product & Process Design
Department of Bioengineering
University of Illinois at Chicago

The following two pages are a statement through email correspondence from American Scientific Publishers granting permission for use of my article (32).

From: Dr. H. S. Nalwa [mailto:nalwa@mindspring.com]
Sent: Wednesday, January 07, 2015 8:27 PM
To: Perumal, Omathanu; eluesh2@uic.edu
Subject: RE: permission to use my accepted manuscript (13-543) in dissertation

Hi Eric:

American Scientific Publishers grants permission to reuse (whole paper/figures) research articles"Implant-Assisted Intrathecal Magnetic Drug Targeting to Aid in Therapeutic Nanoparticle Localization for Potential Treatment of Central Nervous System Disorders" from the Journal of Biomedical Nanotechnology in your forthcoming PhD thesis to be submitted to the University of Illinois at Chicago.

The permission is granted for non-exclusive world English rights limited to print and online formats only. For other languages and media, please reapply separately for each one required. This permission does not include permission for future editions, derivative works, revisions, additional printing, any other electronic forms or medium whether now known or hereafter developed, other languages, or promotional items. Permission is limited one time to the single title specified in your correspondence and single edition of the publication. Reproduction of this material is confined to the purpose for which permission is granted.

H. S. Nalwa, PhD

Publisher

AMERICAN SCIENTIFIC PUBLISHERS

www.aspbs.com

Dr. Hari Singh Nalwa | **Editor-in-Chief**: **Journal of Nanoscience and Nanotechnology** | Web: www.aspbs.com/jnn

Editor-in-Chief: Advanced Science, Engineering and Medicine | **Editor-in-Chief**: Advanced Science Letters

Editor: Encyclopedia of Nanoscience and Nanotechnology (25-Volume set) | Web: www.aspbs.com/enn

American Scientific Publishers | 26650 The Old Road , Suite 208 , Valencia , California 91381-0751 , USA

Phone: (661) 799-7200 | Fax: (661) 799-7230 | Email: nalwa@aspbs.com | Web: www.aspbs.com

From: Perumal, Omathanu [mailto:Omathanu.Perumal@sdstate.edu]
Sent: Wednesday, January 07, 2015 1:04 PM
To: eluesh2@uic.edu
Cc: Dr. H. S. Nalwa
Subject: Re: permission to use my accepted manuscript (13-543) in dissertation

Im forwarding your request to the publisher.

Regards

Om

Om Perumal, Ph.D.

Professor & Head

Dept of Pharm Sci

College of Pharmacy

Box 2202C

Bookings, SD 57007

Director-Translational Cancer Research Center

On Jan 7, 2015, at 3:00 PM, "eluesh2@uic.edu" <eluesh2@uic.edu> wrote:

> Dear Dr. Perumal,
>
> I am writing to ask permission to use an accepted manuscript of mine in the Journal of Biomedical Nanotechnology in my dissertation (13-543 -- "Implant-Assisted Intrathecal Magnetic Drug Targeting to Aid in Therapeutic Nanoparticle Localization for Potential Treatment of Central Nervous System Disorders"). Any help regarding this matter would be greatly appreciated as I am wanting to defend my dissertation in the very near future. Thank you.
>
> Best regards,
>
> Eric Lueshen
> PhD Candidate & Research Assistant
> Laboratory for Product & Process Design
> Department of Bioengineering
> University of Illinois at Chicago

APPENDIX B - MULTIPHYSICS SIMULATION-BASED DETERMINATION OF OPTIMUM MAGNETIC FIELD

The computer platform used to run the COMSOL simulations was a Dell Precision 690 with two Intel Xeon 5300 sequence quad-core processors and 64 GB of RAM. By applying the equations described in this section, we were able to determine the best magnets with optimum magnetic field strength and gradients for the most efficient intrathecal magnetic drug targeting experiments.

Maxwell-Ampere's equation, shown below in Eq. (45), states that an electric current induces a magnetic field around it. However, in our experiments static permanent magnets were used; therefore, the electric current density ($\vec{J}$) and the electric flux density ($\vec{D}$) reduced to the zero vector, which resulted in Eq. (46).

$$\nabla \times \vec{H} = \vec{J} + \frac{\partial \vec{D}}{\partial t} \tag{45}$$

$$\nabla \times \vec{H} = \vec{0} \tag{46}$$

Here $\vec{H}$ represents the magnetic fields intensity (A/m). Since Eq. (46) holds true, it was possible to define a magnetic scalar potential (V_m) by the relationship shown in Eq. (47) due to the vector calculus identity which states that the curl of the gradient of any scalar field is always the zero vector. The magnetic scalar potential equation, Eq. (47), was one of the three main equations used to solve for the static magnetic field of our system.

$$\vec{H} = -\nabla V_m \tag{47}$$

Using the constitutive relations for magnetic fields, Eq. (48), along with Gauss's Law for magnetism, Eq. (**49**), we obtained the magnetic flux conservation equation depicted in Eq. (**50**), which was our second main equation.

$$\vec{B} = \mu_0 \mu_r \vec{H} = \mu \vec{H} \tag{48}$$

$$\nabla \cdot \vec{B} = 0 \tag{49}$$

$$\nabla \cdot \left(\mu_0 \mu_r \vec{H}\right) = 0 \tag{50}$$

Here $\vec{B}$ is the magnetic flux density (T) and μ is the magnetic permeability (H/m) which can also be defined as the product of the magnetic permeability of vacuum (μ_0) with the relative magnetic permeability of the material (μ_r). Eq. (47) and Eq. (**50**) were used to define the magnetic flux conservation boundary condition for both the targeting and barrier magnets. Magnetic insulation boundary conditions, shown in Eq. (51) were used at the boundaries of the air box surrounding the entire spine model system.

$$\vec{n} \cdot \vec{B} = 0 \tag{51}$$

With the boundary conditions set, both the targeting and barrier magnets were then given a remanent flux density value according to their material properties in the positive z-direction (direction in which they were magnetized). The entire *in silico* human spine model was then discretized using an unstructured tetrahedral volume mesh, which resulted in nearly one million mesh cells. The finite-element method was applied to each mesh cell and the entire system of equations solved simultaneously.

VITA

Eric Lueshen

Education:

University of Illinois at Chicago
PhD Candidate in Bioengineering, 8/2009 - present
GPA of 3.82

University of Nebraska-Lincoln
B.S. in Chemical & Biomolecular Engineering, 5/2007

Fellowships, Honors & Awards:

2013 Best Paper Award for Computers & Chemical Engineering (Vol. 54, pp. 97-110).
UIC Graduate Student Council Travel Award to attend ASME NEMB2013 Conference.
Best Research Poster (1st place), 2011 Midwest Biomedical Engineering Career Conference.
CAST Directors Award honorable mention (2nd place), 2010 AIChE National Meeting.
National Science Foundation Fellowship to attend ASME NEMB2010 Conference.
Certificate of Engineer Intern (EI), 2007.
Phi Lambda Upsilon Honorary Chemical Society, 2004-present.
Dean's List Honor, Fall 2006 and Spring 2005, 2007.
Honors Medallion 2005 and 2006 UNL Student Athlete Recognition Banquet.
Big 12 Commissioner's Fall Honor Roll 2003, 2004, 2006.
Big 12 Commissioner's Spring Honor Roll 2004, 2005.
Brook Berringer Citizenship Team Award, 2005 and 2006.
2005 Life Skills Award of Excellence.

Publications in Refereed Journals:

E. Lueshen, A. Linninger. *Backflow-Free Catheters for Efficient and Safe Convection-Enhanced Delivery of Therapeutics.* Medical Engineering & Physics, Under review, January 2015.

E. Lueshen, M. LaRiviere, B. Yamini, A. Linninger. *Computer Simulations and in vivo Convection-Enhanced Delivery of Fluorescent Nanoparticles Demonstrate Variable Distribution Geometry.* Computers & Chemical Engineering, published online September 29, 2014.

E. Lueshen, I. Venugopal, T. Soni, A. Alaraj, A. Linninger. *Implant-Assisted Intrathecal Magnetic Drug Targeting to Aid in Therapeutic Nanoparticle Localization for Potential Treatment of Central Nervous System Disorders.* Journal of Biomedical Nanotechnology, Accepted for publication, Nov. 2013.

E. Lueshen, I. Venugopal, J. Kanikunnel, T. Soni, A. Alaraj, A. Linninger. *Intrathecal Magnetic Drug Targeting using Gold-Coated Magnetite Nanoparticles in a Human Spine Model.* Nanomedicine, published online July 18, 2013.

A. Mošať, ***E. Lueshen***, M. Heitzig, C. Hall, A. Linninger, G. Sin, R. Gani. *First Principles Pharmacokinetic Modeling: A Quantitative Study on Cyclosporin.* Computers & Chemical Engineering, Vol. 54, pp. 97-110, 2013.

C. Hall, ***E. Lueshen***, A. Mošať, A. Linninger. *Interspecies Scaling in Pharmacokinetics: A Novel Whole-Body Physiologically Based Modeling Framework to Discover Drug Biodistribution Mechanisms In Vivo.* Journal of Pharmaceutical Sciences, Vol. 101, Issue 3, pp. 1221-1241, 2012.

O. Ivanchenko, N. Sindhwani, ***E. Lueshen***, K. Prem, A. Linninger. *Methods for Determining Agent Concentration Profiles in Agarose Gel During Convection-Enhanced Delivery*. IEEE Transactions on Biomedical Engineering, Vol. 58, pp. 626-632, 2011.

D. Li, O. Ivanchenko, N. Sindhwani, ***E. Lueshen***, A. Linninger. *Optimal Catheter Placement for Chemotherapy*. Computer Aided Chemical Engineering, Vol. 28, pp. 223-228, 2010.

Refereed Proceedings Articles:

A. Linninger, K. Tangen, I. Venugopal, ***E. Lueshen***. *Simulations of CSF Flow Dynamics in a Global CNS Model With Magnetically Targeted Intrathecal Drug Delivery.* Proc. of the 2013 AIChE Annual Meeting, San Francisco, CA, November 3-8, 2013.

E. Lueshen, I. Venugopal, A. Linninger. *Intrathecal Magnetic Drug Targeting: A New Approach to Treating Diseases of the Central Nervous System.* Proc. of the ASME 2013 2nd Global Congress on Nanoengineering for Medicine & Biology, NEMB2013. Boston, MA, February 4-6, 2013.

E. Lueshen, C. Hall, A. Mošať, A. Linninger. *Physiologically-Based Pharmacokinetic Modeling: Parameter Estimation via Global Optimization for Cyclosporin A*. Proc. of the 21st European Symposium on Computer-Aided Process Engineering, ESCAPE21. Chalkidiki, Greece, May 29 - June 1, 2011.

E. Lueshen, C. Hall, A. Mošať, A. Linninger. *Pharmacokinetic Parameter Estimation of Drug Distribution in an Entire Organism*. Proc. of the 2010 AIChE Annual Meeting, Salt Lake City, UT, November 7-12, 2010.

E. Lueshen, C. Hall, A. Mošať, A. Linninger. *Quality by Design Approach to Pharmacokinetic Modeling. A Case Study on Cyclosporin A*. Proc. Of the 2010 AIChE Annual Meeting, Salt Lake City, UT, November 7-12, 2010.

Oral Presentations:

E. Lueshen, I. Venugopal, A. Linninger. *Intrathecal Magnetic Drug Targeting: A New Approach to Treating Diseases of the Central Nervous System.* ASME 2013 2nd Global Congress on Nanoengineering for Medicine & Biology, NEMB2013. Boston, MA, February 4-6, 2013.

Y. Hsu, I. Venugopal, ***E. Lueshen***, A. Linninger. *Improving Gene Silencing Efficiency in vivo with Organ-wide Quantitative Design of siRNA Infusions*. Oral presentation selected from Exemplary Submitted Abstracts. 2012 RNAi Research and Therapeutics Conference, Boston, MA, May 30-31, 2012.

E. Lueshen, C. Hall, A. Mošať, A. Linninger. *Pharmacokinetic Parameter Estimation of Drug Distribution in an Entire Organism*. AIChE Annual Meeting, Salt Lake City, UT, November 7-12, 2010.

E. Lueshen, C. Hall, A. Mošať, A. Linninger. *Quality by Design Approach to Pharmacokinetic Modeling. A Case Study on Cyclosporin A*. AIChE Annual Meeting, Salt Lake City, UT, November 7-12, 2010.

Poster Presentations:

A. Linninger, K. Tangen, I. Venugopal, ***E. Lueshen***. *Simulations of CSF Flow Dynamics in a Global CNS Model With Magnetically Targeted Intrathecal Drug Delivery.* Proc. of the 2013 AIChE Annual Meeting, San Francisco, CA, November 3-8, 2013.

E. Lueshen, I. Venugopal, A. Linninger. *Implant-Assisted Intrathecal Magnetic Drug Targeting: A New Approach for Treatment of CNS Diseases*. Biomedical Engineering Society (BMES 2013) Annual Meeting, Seattle, WA, September 25-28, 2013.

E. Lueshen, I. Venugopal, A. Linninger. *Feasibility of Intrathecal Magnetic Drug Targeting: Nanoparticle Guidance in a Spinal Canal Model*. Biomedical Engineering Society (BMES 2012) Annual Meeting, Atlanta, GA, October 24-27, 2012.

C. Hall, ***E. Lueshen***, M. Heitzig, A. Linninger. *Pharmacokinetic Scaling and Discovery of In Vivo Drug Distribution Mechanisms with A Novel Whole-Body Physiologically-Based Modeling Framework.* Midwest Biomedical Engineering Career Conference (MBECC), April 1, 2011.

A. Mošať, ***E. Lueshen***, C. Hall, A. Linninger. *Parameter Estimation in Global Pharmacokinetic Models for Drug Delivery*. AIChE Annual Meeting, Salt Lake City, UT, November 7-17, 2010.

C. Hall, ***E. Lueshen***, A. Mošať, A. Linninger. *Parameter Estimation of Drug Distribution in Physiologically-Based Pharmacokinetic Modeling: A Case Study on Cyclosporin-A.* 2010 AIChE Midwest Regional Conference, Sept. 30, 2010.

E. Lueshen, O. Ivanchenko, N. Sindhwani, Y. Rawash, and A. Linninger. *Design of Backflow-Free Catheters Based on Micro-fluid Dynamics*. Biomedical Engineering Society (BMES 2010) Annual Meeting, Austin, TX, October 6-9, 2010.

Teaching Experience:

TA for Dr. Patton's BioE 452 *Biocontrol* course, 1/2013 – 5/2013.
TA for Dr. Linninger's BioE 310 *Biological Systems Analysis* course, 8/2012 – 12/2012.
TA for Dr. Patton's BioE 472 *Models of the Nervous System* course, 8/2010 – 12/2010.
TA for Dr. Hetling's BioE 250 *Clinical Problems in BioEngr* course, 1/2010 – 5/2010.
TA for Dr. Linninger's BioE 310 *Biological Systems Analysis* course, 8/2009 – 12/2009.
Laboratory advisor for several undergraduate students, 8/2009 - 12/2013.

Associations & Activities:

Biomedical Engineering Society, 2009 - present.
Institute of Nanotechnology, 2009 - present.
American Institute of Chemical Engineers, 2003-present.
Student-Athlete, University of Nebraska-Lincoln Football Team, 2003-2007.
Active Member of Football Team Outreach Programs, 2003-2007.

Specialized Skills:

Exceptional precision in designing and conducting scientific experiments.
Technical expertise in numerous engineering and computer programs such as: MATLAB, COMSOL Multiphysics, Mathcad, ANSYS, Fluent, Gambit, Delphi, Aspen Plus, AutoCAD, Photoshop, Microsoft Office (Word, Excel, Powerpoint), among others.
Remarkable presentation and writing skills, along with experience writing grants.
Understanding and experience with various analytic, spectroscopic, and chromatographic techniques such as: HPLC, FTIR, NMR, Mass Spec.
Admirable personal qualities: superior work ethic, excellent communication skills, self-motivated, reliable, organized, dedicated, friendly, thorough.